

**SYNTHESIS, CHARACTERIZATION AND
UTILIZATION OF SUPER PARAMAGNETIC
IRON OXIDE NANOPARTICLES (SPIONs) FOR
SUSTAINED DRUG DELIVERY AND IMAGING**

A THESIS

Submitted by

C. JUSTIN

[Reg. No. 2013199606]

in partial fulfilment for the award of the degree

of

DOCTOR OF PHILOSOPHY



FACULTY OF BIOTECHNOLOGY

SATHYABAMA

INSTITUTE OF SCIENCE AND TECHNOLOGY


JEPPIAAR NAGAR, CHENNAI – 119

JULY 2019

BONA FIDE CERTIFICATE

Certified that this thesis titled “**SYNTHESIS, CHARACTERIZATION AND UTILIZATION OF SUPER PARAMAGNETIC IRON OXIDE NANOPARTICLES (SPIONs) FOR SUSTAINED DRUG DELIVERY AND IMAGING**” is the bona fide work of **Mr. JUSTIN C** [Reg. No: 2013199606] who carried out the Research under my supervision. Further I certify that, to the best of my knowledge the work reported in this has not found part of any other thesis or dissertation on the basis of which a degree or award was conferred on an earlier occasion of thesis of any other candidate.

SUPERVISOR

Signature : 

Name : **Dr. ANTONY V. SAMROT**
M.Sc., M.Phil., M.Tech., Ph.D.,
MABMS.,

Academic Designation : Associate Professor

Department : Department of Biotechnology

University/College/Organization : Sathyabama Institute of Science
and Technology

With address : Jeppiaar Nagar,
Rajiv Gandhi Salai,
Chennai – 600 119, Tamil Nadu,
India.

ACKNOWLEDGEMENT

I am pleased to acknowledge my sincere thanks to the Board of Management of SATHYABAMA INSTITUTE OF SCIENCE AND TECHNOLOGY for their kind encouragement in doing this project and for completing it successfully. I am grateful to them.

I wish to express my sincere thanks to **Dr. S. Sundar Manoharan** Ph.D., Vice Chancellor for his inspiration and consideration regarding my academic requirements. I also wish to express my sincere gratitude to **Dr. T. Sasipraba**, Ph.D., Pro Vice Chancellor, **Dr. S. S. Rau**, MBA., Ph.D., Registrar, **Prof. Igni Sabasti Prabu**, Ph.D., Controller of Examinations and **Dr. B. Sheelarani**, M.S., (By Research), Ph.D., Director-Research, Sathyabama University for their support.

I convey my thanks to **Dr. Ramesh Kumar**, Head of the **Department, Dept. of Biotechnology** for providing me necessary support and details at the right time during the progressive reviews.

I would like to express my sincere and deep sense of gratitude to my Project Guide **Dr. Antony V Samrot**, Senior Lecturer, Department of Biomedical Sciences, MAHSA University, Malaysia, for his valuable guidance, and encouragement which paved way for the successful completion of my project work.

I express my sincere thanks to my Doctoral committee experts, **Dr. T. Thirunala Sundari**, Professor & Head, Department of Industrial Biotechnology, Bharathidasan University, Tiruchrapalli-24, Tamil Nadu

and **Dr. Ganesh Kumar**, Scientist, Sathyabama Institute of Science and Technology, Chennai, Tamil Nadu, for their encouragement, insightful comments and hard questions.

I wish to express my thanks to all Teaching and Non-teaching staff members of the Department of Biotechnology, Sathyabama Institute of Science and Technology who were helpful in many ways for the completion of the project.

I am greatly indebted to the Principal and the staff of **Kristu Janthi College**, Bangalore, where I carried out all the laboratory works. More specifically I am indebted to **Dr. Elcy**, Professor and Head, Department of Biotechnology, **Mr. Binu**, the lab technician, for their unconditional support and guidance. I am grateful to IISc, Bangalore, where I carried out all the instrumental analyses, and to Stellixir Biotech Pvt. Ltd., Bangalore where I carried out experiments in cancer cell lines.

I am thankful to **Dr. C. Valli Nachiyar** the Former Head, Department of biotechnology for having appointed Dr. Antony V Samrot as my research guide. I also express my sincere gratitude to **Mrs. Raji P**, Assistant Professor, Department of Biotechnology, Sathyabama Institute of Science and Technology for her unconditional help and suggestions and **Guanellian Fathers** and **GPN community**, Bangalore without them this work would not be successfully completed.

Sincere thanks to **His Beatitude Moron Mor Baselios Cardinal Cleemis Catholicos** for his patronizing care and love, sincere thanks to His Excellency **Most Rev. Yoohanon Mar Chrysostom**, the former Bishop of Marthandom, for having initiated me in to the field of

science, and to His Excellency **Most Rev. Vincent Mar Paulos** for having permitted me to do Ph.D., and to His Excellency **Most Rev. Thomas Mar. Eusebius** for his constant support by which I continue to become cherished in the ministry of education. Sincere thanks to all my priests' friends especially **Fr. Premkumar, Fr. George C, Fr. Albin, Fr. Jenan Gerald, Fr. Baburaj, Fr. Bernard, Fr. Aruldas, Fr. Crispin Guru, Fr. Isaac Mavaravilagam, Fr. Aby, Bro. Kinna, the staff of St. Joseph's Public School, Chemboor, both Native and Pastoral Parish members.** Sincere thanks to **Rev. Sisters** from the congregations of **DM, SIC, and Sisters of Charity.**

I also thank students **Mr. Padmanaban S, Mr. Sanjay Kumar S, Ms. Ujjala Burman, Ms.Sree Samanvitha, Ms. Sahiti, Ms. Sheryl Ann Philip, Ms. Jenifer Selvarani A, Ms. SaiPriya C, Ms. Chamorthy Sai Sahithya, Saigeetha S, and Srinivasan (KJC Bangalore)** for their support and help which I cherished during the course of my work.

Heartfelt thanks to my beloved **Mother Kunjammal** and my devoted **Father Chellappan** who is in eternal bliss, my brothers **Kirar** and **Jillas**, sisters **Felcine** and **Ranvi**, loving **Brothers-in-law** and **Sisters-in-law**, beloved **Nephews and Nieces** for their constant moral and financial support, care, affection and blessings.

C. JUSTIN

ABSTRACT

In this research work, super paramagnetic iron oxide nanoparticles (SPIONs) were produced, and the precursor iron molecular solution for SPIONs synthesis was optimized. Thus produced SPIONs were subjected for Coreshell-SPIONs synthesis for drug delivery, which had the following four major stages (1) synthesis of SPIONs, (2) functionalization of SPIONs, (3) curcumin loading/tagging, and (4) biopolymer coating (Chitosan). Every stage of the synthesis was analyzed using various microscopic (TEM, SEM, AFM) and spectroscopic (UV Vis, FTIR, Zeta Analyzer, Raman Spectroscopy, GIXRD, PXRD, XPS, SQUID, VSM) analyses. Through spectroscopic techniques mainly the elemental nature and the energy states of elements present all through the Coreshell-SPIONs production was studied. The Coreshell-SPIONs were subjected for drug delivery studies against HCT 116 and HeLa cells. Coreshell-SPIONs were showing IC_{50} at 30 μg and 80 μg concentration against HeLa and HCT 116 cell lines respectively. IC_{50} concentration was subjected for further anticancer studies and analyzed through nuclear staining, flow cytometry and expression of caspase-3 at four time durations: 2 hours, 6 hours, 12 hours and 24 hours. The Coreshell-SPIONs were found to induce cancer apoptosis which was analyzed using quadrant and histogram statistics obtained as per flow-cytometer. Caspase-3 expression was analyzed using caspase-3 expression assay. Further they were evaluated by histogram statistics. SPIONs were also utilized as contrasting agent for X – ray imaging, where it was showing the egg matter clearly. The response of SPIONs to

X-ray was studied with and without applied magnetic field. Later, the SPIONs were subjected for toxicity study against earthworm. It was not found causing any evident activity on morphology but it was causing lipofuscin like accumulation in the animal model.

Key words: SPIONs; Coreshell-SPIONs; Precursor iron molecular solution; Stabilization; Functionalization; Sodium dodecyl Sulphate (SDS); Chitosan; Curcumin loading; Drug carrier; Microscopy; Spectroscopy; Sustained drug delivery; HeLa and HCT 116 cell lines; Four time durations; X-ray imaging; Quills egg; Toxicity assays.

TABLE OF CONTENTS

CHAPTER NO.	TITLE	PAGE NO.
	ABSTRACT	vi
	LIST OF TABLES	xvi
	LIST OF FIGURES	xx
	LIST OF SYMBOLS AND ABBREVIATIONS	xxvii
1	INTRODUCTION	1
1.1	PROPERTIES OF SPIONs	2
1.1.1	Superparamagnetism	2
1.1.2	Surface and Spin Resonance Effects	3
1.1.3	Physical Properties	3
1.1.4	Structural Properties	4
1.1.5	Size of SPIONs	5
1.1.6	Shape of SPIONs	5
1.1.7	Charge of SPIONs	6
1.1.8	Magneto-Optic Property of SPIONs	6
1.2	VARIOUS METHODS EMPLOYED IN SYNTHESIS OF SPIONs	7
1.2.1	Microwave Assisted Method	7
1.2.2	Chemical Co-Precipitation Method	8
1.2.3	Microemulsion Method	8
1.2.4	Hydrothermal Method	9
1.2.5	Sol-gel Method	9
1.2.6	Microbial Methods	10

CHAPTER NO.	TITLE	PAGE NO.
	1.2.7 Green Biosynthesis	10
1.3	SIGNIFICANCE OF SPIONs IN CLINICAL SETTING	10
	1.3.1 Diagnosis	11
	1.3.1.1 Magnetic Resonance Imaging (MRI) Contrast Agents	11
	1.3.1.2 SPIONs as X-ray Enhancers	11
	1.3.1.3 Other Potential Imaging Techniques and Diseases	12
	1.3.2 Therapeutics	13
	1.3.2.1 Hyperthermia	13
	1.3.2.2 Targeted Drug Delivery	14
	1.3.2.3 Other Potential Therapeutics	15
1.4	BENEFITS OF SPIONs IN ENVIRONMENTAL SCIENCES	15
1.5	MULTIFARIOUS USES OF SPIONs IN ENGINEERING AND TECHNOLOGY	16
1.6	PHARMACOKINETICS OF SPIONs	16
	1.6.1 Absorption	17
	1.6.2 Distribution	18
	1.6.3 Metabolism	19
	1.6.4 Excretion	20
1.7	STABILIZATION OF SPIONs	20
	1.7.1 Stabilization While Being Synthesized	21
	1.7.2 Post-synthesis stabilization	21
	1.7.3 Bimetallic Stabilization	22

CHAPTER NO.	TITLE	PAGE NO.
1.8	FUNCTIONALIZATION OF SPIONs	23
1.8.1	Importance of Functionalization	23
1.8.2	Factors of Functionalization	23
1.8.3	Chemicals Known for Functionalization	24
1.8.4	Multi-functionalization	24
1.9	DRUG CARRYING AND DELIVERY	
	EFFICIENCY OF SPIONs	25
1.9.1	Loading of Bioavailable Drugs	25
1.9.2	Loading of Non-Bioavailable Drugs	26
1.9.3	Passive Targeting	27
1.9.4	Active Targeting	27
1.9.5	Magnetic Targeting	27
1.9.6	Drug Release	28
1.10	ENCAPSULATION OF SPIONs	28
1.10.1	Encapsulation of Bare / drug loaded SPIONs	29
1.11	BIOCOMPATIBILITY AND TOXICOLOGICAL PROFILES OF SPIONs	29
1.11.1	Biocompatibility	30
1.11.2	Toxicity	31
1.11.3	Cellular Responses	31
1.11.4	Alteration in Biochemical Pathways	32
1.11.5	Changes in Gene Expression	33
1.11.6	SPIONs Toxicity Assays	33
1.12	SPIONs AVAILABLE IN THE MARKET	34
1.13	OBJECTIVES AND SCOPE	34

CHAPTER NO.	TITLE	PAGE NO.
	1.13.1 Scope of the work	35
	1.14 ORGANISATION OF THESIS	35
2	MATERIALS AND METHODS	36
	2.1 MATERIALS	36
	2.1.1 Synthesis of SPIONs	36
	2.1.2 Coreshell-SPIONs Preparation	36
	2.1.3 <i>In Vitro</i> Drug Delivery	37
	2.1.4 X-ray Imaging	37
	2.1.5 Toxicity Experiment	37
	2.1.6 Tissue Preparation for Histopathological Observations	38
	2.2 METHODS	38
	2.2.1 Standardization of SPIONs Synthesis	38
	2.2.2 Optimization of Synthesis of SPIONs	40
	2.3 PREPARATION OF CURCUMIN LOADED CORESHELL-SPIONs	40
	2.3.1 Synthesis of SPIONs	41
	2.3.2 Functionalization of SPIONs	41
	2.3.3 Curcumin Loading	43
	2.3.4 Method of Encapsulation	43
	2.3.4.1 Preparation of Chitosan Polymer	43
	2.3.4.2 Encapsulation of Curcumin Loaded SPIONs	44

CHAPTER NO.	TITLE	PAGE NO.
2.4	CHARACTERIZATION OF SPION _s SYNTHESIZED AT 0.133% OF PRECURSOR IRON MOLECULAR SOLUTION AND THE CORESHELL-SPION _s	45
2.4.1	Microscopy	45
	2.4.1.1 Transmission Electron Microscopy (TEM)	45
	2.4.1.2 Scanning Electron Microscopy (SEM)	46
	2.4.1.3 Atomic Force Microscopy (AFM)	46
2.4.2	Spectroscopy	46
	2.4.2.1 Ultra Violet Visible Spectroscopy (UV-Vis)	46
	2.4.2.2 Fourier Transform Infrared Spectroscopy (FTIR)	47
	2.4.2.3 Raman Spectroscopy	47
	2.4.2.4 X-ray Diffraction Spectroscopy (XRD)	47
	2.4.2.5 X-ray Photoelectron Spectroscopy (XPES)	47
	2.4.2.6 Nuclear Magnetic Resonance Spectroscopy (NMR)	48
	2.4.2.7 Zeta Potential Analyzer	48
	2.4.2.8 Superconducting Quantum Interference Device (SQUID)	48

CHAPTER NO.	TITLE	PAGE NO.
	2.4.2.9 Vibrating Sample Magnetometer (VSM)	49
2.5	<i>IN VITRO</i> SUSTAINED CURCUMIN DELIVERY AND ASSAYS	49
2.5.1	Anticancer activity	49
	2.5.1.1 MTT Assay for HeLa / HCT 116 cells	49
	2.5.1.2 Nuclear Staining Assay of HeLa and HCT 116 cells	51
	2.5.1.3 Apoptotic Assay of HeLa / HCT 116 cells	51
	2.5.1.4 Caspase-3 Expression Assay of HeLa / HCT 116 cells	53
2.6	X RAY IMAGING	54
2.7	TOXICITY STUDIES	54
	2.7.1 Pretreatment of Earthworm	55
	2.7.2 Treatment with Nanoparticles	55
	2.7.3 Tissue Fixation	55
	2.7.4 Staining (Hematoxylin and Eosin)	56
	2.7.5 Prussian Blue Staining	57
3	RESULTS AND DISCUSSION	58
3.1	SYNTHESIS OF SPIONs	58
	3.1.1 TEM Analysis	58
	3.1.2 UV-Vis Spectroscopy	61
	3.1.3 SEM – EDX	62

CHAPTER NO.	TITLE	PAGE NO.
3.1.4	Fourier Transform Infra-Red Spectroscopy (FTIR)	63
3.1.5	Raman Spectroscopy	64
3.1.6	X-Ray Diffraction Spectroscopy	65
3.1.7	X-Ray Photoelectron Spectroscopy (XPES)	68
3.1.8	Zeta Potential	73
3.1.9	Nuclear Magnetic Resonance Spectroscopy (NMR)	73
3.1.10	Superconducting Quantum Interference Device (SQUID)	77
3.2	SYNTHESIS OF CORESHELL-SPIONS AND THEIR CHARACTERIZATION	80
3.2.1	UV Vis Spectroscopy	80
3.2.2	Fourier Transform Infra-Red Spectroscopy (FTIR)	83
3.2.3	Raman Spectroscopy	86
3.2.4	X-Ray Diffraction Spectroscopy (XRD)	88
3.2.5	Zeta potential	91
3.2.6	Microscopic Analysis	93
	3.2.6.1 SEM	93
	3.2.6.2 AFM	96
3.2.7	X-Ray Photoelectron Spectroscopy (XPES)	96
3.2.8	SQUID Analysis	107
3.2.9	VSM Analysis	111

CHAPTER NO.	TITLE	PAGE NO.
3.3	IN VITRO DRUG DELIVERY ASSAYS	114
3.3.1	MTT Assay	114
3.3.2	Nuclear Staining	114
3.3.3	Apoptotic Assay	117
3.3.3.1	Flow Cytometry Analysis of HeLa Cells	119
3.3.3.2	Flow Cytometry Analysis of HCT 116 Cells	129
3.3.4	Caspase 3 Expression Assay	137
3.3.4.1	HeLa cells	137
3.3.4.2	HCT 116 cells	145
3.4	X RAY IMAGING	152
3.5	TOXICITY STUDIES	153
4	SUMMARY	155
5	CONCLUSION	157
	REFERENCES	159
	LIST OF PUBLICATIONS	175
	CURRICULUM VITAE	176

LIST OF TABLES

TABLE NO.	TITLE	PAGE NO.
2.1	Summary of obtaining six different concentrations of precursor iron molecular solution	39
2.2	Standardization of the dissolution of chitosan in pyridoxine hydrochloride solution	44
3.1	GIXRD Measurement conditions and Peak list of SPIONs Synthesized at 0.133% iron molecular concentration	66
3.2	PXRD Measurement conditions and Peak list of SPIONs synthesized at 0.133% of iron molecular solution	67
3.3	Binding energy states of elements present in SPIONs synthesized at 0.133% (a) Fe (b) Oxygen (c) Carbon	71
3.4	pH values taken for precursor iron molecular solution (before the synthesis of SPIONs) and after the synthesis of SPIONs	74
3.5	NMR spectral values: (a) Spectral values of Carbon present in the precursor iron molecular solution; (b) Spectral values of Carbon present in SPIONs.	76

TABLE NO.	TITLE	PAGE NO.
3.6	NMR spectral values. (a) Spectral values of Hydrogen present in precursor iron molecular solution; (b) Spectral values of Hydrogen present in SPIONs	77
3.7	Tabulation of UV-vis spectral data of the four phases of Coreshell preparation	83
3.8	List of the possible functional groups analyzed in FTIR all through the four phases of core-shell preparation	84
3.9	Table of the complete zeta potential readings which shows the increase of stability in all through the Coreshell-SPIONs preparation and the change of surface charge	93
3.10	Energy Levels of Fe (a) naked SPIONs, (b) after functionalizing with SDS, (c) after loading curcumin, (d) after encapsulating with biopolymer coating	99
3.11	Energy Levels of Oxygen (a) naked SPIONs, (b) after functionalizing with SDS, (c) after loading curcumin, (d) after encapsulating with biopolymer coating	101
3.12	Energy Levels of Carbon (a) naked SPIONs, (b) after functionalizing with SDS, (c) after loading curcumin, (d) after encapsulating with biopolymer coating	103

TABLE NO.	TITLE	PAGE NO.
3.13	Tabulation of the energy level of Mg present in different phases of Coreshell-SPIONs production	104
3.14	Tabulation of the energy levels of Cl, and Na present in different phases of Coreshell-SPIONs production	105
3.15	Energy states of elements summarized from the complete spectra of coreshell-SPIONs production	107
3.16	Tabulation of HeLa apoptosis obtained from quadrant statistics	107
3.17	Comparing HeLa apoptosis obtained in histogram statistics where Annexin V positive (M2) increases while Annexin V negative (M1) decreases as curcumin is released from the coreshell-SPIONs	128
3.18	Comparing HCT 116 apoptosis obtained in histogram statistics where Annexin V positive (M2) increases while Annexin V negative (M1) decreases supporting the response of cells to the slow and steady release of curcumin	136

TABLE NO.	TITLE	PAGE NO.
3.19	Tabulation of histogram statistics of caspase-3 expression in HeLa cells. As the caspase-3 negative cells (M1) decreases caspase-3 positive cells increase (M2). At 24 hours both negative and the positive appear almost equal with a slight variance in expression	144
3.20	Tabulation of histogram statistics of caspase-3 expression in HCT 116 cells. As the caspase-3 negative (M1) cells decreases caspase-3 positive (M2) cells increase. At 24 hours positive appear out-high in caspase expression	151
3.21	Phenotypic changes observed in earthworm	154

LIST OF FIGURES

FIGURE NO.	TITLE	PAGE NO.
2.1	Precursor iron molecular solutions kept in the magnetic field for the synthesis of SPIONs	40
2.2	Cyclo-rotator designed to give specific agitation during functionalization, drug loading and encapsulation	42
3.1	Behavior of SPIONs synthesized at 0.133% precursor iron molecular solution when a bar magnet is moved along (up and down) the reaction tube.	59
3.2	Behavior of SPIONs in a droplet when hanged over the microscopic light. (a) a droplet of SPIONs magnetic field not applied, (b) a droplet of SPIONs magnetic field applied, (c) a single droplet without SPIONs.	59
3.3	TEM images of SPIONs synthesized at six different concentrations of precursor iron molecular solution	60
3.4	UV vis analysis of SPIONs synthesized at 0.133% of iron molecular solution	61

FIGURE NO.	TITLE	PAGE NO.
3.5	SEM image of SPIONs synthesized at 0.133% of precursor iron molecular solution	62
3.6	EDX spectrum of SPIONs synthesized at 0.133% of precursor iron molecular solution	63
3.7	FTIR spectrum for the SPIONs synthesized at 0.133% of iron molecular solution	64
3.8	Raman spectra taken for the SPIONs synthesized at 0.133% of iron molecular solution	65
3.9	Gracing Incident X-Ray Diffraction (GIXRD) of SPIONs synthesized at 0.133% iron molecular concentration	67
3.10	Powder X-Ray Diffraction (PXRD) for SPIONs synthesized at 0.133% of iron molecular concentration	68
3.11	XPES spectra of SPIONs synthesized at 0.133% of iron molecular solution (a) Fe, (b) Oxygen, (c) Carbon	69
3.12	XPES spectra for Cl and its energy states SPIONs synthesized at 0.133% of iron molecular solution (b) the complete spectra of SPIONs	72

FIGURE NO.	TITLE	PAGE NO.
3.13	Zeta Potential value of SPIONs synthesized at 0.133% of iron molecular solution	73
3.14	NMR spectra for Carbon present in the precursor iron molecular solution prepared at 0.133%	75
3.15	NMR spectra for Carbon in the SPIONs synthesized at 0.133% of solution	75
3.16	NMR Spectra for Hydrogen present in the precursor iron molecular solution prepared at 0.133%	76
3.17	NMR spectra for Hydrogen present in the SPIONs synthesized at 0.133% solution	77
3.18	SQUID magnetic analysis: (a) Hysteresis of SPIONs synthesized at 0.133% iron molecular solution; (b) field cooled (FC) magnetization measurement; (c) zero-field cooled (ZFC) magnetization measurement	79
3.19	UV-Vis Spectra of curcumin dissolved in N, N-dimethylformamide	81
3.20	UV – Vis analysis of the four phases of Coreshell-SPIONs preparation	82
3.21	FT-IR analysis of the four phases of Coreshell-SPIONs preparation	85

FIGURE NO.	TITLE	PAGE NO.
3.22	Raman Spectra of curcumin powder and curcumin dissolved in N, N-dimethylformamide	87
3.23	Raman Spectroscopy analysis of the four phases of Coreshell-SPIONs preparation	88
3.24	XRD spectra of curcumin dissolved in N, N-dimethylformaide	89
3.25	XRD analysis of the four phases of Coreshell-SPIONs preparation	90
3.26	Zeta potential analysis of the four phases of Coreshell-SPIONs preparation	92
3.27	SEM – EDX analysis of the four phases of Coreshell-SPIONs preparation	94
3.28	AFM analysis of the four phases of Coreshell-SPIONs preparation	96
3.29	XPES spectra for the energy states of Fe over the four phases of Coreshell-SPIONs preparation	98
3.30	XPES spectra for the energy states of oxygen over the four phases of Coreshell-SPIONs preparation	100
3.31	XPES spectra for the energy states of carbon over the four phases of Coreshell-SPIONs preparation	102

FIGURE NO.	TITLE	PAGE NO.
3.32	XPES energy spectra of Mg present after (a) synthesis of SPIONs, (b) after drug loading, and (c) after biopolymer coating	104
3.33	XPES energy spectra of cl analyzed after (a) Synthesis of SPIONs and (b) after Coreshell preparation. (c) Spectrum for Na	105
3.34	Complete XPES energy spectrum of four phases of Coreshell-SPIONs preparation	106
3.35	Magnetic hysteresis obtained from SQUID for the four phases of Coreshell-SPIONs preparation.	108
3.36	Magnetization measurement of SPIONs (FC mode) through the Coreshell preparation	109
3.37	Magnetization measurement of SPIONs (ZFC mode) through the Coreshell preparation	110
3.38	Magnetic hysteresis obtained from VSM for the four phases of Coreshell-SPIONs preparation	111
3.39	Magnetization measurement obtained from VSM (ZFC mode) for the four phases Coreshell-SPIONs preparation	112
3.40	Magnetization measurement obtained from VSM (FC mode) for the four phases of Coreshell-SPIONs preparation	113

FIGURE NO.	TITLE	PAGE NO.
3.41	MTT assay of Coreshell-SPIONs	114
3.42	Nuclear staining of HeLa cells treated with Coreshell-SPIONs	115
3.43	Nuclear staining of HCT 116 cells treated with Coreshell-SPIONs	116
3.44 – 3.51	Flow cytometry analysis of HeLa apoptosis for Coreshell-SPIONs depicted in quadrant and histogram statistics (3.44 – CPT), (3.45 – UT), (3.46 - 2 hours), (3.47 - 6 hours), (3.48 - 12 hours), (3.49 - 24 hours), (3.50 – comparison of quadrant statistics and (3.51) comparison of histogram statistics	120-128
3.52 – 3.59	Flow cytometric analysis of HCT 116 apoptosis for Coreshell-SPIONs depicted in quadrant and histogram statistics (3.52 – CPT), (3.53 – UT), (3.54 - 2 hours), (3.55 - 6 hours), (3.56 - 12 hours), (3.57 - 24 hours), (3.58 – comparison of quadrant statistics and (3.59) comparison of histogram statistics	129-136
3.60 – 3.67	Caspase 3 Expression assay of HeLa cells treated with Coreshell-SPIONs (3.60 – CPT), (3.61 – UT), (3.62 - 2 hours), (3.63 - 6 hours), (3.64 - 12 hours), (3.65 - 24 hours), (3.66 – comparison of quadrant statistics (3.67) comparison of histogram statistics	137-144

FIGURE NO.	TITLE	PAGE NO.
3.68	Overlay of caspase-3 Expression assay of HeLa cells treated with Coreshell-SPIONs	145
3.69 – 3.75	Caspase 3 Expression assay of HCT 116 cells treated with Coreshell-SPIONs (3.69 – CPT), (3.70 – UT), (3.71 - 6 hours), (3.72 - 12 hours), (3.73 - 24 hours), (3.74 – comparison of quadrant statistics (3.75) comparison of histogram statistics	145-151
3.76	Overlay of caspase 3 Expression assay of HeLa cells treated with Coreshell-SPIONs	152
3.77	X-ray imaging of quail's egg	152
3.78	H&E staining of earthworm exposed to SPIONs	153
3.79	Prussian blue staining of earthworm exposed to SPIONs	154

LIST OF SYMBOLS AND ABBREVIATIONS

AFM	- Atomic Force Microscopy
T _B	- Blocking Temperature
BBB	- Blood Brain Barrier
BSA	- Bovine Serum Albumin
BSA	- Bovine Serum Albumin
C-TAB	- Cetyl Trimethylammonium Bromide
CMC	- Critical Micellation Concentration
CV	- Cyclic Voltammetry
DPX	- Dibutylphthalate Polystyrene Xylene
DMSO	- Dimethyl Sulfoxide
DMEM	- Dulbecco's Modified Eagle Medium
DPBS	- Dulbecco's Phosphate Buffer Saline
EDX	- Energy Dispersive X-ray Spectroscopy
ELISA	- Enzyme Linked Immuno Sorbent Assay
FC	- Field Cooled
FTIR	- Fourier Transform Infrared Spectroscopy
GIXRD	- Grazing Incident X-ray diffraction
g	- grams
HE	- Hematoxylin and Eosin
HeLa	- Henrietta Lacks
HCl	- Hydrochloric acid
IC 50	- Inhibitory Concentration
L	- Liter
MPMS	- Materials Properties and Measurement System

μg	-	microgram
mg	-	milligram
ml	-	milliliter
PS	-	Phosphatidylserine
PXRD	-	Powder X-ray diffraction
PIMS	-	Precursor Iron Molecular Solution
PI	-	Propidium Iodide
SEM	-	Scanning Electron Microscopy
R_{SD}	-	Single Domain Radius
SDS	-	Sodium dodecyl Sulphate.
NaOH	-	Sodium Hydroxide
SQID	-	Super Conducting Quantum Interference Device
SPIONs	-	Super Paramagnetic Iron Oxide Nanoparticles
R_{SPM}	-	Superparamagnetic Radius
TEM	-	Transmission Electron Microscopy
UV – Vis	-	Ultra Violet – Visible Spectroscopy
VSOP	-	Very Small Iron Oxide Particles
VSM	-	Vibrating Sample Magnetometer
VBP	-	Volume of Black Precipitate
XRD	-	X-ray Diffraction Spectroscopy
XPS	-	X-Ray Photon Spectroscopy
ZFC	-	Zero Field Cooled
EPR	-	Enhanced Permeability and Retention
AMF	-	Alternating Magnetic Field
SAR	-	Specific Absorption Rate
ROS	-	Reactive Oxygen Species

CHAPTER 1

INTRODUCTION

The inception of conceptual origins of nanotechnology started in 1950S and through the experimental advances occurred in the following decades, the novelties of nanoparticles of various kinds intrigued the scientific community to contemplate for solutions over the unresolved problems existed in the arena of science and technology. Though the intervention of this inevitable field of science is still at its infancy, especially in the field of medicine, it foreshadows far reaching ends in the scenario of health care treatments. One of the major techniques researched for this purpose is nanoparticle-based theranostics where iron oxide nanocrystals are of vital importance (Xie *et al.*, 2012). Theranostics is a newly incipient thought which involves simultaneous implementation of therapeutic and diagnostic methods for personalized medicine (Schleich *et al.*, 2013). Ever since the realization of the nobility of iron oxide nanocrystals in theranostics, the researchers have been comprehending different methods of synthesis and their surface engineering for the anticipated applications. Among the wide range of iron oxide nanocrystals synthesized through various ways and means, in general, superparamagnetic iron oxide nanoparticles (SPIONs) are preferred for their multifarious use in biomedical applications.

1.1 PROPERTIES OF SPIONs

SPIONs display a variety of unusual and interesting properties that are not present in bulk systems. The unique properties of SPIONs include, superparamagnetism, surface and spin resonance effects, magneto-optic phenomenon, morphological properties, dipole moment, easy axis orientation

1.1.1 Superparamagnetism

Superparamagnetism occurs when a ferri/ferromagnetic material is reduced in size below about 50nm in the largest dimension. At any temperature, all the magnetic ions in the nanoparticle are locked together and produce a large permanent magnetic dipole moment. However, for temperature higher than a so-called “blocking” temperature, T_B , the moment flips 180° very rapidly and the resulting average moment reaches near zero. Only for temperatures below T_B does the moment stay fixed in one direction during the time of measurement. Thus the particles exhibit a ferromagnetic-like response for temperatures below T_B , but possess a paramagnetic-like property above T_B . The “super” part of superparamagnetism arises from the large magnetic moment of the entire magnetic ions which aligns in the field, where as in normal paramagnetism only the small moments of single ions are aligning in the field (Heiman 2009). On removal of the field the magnetic moments of SPIONs relapse back to their unique easy axis positions owing to their longitudinal and transverse relaxivities (Kandasamy *et al.*, 2015) resulting in zero magnetic remanence and zero coercivity.

1.1.2 Surface and Spin Resonance Effects

Large surface to volume ratio is one of the distinctive properties of all kinds of nanoparticles in general. The magnetic properties of a nanostructured superparamagnetic particles are strongly dependent on surface layer (Nedkov *et al.*, 2006). Since surfaces of SPIONs are at their reduced sizes are so reactive due to the increased surface area-to-volume ratio. The magnetic properties of a nanostructured superparamagnetic particle are strongly dependent on the surface layer. The interpretation of this influence vacillates between a critical “finite size effect” and surface spin disorder (Nedkov *et al.*, 2006). Unusual spin resonance effects arise from the spin disorder which is due to the lower coordination of the surface atoms. Broken exchange bonds would produce a spin glass (SG) like state of spatially disordered spins in the surface cations with high anisotropy surface layers. The degree of spin canting depends on the particle size. Spin canting phenomenon is observed especially in ultrafine maghemite particles (Linderoth *et al.*, 1994).

1.1.3 Physical Properties

Physical and structural properties of SPIONs depend on the characteristic synthesis methods employed and the very elemental nature of reagents used for synthesis. Temperature and pH also considerably influence the physical and structural characteristics of SPIONs. SPIONs of transition elements exhibit adverse change in the very chemistry, for instance, magnetite (Fe_3O_4) into meghamite ($\gamma\text{-Fe}_2\text{O}_3$). Both nanoparticles are crystalline in structure, and each is made of a magnetic domain (Yadollahpour *et al.*, 2016). Magnetic nanocrystals appear as single-core particles and multi-core nanostructures (Bogren *et al.*, 2015).

1.1.4 Structural Properties

There are at least seven varied crystalline phases in ferrous and ferric metal oxide particles. Among them the most common are magnetite (Fe_3O_4), hematite ($\alpha\text{-Fe}_2\text{O}_3$), maghemite ($\gamma\text{-Fe}_2\text{O}_3$), and Fe_{1-x}O (wustite); the less commonly found are $\beta\text{-Fe}_2\text{O}_3$ and $\varepsilon\text{-Fe}_2\text{O}_3$ phases and the low temperature rhombohedral structure (Tharani *et al.*, 2015). Among the various types investigated, magnetite and maghemite are noteworthy. The two differ from each other in the final structure; one occupies positions in the octahedral and tetrahedral sites, and the other, maghemite, has cationic vacancies in the octahedral position (Lodhia *et al.*, 2010). Gamma ferric oxide is a spinel, and is usually assumed to have a collinear magnetic structure consisting of two sublattices (Morrish *et al.*, 1976). The inverse spinel crystal configuration is the most common case of maghemite and general formation of hematite is found to be rhombohedrally hexagonal (Ashraf *et al.*, 2017), and cubic crystal lattice with three orthogonal easy axes. Those axes are accepted choice to define the particle's placement in space. The magnetic moment minimizes its internal potential energy (anisotropy energy) when it is focused on along one of the axes (Dolgovskiy *et al.*, 2015). Maghemite nanoparticles are generally pertinent in biomedicine due to their outstanding magnetic properties. It is typically described both in a cubic system (space group $P4_3 32$) with disordered Fe vacancy or in a tetragonal system (space group $P4_1 2_1 2$) with full site ordering and $c / a \approx 3$. Magnetite and maghemite have analogous spinel crystalline configuration, therefore identical electron diffraction pattern (Yadolhpour *et al.*, 2017).

1.1.5 Size of SPIONs

Two of the most significant magnetic scale measurements that describe magnetic NP structures are the superparamagnetic radius (R_{SPM}) and single domain radius (R_{SD}). With reference to particle size, the investigators employed on IONPs in medicine and biology – specially in the MRI community – use an informal organization divided into different ranges as follows: below 10 nm, very small superparamagnetic iron oxide NPs (VSPIONs); between 10 and 50 nm, ultra-small superparamagnetic iron oxide NPs (USPIONs); and between 50 and 180 nm, superparamagnetic iron oxide NPs (SPIONs). Although this cataloging might be suitable only for collecting some size choices presenting similar circulation and relaxation properties for precise applications, IONPs are persistently mentioned to in the literature as SPIONs (Cortajarena *et al.*, 2014) if magnetic hysteresis occurs at zero magnetic remanence.

1.1.6 Shape of SPIONs

The modification in the shape of magnetic nanostructures has been used to improve r_2 relaxivity. Faceted CoFe_2O_4 show higher relaxivity than that of spherical CoFe_2O_4 (Jun *et al.*, 2005). Shape and chemical structure strategies range considerably from particle suspensions, sheets, tubes, shells, and arrays (Shubayev *et al.*, 2009). On the biological side, the shape of a nanoparticle decides the magnitude to which the nanoparticle will interrelate with membrane receptors and henceforth the amount of internalization (Cortajarena *et al.*, 2014).

1.1.7 Charge of SPIONs

Charge also governs a major role in *in vivo* system. Since subatomic particles are with respective charge the dissemination of these particles in the body and their vital parameter affecting internalization of nanoparticles in their target cells depends on their surface charge. The surface charge of nanoparticles provides a sign of their colloidal permanency. Either the nanoparticles having high positive or high negative zeta potential show better dispersion and good stability. Moreover, such particles do not agglomerate on storage (Wahajuddin *et al.*, 2012).

1.1.8 Magneto-Optic Property of SPIONs

It is reportedly said (Apreotesei *et al.*, 2008) that in the applied magnetic field the ferrofluid befits anisotropic. Their anisotropy is manifested depending on at least the four of the following properties, (1) mechanical properties; (2) electrical properties; (3) magnetic properties; and (4) optical properties. Furthermore, the direction of the applied magnetic field and the intensity of the magnetic field applied are relevant in anisotropy. The analysis of magneto-optical properties (linear dichroism and linear birefringence) in ferrofluids is a way to emphasize and evaluate the structuring of ferrofluids in the presence of applied magnetic field. Such a phenomenon arises due to aggregates of particles that occur at a relatively low density within the fluid (Ziyun *et al.*, 2006). Magnetically induced particle chaining should be considered as one of the main causes of the linear dichroism and birefringence in concentrated ferrofluids (Jian *et al.*, 2004). The relaxation of birefringence in ferrofluids is adopted as a tool for testing the spatial

structure while functionalizing them with poly vinyl alcohol base for drug delivery purpose (Apreotesei *et al.*, 2007). Polarized Microscopy, named for numerous applications, is one of the instrumental tools for observing the phenomenon of birefringence (Delly 2008). Moreover, a small strong magnet could be used to wave back and forth around the lower end of the objective to study a magnetic sample. Anything magnetic will 'wave back' and them be studied (Delly 2008). Birefringence which is an optical phenomenon and the associated photosensitive properties show a significant part in quantum science and its forth coming uses in biomedical applications. Nonlinear processes which is an important area in theoretical physics is also highly relevant in the studies of iron oxide nanoparticles, along with their numerous applications in medical diagnostics (Zhang *et al.*, 2015).

1.2 VARIOUS METHODS EMPLOYED IN SYNTHESIS OF SPIONs

There are different ways and means developed for the synthesis of SPIONs. The basic strategies involve physical methods, wet chemical methods, and microbial methods. Each technique has its own advantages and disadvantages. There is a greater influence on the various properties of SPIONs depending on the selection of techniques employed for synthesis.

1.2.1 Microwave Assisted Method

In microwave assisted method the substance is heated uniformly. It is done through a glass/plastic reaction vessel. Microwave assisted method would lead to a homogenous nucleation. It also leads to

shorter crystallization period. In comparison with other conventional heating methods microwave assisted method is more preferable. Because, microwave assisted method is beneficial for the synthesis of uniform colloidal iron oxide nanoparticles. (Hasany *et al.*, 2012).

1.2.2 Chemical Co-Precipitation Method

Chemical co-precipitation technique is the simplest chemical pathway to obtain SPIONs. Either magnetite (Fe_3O_4) or maghemite ($\gamma\text{Fe}_2\text{O}_3$), are synthesized by co-precipitating stoichiometric combination of ferrous salts and ferric salts in an aqueous medium. The thermodynamics of the reaction require the ratio of 2:1 for $\text{Fe}^{2+}/\text{Fe}^{3+}$, and the pH between 8 and 14 (Lodhia *et al.*, 2010). Both pH and ionic strength affect the chemical conformation of the particles. It also affects the surface properties of the particles. Accordingly, the electrostatic surface charge/properties of the particles could be tuned in accordance with required application of SPIONs. Alterations of this technique sanction for the production SPIONs in the presence of dextran polymer; or else any additional substance that renders the magnetic nanoparticles biocompatible and thus make this technique chiefly suitable for *in vivo* medical related applications (Tartaj *et al.*, 2003).

1.2.3 Microemulsion Method

Microemulsion method is otherwise called two-phase method. Mainly two immiscible (oil and water) phases are employed to form SPIONs. Stabilizing agents are another prerequisite elements for the better synthesis of SPIONs. In microemulsion method a single monolayer is formed at the interface between two immiscible phases.

For instance, using polyvinyl pyrrolidone as surfactant (Mitchel *et al.*, 2014) SPIONs can be synthesized. Metal nanoparticles formed in microemulsion method are not always morphologically same and would be varying with internal structures (Morsy 2014).

1.2.4 Hydrothermal Method

In hydrothermal method, organometallic precursors, such as iron acetylacetonate or iron carbonates, are thermally decomposed in the presence of different surface surfactants. Typically, this method is performed in an aqueous solvent at temperature above 200° C (Cordova 2012). Hydrothermal method relies on the ability of water to hydrolyze and dehydrate metal salts on elevated conditions, and the very low solubility of the resulting metal oxides in water at these conditions to generate supersaturation (Hasany *et al.*, 2012).

1.2.5 Sol-gel Method

Traditionally sol-gel technique employs the procedure of metal alkoxide precursors that readily undergo catalyzed hydrolysis and leading to condensation to arrange the precursors a sol of iron oxide elements per nanoscale sizes. Transition metal oxide precursors also are employed in synthesizing Fe₃O₄ (Gash *et al.*, 2000). Sol-gel iron oxide constituents are equipped in the Fe₂O₃ – SiO₂ structure might exhibit precise a number of novelties in SPIONs; (1) magnetic uniqueness (2) electrical uniqueness and, (3) catalytic uniqueness. By means of diverse approaches, iron oxide nanoparticles are in glass, polymers, LB films, zeolites, clays and mesoporous silicate have been organized (Jitianu *et al.*, 2001).

1.2.6 Microbial Methods

Magnetotactic microorganisms, a collection of Gram-negative prokaryotes, have confirmed capability to combine fine metal oxide nanoparticles in the dimension range of 50 – 100 nm. These microbial iron oxide magnetic nanoparticles are shielded within the microbial system phospholipid coatings. Magnetic nanoparticles formed accordingly are more biocompatible. Henceforth they are advantageous for number of biological applications (Xiaming *et al* 2012).

1.2.7 Green Biosynthesis

Green biosynthesis method uses (BS) brown seaweed (*Sargassummuticum*). The adding of ferric chloride solution as iron precursor to the BS extract comprising sulphated polysaccharides as a chief module which has sulphate, hydroxyl and aldehyde assemblage can effect the reduction of Fe^{3+} and stabilization of nanoparticles (Mahdavi *et al.*, 2013).

1.3 SIGNIFICANCE OF SPIONs IN CLINICAL SETTING

The fabulous phenomenon of SPIONs is investigated for various clinical applications. There are single-core and multi-core iron oxide nanoparticles. Among them the single-core particles with sizes ranging from few nanometers are highly relevant in biomedical applications. The said multi-core particles with their sizes ranging up to few micrometers could also be found worthy of many kinds of biomedical applications. All such particles are relevant in the fields of diagnosis (ex. MRI), therapy (drug delivery), and imaging (ex. X-ray) etc. (Bogren 2015).

1.3.1 Diagnosis

1.3.1.1 Magnetic Resonance Imaging (MRI) Contrast Agents

In common, MRI is a biomedical imaging method. It is used to image soft muscles of animal body in very resonant portions in two dimensional as well as three dimensional spaces. The hydrogen nucleus existent in the liquid content of the body plays an essential part in gaining MRI descriptions dependent on their communication with the applied magnetic field, applied radiofrequency signal and also with regard to their relaxation time. There are two relaxation times mainly observed: (1) T1 (longitudinal – spin – lattice relaxation) and (2) T2 (transverse – spin –spin relaxation) relaxation times. The two relaxation times are dependent on the duration needed for the modules of respective magnetization vectors. Necessarily, in both cases, they are to return to their original thermal equilibrium state. Both T1 and T2 relaxations can be enriched by SPIONs separately as positive contrast and negative contrast and also as dual-mode MRI contrast enhancement (Kandasamy *et al.*, 2015). Moreover, among the number of formulations with SPIONs investigated for enhancing MRI contrast, iron oxide nanoparticles to which curcumin was firmly bound also are characterized for owing good properties as MRI contrast agent (Magro *et al.*, 2014).

1.3.1.2 SPIONs as X-ray Enhancers

Diverse mechanisms of interaction between X-rays and NPs are predictable bestowing to NPs elemental nature (Retif *et al.*, 2015). Superparamagnetic iron oxide nanoparticles (SPIONs) are thought to be

good candidates as X-ray enhancers. When such enhancers are employed the dose of the applied radiation is tremendously decreased. Hence SPIONs are investigated for this purpose of low-dose radiation therapy. It is slowly getting momentum in the research field. To make it more effective mixed-phase-composition of SPIONs are preferred - (γ -Fe₂O₃) (1-x) (Fe₃O₄) x and sizes between 9 and 20 nm size particles are researched for this purpose (Klein S, *et al.*, 2014). The density packed metal particles can selectively scatter radiations and they have the ability to absorb radiations of high energy gamma or X-ray radiations. This paves way for better aiming of animal cellular components present within the cancer tissues. Thus SPIONs synthesized in the mixed phase are able to allow the removal of more localized and consolidated damage through low dose radiation therapy (Kwatra *et al.*, 2013).

1.3.1.3 Other Potential Imaging Techniques and Diseases

The SPIONs are adjoined with supplementary contrast agents like fluorescence tags and dyes, and very smaller scale quantum dots, *etc.* Such kind of formulation is interested for the imaging of tumor cells/muscles/tissues. The technique could be well developed combining the techniques like, (1) fluorescence imaging technique, (2) near infra-red (NIR) imaging technique, (3) computed tomography (CT), (4) ultrasound imaging technique, (5) positron emission tomography (PET) technique, (6) single photon emission computed tomography (SPECT) technique *etc.* (Kandasamy *et al.*, 2015), Diagnosis in immunological ailments, cardiovascular and cerebrovascular illnesses, tumor analysis *etc.* could be tracked by using the above techniques.

1.3.2 Therapeutics

1.3.2.1 Hyperthermia

In magnetic fluid hyperthermia (MFH) SPIONs are intravenously injected into the body. When they are designed and used as mediators they can selectively diffuse into cancerous tissue. SPIONs get heated up under the application of high-frequency alternating magnetic field (AMF). Through this technique temperature at a particular site of the cancer tissue is increased. Rising temperature of the tumor cells at 42 – 45⁰C is enough for initiating apoptosis without affecting the surrounding good and healthy tissue. The generated raised heat can be regulated by using SPIONs more specifically with an adjustable Curie temperature. This is possible if SPIONs are tuned/ designed by changing their chemistry, crystallinity, particle size and shape, and different surface modifications (Choi *et al.*, 2011). One of the main parameters in this regard is specific absorption rate (SAR). It is a parameter which measures qualitatively/quantitatively the efficacy of SPIONs which in essence converting AMF into heat. This parameter is basically based on both Brownian and the Neel relaxations of individual SPIONs (Kandasamy *et al.*, 2015). The iron oxide nanoparticle concentration required for efficient hyperthermia generally greater than 18 mM (=1 mg/ml) of Fe (Zhang *et al.*, 2014). Furthermore, the heating potential still is powerfully reliant on the size of the particle shape of the particle and uniformity of the particle which are essential in temperature control (Tartaj *et al.*, 2003). Intrinsic properties like anisotropy value, easy axis orientation and extrinsic properties like AC amplitude, AC field frequency, role of dipole interactions are also major

concerns in regulating temperature. Some initial researches have confirmed that the amalgamation of radiation with hyperthermia leads to a higher level results in tumor depletion (Gupta *et al.*, 2007). Such a kind of therapy is reported to be in phase II trial for the patients of glioblastoma multiform (GBM) (Hauff *et al.*, 2010).

1.3.2.2 Targeted Drug Delivery

Human body with numerous physiological and plenty of cellular barriers. It is a highly a multifaceted complex living system. Therefore, the success of targeted drug delivery depends on the design/tuning of the iron/metal core and the complete coreshell-SPIONs which contains the payload. The payload could be specific genes, desired proteins, preferred chemotherapy drugs, or else the combination of any of these molecules (Kievit *et al.*, 2011). Moreover, some curcumin like potential drugs which are of poor bioavailability can be made more bioavailable if carried by SPIONs and delivered at the desired location. Drug carrying systems must meet minimum biocompatibility requirements. Foreign materials that enter the body can induce an immediate response from the immune system to remove it from the body. Additional steps are required to reduce premature metabolism, immunological reactions, rapid excretion and specific and nonspecific toxicities of the material. One common method to increase the biocompatibility is to coat the particles with a biocompatible material (Bolden *et al.*, 2008). For a better administration the coreshell-SPIONs must be small and must be in the desired colloidal state. In such cases the resultant larger surface curvature and obtained surface free energy, in turn can promote the SPIONs particle dissolution in to the *in*

vivo system. Therefore, the chemical stability and the other parameters of the coreshell-SPIONs are the key parameters when injected in biological system (Tombacz *et al.*, 2013). There are several physiological barriers to be overcome. The barriers to be noted are liver, kidneys, and spleen. Devising to bypass these barriers is one of the major challenges in drug delivery applications. It demands tuning of Coreshell-SPIONs chemistry, their size and the strategies which promote maximization of blood half-life and designing to navigate in the biological system (Kievit *et al.*, 2011).

1.3.2.3 Other Potential Therapeutics

Cellular labeling and & targeting, cell separation, transfection (magnetofection), tissue repair, bio-sensing, immunotherapy, to regenerate bone tissue, activation of naïve T cells are some of the therapeutic approaches researched in combination with SPIONs. Other than the said therapeutics the desirable therapeutics are photodynamic therapy in combination with SPIONs, photothermal therapy in combination with SPIONs, sonodynamic therapy in combination with SPIONs *etc* are investigated (Gupta *et al.*, 2007, Huang *et al.*, 2013).

1.4 BENEFITS OF SPIONs IN ENVIRONMENTAL SCIENCES

Magnetism is one of an exceptional physical property that unconventionally aids in water decontamination. The electron distribution in the valence band is highly advantageous for this purpose. Adsorption processes in combination with magnetic parting has consequently been used broadly in water management and for eco-

friendly tenacities. The main advantage of this technology is that it can clean out a mass of wastewater in a very short period of time and produce no contaminants. The important constituents of concern in wastewater are suspended solids, pathogens, priority pollutants etc. Iron oxide NPs can be a good photocatalyst absorbing visible light, compared with commonly applied TiO_2 which absorbs wave lengths of UV light. Varied types of Fe (III) oxides have been proposed, such as $\alpha\text{-Fe}_2\text{O}_3$, $\gamma\text{-Fe}_2\text{O}_3$, $\alpha\text{-FeOOH}$, $\beta\text{-FeOOH}$, and $\gamma\text{-FeOOH}$, to degrade organic pollutants and reduce their toxicity due to enhanced photocatalysis effect (Xu *et al.*, 2012).

1.5 MULTIFARIOUS USES OF SPIONs IN ENGINEERING AND TECHNOLOGY

Iron oxide nanoparticles, other than the above biological and environmental sciences, are desired for nanocoatings, nanocomposites, nanoscale sensors, smart materials, additives in catalysts and lubricants, fuel cells, composite fillers, nanofibers, printed electronics, nanoscale memory, nanowires, spintronics, quantum dots etc.

1.6 PHARMACOKINETICS OF SPIONs

The fate of SPIONs, i.e., toxic or biocompatible *in vivo* is determined by investigating their pharmacokinetics which includes absorption, distribution, metabolism, and excretion. There are two central factors that govern the pharmacokinetics: (1) surface characteristics of SPIONs and (2) hydrodynamic size of SPIONs (Nandwana *et al.*, 2015). Based on bio-kinetics of iron oxide particles,

the sizes of 10 – 100 nm are ideal for *in vivo* drug delivery/targeting (Shubayev *et al.*, 2009).

1.6.1 Absorption

SPIONs desired in the medical arena which are injected intravenously either for diagnosis or for curative purposes have to cross the vascular endothelium. Vascular endothelium is a primary barrier which has to be crossed by the SPIONs in order to reach the target site. (Wahajuddin *et al.*, 2012). The success of this technique depends primarily on the development of biocompatible SPIONs. In order to make biocompatible the researchers tend to functionalize them. If functionalized for the specific need SPIONs with that particular domain are capable of better distribution and intracellular uptake by the target cells/tissues. It is influenced by numerous aspects including their size, surface-area-to-volume-ratio, the specific physiochemical and required biochemical properties of the encapsulating shell/biomolecule, and predominantly the cell type too (Cengelli *et al.*, 2006). Upon administration of SPIONs into the blood stream, the opsonization process occurs. To avoid this event, SPIONs are coated with organic layer such as surfactants and polymers or inorganic species such as silica and carbon. This additional layer can increase the circulation time and colloidal stability (Yadollahpour 2015). Cells are found to effectively uptake the aminodextran coated particles which are positively charged. There also found minimum uptake of particle coated with dextran which are of neutral charge. Further the researchers found low uptake of negatively charged DMSA coated particles (Nandwana *et al.*, 2015). There are various mechanisms involved in intracellular

uptake/internalization of iron oxide nanoparticles. To be more specific they are phagocytosis (facilitated by mannose, biological complements, targeted scavenger receptors), endocytosis (clatrin- and calveolin-mediated, fluid-phase) and diffusion (Shubayev *et al.*, 2009). Polyethylene glycerol (PEG) coated particles has been shown to delay macrophages particles phagocytosis, potentially prolonging circulation time (Edge *et al.*, 2016).

1.6.2 Distribution

While the particles are absorbed into the body, either for diagnosis or for therapeutics, obviously they are distributed intercellular or intracellular levels according to their intended utilities. Widespread dissemination of SPIONs in numerous target organs, structures, cells, muscles and tissues, including the heart, liver, spleen, lungs, kidney, brain, stomach, small intestine, and bone marrow are found positive for the uptake of SPIONs in the recent research reports. However, the concentration of SPIONs was highest in liver and spleen. Such highest concentration is thus validating additional noticeable remedial effects of SPIONs in these organs (Wang *et al.*, 2010). Unwanted accumulation of particles in these organs would happen 'due to higher dosage' (Edge *et al.*, 2016) leading to lethal effects. In case of intracellular levels, as cells divide over time the daughter cells are exposed to relatively low concentration of NPs due to the fact that highly stable SPIONs concentration gets diluted with successive cell divisions; this could affect various cellular processes such as cellular uptake, cell viability and cell toxicity. The successive dilution or distribution of SPIONs also would result in cellular perturbations including the

modulation of actin cytoskeleton (Neenu *et al.*, 2010). Furthermore, the other factors like adhesion capacity, endocytosis behavior and effect on cytoskeleton organization etc. are important when SPIONs are used in vivo (Gupta *et al.*, 2004).

1.6.3 Metabolism

Rapid clearance of SPIONs is an essential aspect after their distribution. The clearance of SPIONs from the systemic circulation is a primary prerequisite. It is accomplished principally by the action of macrophages present in liver and also in spleen. Generally, clearance and opsonization of SPIONs depend on their sizes and surface characteristics (Lei *et al.*, 2013). After cellular uptake, it is reported that SPIONs commonly reside in endosomes/lysosomes. In endosomes/lysosomes they decompose into free irons. Such irons which slowly released to the cytoplasm. Then they eventually contribute to the total cellular iron pool (Lei *et al.*, 2013). In fact, iron cations are essential for normal cell cycle and growth. Though they are essential in this aspect but adversely metabolized or catabolized SPIONs can lead to the increase of concentration in the intra cellular environment. There SPIONs could behave intracellular unbound iron. Such a phenomenon might be catastrophic for the neighboring cells and eventually leading cell injury or death. Another possible mechanism involved in SPION cytotoxicity is related to the development of reactive oxygen species (ROS). The possible ROS could be hydrogen peroxide, hydroxyl radicals, hydroperoxyl radical and superoxide anion (e.g. H_2O_2 , OH , HO_2 , O_2) which provide oxidative stress (Klein *et al.*, 2012). Hydrophobic groups on the surface of magnetic nanostructures induce

agglomeration upon injection, leading to rapid removal by the reticuloendothelial system (RES). The rate of clearance, however, can be reduced by modifications of surfaces with coatings which resist RES interactions (Nandwana *et al.*, 2015).

1.6.4 Excretion

Therefore, it is essential that SPIONs must be chemically highly stable and must be oxidation resistant in a biological system without compromising on cellular damage. Such particles would be expelled or excreted out of the body with very less toxic effect. Both the circulation and the eventual *in vivo* fate of IONPs inside the body are also determined by particle size and shape for a greater extend (Cortajarena *et al.*, 2014). Kidney is the desirable pathway for the excretion of SPIONs from biological systems. While excretion happens through kidney there involves nominal intracellular catabolism. Such intracellular catabolism may reduce the probability of generating insignificant amount of reactive oxygen species. Hence associated toxicity would be reduced. Renal excretion also represents the harmless means of the eradication of SPIONs. However, several factors as noted earlier (a) the shape, (b) hydrodynamic size, (c) surface coating, and (d) surface charge of SPIONs play a key part in regulating their renal clearance (Wahajuddin *et al.*, 2012).

1.7 STABILIZATION OF SPIONs

Stabilization of magnetic particles is an essential aspect when needed for biomedical applications. It could be achieved by playing on one or both of the two repulsive forces: (1) electrostatic and (2) steric

repulsion (Laurent *et al.*, 2008). Primarily there are two ways followed to synthesize stabilized SPIONs: (1) Synthesizing of SPIONs in the presence of stabilizing agents and, (2) SPIONs coated after synthesis with organic polymers, organic surfactants, inorganic metals like gold, inorganic oxides like silica and carbon, and bioactive molecules and structures such as liposomes, peptides, and ligand/receptors (Shubayev *et al.*, 2009).

1.7.1 Stabilization While Being Synthesized

SPIONs synthesized in the micro emulsion method show comparatively higher stabilization. Because the hydrophobic and hydrophilic parts of the micro emulsion immiscible phases play major role in stabilizing the SPIONs while being synthesized. The major drawback of such methods is regarding the removal unreacted precursors which are intricate in the final byproduct (Kandasamy *et al.*, 2015). The emulsifying agents work as capping agents for SPIONs. Hydrophobic SPIONs are synthesized by co-precipitating method the iron medium containing oleic acid (Schleich *et al.*, 2013). SPIONs are synthesized synergistically with folic acid called SPIO-FA.

1.7.2 Post-synthesis Stabilization

Since the surfaces of SPIONs are highly reactive. They are coated with surfactants like oleic acid, lauric acid, alkane sulfonic acids, alkane phosphonic acids, capping agents/polymers like to prevent agglomeration in colloidal solution, and to maintain the size and shape of SPIONs. Coating with such stabilizing agents are called steric stabilization. Fe₃O₄ SPIONs coated with dimercaptosuccinic acid

(DMSA) by a ligand exchange process are said to be higher in colloidal suspension stability dispersed in water (Teran *et al.*, 2012). Adsorption of polyacrylic acid (PAA) at pH~8 shifts the zeta potential of magnetite from 0 to – 40 mV. SPIONs coated with polyvinyl alcohol (PVA) appears both functionalized and stabilized for lading of doxorubicin for cancer treatment. Coating mercapto-silica on magnetite increases particle size, surface area, and chemical stability. It also maintains the magnetic property. Silica coating electrostatically stabilizes the SPIONs using negative charges (Maurizi *et al.*, 2015), SPIONs are coated with dextran for clinical cancer imaging (McCarthy *et al.*, 2009). Smooth and jagged-shaped SPIONs coated with gold increased in stability providing the zeta potential value around –35mV (Mahmoudi *et al.*, 2011). Gold is often employed to passivate the surface of magnetite nanoparticles to avoid oxidation (Quanguo *et al.*, 2008). Carboxylated PAMAM dendrimers have been used as a stabilizing iron oxide coating. (Laurent *et al.*, 2008).

1.7.3 Bimetallic Stabilization

Bimetallic nanoparticles (BNPs) are formed by the combination of two different metals. (Sharma *et al.*, 2017). The Fe^{2+} cations can be substituted with other metal cations, which produce different types of metal ferrites, such as CoFe_2O_4 , MnFe_2O_4 , ZnFe_2O_4 , and NiFe_2O_4 . The substituting ions are adjusted by the expansion or contraction of the oxygen framework to compensate the size difference Fe^{2+} (Yadoollhpour *et al.*, 2017).

1.8 FUNCTIONALIZATION SPIONs

The functionalization or modification depends on the types of NPs that provide specific functional groups on the surface (Zhang *et al.*, 200). Most commonly, functional groups including, amines or carboxylates, phosphates, and sulfates are present on nanoparticle surface for reaction with ligands. These groups are readily interchangeable (Laurent *et al.*, 2008).

1.8.1 Importance of Functionalization

Functionalization of SPIONs is a subject of great interest mainly for two reasons; (1) as drug carriers to tackle the drug resistance of cancer cells and increase drug concentrations, (2) to improve the selectivity of the cells in the target tissue (Wahajuddin *et al.*, 2012) (3) protects against agglomeration, (4) provides biocompatibility and chemical handles for the conjugation of drugs and targeting ligands, (5) limits nonspecific cell interactions, (6) enhancement of pharmacokinetics (Nandwana *et al.*, 2015).

1.8.2 Factors of Functionalization

The size and type of surface functional groups are two crucial factors that determine the biological safety of SPIONs as these factors are known to be directly related to cytotoxicity and genotoxicity which are pivotal for in vivo applications such as drug delivery and targeted imaging (Hong *et al.*, 2011). Iron oxide nanoparticles suspended into aqueous or organic solvent mixtures systems containing water bear large number of hydroxyl (-OH) groups on their surfaces.

1.8.3 Chemicals Known for Functionalization

For better functionalization, cell-penetrating peptides (CPPs), also known as protein transduction domains (PTDs), antibodies, aptamers which are single-stranded oligonucleotides, carbohydrates etc. Carbohydrates provide higher hydrophobicity, biocompatibility, increase circulation in blood stream and uptake through specific sugar receptors (Cortajarena *et al.*, 2014). Functional groups, including carboxylates, phosphates, and sulfates (Sushilkumar *et al.*, 2012), monomers, polymers, and inorganic biomaterials, dopamine, alkylated polyethylenimine (PEI), polyethylene glycol (PEG) (Illes *et al.*, 2014), polyacrylic acid (PAA), tetraethyl orthosilicate (TEOS), 3-aminopropyltrimethoxysilane (APTMS) (Yang *et al.*, 2013), Polyvinyl alcohol (PVA) (Mahmoudi *et al.*, 2009), silica coated and aminofunctionalized SPIONs cross-linked with PVA (Maurizi *et al.*, 2015), dimercaptosuccinic acid (DMSA) (Shubayev *et al.*, 2009) are known to bind to the surfaces of SPIONs and exhibit functional domains for loading specific therapeutic drug molecules.

1.8.4 Multi-functionalization

Multi-functionalization is an important aspect when SPIONs used for biomedical applications. In order to achieve multi-functionalization more than one type of ligand is used. Such ligands are termed multifunctional. Multi-functionalized SPIONs opens new doors and vistas to multimodal therapeutic methodologies by merging the dual effects of hyperthermia and chemotherapy. By the use of multiple drugs in the same SPION formulation is one of the promising methods in this aspect (Cortajarena *et al.*, 2014). Conjugation of anti-VCAM-1

(Vascular cell adhesion molecule-) or IgG antibodies is accomplished by activation of carboxylic acid functionalized CLIO with EDC/NHS followed by reaction with respective antibody to yield 0.87mg anti-VCAM-1 (~3 per particle) and 0.3 mg IgG (~2 per particle) per mg of iron (McCarthy et al., 2008). Polyelectrolytes like polysodium 4-syrenesulfonate (PSSS) is reported as one of the best excellent stabilizer for the preparation of multifunctional magnetic nanocomposites (William *et al.*, 2016). Multifunctional iron oxide nanoparticles provide the possibility to deliver therapeutic agents to the brain and concurrently monitor their tissue distribution using MRI (Dan *et al.*, 2013).

1.9 DRUG CARRYING AND DELIVERY EFFICIENCY OF SPIONs

SPIONs can be engineered as nano-carriers to transport multi types of drugs to the intended location. NP drug loading is highly variable and often dependent upon the fabrication process. The design parameters include the particle geometry, size, shape dependent properties, surface chemistry etc. (Chu *et al.*, 2013). In general, drug loading capacity via direct conjugation is low due to the small number of functional groups on the surface of the magnetic nanostructures. The therapeutic moieties can be covalently bonded to magnetic nanostructures with cleavable linkages, encapsulated in the hydrophobic coating on magnetic structures, or physically absorbed on their surfaces (Nandwana *et al.*, 2015).

1.9.1 Loading of Bioavailable Drugs

Varying the biochemical characteristics of the coating polymer may allow for selective intracellular or extracellular delivery of the

drugs to the target cells (Cengelli *et al.*, 2006). SPIONs with appropriate coatings can be easily coupled with drug molecules; for instance, methotrexate (MTX), an anticancer drug could be loaded onto engineered IONP's surface. Therapeutic molecules can also be co-capsulated with IONPs into polymeric matrices; for instance, doxorubicin (DOX) and PTX, along with oleic acid coated SPIONs, loaded into pluronic-stabilized nanoparticles. Small molecules can be loaded porous nanostructures via physical absorption and, along that line, there have been efforts to achieve hollow iron oxide nanostructures. By controlled oxidation and acid etching of Fe particles are used to achieve porous IONPs with a sizable cavity into which cisplatin loaded (Xie *et al.*, 2010).

1.9.2 Loading of Non-Bioavailable Drugs

Magnetic nanoparticles emulsified with nano-emulsions like surfactants with other emulsifying agents is an innovative approach for carrying non bioavailable drugs. The major advantages of nanoemulsions as drug delivery carriers include increased drug loading, enhanced drug solubility and bioavailability, reduced patient variability, controlled drug release, and protection from enzymatic degradation (Chime *et al.*, 2014). Surfactants in solution below their critical micellization concentration (CMC) improve drug solubility by providing regions of hydrophobic drug interactions in solution. Several kinds of molecules including non-ionic surfactants and alcohols can function as cosurfactants in a given system. The physical nature of these systems, mechanism of drug entrapment, as well as physicochemical interactions

of constituents determine their drug solubilization capacity and physical stability during storage and upon dilution (Narang *et al.*, 2007).

1.9.3 Passive Targeting

Passive targeting is a noble method employed in medical research. It uses the predetermined physiochemical properties of magnetic nanostructures. Such structures can specifically migrate to selected tissues. The most common example of passive targeting is the enhanced permeability and retention (EPR) effect. In EPR the particles can accumulate in many tumor tissues passively in solid tumors. The effect of EPR effect is dependent on a various factors such as lymphatic damage rate, degree of capillary disorder, and blood flow. The mentioned biological factors are exhibited differently in different tumor types (Nandwana *et al.*, 2015).

1.9.4 Active Targeting

In active targeting variety of targeting agents like small molecules, peptides, proteins, antibodies. Targeting agents can be designed to facilitate internalization via endocytosis (Nandwana *et al.*, 2015) Ex. Antibodies. SPIONs loaded with PECAM-1 antibody enhanced flux across the blood brain barrier (BBB) in to the brain.

1.9.5 Magnetic Targeting

The process of drug localization is an essential aspect in drug delivery. Magnetic delivery systems are based on mainly two different factors: (1) the competition between forces exerted on the particles by blood compartment, and (2) magnetic forces generated from the applied

magnetic field. When the magnetic forces exceed the linear blood flow rates in arteries (10 cm s^{-1}) or capillaries (0.05 cm s^{-1}), the magnetic particles are retained at the target site. Once the particles are retained at the target site they could be internalized by the endothelial cells of the target tissue (Tartaj *et al.*, 2003). The magnetic field characteristics (magnetic field strength and gradient) are important factors in this type of application and the active manipulation of the NPs is mainly dependent on it (Zhang *et al.*, 200). There are bimetallic nanocomposites containing iron oxide are designed for drug delivery. Such products can pave way for the nanoparticles to be directed towards the target site by the magnetic field. This allows the specific delivery of the drugs to the stents placed in arteries (Sharma *et al.*, 2017).

1.9.6 Drug Release

Thermal energy is used to trigger the drug from the magnetic nanostructures. It has been used as an external trigger for controlled drug release. Particles coated with thermally responsive agents can involve in sustained drug delivery. Substances like hydrogels, thermosensitive polymers, lipids are researched and are believed to be noteworthy for sustained drug delivery by thermal external triggering (Nandwana *et al.*, 2015).

1.10 ENCAPSULATION OF SPIONs

Encapsulation of SPIONs greatly depends on their intended use: primarily for imaging techniques or therapeutic techniques or the confluence of the two. Encapsulation is also employed when SPIONs are intended for environmental applications too. Both organic polymers

and inorganic polymers are extensively used for encapsulation of SPIONs. In organic encapsulation, both synthetic polymers and natural polymers are employed.

1.10.1 Encapsulation of Bare /Drug-loaded SPIONs

Naked SPIONs which are not functionalized for the specific purpose can oxidize and aggregate readily. Such bare SPIONs lead to poor magnetic properties. They also lead to undesired agglomeration during profusion. It can be avoided by stabilizing the SPIONs with a long chain hydrophobic molecules. Further it could be stabilized for the specific purpose by the introduction of a hydrophilic ligand. Such a capping process is dynamic. In general, such hudrophilic ligands behave as strong chelators such as phosphonate based ligands and catechol-based ligands. They have higher affinity towards SPIONs surface. It also increases their water soluble property as well as colloidal property (Lam *et al.*, 2016). Bare SPIONs encapsulated with silica is investigated for their potentiality as photoacoustic contrast agents (Alwi 2012). Silica is noteworthy in encapsulation of bare SPIONs, which can also as a linkage molecule between SPIONs and other polymer coatings (Kandasamy *et al.*, 2015). Similarly, Sruthi *et al.*, (2018) have encapsulated SPIONs loaded with itraconazole with polysaccharides.

1.11 BIOCOMPATIBILITY AND TOXICOLOGICAL PROFILES OF SPIONs

In general, nanoparticles are able to organize around the protein concentration that depends on particles' size, curvature, shape and surface characteristics, charge, functional groups and free energy.

Due to this binding, some particles generate adverse biological outcomes through protein unfolding, fibrillation, thiol cross linking, and loss of enzymatic activity. Another paradigm is the release of toxic ions when the thermodynamic properties of materials favor particles dissolution in a suspending medium or biological environment (Khan *et al.*, 2017).

1.11.1 Biocompatibility

Intravenous injection ($5\mu\text{M Fe/kg}$ – $40\ \mu\text{M Fe/kg}$) of Ferucarbotran, a clinically approved SPIONs coating with carboxydextran, is demonstrated to be safe except for a transient decrease in specific clotting activity of blood coagulation Factor XI, which did not cause any clinically relevant adverse effects (Lei *et al.*, 2013). Magnetic nanoparticles coated with a layer of gold (Au) said to increase the magnetic ability and biocompatibility (Zhang *et al.*, 2006). Pre-coating oxide nanoparticles with PVA and then using a classical sol-gel route to encapsulate them in silica shells is an interesting and promising method to develop biocompatible nanoparticles for industrialized nanomedicine (Maurizi *et al.* 2015). Two types of dimercaptosuccinic (DMSA) coated magnetite nanoparticles, MF66, OD 15, synthesized by MULTIFUN, a European project, are said to be nontoxic when used in pig model (Edge *et al.*, 2016). SPIONs functionalized with biological molecules will greatly improve the particles' biocompatibility. Such magnetic nanoparticles can be very useful to assist an effective separation of proteins, DNA, cells, biochemical products etc. (Quanguo *et al.*, 2008).

1.11.2 Toxicity

Though there are reports regarding the biocompatibility of SPIONs all through the phases of pharmacokinetics, there are so much of concerns regarding the occurrence of the adverse effects stimulated by SPIONs in the body. Cellular responses to nanoparticles are determined by quantifying metabolic activity, membrane integrity, DNA stability (Yang *et al.*, 2013).

1.11.3 Cellular Responses

While all MNPs induced just about 5% or less cytotoxicity and genotoxicity in fibrosarcoma cells at lower than 500 μ l/ml, APTMS-coated MNPs resulted in greater than 10% toxicity against normal cells (Yang *et al.*, 2013). Cellular binding of cationic NPs is enhanced and anionic NPs is inhibited by serum proteins (Fleischer *et al.*, 2012). SPIONs are believed to promote cytotoxicity of human fibroblasts through the action of proinflammatory cytokines, chemokine, and metalloproteinase (MMPs). Numerous iron oxide nanoparticles of 20 – 45 nm produced dose dependent apoptosis and membrane function in mouse neuro-2A cells that were measured by membrane leakage of lactate dehydrogenase and MTT reduction (Shubayev *et al.*, 2009). Particles can damage mitochondria, which results in decreased conversion of the formation of depolarizing mitochondrial membrane. Mechanical interference between ultra-fine iron oxide nanoparticles and components of the cytoskeleton during cell division may play a role. Based on the characteristics and the effects of Fe₃O₄-MNPs on splenocyte proliferation, cytokine production, T-lymphocyte proliferation in ICR mice, a high dose could influence in vivo immune

function of normal ICR mice (Wang *et al.*, 2011). Degradation of particles cell functionality, homeostasis and diminish the proliferative capacity of cultured cells. 'Endorem', the FDA-approved, dextran-coated iron oxide cores are intrinsically not well suited for cell labelling due to their inefficient uptake (Soenen *et al.*, 2010).

1.11.4 Alteration in Biochemical Pathways

SPION uptake can induce signaling events such as Akt pathway. Since SPIONs can induce Akt pathway, there is a possibility that this pathway is involved in cellular proliferation and viability following exposure to SPIONs given that the PI3/AKT pathway can cause the cells to escape apoptosis. Moreover, disturbance in iron homeostasis and altered cellular responses such as activation of signaling pathways and impairment of cell cycle regulation. (Neenu *et al.*, 2010). Although increased ROS level stress confers mutation advantages in some cases, it also makes the cancer cells more susceptible for ROS-induced toxicity, Fenton reactions [$\text{H}_2\text{O}_2 + \text{Fe}^{2+} \rightarrow \text{Fe}^{3+} + \text{HO}^- + \text{HO}^*$]. Therefore, manipulating ROS levels by redox modulation can better work in cancer therapy. Similar techniques from exogenous agents may provide a useful strategy to selectively kill cancer cells without causing significant toxicity to normal cells (Huang *et al.*, 2013). Uptake of particles via phagocytosis can lead to an activation of the membrane-bound NADPH oxidase, activation of c-Jun N-terminal kinase (JNK), pro-inflammatory cytokine tumor necrosis factor-alpha ($\text{TNF}\alpha$).

1.11.5 Changes in Gene Expression

The toxicity of SPIONs with regard to DNA damage is widely researched by the scientific community. SPIONs might result in DNA damage via magnetic oxidation and via other potential interactions. However, SPIONs rarely show genotoxicity below 100 ppm. So, it is understood that higher SPION concentration leads to higher genotoxicity. It leads to lower cell viability also. (Hong *et al.*, 2011). ROS induced by SPIONs also play a vital role in genotoxicity and are able to cause stable chromosomal damage in concentration dependent manner (Konczol *et al.*, 2011). Genotoxicity of MNPs is dependent on their dose, size, and surface charge. Researches are showing positively charged MNPs induced appreciable DNA aberrations. DNA aberrations are irrespective of cell type. Smaller and positively charged MNPs are of more concern in genotoxicity. Reportedly they led to more severe toxicity in normal cells. Normal cells are more vulnerable to the SPIONs of smaller positively charged ones than their counterparts. Normal cells are shown to be more vulnerable to internalized MNPs than cancer cells (Yang *et al.*, 2013). Oxidative and lipid peroxide-related DNA adduct formation is observed in lungs of imprinting control region (ICR) mice at the application of magnetic nanoparticles Totsuka *et al.*, 2014).

1.11.6 SPIONs Toxicity Assays

MTT (3-(4,5-dimethylthiazol-20yl)-2-diphenyltetrazolium bromide) Assay (Mahmoui *et al.*, 2009), CCK-8 Assay, LDH Assay for toxicity determination. Comet Assay for genotoxicity evaluation (Yang *et al.*, 2013), WST Assay which assesses metabolic competence of cells, neutral red (NR) uptake assay which indicates lysosomal activity, dichlorfluorescein-dictate (DCFH-DA) assay which does

oxidative stress measurement, bicinichoninic (BCA) assay which determines the total protein content (Konczol *et al.*, 2011), enzyme linked immune sorbent assay (Wang *et al.*, 2011). Competition assays, quantified with flow cytometry, show that the protein-nanoparticle complex formed from cationic nanoparticles binds to scavenger receptors on the cell surface (Fleischer *et al.*, 2012).

1.12 SPIONs AVAILABLE IN THE MARKET

Resovist from Schering (Berling, Germany), Endorem from Guerbet (Villepinte, France), very small iron oxide particles (VSOP) C200 from Ferropharm (Teltow, Germany) (Soenen *et al.*, 2010), Carboxyl TCL-SPIONs. The use of Endorem is reportedly used as stem cell marker for the noninvasive *in vivo* MR (magnetic resonance) tracking of cell fate following implantation in rat model (Jendelova *et al.*, 2004). Lumirem, Gastromark, Ferumoxil, Abdoscan, Fridex, Ferumoxide are approved for clinical trials. Resovist, Sinerem, Combidex, Ferumoxtran are in phase III clinical trial. Clariscan was discontinued after phase II trial (Thorek *et al.*, 2005).

1.13 OBJECTIVES AND SCOPE

To produce iron oxide nanoparticles and to surface engineer in order to tag curcumin and to encapsulate with a biopolymer to make as an effective anticancer drug nano-carrier.

To explore curcumin release and cytotoxicity of cancer cells *in vitro* condition at different time durations.

To evaluate its efficiency as contrasting agent in x ray imaging

To evaluate toxicity of SPIONs on *in vivo* system.

1.13.1 Scope of the Work

Iron oxide nanoparticles are non-toxic and biodegradable nanoparticles that possess unique properties such as paramagnetic properties which can be used for targeted drug delivery as it obeys to magnetic field. These can be used as contrasting agent for imaging, thus pave way for imaging and drug delivery at same time.

1.14 ORGANISATION OF THESIS

Thesis is organized to have five chapters.

In Chapter 1: An elaborate introduction with a thorough review literature is presented.

In Chapter 2: Materials and Methods followed in this research is given in details.

In Chapter 3: Results and discussion is presented.

In Chapter 4: A brief summary of the research work is given.

In Chapter 5: Conclusion in brief is given.

CHAPTER 2

MATERIALS AND METHODS

2.1 MATERIALS

2.1.1 Synthesis of SPIONs

Ferric chloride hexahydrate ($\text{FeCl}_3 \cdot 6\text{H}_2\text{O}$) m/w 270.30 from Thomas Baker (chemicals) PVT limited, Mumbai; Ferrous Sulphate heptahydrate (Extrapure) ($\text{FeSO}_4 \cdot 7\text{H}_2\text{O}$) m/w 278.01 which had the maximum impurities as given (Copper (Cu) 0.005%, Lead (Pb) 0.005% from Highmedia; Tetramethyl ammonium hydroxide ($\text{C}_4\text{H}_{13}\text{NO}$) 25% aq. Solution, m.w: 91:15, analysis, assay (acidimetric) 24.5-25.5 from Spectrochem. Pvt.ltd, Mumbai, and Formaldehyde solution, (CH_2O) (37-41%), Acetone (2-Propanone, Dimethylketone) ($\text{C}_3\text{H}_6\text{O}$), from SDFCL (s d fine – chem. limited), Mumbai; Magnets with the strength of 30 Gauss from Anzar fancy shop, Marthandom; Nitrogen gas from Eagle, Bangalore were used for the synthesis of SPIONs.

2.1.2 Core-shell Preparation

Sodium dodecyl sulphate (SDS) ($\text{C}_{12}\text{H}_{20}\text{NaO}_4\text{S}$) from Karnadaga Fine Chem, Bangalore; Cetyltrimethyl Ammonium Bromide (CTAB) ($\text{C}_{19}\text{H}_{42}\text{BrN}$) from SDFCL, N, N Dimethylformamide ($\text{HCON}(\text{CH}_3)$) from Fisher Scientific – Qualigens, Mumbai; Curcumin ($\text{C}_{21}\text{H}_{20}\text{O}_6$) from SDFCL, Chitosan – cell culture tested ($\text{C}_6\text{H}_{11}\text{NO}_4$)_n

from Himedia; Pyridoxine hydrochloride (pure) (C₈H₁₁NO₃HCL) from Sisco Research Laboratories (SRL), Mumbai were used for producing Coreshell-SPIONs.

2.1.3 *In Vitro* Drug Delivery

D-MEM (#AL 111, HiMedia); Fetal Bovine Serum (RM10432), HiMedia; MTT Reagent (#4060 HiMedia); Camptothecin (#C9911, Sigma); FTC Rabbit Anti-Active Caspase-3 (Cat No: 560901), BD Biosciences; D-PBS (#TL1006) HiMedia; FITC Annexin V (Apoptosis Detection Kit, BD Biosciences Cat no. 556547); Propidium Iodide (PI) (component no. 51-66211E); HeLa and HCT-116 cell lines derived from Stellixer Biotech. Drug delivery experiments and analysis were carried out in Stellixir Biotech, Bangalore.

2.1.4 X-ray Imaging

Quill's egg from LuLu retail shop, Bangalore were purchased and used as the experimental model for X-ray imaging. BD Duscardt II syringe from Becton Dickinson was used to inject SPIONs into the experimental eggs. Bar magnets were used with the strength of 50 Gauss in order to enhance the intensity of imaging. The magnets were purchased from Cello fancy, Bangalore.

2.1.5 Toxicity Experiment

Earth worms (*Eudiluseugeniae*) collected from Mahabalipuram solid waste management were used as the toxicity experimental animals. *E. eugeniae* is otherwise named African night crawler. It is able to grow in warm climatic conditions around 25 – 30 C.

Its reproductive cycle is comparatively faster. The earthworms were freed to crawl over a raft of wet tissue to remove the impurities. Totally ten earthworms were inoculated for the purpose. Dry cow dung was fed to the earthworms at different intervals and maintained moisture condition (Sherman 2003). The system was kept undisturbed for 5 days for the experimental species to get accustomed with the environment.

2.1.6 Tissue Preparation for Histopathological Observation

Hematoxylin crystals, Ammonium Potassium Alum (Potassium Aluminium Sulphate Dodecahydrate (Purified)), and Eosin Yellow from MERCK; Absolute alcohol (C₂H₅OH) from HAYMAN; Glacial Acetic Acid, and Phloxine B (M.S) from S.D fine chemicals, Xylene (Sulphur free) (C₆H₄(CH₃)₂) from Fisher Scientific, staining rack, staining tray and Microtome cutting wood; Microscope-slides (Double frosted) from Rohem. Histopathological experiments were carried out in the department of Pathology, Madras Veterinary College, Chennai.

2.2 METHODS

The whole work is divided into five parts; (1) Synthesis and characterization of SPIONs, (2) Preparation and characterization of curcumin loaded coreshell-SPIONs for drug delivery, (3) Biological application (*in vitro drug delivery against cancer cell lines and application of SPIONs in the imaging technique of X-ray used in the present medical diagnosis*), (4) Toxicity and Histopathology of SPIONs.

2.2.1 Standardization of SPIONs Synthesis

FeSO₄ 7H₂O and FeCl₃ 6H₂O were dissolved discretely in 1ml of nitrogenized double distilled water. Both iron sources prepared

discretely were mixed together and vortexed for two minutes and nitrogenized for five minutes. 500 μ l of nitrogenized iron source solution was added to 500 μ l of $C_4H_{13}NO$ and vortexed for five minutes to derive fine black precipitate. Different volumes of fine black precipitate were washed in C_3H_6O and dried in hot air oven at 60 $^{\circ}$ C. The obtained pellets were further dissolved in CH_2O and H_2O for attaining the optimum percentage of precursor iron molecular solution as given in Table 2.1. Source solutions were aerated with nitrogen gas. Freshly nitrogenized double distilled water was used as the solvent. Prior to the experiment $C_4H_{13}NO$ was also nitrogenized for five minutes and the subsequent reaction product (black precipitate) also was nitrogenized for two to three minutes followed by vortexing, and palletization. For every time freshly prepared pellets were used for obtaining precursor-iron-molecular-solution (p.i.m.s). The readily prepared precursor iron molecular solution was used for the production of SPIONs.

Table 2.1 Summary of obtaining six different concentrations of precursor iron molecular solution

No	v.b.p	Acetone	Pellet	Temp/Time	$CH_2O:H_2O:CH_2O$	% of p.i.m.s
1	30 μ l	1ml	0.003g	60 $^{\circ}$ /30mins	700 μ l:300 μ l:500 μ l	0.2%
2	25 μ l	1ml	0.0025g	60 $^{\circ}$ /30mins	700 μ l:300 μ l:500 μ l	0.166%
3	20 μ l	1ml	0.002g	60 $^{\circ}$ /30mins	700 μ l:300 μ l:500 μ l	0.133%
4	15 μ l	1ml	0.0015g	60 $^{\circ}$ /30mins	700 μ l:300 μ l:500 μ l	0.1%
5	10 μ l	1ml	0.001g	60 $^{\circ}$ /30mins	700 μ l:300 μ l:500 μ l	0.066%
6	5 μ l	1ml	0.0005g	60 $^{\circ}$ /30mins	700 μ l:300 μ l:500 μ l	0.033%

v.b.p -volume of black precipitate, p.i.m.s - precursor iron molecular solution'.

2.2.2 Optimization of Synthesis of SPIONs

The above six precursor iron molecular solutions were kept in the magnetic field for two days for the synthesis of SPIONs (figure 2.1). After two days of incubation the obtained SPIONs were dispersed into the same solution by vortexing for 30 seconds. Maximum care was taken that the precursor iron molecular solution be free of un-dissolved fragments of black precipitated pellets. The optimum concentration of the precursor iron molecular solution was determined on the basis of the morphology obtained in TEM.



Figure 2.1 Precursor iron molecular solutions kept in the magnetic field for the synthesis of SPIONs

2.3 PREPARATION OF CURCUMIN LOADED CORE-SHELL

Principally, there were four phases involved in preparing core-shell: (1) Synthesis of SPIONs (2) Functionalization of SPIONs, (3) Loading of curcumin, (4) Encapsulating with biopolymer.

2.3.1 Synthesis of SPIONs

For core-shell preparation the SPIONs obtained at 0.133% of precursor iron molecular solution was used. Accordingly, $\text{FeSO}_4 \cdot 7\text{H}_2\text{O}$ and $\text{FeCl}_3 \cdot 6\text{H}_2\text{O}$ were dissolved discretely in 1ml of nitrogenized double distilled water. Both iron sources were mixed together and vortexed for two minutes and nitrogenized for five minutes. 500 μl of nitrogenized iron source solution was added to 500 μl of $\text{C}_4\text{H}_{13}\text{NO}$ and vortexed for five minutes to derive fine black precipitate. 20 μl of black precipitate was washed in 1 ml of acetone by vortexing until the precipitate becomes pellet. The pellet was then dried in hot air oven at 60⁰C for 30 minutes. The dried pellet was dissolved in 700 μl of formaldehyde. 300 μl of water was drop by drop added and vortexed. Again 500 μl of formaldehyde was added drop by drop and vortexed. The resultant solution was kept in the magnetic field for two days. After the incubation of two days, the magnets were removed and the SPIONs formed was dispersed into the same solution by vortexing for 30 seconds.

2.3.2 Functionalization of SPIONs

Two surfactants (SDS and CTAB) were investigated their ability to functionalize the SPIONs. Among the two SDS was found better preserving the nature of SPIONs. Therefore, the effect of SDS, in functionalization, was investigated by means of three different concentrations (0.02%, 0.04%, 0.08%). The surfactants were dissolved in double distilled water. The foam was collected in separate test tubes according to the different concentrations and kept undisturbed until the foam turned into solution. The resultant solutions were warmed in water-bath at 70⁰C for 20 minutes. Every 3 minutes the solutions were

gently shaken for permeating the uniform temperature in the solution. It was then centrifuged at 10000 rpm. The obtained clear solution was collected in 50 ml screw cap tubes for further use. Meanwhile, three different sets SPIONs each containing 0.008g was magnetically separated and washed four times in double distilled water and dispersed in 5ml of N, N dimethylformamide. It was further decanted into the freshly prepared different percentage of surfactant solutions and gently mixed for five minutes followed with mixing in cyclo-rotator for every one hour for three days. The cyclo-rotator (figure 2.2) was designed to fit for the method of the present research. It was fixed to rotate for every one hour that it would give gentle agitation for the SPIONs and to make them remain suspended in the solution until the SPIONs are surface saturated with the respective surfactants.



Figure 2.2 Cyclo rotator designed to give specific agitation during functionalization, drug loading and encapsulation

2.3.3 Curcumin Loading

Curcumin ($C_{21}H_{20}O_6$) 0.02g was dissolved in 2ml of N, N Dimethylformamide which was used as the stock solution. 400 μ l of the dissolved curcumin was decanted into the functionalized SPIONs. Gentle mixing was done for five to six minutes followed with mixing in the designed cyclo-rotator, as set the instrument for every single one hour for three days. After three days of incubation the drug tagged SPIONs solutions were moved into 2 ml micro centrifuge tubes and heated in water bath at 70 $^{\circ}$ C for 20 minutes. During the experiment every three to four minutes the mixtures were moderately shaken outside the water bath for permeating uniform temperature. Then the curcumin tagged SPIONs were separated with the help of bar magnets and surface washed three times with 0.1% of pyridoxine hydrochloride solution and disseminated into 5ml of 0.1% hydrochloride solution.

2.3.4 Method of Encapsulation

Chitosan was researched for its efficiency to encapsulate the curcumin loaded SPIONs. It involved two major steps: (1) Preparation of chitosan polymer, (2) Encapsulation.

2.3.4.1 Preparation of Chitosan Polymer

Chitosan was investigated for its ability to coat the curcumin loaded SPIONs. The optimum concentration, for a considerable efficacy of coating, was researched by dissolving chitosan in pyridoxine hydrochloride solution of different concentrations (Table 2.2). The final concentration was determined with its maximum dissolution in

pyridoxine hydrochloride solution and the gelatinous appearance of the dissolved chitosan. After obtaining the viscous/gelatinous polymer the same was subjected for centrifugation at 3000 rpm for 10 minutes. After centrifugation the obtained supernatant was collected for encapsulation.

Table 2.2 Standardization of the dissolution of chitosan in pyridoxine hydrochloride solution

No	Chitosan	Pyridoxine hydrochloride	Water	Dissolution & gelatinous appearance
1	0.10g	0.50g	100ml	Nil
2	0.20g	0.70g	100ml	Nil
3	0.30g	0.90g	100ml	Nil
4	0.40g	0.100g	100ml	Nil
5	0.50g	1.10g	100ml	Nil
6	0.55g	1.20g	100ml	Partial
7	0.60g	1.40g	100ml	Partial
8	0.63g	1.50g	100ml	Partial
9	0.65g	1.55g	100ml	Not complete
10	0.67g	1.67g	100ml	Complete dissolution

2.3.4.2 Encapsulation of Curcumin Loaded SPIONs

Curcumin loaded SPIONs kept in 5ml of 0.1% pyridoxine hydrochloride solution was transferred into the 20 ml of freshly prepared gelatinous/jelly like chitosan biopolymer. After gently mixing it for 5 minutes it was retained in the cyclo-rotator for next three consecutive days. After three days of incubation the resultant Coreshell-SPIONs were separated with the help of bar magnets and again dispersed them in

to 5 ml of freshly prepared 0.1% of pyridoxine hydrochloride solution for *in vitro* drug delivery experiments.

2.4 CHARACTERIZATION OF SPIONs SYNTHESIZED AT 0.133% PRECURSOR IRON MOLECULAR SOLUTION AND THE CORE-SHELL SPIONs

2.4.1 Microscopy

Transmission Electron Microscope (TEM), Scanning Electron Microscope (SEM) and Atomic Force Microscope (AFM) were employed to understand the morphology of SPIONs and the different phases of Coreshell-SPIONs preparation. The optimum concentration of the 'precursor iron molecular solution' for the synthesis SPIONs was decided by observing resultant SPIONs of the six precursor iron molecular solutions under TEM.

2.4.1.1 Transmission Electron Microscopy (TEM)

TEM images were obtained in TEECNAI G2 Spirit Biotwin – 120 KV. Earlier to the imaging, the analytic samples were loaded in Formvar/Carbon copper grids # 300 mesh. 10 μ l of sample was loaded onto the grids and kept undisturbed for 2 minutes. The top part of the drop was then absorbed by water absorbent paper and the SPIONs loaded grids were dried under the heat of 100 Volt bulb. This was done separately for the SPIONs synthesized in all the six respective concentrations of precursor iron molecular solutions. Morphologically adequate SPIONs produced in the most favorable concentration was

used for the further microscopic and spectroscopic analysis and biological applications.

2.4.1.2 Scanning Electron Microscopy (SEM)

SEM images were obtained in Zeiss Ultra55. 10 μ l of sample was loaded onto silicon wafer metal. The samples were desiccated in hot air oven at 40⁰C for 30 minutes. Prior to imaging the bare SPIONs samples were coated with gold coating. Gold coating was done in Quorum, Q 150R ES. 8 nm Au (gold) coating was done for 80 seconds. The samples of the core-shell preparation (encapsulation) were desiccated at room temperature in aseptic condition and were imaged without gold coating.

2.4.1.3 Atomic Force Microscopy (AFM)

AFM images were obtained in Bruker, Dimension icon model. Samples (SPIONs) were loaded onto clean glass slides and desiccated in hot air oven at 40⁰C for 30 minutes. The samples of the core-shell preparation were dried at room temperature in aseptic condition. For AFM imaging tapping mode was used as per Bruker AFM probes Otespa R3 and the cantilever as $K = 35$ N/M and $f_0 = 300$ kHz.

2.4.2 Spectroscopy

2.4.2.1 Ultra Violet Visible Spectroscopy (UV-Vis)

UV-Vis spectra were recorded in UV 3600 Shimadzu spectrophotometer. The UV-Vis absorbance was done between 200 nm and 800 nm.

2.4.2.2 Fourier Transform Infrared Spectroscopy (FTIR)

FTIR spectra were documented by means of IR Affinity IS (Shimadzu, Japan) which was made available in the Department of Organic Chemistry, IISc, Bangalore. The samples for the spectra were loaded to form thick layers onto the glass slides and desiccated in hot air oven at 40⁰C for 30 minutes. The samples of the core-shell preparation were dried at room temperature in aseptic condition. The spectra were documented with the transmission mode scan in the spectral region of 4000 – 500 cm⁻¹.

2.4.2.3 Raman Spectroscopy

Raman spectra were recorded in LabRam HR 800 model of Horiba Jobinyvon. The samples were loaded to form thick layers onto clean glass slides and desiccated in hot air oven at 40⁰C for 30 minutes. 785 nm diode laser was used for obtaining the spectra.

2.4.2.4 X-ray Diffraction Spectroscopy (XRD)

XRD spectra were documented in Smart lab XRD model of Rigaku. The samples were loaded to form thick layers onto clean glass slides and desiccated in hot air oven at 40⁰C for 30 minutes. Copper K α was used as the X-ray source and the power used was 1.2kw.

2.4.2.5 X-ray Photoelectron Spectroscopy (XPES)

XPS spectra were recorded in Ultra DLD model of Kratos. The samples were prepared to form a thick layer and desiccated in hot air oven at 40⁰C for 30 minutes. Monochromatic source Al K α at the

condition of 10K eV as accelerating voltage and 9 mA current (90 W) at the vacuum of $2e^{-9}$ torr was used. Spectra for Fe, spectrum for metal oxide, carbon, oxygen, and nitrogen were recorded.

2.4.2.6 Nuclear Magnetic Resonance Spectroscopy (NMR)

NMR spectra was recorded in Bruker NMR spectrophotometer, using BBFO Probe. NMR was used to examine the difference between the precursor iron molecular solution of 0.133% and the resultant SPIONs. The difference occurred was tabulated. It was done for hydrogen and carbon atoms.

2.4.2.7 Zeta Potential Analyzer

Zeta potential value was documented in zeta potential analyzer by means of Brookhaven ZetaPALS. The measurement parameters: conductance 8042 μ s, electric field 5.43 V/cm, Sample count rate = 260 kcps, Ref.count rate 1328 kcps.

2.4.2.8 Superconducting Quantum Interference Device (SQUID)

Magnetic hysteresis spectra were recorded in SQUID from Quantum Design, the material properties and measurements system (MPMS) model no. MPMS 3 – 111 was used. Maximum field used was 5T. Temperature range was from 5K to 400K. MPMS squid field ramping was +7T to -7T. Magnetic measurements were recorded at both field cooled (FC) and zero field cooled (ZFC) modes also were recorded.

2.4.2.9 Vibrating Sample Magnetometer (VSM)

Magnetic hysteresis spectra were recorded in VSM. Maximum field used was 5T. Temperature range was from 5K to 400K. Magnetic measurements were recorded at both field cooled (FC) and zero field cooled (ZFC) modes also were recorded.

2.5 *IN VITRO* SUSTAINED CURCUMIN DELIVERY AND ASSAYS

The efficacy of curcumin delivery was investigated *in vitro* in cancer cell lines. There were four assays carried out: (1) MTT assay, (2) Apoptotic assay, (3) Gene expression assay (Caspase 3), and (4) Nuclear staining assay. Two types of cell lines were used for this purpose: (1) HeLa, (2) HCT-116. Cytotoxic effect of the test compound (curcumin loaded core-shell) was tested, with regard to each cell line, at four different time durations; 2 hours, 6 hours, 12 hours and 24 hours.

2.5.1 Anticancer Activity

2.5.1.1 MTT assay for HELA / HCT 116 cells

For doing MTT assay there were six steps involved: (1) Retrieval of cryopreserved cells, (2) Sub culturing, (3) Trypsinization and cell counting, (4) Seeding of cell in 96 well plate, (5) Application of the test compound (Core-shell), and (6) Addition of MTT reagent and determination of IC50 value. Cells were retrieved from cryo-vials kept in liquid nitrogen for two months. To the vials, 10% of BSA mixed fresh media (DMEM) (500 μ l) was added and the cells were dispersed. It was centrifuged at 2000 rpm for five minutes at

25⁰C. There discarded the supernatant and the live cells were re-suspended in 1ml of fresh media by gentle pipetting. The re-suspended cells were transferred to T-25 culture flasks where 4 ml of fresh media already kept ready and mixed gently. The culture was then allowed to grow for 24 hours in CO₂ incubator at 37⁰C. The cells were observed microscopically before and after the incubation. After 24 hours of incubation the media was aspirated from the T-25 flasks. The cells were endowed with surface wash by 1 ml Phosphate Buffer Saline to remove the traces of culture-media. After aspirating the PBS, 500 µl of trypsin was added to detach the adherent cells from the surface of T-25 flasks. It was kept in CO₂ incubator for 5 minutes for the complete detachment of the cells. After five minutes' incubation 1 ml of fresh media was added stop the effect of trypsin. Subsequently centrifugation done for 5 minutes at 2000 rpm. Then the supernatant was discarded and the resultant pellet was re-suspended in 1 ml of fresh media. The cells (100 µl) was stained with trypan blue at 1:1 ratio. 10 µl of the stained cells were counted in chemo cytometer. The cells were further re-suspended in 7 ml of fresh media prior to seeding for obtaining the appropriate cell suspension. 250 µl of cell suspension, taken from the previous cell suspension, was seeded into a sterile 96 well plate at the requisite concentration (2x10⁴ cells/well). It was then kept to grow for 12 hours in CO₂ incubator at 37⁰C. The cells were microscopically observed before and after incubation. After 12 hours' incubation the media was removed from the wells using multichannel pipette. The test compound (curcumin loaded Coreshell-SPIONs) was then diluted into different concentrations in DMEM and added to wells. Each concentration in duplicate. It was incubated for 24 hours in CO₂ incubator, at 37⁰C. After the period of incubation Coreshell-SPIONs diluted media was removed by using

multichannel pipette and added 100 μ l of 10% MTT reagent. The plate was wrapped with aluminum foil and kept in CO₂ incubator for 2 hours at 37⁰C. After incubation, the plate was removed from CO₂ incubator and MTT reagent was removed. Then, 100 μ l of solubilizing solution (DMSO) was added to each well. Absorbance was read on ELISA reader at 570 nm and 630 nm was used as reference wavelength. The IC50 value was determined.

2.5.1.2 Nuclear staining assay of HELA and HCT 116 cells

Nuclear staining for the cells to detect apoptosis was performed (Crowley *et al.*, 2016). Cells were treated with core-shell test drugs (IC50 values) for 2, 6, 12 and 24 hours and CPT(25 μ M) and incubated at 37⁰C, in a CO₂ incubator for 24 hrs. Then there prepared the nuclear stain (Hoechst stain) – 10mg/mL stock in distilled water. Working solution was prepared at 1:2000 in PBS. The spent media was discarded from all the wells and washed with D-PBS (~500 μ L). Then, 2% PFA was supplemented to the wells and incubation done at RT for 10 min. Then the spent PFA was discarded and washed the cells with D-PBS (~500 μ L), twice. Then, D-PBS was discarded and there added staining solution onto the cover slips. The slips were incubated for 5-10mins in dark. There prepared permanent slides, using glycerin. Then the slides were observed for the cells under fluorescence microscope

2.5.1.3 Apoptotic assay of HELA / HCT 116 cells

Cells (HeLa / HCT 116) were retrieved from cryopreservation vials. To the vials, 500 μ l of 10% of BSA mixed fresh media (D-MEM) was added and the cells were suspended. It was centrifuged at 2000 rpm

for five minutes at 25⁰C. The supernatant was discarded and the cells were re-suspended in 1ml of fresh media by gentle pipetting. The re-suspended cells were transferred to T-25 culture flasks where 4 ml of fresh media already kept ready and mixed gently. The culture was then allowed to grow for 24 hours in CO₂ incubator at 37⁰C. After 24 hours of incubation the media was aspirated from T-25 flasks. The cells were done surface washing with PBS (1 ml) to remove the traces of media. After aspirating the PBS, trypsin (500 µl) was added to detach the cells from the surface of T-25 flasks. It was kept in CO₂ incubator for 5 minutes for the complete detachment of the cells. After five minutes' incubation 1 ml of fresh media was added to stop the effect of trypsin. Centrifugation was done for 5 minutes at level of 2000 rpm. The resultant supernatant was discarded and the pellet was re-suspended in 1 ml of fresh media. The cells (100 µl) was stained with trypan blue at 1:1 ratio. 10 µl of the stained cells were counted in hemo cytometer. The cells were cultured in six-well plates and to each well the cells were added at a density of 3x10⁵ cells/2ml and incubated in CO₂ incubator at 37⁰C for 24 hours. The spent medium was aspirated and then the cells were washed with 1x PBS. The concentration of core-shell as determined according to the IC50 value was added to the wells in triplicates and incubated in CO₂ incubator at 37⁰C for four time durations (2, 6, 12, 24 hours). After the respective time durations, the Coreshell-SPIONs applied culture medium was removed and the wells were washed with 500 µl of PBS. Then the PBS was removed and 180 µl of trypsin-EDTA solution was supplemented and incubation done at 37⁰C for 4 minutes. Culture medium was added to the wells and the cells were harvested directly into 12 x 75 mm polystyrene tubes. Then the polystyrene tubes were centrifuged for five minutes at 300 rpm at 25⁰C.

the supernatant was carefully emptied and the pellet was washed with PBS twice. Then the PBS was decanted and the cells were re-suspended in 1x Binding buffer at a concentration of 1×10^6 cells/ml. Then 100 μ l of the solution (1×10^5 cells) was added to a 5 ml culture tube and into it 5 μ l of FITC Annexin V was added. It was then vortexed gently and incubated for 15 minutes at RT (25°C) in the dark. Then there added 5 μ l of PI (Propidium Iodide) and 400 μ l of 1x Biding Buffer to each tube and vortexed gently. The following controls were used to set up compensation and quadrants: (1) Unstained cells, (2) Cells stained with FITC Annexin V (no PI), and (3) Cells stained with PI (no FITC Annexin V).

2.5.1.4 Caspase 3 expression assay of HELA / HCT 116 cells

The cells chosen for experiment were cultured in six-well plates and to each well the cells were added at a density of 3×10^5 cells/2ml and incubated in CO_2 incubator at 37°C for 24 hours. The spent medium was then aspirated from the wells. The cells were then washed with 1x PBS. The concentration of core-shell as determined according to the IC_{50} value was added to the wells in triplicates and incubated in CO_2 incubator at 37°C for four time durations (2, 6, 12, 24 hours). After the respective time durations, the core-shell applied medium was removed and the wells were washed with 500 μ l of PBS. Then the PBS was removed and 200 μ l of trypsin-EDTA solution was added and incubated at 37°C for 4 minutes. Then 2ml of culture medium was added to the wells and the cells were harvested directly into 12 x 75 mm polystyrene tubes. The tubes were centrifuged for five minutes at 300 rpm at 25°C . The supernatant was carefully decanted and the pellet

was washed with PBS twice. Then 0.5 ml BDCytofix/Cytoperm solution was added and waited for 10 minutes. It was then washed with 0.5% of bovine serum albumin (BSA) in 1x Phosphate-buffered saline (PBS) and 0.1% sodium azide. It was then added with 20 μ l of Anti-Caspase-3 antibody. It was mixed thoroughly and incubated for 30 minutes in the dark at 20⁰ to 25⁰C. After the incubation it was washed with 1x PBS with 0.1% sodium azide. Prior to the analysis the samples were mixed thoroughly in 0.5 ml of PBS.

2.6 X-RAY IMAGING

Quail's eggs were purchased and used for investigating the contrasting effect of the SPIONs. Egg content (white substance) (2 ml) was taken out from the egg with the help of a sterile syringe. 1.8 ml of washed SPIONs suspended in double distilled water which was then injected into the egg. The injected SPIONs were further dispersed inside the egg. SPIONs were dispersed with gentle hand-shaking for two minutes. Hospital-based X-ray was used for the imaging purpose. It was done to observe if the SPIONs exhibit the required magnetic and contrast property inside the egg system. In order to make it observable magnetic field was applied by using a bar magnet near to the experimental quail's eggs. The difference was analyzed in comparison with the control.

2.7 TOXICITY STUDIES

Eudriluseugeniae was selected for the study and procured from Solid Waste Management, Mahabalipuram, Chennai, Tamil Nadu, India.

2.7.1 Pretreatment of Earthworm

Prior to treatment, earthworms were introduced to a container with wet tissue paper to creep around freely to remove impurities. 10 earthworms were introduced to box (16 cm x 9.12 cm x 9.7 cm) containing soil and cow dung, the set up was kept undisturbed for 5 days. Dried and powdered cow dung was fed and water was sprinkled at regular intervals to favor the conditions for its reproduction (Sherman 2003).

2.7.2 Treatment with nanoparticles

Nanoparticles were dispersed at different concentrations in 10 ml distilled water. Ten experimental earthworms were allowed to interact with nanoparticles for 1 h/ day for ten days. After exposure, it was kept in the box where it was maintained.

2.7.3 Tissue Fixation

The tissues (earthworm and fish gut) stored in 10 % of formalin were cut into small pieces and put into isopropanol alcohol (100 %) and incubated for an hour in hot air oven at 58 – 60⁰C. It was repeated thrice. Then the tissues were put into Xylene (100 %) and kept in the room temperature for 20 minutes. This was repeated thrice. Then the tissues were placed towards the bottom of the melted wax (approximately 5 ml) kept hot in processing cup and waited until the wax got solidified. Then the tissue fixed wax was fixed onto a microtone cutting wood and immediately kept in the ice cube. This setup was then fit into the microtone and 10 micron sections were sliced until clear tissue appeared. It was removed from the microtone and kept in the ice

cube. Then it was fixed into the microtone and the size of cutting the tissue was adjusted 4 microns in the microtone. The finely sliced 4 micron tissues along with the adherent wax was put into the water-bath at 40 – 45 °C. The floating tissue section was gently made to attach onto clean glass slides where egg albumin fixative readily applied and the slides were kept in hot air oven at 58 – 60°C until the adherent wax melted. Then the slides were removed from the hot air oven immersed in Xylene (100%) for 5 minutes for the removal of melted wax from the slides. Then the slides were kept immersed in isopropyl alcohol (100%) twice 5 minutes each. The slides were then washed with tap water for 5 minutes and kept for drying in room temperature and thus the tissue was fixed on to the glass slide. NB: While staining and washing the slides were kept in staining rack which was placed in staining tray.

2.7.4 Staining (Hematoxylin and Eosin)

The tissue fixed slides were then immersed in Hematoxylin solution and kept undisturbed for 10 minutes. Then the slides were removed from the Hematoxylin solution and washed by immersing in tap water for 5 minutes. After washing with water the slides were immersed in counter staining (Eosin) for 1 minute. The slides were removed from the Eosin solution and washed with tap water for two minutes. The slides were then dried in room temperature. A drop of D.P.X mounting medium for microscopy was dropped over the fixed tissue and over it a cover slip. This setup was kept undisturbed in the room temperature for 24 hours for drying. NB: While staining and washing the slides were kept in staining rack which was placed in staining tray.

2.7.5 Prussian Blue Stainig

Solution 1: 1 g of Potassium ferrocyanide was dissolved in 50 ml of double distilled water. *Solution 2*: 1 ml of HCL was added to 50 ml of double distilled water. Solution 1 & 2 were mixed together. The tissue fixed slides were immersed into the solution and kept in hot air oven at 58 – 60⁰C until the whole solution becomes blue. Then the setup was removed from hot air oven and the slides were washed with tap water and dried in room temperature for 5 minutes. The slides were then immersed into counter stain (Eosin) and kept for 3 minutes. The slides were removed from Eosin and washed with tap water. The slides were kept in room temperature for drying. After the slides completely dried a drop of D.P.X mounting medium was added on to the stained tissue and a cover slip was overlaid. This setup was kept in the room temperature for 24 hours for complete drying. NB: While staining and washing the slides were kept in staining rack which was placed in staining tray.

CHAPTER 3

RESULTS AND DISCUSSION

3.1 SYNTHESIS OF SPIONs

3.1.1 TEM Analysis

Transmission Electron Microscopic images (Figure 3.3) illustrate the size and morphology of SPIONs synthesized in different concentrations (0.2%, 0.166, 0.133%, 0.1%, 0.066%, 0.033%). The average size of the particles is determined with 15 nm. Apart from the SPIONs synthesized at the optimum concentration, in all other concentrations, aggregation is relatively higher. SPIONs synthesized at 0.113% was found to behave in the magnetic field as given in Figure 3.1. When a bar magnet is moved up and down closer to the reaction tube the particles well obey the magnetic field in a uniform fashion. SPIONs of other concentrations were not as distinct as that of the SPIONs of optimum concentration. Moreover, the SPIONs of other concentrations were found depositing at the bottom of the reaction tube relatively faster than that of the SPIONs of optimum concentration. This is because, SPIONs in general, tend to aggregate in suspension due to three kinds of different forces: (1) hydrophobic-hydrophobic interactions, (2) magnetic interactions, (3) van der Waals forces. When they aggregate micron size clusters could be formed if magnetic dipole-

dipole interactions become closer and closer and develop magnetization by neighboring clusters (Mahmoudiet *et al.*, 2011). In Figures 3.3 (a) and (b) the particles appear aggregated. The aggregated particles usually tend to sediment fast in the reaction tubes.

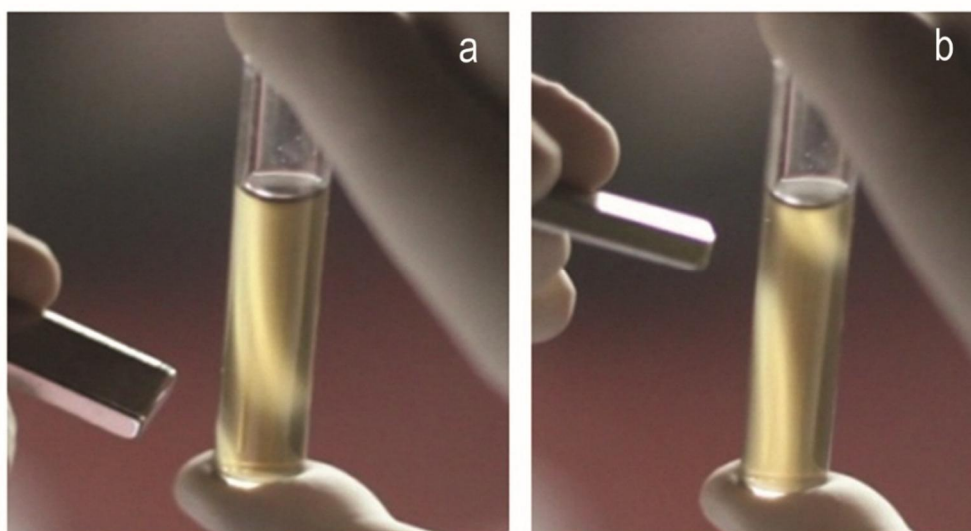


Figure 3.1 Behavior of SPIONs (synthesized at 0.133% precursor iron molecular solution) when a bar magnet is moved along (up and down) the reaction tube.

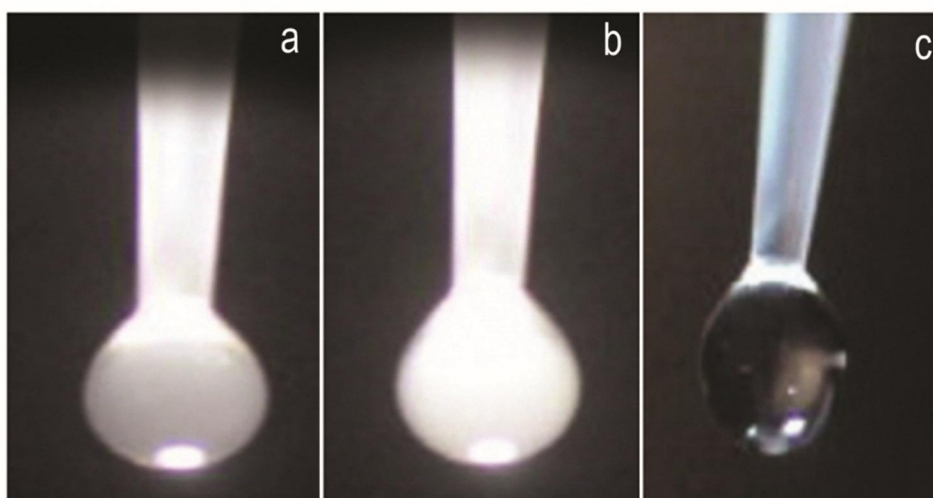


Figure 3.2 Behavior of a droplet of SPIONs when hanged over the microscopic light. (a) a droplet of SPIONs magnetic field *not* applied, (b) a droplet of SPIONs magnetic field applied, (c) a single droplet without SPIONs.

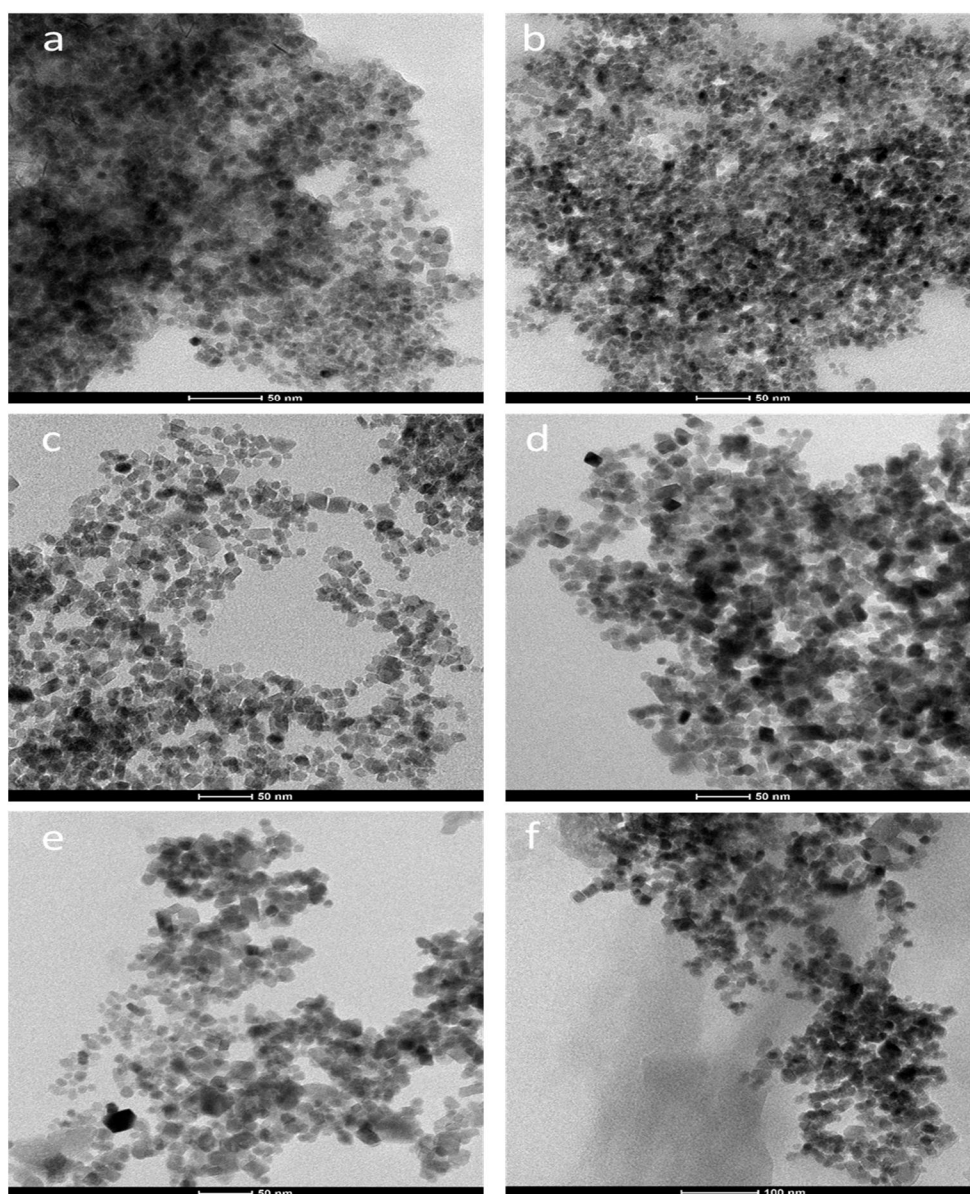


Figure 3.3 TEM images of SPIONs synthesized at six different concentrations of precursor iron molecular solution: (a) 0.2%, (b) 0.166, (c) 0.133%, (d) 0.1%, (e) 0.066%, (f) 0.033%

In Figure 3.3 (c) the particles seem to be more dispersed and uniform. These are the resultant particles synthesized in 0.133% of precursor iron molecular solution. These particles remained suspended for longer period of time except a few percentage of aggregate particles. The size of such particles tend to be in between 5 to 20 nm. In figure 3.3 (a and b) higher level of aggregation is observed and cloudy too. In

Figures 3.3 (d) (e) and (f) apart from the particles there are hazy shades which represent the molecules which did not involve in reaction and did not turn to particles which remained non-reactant molecules. Such molecules would tend to interrupt the particle formation. The particles synthesized at 0.133% were subjected for further instrumental analysis.

3.1.2 UV-Vis Spectroscopy

Outer electrons present in the atoms or molecules tend to absorbance of radiant energy like UV-Vis and undergo transitions to higher and higher energy levels, which can be studied through UV-Vis spectrometry. Only the SPIONs produced at 0.133% precursor iron molecular solution was taken onward for further studies. Absorption spectrum of the SPIONs was taken between 200 and 800 nm (Figure 3.4). It displays an onset of absorption peak at 300 nm and absorption maxima at 250 nm. The absorption peak around 250 nm is the characteristic peak for magnetic nanoparticles as reported by Wang *et al.*, (2014). The corresponding peak at 300 nm is the peak for the organic molecules.

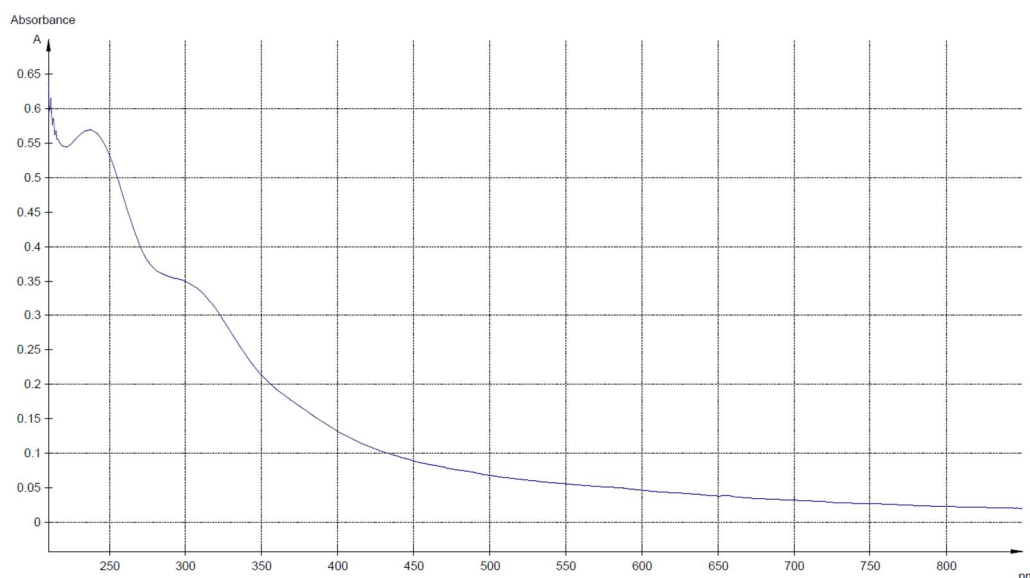


Figure 3.4 UV vis analysis of SPIONs synthesized at 0.133% of precursor iron molecular solution

3.1.3 SEM – EDX

The Scanning Electron Microscopic image of SPIONs synthesized at 0.133% concentration (Figure 3.5) illustrate the particle size at 20 nm and below. The size distribution could be co-related with that of the TEM image of the same concentration (Figure 3.3c). There was a considerable amount of nanoaggregates as signposted in the image. EDX analysis showed the spectra with peaks corresponding to Fe and FeO (Figure 3.6).

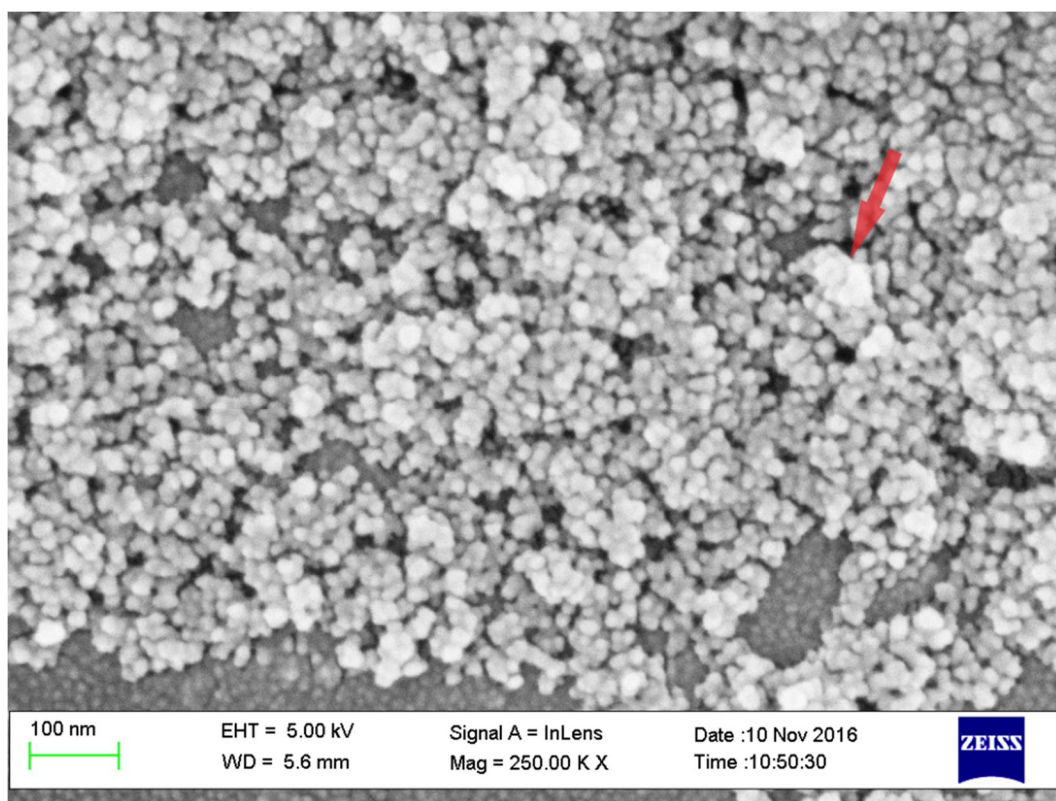


Figure 3.5 SEM image of SPIONs synthesized at 0.133% of precursor iron molecular solution

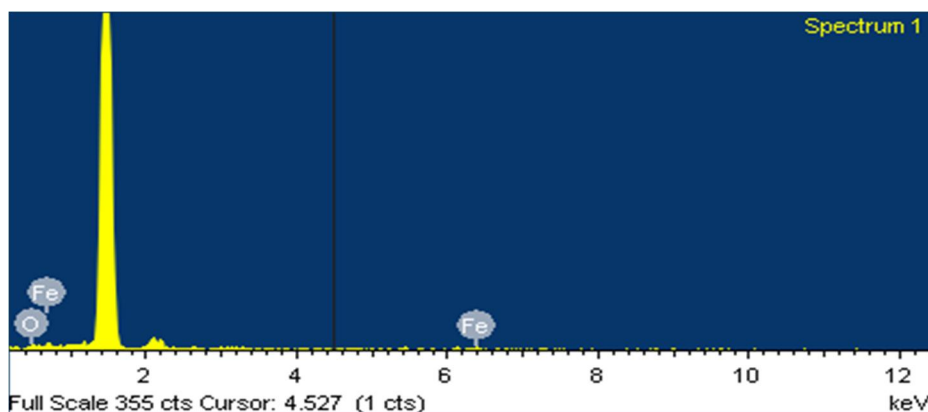


Figure 3.6 EDX spectrum of SPIONs synthesized at 0.133% of precursor iron molecular solution

3.1.4 Fourier Transform Infra-Red Spectroscopy (FTIR)

The IR spectra of SPIONs was taken for the range of 900 – 4000 cm^{-1} (Figure 3:7). The absorption bands were seen at band at 3323.88 cm^{-1} could be assigned to the stretching mode of surface H_2O molecules or to an envelope of hydrogen bonded surface OH groups. Accordingly, the FTIR spectrum shows one broad IR band at 1645.39 cm^{-1} close to the position of H_2O bending vibrations. The bands at 1308.78, 1270.63, 1240.42, 1202.60 cm^{-1} could be assigned to specifically absorbed sulphate groups. The bands at 1176.03, 1109.16 cm^{-1} could be inferred that a significant amount of sulphate groups which occupy external as well as internal surfaces of the particles. 1028.47 cm^{-1} with its shoulder peak and 924.55 cm^{-1} are due to Fe-O-H bending vibrations in the particles. The IR bands at 2985.02 and 2915.51 cm^{-1} The spectral bands are interpreted here in association with the already reported analysis by Gotic *et al.*, (2007) and Fouda *et al.*, (2012), which may be attributed to organic residuals of symmetric and asymmetric stretching of CH_2 . When SPIONs are synthesized in chemical method, as reported by Tombacz *et al.*, (2015), high absorption

affinity would result from π -electron interaction with polar surface of magnetic nanoparticles, as well as complex bond formation at $\equiv \text{Fe}-\text{OH}$ sites.

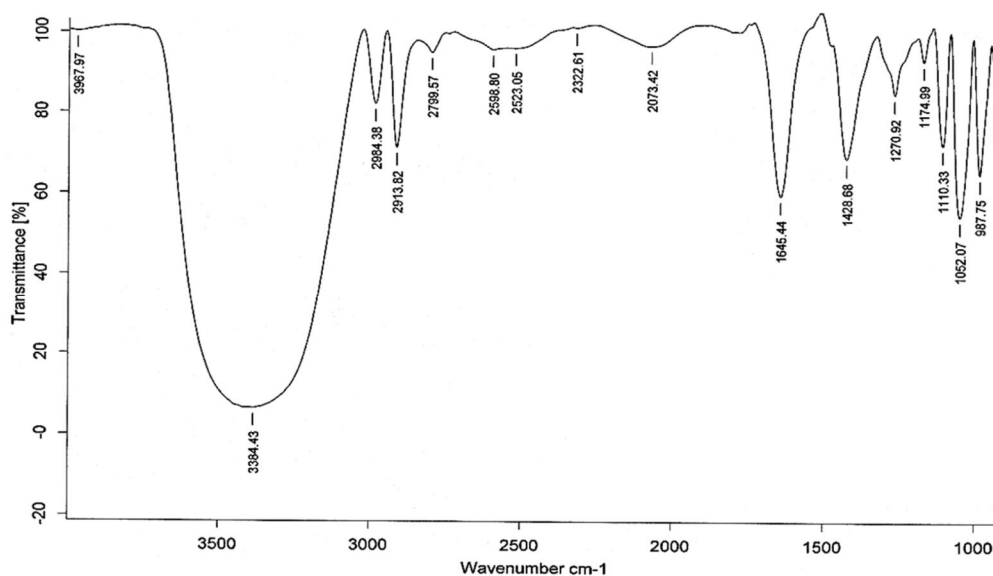


Figure 3.7 FTIR spectrum for the SPIONs synthesized at 0.133% of precursor iron molecular solution

3.1.5 Raman Spectroscopy

Raman molecular effects displayed six peaks located at 220, 280, 400, 470, 600, and 1308 cm^{-1} when 785 nm diode laser with the power of 1.2mW was applied (Figure 3.8). These peak positions were very closely consistent with the typical frequencies observed for Fe_2O_3 as reported (221, 287, 403, 493, and 601 cm^{-1}) by Zhang *et al.*, (2007) and Bersani *et al.*, (1999). The peak positions correspond to E_g mode and A_1g mode of the iron oxide. Moreover, above some critical value of the laser power, the Raman spectra passed to indicate the characteristics of maghemite bands due to the effects of oxidation of the material. Similarly, when Panta *et al.*, (2015) investigated iron oxide samples with two different laser powers, 514 nm laser with the power of 0.75

mW and 785 nm laser with the power of 1.2 mW. They found the characteristic peak shifting from 670 to 654 cm^{-1} suggesting the incident oxidation due to increase in laser power. In accordance with these reports the SPIONs investigated here come under any one type of Fe_2O_3 .

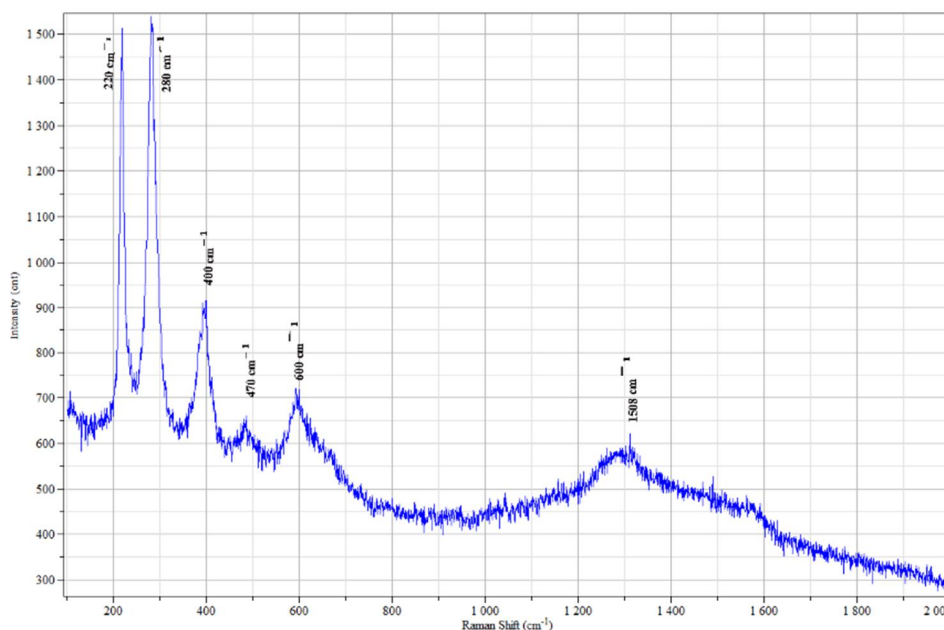


Figure 3.8 Raman spectra taken for the SPIONs synthesized at 0.133% of precursor iron molecular solution

3.1.6 X-Ray Diffraction Spectroscopy

Crystalline phase was investigated by Grating Incident X-Ray Diffraction (GIXRD) and Powder X-Ray Diffraction (PXRD). The measurement conditions and the peak lists are given in tables 3.1 and 3.2 respectively. Accordingly, the peaks identified by GIXRD (Figure 3.9), 30.20, 35.64, 43.1333, 57.00, and 62.68 are associated to Fe_2O_3 in comparison with what is already reported by Layek *et al.*, (2010). Further, the peaks obtained by PXRD is supporting it (Figure 3.10). The two peaks in GIXRD (29.41 and 72.1333) remain unknown which are not further identified in PXRD. Since Fe_3O_4 and Fe_2O_3 are related

species, the SPIONs could be in a mixed phase of iron oxide nanoparticles with modifying elements.

Table 3.1 GIXRD Measurement conditions and Peak list of SPIONs Synthesized at 0.133% precursor iron molecular solution

Measurement conditions

X-Ray	40 kV , 30 Ma	Scan speed / Duration time	4.0000 deg/min
Goniometer	SmartLab	Step width	0.0100 deg
Attachment	Chi	Scan axis	2-Theta
Filter	None	Scan range	10.0000 - 90.0000 deg
CBO selection slit	PB	Incident slit	0.100deg
Diffrected beam mono.	Flat	Length limiting slit	5.0mm
Detector	SC-70	Receiving slit #1	10.000deg
Scan mode	CONTINUOUS	Receiving slit #2	10.000mm

Peak list

No.	2-theta (deg)	d (ang.)	Height (cps)	FWHM (deg)	Size (ang.)	Phase name	Chemical formula
1	29.41(3)	3.035(3)	52(19)	0.28(3)	302(31)	Unknown	Unknown
2	30.20(4)	2.957(4)	23(12)	0.82(12)	105(15)	Iron Oxide(2,2,0)	Fe ₂ O ₃
3	35.64(5)	2.517(3)	60(20)	1.07(4)	81(3)	Iron Oxide(3,1,1)	Fe ₂ O ₃
4	43.1333	2.09557	16.7079	0.821891	108.554	Iron Oxide(4,0,0)	Fe ₂ O ₃
5	57.00(5)	1.6143(14)	13(9)	0.51(11)	185(39)	Iron Oxide(5,1,1)	Fe ₂ O ₃
6	62.68(3)	1.4811(7)	14(9)	0.95(9)	102(10)	Iron Oxide(4,4,0)	Fe ₂ O ₃
7	72.1333	1.30841	7.566	0.821891	124.892	Unknown	Unknown
8	74.6	1.27114	8.94303	0.821891	126.911	Iron Oxide(5,3,3)	Fe ₂ O ₃

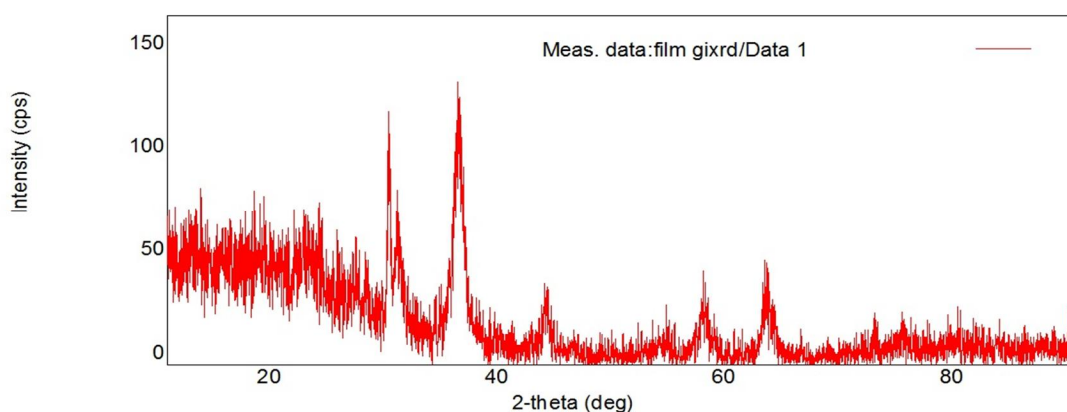


Figure 3.9 Grating Incident X-Ray Diffraction (GIXRD) of SPIONs synthesized at 0.133% precursor iron molecular solution

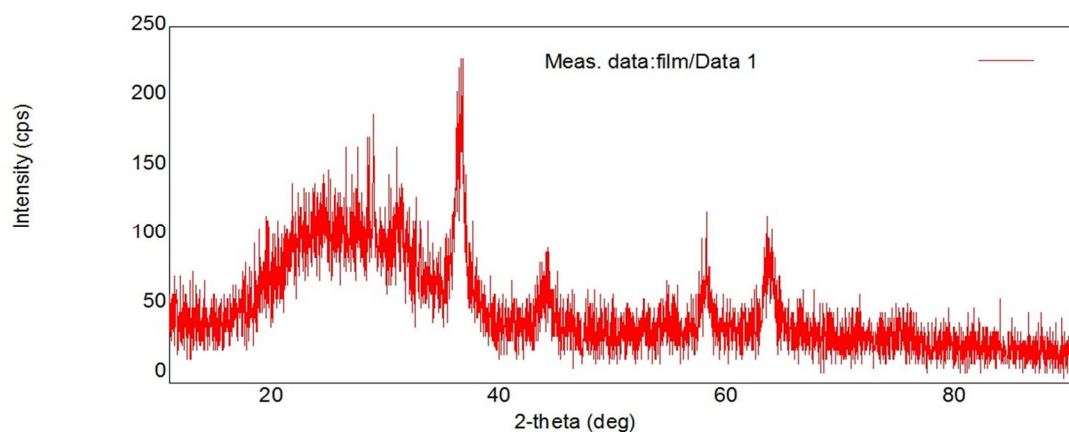
Table 3.2 PXRD Measurement conditions and Peak list of SPIONs synthesized at 0.133% precursor iron molecular solution

Measurement conditions

X-Ray	40 kV , 30 mA	Scan speed / Duration time	4.0000 deg/min
Goniometer	SmartLab	Step width	0.0200 deg
Attachment	Chi	Scan axis	Theta/2-Theta
Filter	None	Scan range	10.0000 - 90.0000 deg
CBO selection slit	BB	Incident slit	1.000deg
Diffrected beam mono.	Bent	Length limiting slit	5.0mm
Detector	SC-70	Receiving slit #1	1.000deg
Scan mode	CONTINUOUS	Receiving slit #2	1.000mm

Table 3.2 (Continued)**Peak list**

No.	2-theta (deg)	d (ang.)	Height (cps)	FWHM (deg)	Size (ang.)	Phase name	Chemical formula
1	18.4	4.81793	32.3092	1.04215	80.6552	Iron Oxide(1,1,1)	Fe ₂ O ₃
2	30.1333	2.96333	34.8775	1.04215	82.452	Iron Oxide(2,2,0)	Fe ₂ O ₃
3	35.4	2.53359	71.0853	1.50689	57.831	Iron Oxide(3,1,1)	Fe ₂ O ₃
4	42.9(2)	2.108(10)	15(7)	1.04(19)	86(15)	Iron Oxide(4,0,0)	Fe ₂ O ₃
5	57.17(12)	1.610(3)	26(9)	0.80(11)	119(16)	Iron Oxide(5,1,1)	Fe ₂ O ₃
6	62.50(11)	1.485(2)	35(11)	1.02(10)	95(9)	Iron Oxide(4,4,0)	Fe ₂ O ₃

**Figure 3.10 Powder X-Ray Diffraction (PXRD) for SPIONs synthesized at 0.133% of iron molecular concentration****3.1.7 X-Ray Photoelectron Spectroscopy (XPS)**

X-Ray Photoelectron Spectroscopy is a versatile surface analysis technique which can explore the sample to the depth of 10 nm. It is commonly used for the analysis of elemental composition,

empirical formula determination, chemical state, electronic state, binding energy and chemical and compositional state. The energy states of Fe, Oxygen, and Carbon are given in Figure 3.11 and Table 3.3). Iron compounds can be described as high-spin or low-spin as defined by crystal field theory. Fe_2 spectra of high-spin compounds exhibit complex multiplet splitting and have satellite features where as Fe_3 compounds are always high-spin leading to complex multiplet split Fe_2 spectra. In Figure 3.11 (a) Fe oxide peak (710.8 eV) is significantly shifted to higher binding energy than the metal (706.7 eV). Therefore, a well resolved $Fe_{2p_{3/2}}$ spectra for metal shows a multiplet splitting. The peaks of O1s binding energy of many compounds and species falls within a very narrow range. They tend to be broad with multiple overlapping components i.e., from 529 – 535 (Figure 3.11 b and Table 3.3 b). The components due to water and organic contamination also influences directly with that of the other elements present in the SPIONs. Thus it confirms the presence of organic elements in the SPIONs. C1s spectrum for adventitious Carbon typically has C-C, C-O-C, and O-C+O components (Figure 3.11 c and Table 3.3 c). Since iron is a transition metal which are capable of entrapping smaller atoms such as H, C, and N in their interstitial sites of crystal lattices (Yadav 2003). These trapped atoms get bonded to the atoms of the transition elements. The compositional and chemical states of adventitious elements are further influenced by the presence of applied magnetic field when SPIONs were synthesized. The influence of Cl is also unavoidable since the source materials have such elements present in them, ex $FeCl_3$. The complete spectrum for the SPIONs synthesized in 0.133% iron molecular solution is illustrated in Figure 3.12.

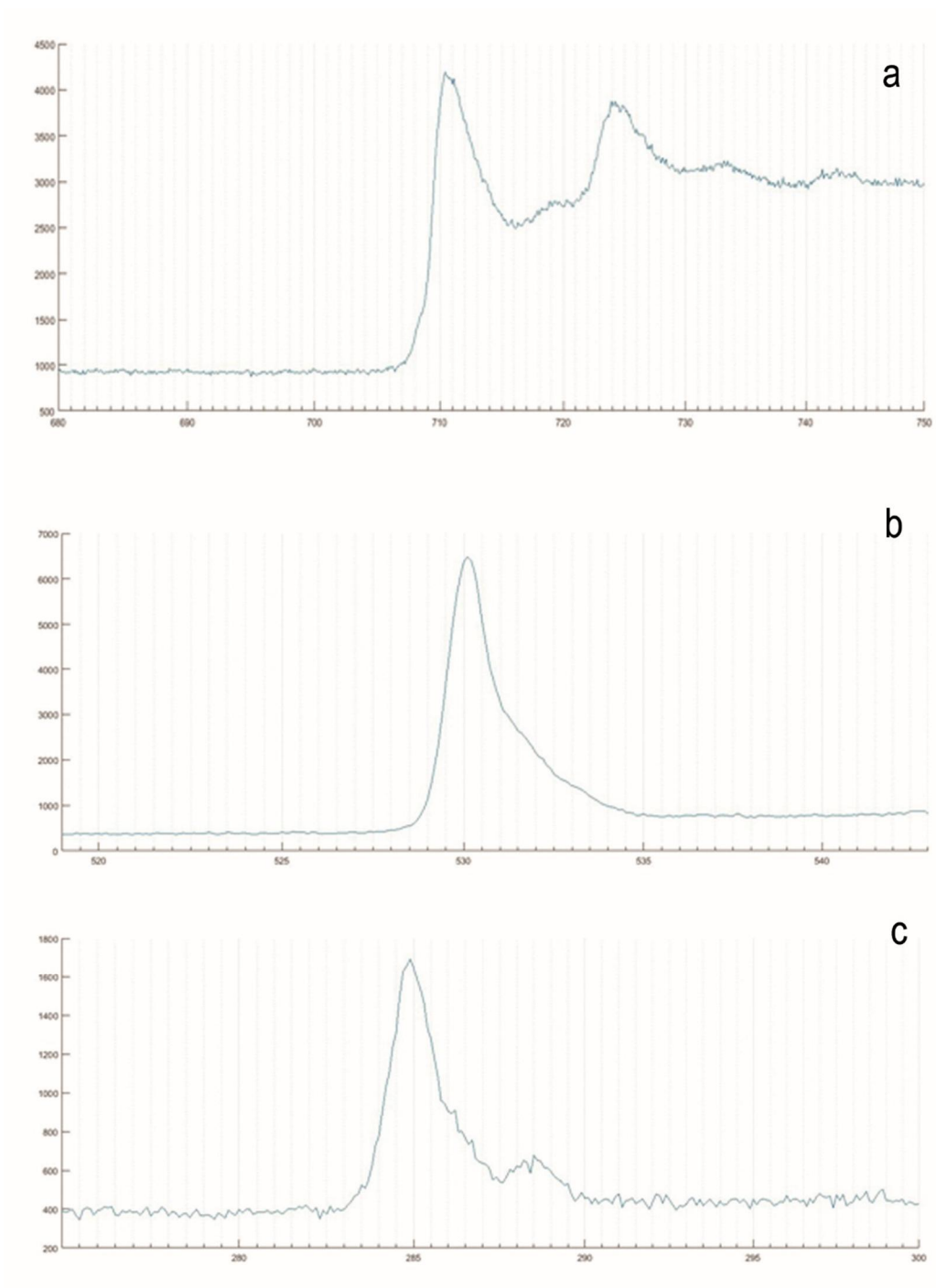


Figure 3.11 XPS spectra of SPIONs synthesized at 0.133% of precursor iron molecular solution (a) Fe, (b) Oxygen, (c) Carbon

Table 3.3 Binding energy states of elements present in SPIONs synthesized at 0.133% (a) Fe (b) Oxygen (c) Carbon

Chemical state	Binding energy Fe2p _{3/2} / eV	
Fe metal	706.7	a
FeO	709.6	
Fe ₂ O ₃	710.8	

Chemical state	Binding energy O1s / eV	
Metal oxides	529–530	b
Organic C-O	531.5–532	
Organic C=O	~533	
O-F _x	~535	

Chemical state	Binding energy C1s / eV	
C-C	284.8	c
C-O-C	~286	
O-C=O	~288.5	

The binding energy of Fe metal in the SPIONs is found in different related energy levels as per its molecular configuration from 706.7 to 710.8 eV (Figure 3.11 a). Binding energy for oxygen is found both for metal oxide and organic oxygen from 529 to ~ 535 eV (Figure 3.11 b). Binding energy for carbon is found from 284.8 to ~288.5 (Figure 3.11 c). The relative binding energies and intensity ratio of the core-level XPES peaks versus satellite features will vary according to compound, e.g. FeCl has a satellite feature compared to organic Cl (Figure 3.12). The binding energy for the organic Cl at 200 eV whereas metal chloride at ~198.5 - 199 eV. Such a phenomenon is

possible because FeCl_3 was one of the source materials used for the synthesis of SPIONs in this experiment. At the time of chemical reaction, there might have occurred a chemical shift in the binding energy for metal chloride. The complete XPS spectra for the SPIONs is given in Figure 3.12 b.

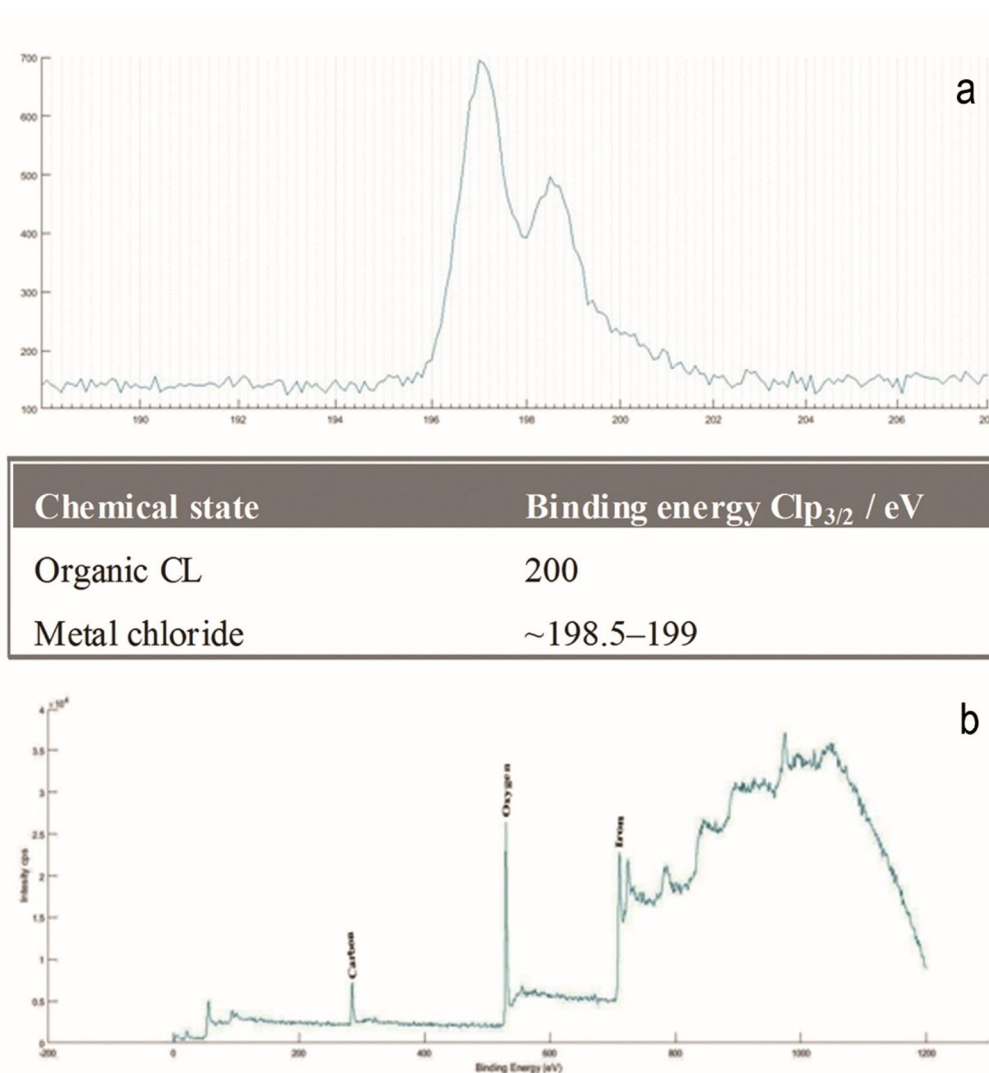


Figure 3.12 XPS spectra of Cl and its energy states in SPIONs synthesized at 0.133% and (b) the complete spectra of SPIONs

3.1.8 Zeta Potential

Particles with zeta potential more than +25 mV or –25 mV are normally considered stable (Khoshnevisan *et. al.*, 2015). SPIONs synthesized at 0.133% show negative charge of –14 (Figure 3.13). The parameters obtained here demand for the stabilization of SPIONs for further application.

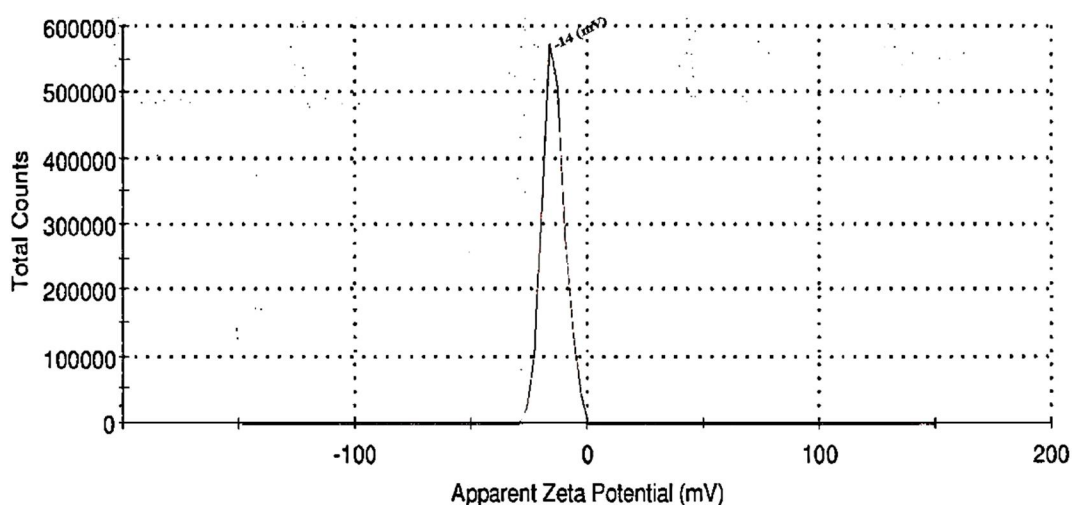


Figure 3.13 Zeta Potential value of SPIONs synthesized at 0.133% precursor iron molecular solution

3.1.9 Nuclear Magnetic Resonance Spectroscopy (NMR)

NMR spectra was taken to study the difference between precursor iron molecular solution and the SPIONs i.e., before the synthesis of SPIONs and after the synthesis SPIONs in the magnetic field. In order investigate the difference, only two elements were selected; carbon and hydrogen. The emergence of new peaks for carbon and hydrogen at 86.235 (Figure 3.15 and Table 3.5) and at 2.168 (Figure 3.17 and Table 3.6) respectively are observable after the synthesis of SPIONs. The NMR spectra for carbon and hydrogen present in

precursor iron molecular solution is given in Figure 3.14 and Table 3.5 and Figure 3.16 and Table 3.6. Thus it has become evident that the molecular carbon and hydrogen have become a part of SPIONs at the given resonance state. Moreover, after the synthesis of SPIONs there is a slight decrease observed in the resonance values at all peaks, which could be associated with a slight drop in the pH values as given in Table 3.4. From the Table it is understood that lower the pH difference better the SPIONs and its precursor iron molecular solution. Both the emergence of new peaks and decrease in resonance values of all the peaks are the proof for the molecular convergence which took place in the applied magnetic field when the SPIONs were synthesized. It was suggested that chemical transformations should be accelerated by magnetic field if they lead from diamagnetic to paramagnetic or vice versa (Steiner *et al.*, 1989). The role of applied magnetic field is evidentially convinced by NMR spectra for Carbon and Hydrogen along with the difference in the pH.

Table 3.4 pH values taken for precursor iron molecular solutions of 6 concentrations (before the synthesis of SPIONs) and after the synthesis of SPIONs

Concentration	0.2%	0.166%	0.133%	0.1%	0.066%	0.033%
Before the synthesis of SPIONs	8.32	8.16	7.90	8.05	8.71	7.82
After the synthesis of SPIONs	7.76	7.88	7.86	7.91	7.81	7.39

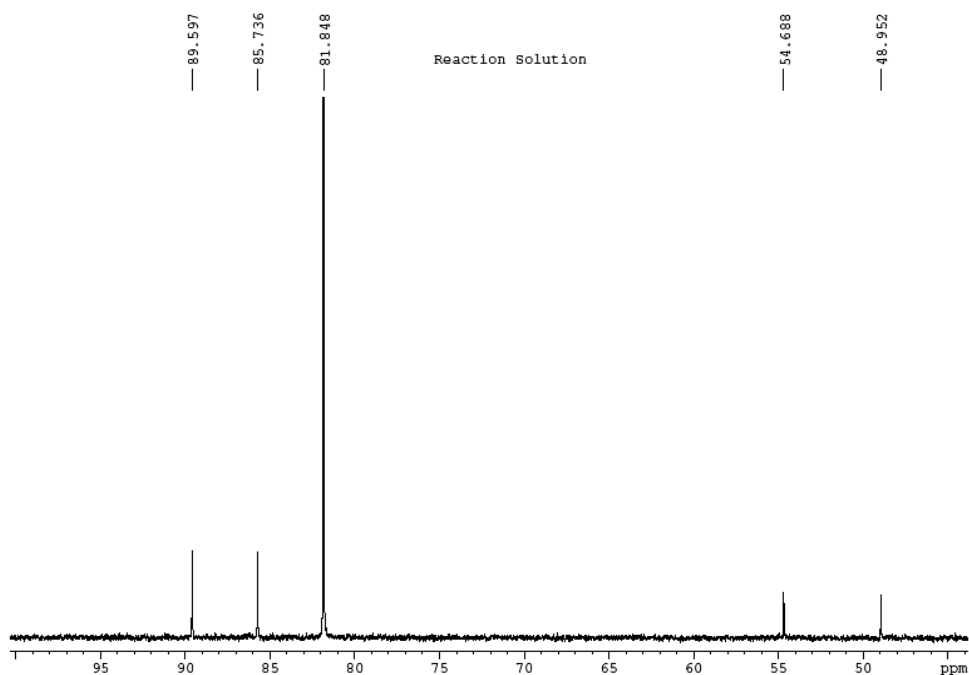


Figure 3.14 NMR spectra for Carbon present in the precursor iron molecular solution prepared at 0.133%

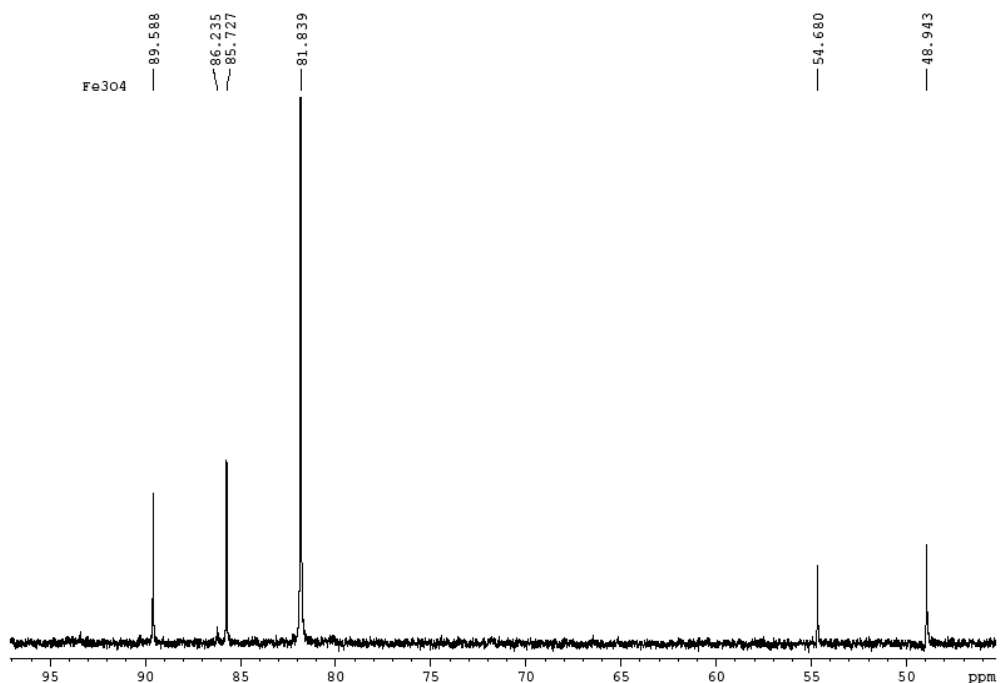


Figure 3.15 NMR spectra for Carbon in the SPIONs synthesized at 0.133% of solution

Table 3.5 NMR spectral values: (a) Spectral values of Carbon present in the precursor iron molecular solution; (b) Spectral values of Carbon present in SPIONs. The difference in spectral values in between precursor molecular solution and SPIONs are underlined. And, the emergence of new spectra is given **bold.**

Carbon	Spectra	1	2	3	4	5	6
A	Figure 3.13	48.9 <u>52</u>	54.6 <u>88</u>	81.8 <u>48</u>	85.7 <u>36</u>	Nil	89.5 <u>97</u>
B	Figure 3.14	48.9 <u>43</u>	54.6 <u>80</u>	81.8 <u>39</u>	85.7 <u>27</u>	86.235	89.5 <u>88</u>

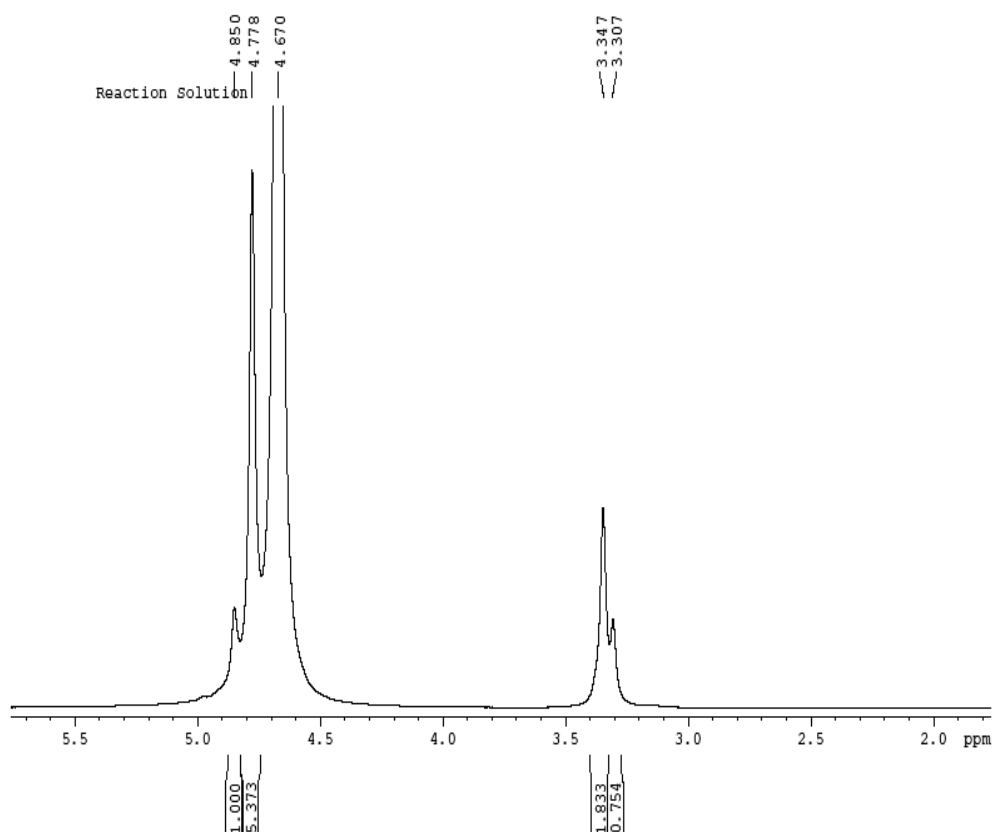


Figure 3.16 Spectra for Hydrogen present in the precursor iron molecular solution prepared at 0.133%

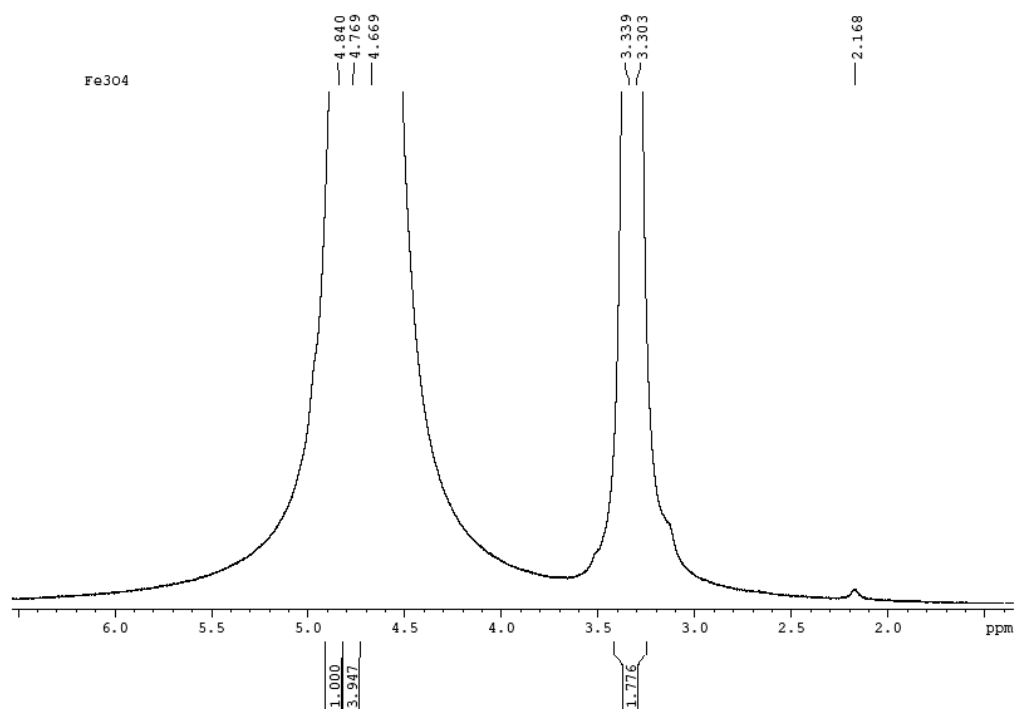


Figure 3.17 NMR spectra for Hydrogen present in the SPIONs synthesized at 0.133% solution

Table 3.6 NMR spectral values. (a) Spectral values of Hydrogen present in precursor molecular solution; (b) Spectral values of Hydrogen present in SPIONs The difference in spectral values in between precursor molecular solution and SPIONs are underlined. And, the emergence of new spectrum is given bold.

Hydrogen	Spectra	1	2	3	4	5	6
A	Figure 3:15	Nil	3.307	3.447	4.670	4.778	4.850
B	Figure 3:16	2.168	3.303	3.339	4.669	4.769	4.840

3.1.10 Superconducting Quantum Interference Device (SQUID)

Superparamagnetic (SP) state is characterized by zero coercivity and remnant magnetization. Magnetic properties of nano-size

particles depend on the factors like energy barriers, measuring time and relaxation time (inverse spin-flip frequency). As expected for superparamagnetic iron-oxide nanoparticles, the hysteresis curve for the particles was normal and tight with no hysteresis losses (Figure 3.18 a). Under an applied low magnetic field, high magnetization (M_s) and the coercivity (H_c) of the particles are at 0.002 emu (DC moment) is observed. In order to test the magnetic susceptibility, temperature was held constant at 300K and the hysteresis was measured under applied magnetic field. Both at Field Cooled (FC) and Zero-field Cooled (ZFC) conditions magnetic susceptibility was investigated. Accordingly, there are different transition fluctuations observed. There observed a steady increase in the magnetic moment when the temperature increased up to 200 K and a sudden decrease at 300 K. Moreover, an immediate increase observed up to 300 – 350 K ending a sudden fall at 400 K. As reported (Martinez-Boubeta *et al.*, 2013) the reduction in coercivity was observed according to the mean particle size that was decreased. Transition fluctuation in magnetic moment probably due to the different molecular arrangements occurred when the particles were formed in the applied magnetic field. In the case of zero-field cooled (ZFC) mode, the sample was initially lowered to K at nil applied field. At the lowest temperature, a very weak magnetic field was applied and the magnetization was recorded as the temperature increased up to 400 K (Figure 3.18 c). At ZFC temperature, the initial value is relatively small which indicates that the magnetic moments are frozen at the temperature 5 K.

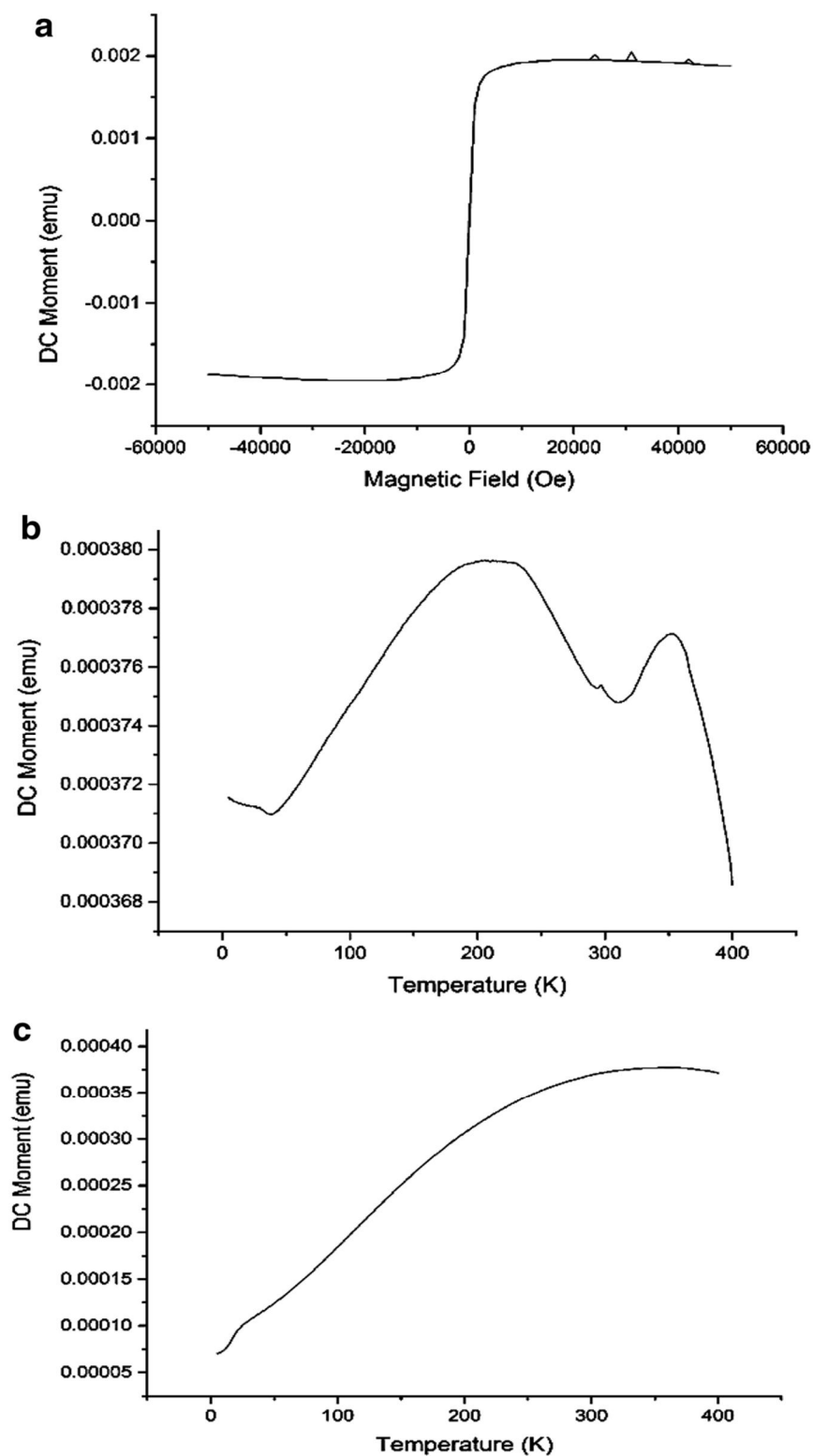


Figure 3.18 SQUID magnetic analysis: (a) Magnetic hysteresis of SPIONs synthesized at 0.133% iron molecular solution; (b) field cooled (FC) magnetization measurement; (c) zero-field cooled

3.2 SYNTHESIS OF CORESHELL-SPIONs AND THEIR CHARECTERIZATION

A 'core-shell superparamagnetic iron oxide nanoparticle' was designed as a drug carrier which demanded several stages of its preparation. There were four major phases of preparation involved: (1) synthesis of SPIONs, (2) functionalization of SPIONs, (3) loading of the desired drug – curcumin and (4) biopolymer encapsulation. Every stage was characterized as given below.

3.2.1 UV Vis Spectroscopy

The UV Vis absorption maximum of SPIONs was found to be 250 nm (Figure 3.20 a) and this was concealed by functionalization with SDS (Figure.3.20 b). The narrowing down of the absorption after functionalization showed the complete masking of iron-oxide molecules. The functionalized SPIONs were used for carrying the drug. The drug used here was curcumin which was dissolved in N, N dimethylformamide (DMF). DMF is a clear colorless hygroscopic liquid with a slight amine odor. The solvent properties of DMF is attractive because of its high dielectric constant. The pharmaceutical industry uses DMF as a reaction and crystallization solvent because of its exceptional solvency parameters. In general, the usual UV Vis absorption spectra for curcumin dissolved in various organic solvents falls in between 400 nm to 500 nm. The absorption spectra for curcumin dissolved in dimethylformamide also falls in between 400 to 500 nm (figure 3.19) which shows that the properties of curcumin are well preserved.

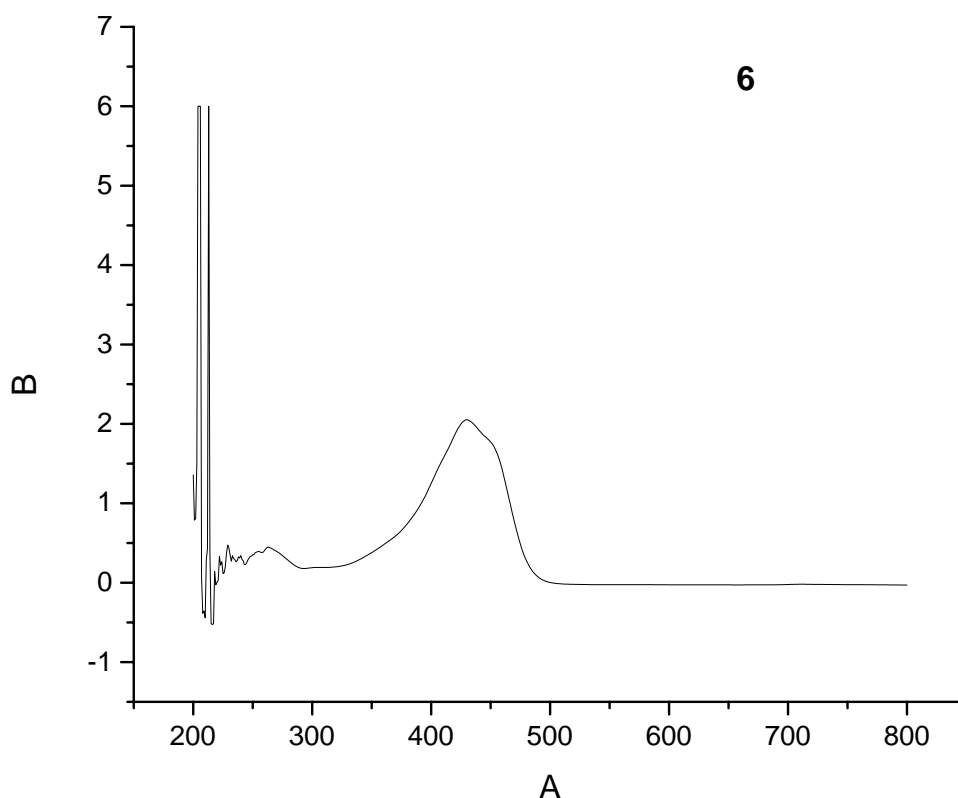


Figure 3.19 UV Vis spectra of curcumin dissolved in N, N-dimethylformamide

Absorption peaks in between 300 and 600 nm were the characteristic spectra for curcumin complexed with the functional regions of SDS: 340 nm, 450 – 492 nm (Figure 3.20 c). The reason for the wide range of spectrum is due to the loading of curcumin with SDS functional regions. After the final coating with chitosan biopolymer the sharp peak around 270 nm is noticed, which is supporting the presence of the phenolic hydroxyl groups, and the peak at ~430 nm along with the shoulder peak towards 450 nm indicates the gelatinous nature of chitosan & pyridoxine hydrochloride compound. UV-Vis absorbance spectrum of 0.01 M HCl containing unmodified chitosan reported appears at 275 nm which is attributed to the existence of phenolic hydroxyl (Ph) groups (Sakai *et al.*, 2008). By introducing Ph groups,

which are cross-linkable *via* peroxidase-catalyzed oxidative reaction, both solubility at neutral pH as well as gelation can be achieved. Pyridoxine hydrochloride was used to dissolve chitosan and the gelatinous nature of polymerization was found at 3.75:0.66 ratio respectively of pyridoxine hydrochloride and chitosan. The complete UV vis spectral data for the four phases of core-shell preparation is given in Table 3.7.

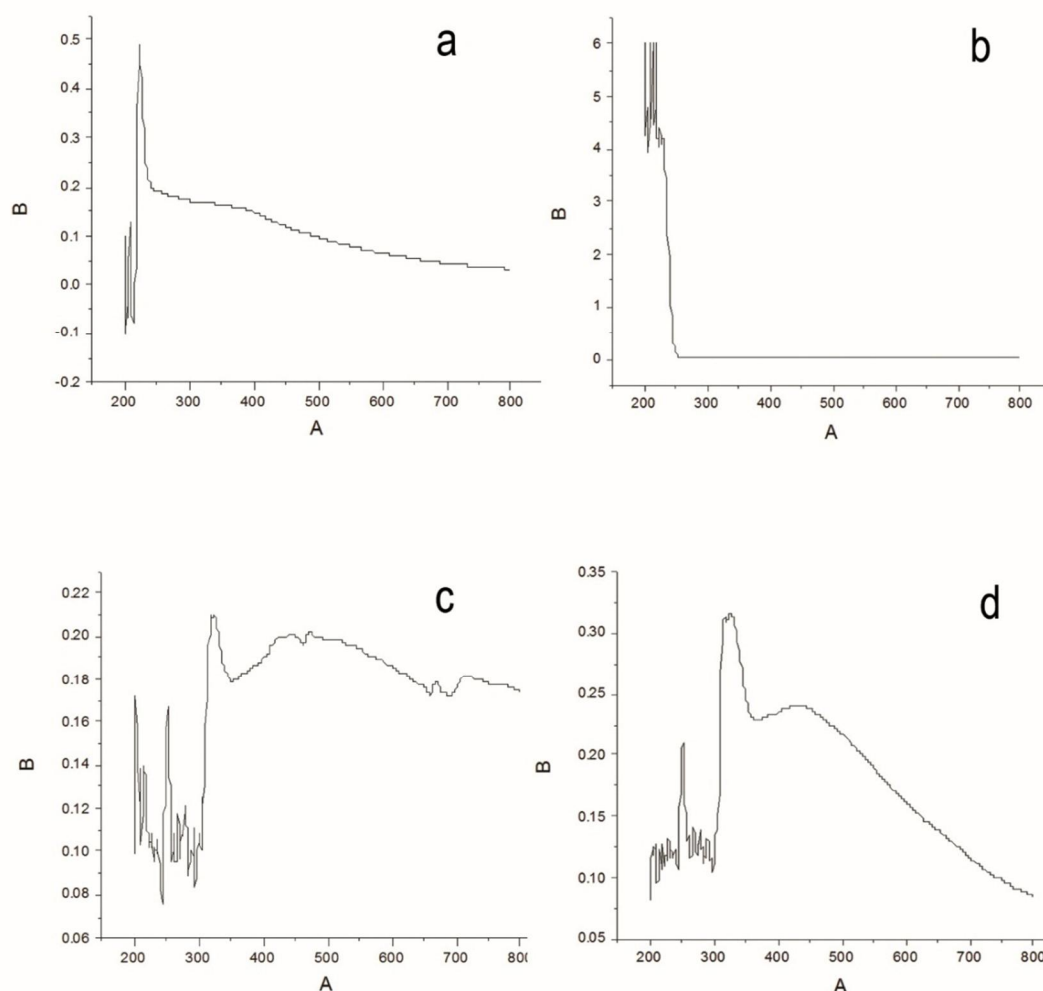


Figure 3.20 UV – Vis analysis of the four phases of producing Coreshell-SPIONs preparation (a) Naked SPIONs, (b) functionalized with SDS, (c) tagged with curcumin, and (d) encapsulated with chitosan

Table 3.7 Tabulation of UV-vis spectral data of the four phases of core-shell preparation

	200-300	300-400	400-500	500-600	600-700	700-800
A	250 nm	-	-	-	-	-
B	Concealed	Concealed	Concealed	Concealed	Concealed	Concealed
C	-	340 nm	450 nm 492nm	-	670 nm	730 nm
D	-	-	~430 nm 450 nm	-	-	-

3.2.2 Fourier Transform Infra-Red Spectroscopy (FTIR)

IR spectrum of SPIONs in between 3745.76 and 2133.27 cm^{-1} manifests the prominent absorption bands which is considered to be the finger print region of the iron-oxide nanoparticles (Figure 3.21 a). During chemical processes of iron-oxide nanoparticles high absorption affinity can result from π -electron interactions with polar surface of magnetic nanoparticles, as well as from complex bond formation at $\equiv\text{Fe-OH}$ sites (Tombacz *et al.*, 2013). Accordingly, within the finger print region there were several bands observed for O-H stretching and $-\text{C}\equiv\text{C}-$ which were the characteristic bands for the interstitial organic molecules present among the crystalline phases of SPIONs. At 3552.88 there observed the presence of $-\text{OH}$, a characteristic spectrum after functionalizing SPIONs with SDS (Figure 3.21 b). Functionalization is a kind of surface modification to add functional groups.

Table 3.8 List of the possible functional groups analyzed in FTIR all through the four phases of producing Coreshell-SPIONs

Sample	IR region or bands (cm ⁻¹)	Description
SPIONs after washing	3552.88	-OH
	2926.01	O-H stretch / carboxylic acid (m)
	2858.51	O-H stretch / carboxylic acid (m)
	2509.39	O-H stretch / carboxylic acid (m)
After functionalizing with SDS	2133.27	-C≡C- stretch / alkynes (w)
	2916.37	O-H stretch / alkanes (m)
	2156.42	-C≡C- stretch / alkynes (w)
	690.52	-C≡C-H:C-H bend / alkynes (b, c)
	646.15	-C≡C-H:C-H bend / alkynes (b, c)
	599.86	C-Br stretch / alkyl halides
After loading curcumin (<i>Curcumin</i> [®]) 3545.16 [®]	2144.84 (2401.38 [®])	-C≡C- stretch / alkynes (w)
	738.74	C-H aromatics (s)
	690.52 (688.59 [®])	-C≡C-H: C-H bend/alkynes (-C≡C-H: C-H bend/ alkynes [®])
	646.15 (648.08 [®])	-C≡C-H: C-H bend/alkynes (-C≡C-H: C-H bend/ alkynes [®])
	607.58 (617.22 [®])	C-Cl stretch / alkyl halides (<i>alkyl halides</i> [®])
	596.00	C-Br stretch / alkyl halides
After chitosan coating (<i>Chitosan</i> [®])	3425.58 (3728.40 [®])	O-H stretch, H – bonded / alcohols, phenols
	3091.89 (3466.08 [®])	C-H stretch alkenes (m) (<i>O-H stretch, H-bonded/alcohols, phenols</i> [®]) (s, b)
	2821.86 (2889.01 [®])	N-H stretch / 1 ⁰ , 2 ⁰ (<i>C-H stretch/alkanes</i> [®]) (m)
	2459.24 (2358.94 [®])	C-C≡N stretch / nitriles (alkynes [®])
	2357.01 (2193.06 [®])	-C≡C- stretch/alkynes

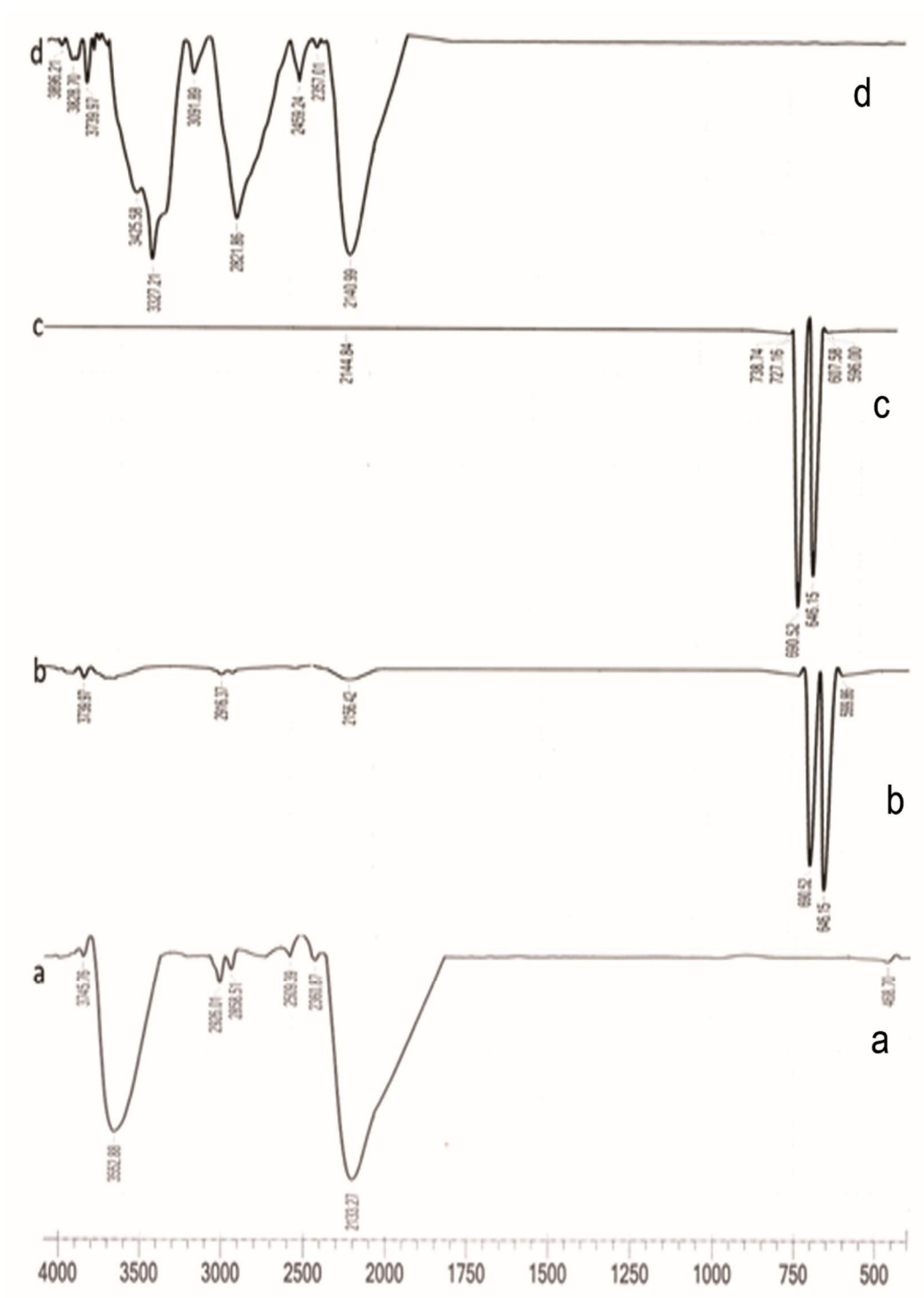


Figure 3.21 FT-IR analysis of the four phases of producing Coreshell-SPIONs (a) Naked SPIONs, (b) functionalized with SDS, (c) tagged with curcumin, (d) encapsulated with chitosan

The organic molecules used to functionalize SPIONs usually have two feature groups: the anchoring group and the charging group. The former anchors itself onto the nanoparticles' surface, while charging group binds to the respective charges dependent on the charge density, modified structure and chain length (Zhang *et al.*, 2006). Accordingly, the shift in the finger print region of the spectrum 500 to 750 cm^{-1} and maintaining some of the adjacent spectral ranges of SPIONs ascertains the association of both the anchoring and the charging groups which involved in functionalization. The finger-print region of which falls in between 500 to 750 cm^{-1} and this region is the characteristic region for the active groups of curcumin dissolved in N,N-dimethyl formamide as given in the supplementary image (Figure 3.21 c). After the bio-polymer coating (pyridoxine hydrochloride & chitosan) the finger print region in the IR spectra has tremendously shifted (Figure 3.21 d). IR spectra validates the fact that the chemistry of the composition was well preserved all through the processes.

3.2.3 Raman Spectroscopy

In Figure 3.23 (a) of the SPIONs the peaks at 213, 274, 384, and 474 cm^{-1} correspond to E_g mode and the peak at 584 cm^{-1} corresponds to A_{1g} mode of the iron oxide. Similar peak ranges were already reported arising when iron oxide nanoparticles are subjected to 514.5 nm wavelength laser excitation (Mitchell *et al.*, 2014). When SPIONs functionalized with SDS, in the spectrum (Figure 3.22 b), all peaks pertaining to iron oxide are present and in addition another shoulder peak at 635 cm^{-1} appears which can be attributed to SO_3 vibration which has become an inclusion complex with that of 584 cm^{-1}

of the iron oxide. The Raman spectrum taken after loading curcumin into the SDS functionalized SPIONs, a steady increase after 1100 cm^{-1} was observed. Figure 3.22 (6-1) gives the Raman spectrum of curcumin powder and Figure 3.2 (5-1) after dissolving in the solvent. As per the Raman spectra the integrity of curcumin is preserved.

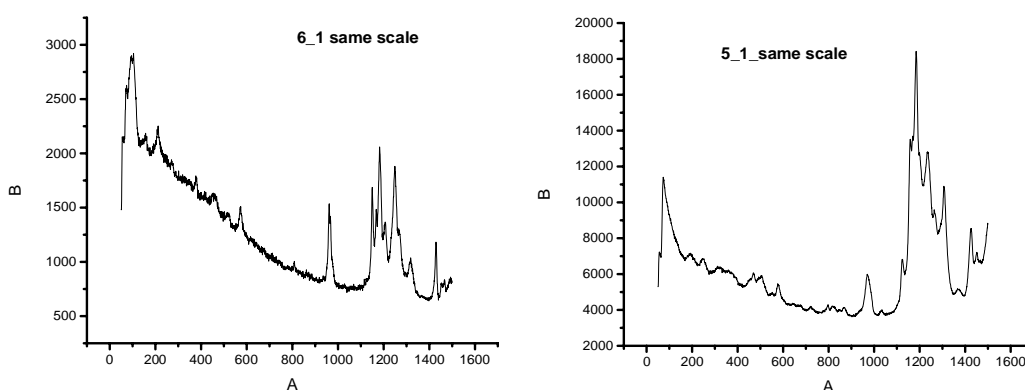


Figure 3.22 Raman spectra of curcumin powder (6-1) and curcumin dissolved in N, N-dimethylformamide (5-1)

After loading curcumin on to the functionalized SPIONs the spectrum range falls in between 1000cm^{-1} to 1400cm^{-1} . A steady rise in 1000cm^{-1} towards 1450cm^{-1} was indicative of the loaded curcumin onto the functionalized SPIONs (Figure 3.23 c). The steady rise in the spectrum could be validated with that of the spectrum for curcumin powder and curcumin dissolved in the solvent (Figures 3.22). And also all through the spectrum shielding is observed (Figure 3.23 c). It was due to the formation of SDS and curcumin inclusion complex. This steady increase in intensity towards 1450 cm^{-1} was due to the curcumin interaction with the SDS thus forming a perfect inclusion complex, i.e., about an unbonded association in which the molecules of one component (curcumin) are contained wholly or partially within the crystal lattice of the other component (SDS). Studies on inclusion

complex are already well studied and reported in detail (Frank *et al.*, 1999) and with special reference to curcumin (Kolev *et al.*, 2005) as reported by Mohan *et al.*, 2012. As shown in Figure 3.23 (d) the whole inclusion complex along with the nanoparticles is shielded off at polymer coating.

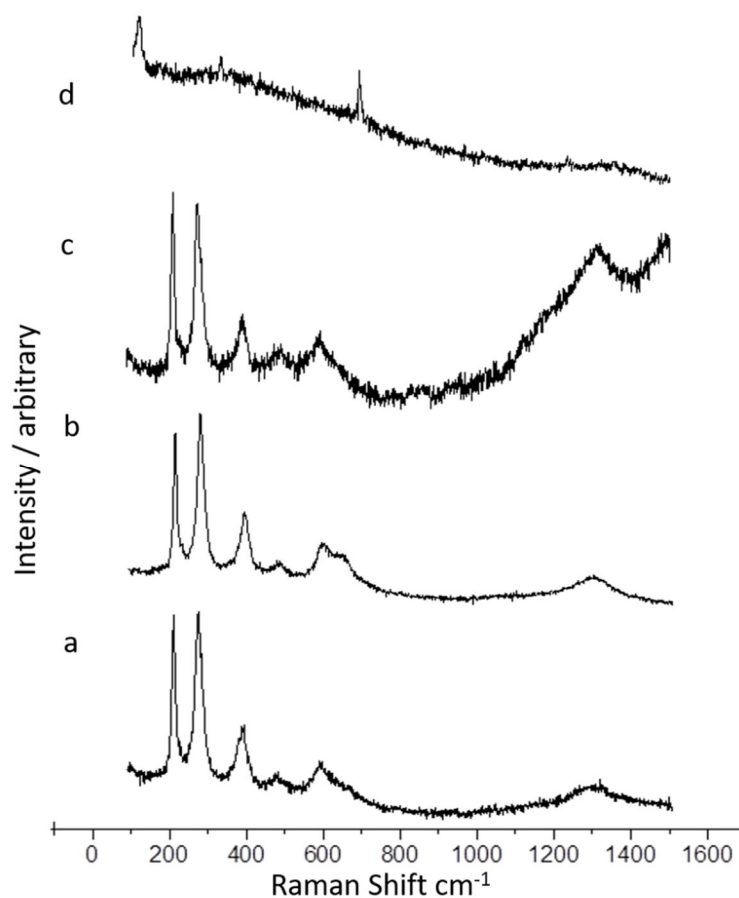


Figure 3.23 Raman Spectroscopy analysis of the four phases of producing Coreshell-SPIONs (a) Naked SPIONs, (b) functionalized with SDS, (c) tagged with curcumin, (d) encapsulated with chitosan

3.2.4 X-Ray Diffraction Spectroscopy (XRD)

Crystallinity was investigated by XRD all through the four phases of core-shell preparation. Crystalline phases of the SPIONs

(Figure 3.25 a) resemble as it is noted already in Figures 3.9 and 3.10. After functionalization with SDS (Figure 3.25 b) though the peaks relevant for the crystallinity of SPIONs appear, somehow they are shielded with the molecules of SDS. Therefore, the intensity of the SPIONs' peaks are not as stronger as that of Figure 3.25 a. The crystalline phase after curcumin loading was analyzed (Figure 3.25 c). In comparison with the XRD spectra for curcumin dissolved in N,N-dimethylformamide (Figure 3.24) the drug loaded spectra emerges in the 2-theta (degrees) axis at 10, 17, 21, 35, which are the characteristic peaks of the respective peaks of the spectral values of curcumin dissolved in N,N dimethylformamide.

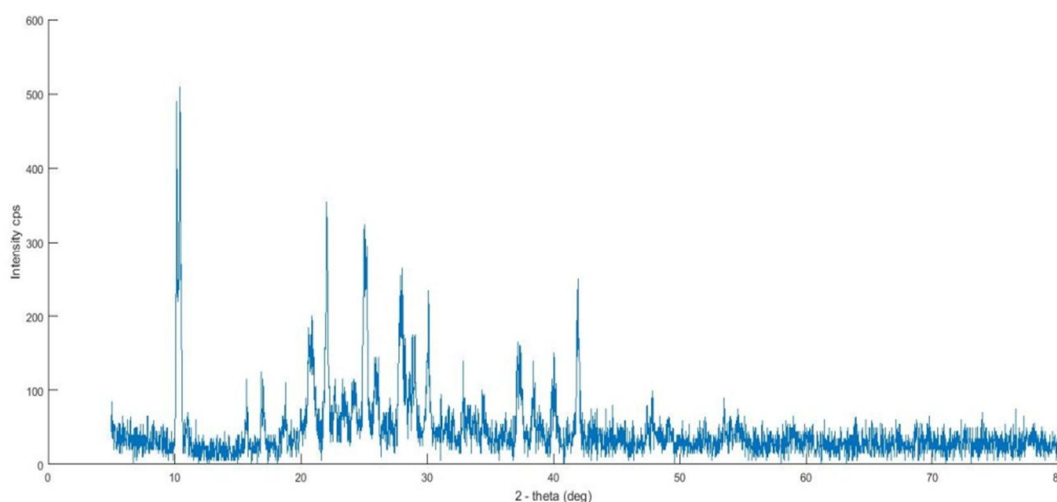


Figure 3.24 XRD spectra of curcumin dissolved in solvent

Moreover, the crystalline phase was preserved further, even after the final coating with the polymer. The characteristic peaks in between 20θ and 30θ would be the spectra representing the crystalline nature of chitosan polymer dissolved in pyridoxine hydrochloride water (distilled) based solution (Figure 3.25 d).

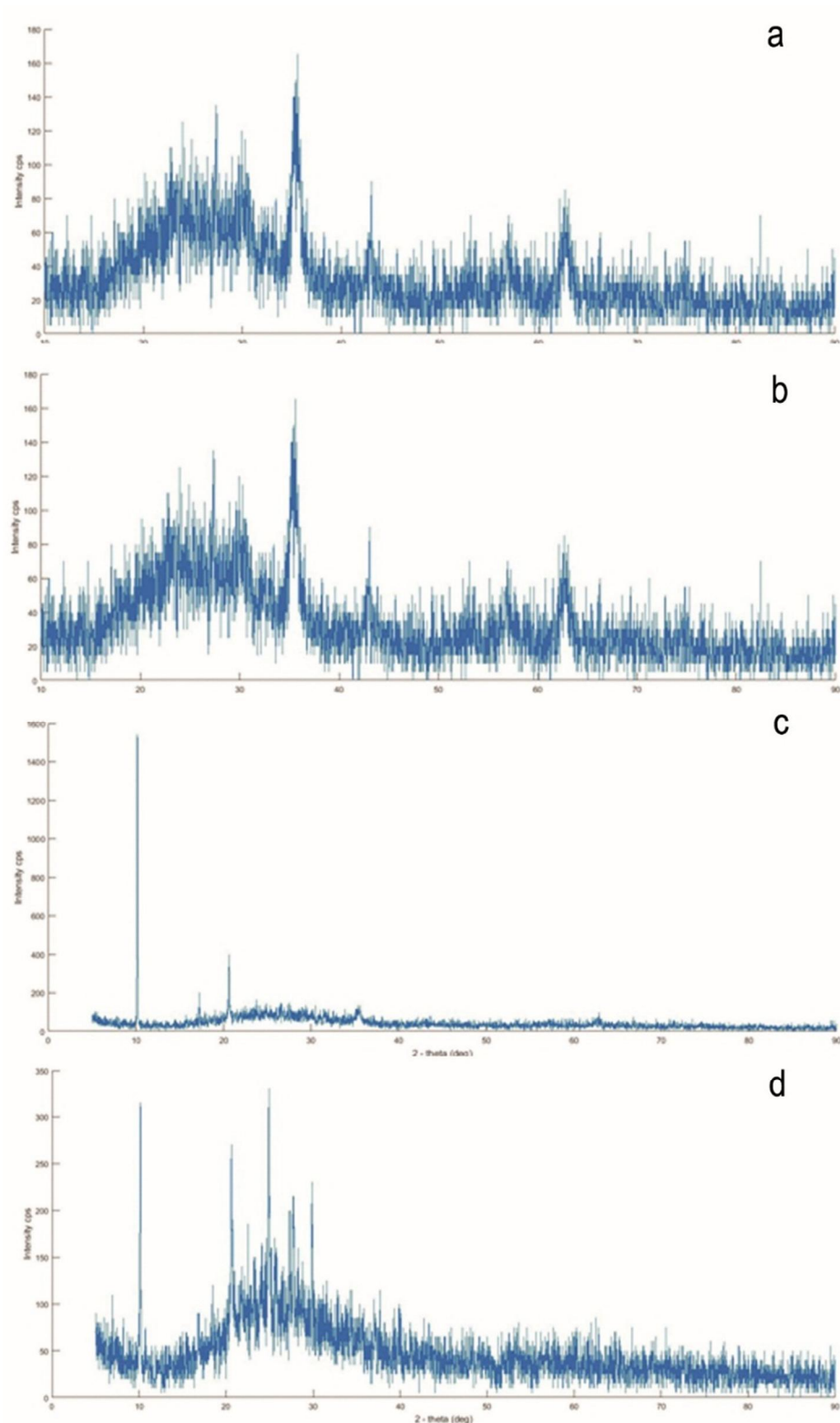


Figure 3.25 XRD analysis of the four phases of producing Coreshell-SPIONs (a) Naked SPIONs, (b) functionalized with SDS, (c) tagged with curcumin, (d) encapsulated with chitosan

3.2.5 Zeta Potential

The optimum concentration of SDS for stabilizing the SPIONs was confirmed in zeta analyzer. It is a significant instrument for understanding the state of the nanoparticles' surface and envisaging the extended constancy of the nanoparticles. The magnitude of the zeta potential is predictive of the colloidal stability. Nanoparticles with zeta potential values greater than + 25mV or less than - 25mV typically have high degrees of stability. Dispersions with a low zeta potential value will eventually aggregate due to Van der Waal inter-particle attractions (Nano Composix. com 2012). Surfactants are often used to disperse nanoparticles entirely in an appropriate medium. Coating of single domain iron-oxide nanoparticles with a double layer of surfactants in an aqueous medium result in stable colloidal dispersions (Tombacz *et al.*, 2013). The zeta potential value derived for naked SPIONs, i.e., before functionalization was -14mV as shown in Figure 3.26 a. Since it was below - 25mV for SPIONs, it was unstable. SDS increased the stability after functionalization for curcumin loading. Three different concentrations of SDS i.e. 0.020%, 0.040%, 0.80% respectively were used for this purpose. Stabilization was found closer at 0.040% and 0.080% of SDS. SDS used beyond the above these concentrations slowly increased agglomerations of the particles. Moreover, surfactants in solution below their critical micellization concentration (CMC) improve drug solubility by providing regions for hydrophobic drug interactions. The hydrophobic core enhances the entrapment of drug, thus increasing its stability too. Mechanism of drug entrapment, as well as the physiochemical interactions of constituents determine their drug solubilization capacity and physical stability (Narang *et al.*, 2007). Drugs can be incorporated by phase inversion temperature (PIV) method

(Brime *et al.*, 2002) by dissolving the drug in the hydrophobic or hydrophilic components. For the loading of curcumin, 0.080% of SDS stabilized SPIONs were used (Figure 3.26 b). And, after three days' incubation for drug loading in the cyclo-rotator, 70⁰C temperature was applied in water bath for inducing PIV for the better incorporation of the drug to form inclusion complex. Accordingly, the anionic state of the SDS functionalized SPIONs turned to cationic and its overall stabilization also was shifted from negative (- 19) to positive (+39) (Figure 3.26 b and c, Table 3.9 b and c).

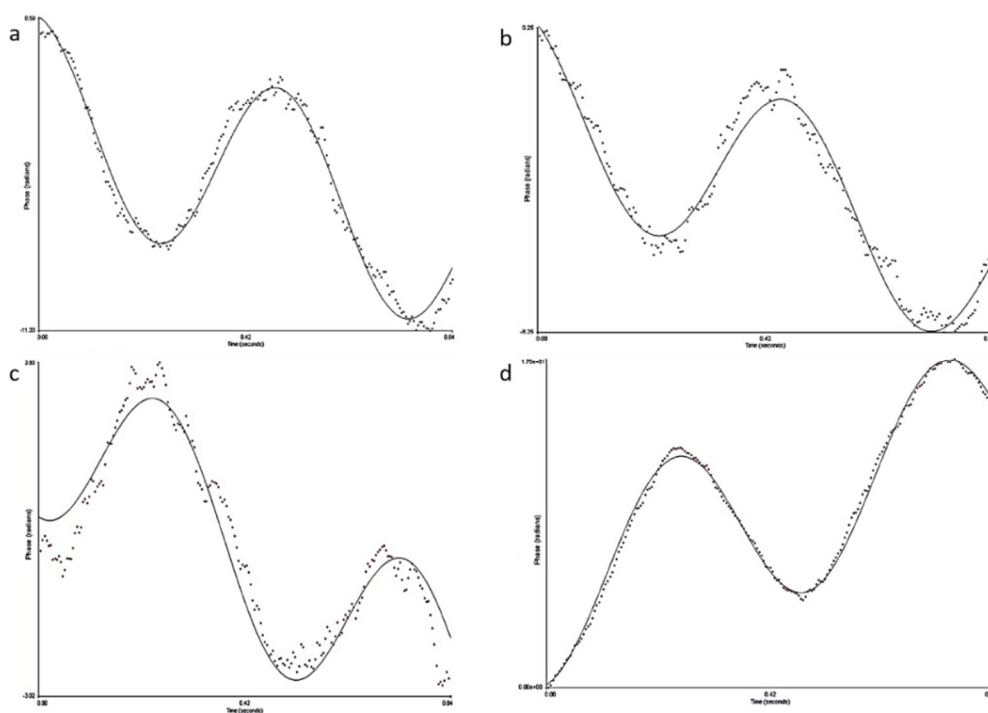


Figure 3.26 Zeta potential analysis of the four phases of producing Coreshell-SPIONs (a) Naked SPIONs, (b) functionalized with SDS, (c) tagged with curcumin, (d) encapsulated with chitosan

The shift in the charge, in fact, is due to the cationic nature of curcumin. After chitosan polymer encapsulation in the subsequent process maintained the required stability for biological application with zeta potential value at +27.48 (Figure 3.26 d and Table 3.9 d).

Table 3.9 Table of the complete zeta potential readings which show the increase of stability in all through the coreshell-SPIONs preparation and the change of surface charge

(a)				(b)			
Run	Mobility	Zeta Potential (mV)	Rel. Residual	Run	Mobility	Zeta Potential (mV)	Rel. Residual
1	-1.59	-20.40	0.0330	1	-1.88	-24.10	0.0346
2	-1.48	-18.98	0.0587	2	-1.95	-24.98	0.0603
3	-0.77	-9.87	0.0205	3	-1.16	-14.87	0.0313
4	-1.34	-17.12	0.0246	4	-1.49	-19.11	0.0318
5	-1.97	-25.16	0.0226	5	-1.33	-17.08	0.0205
Mean	-1.43	-18.31	0.0319	Mean	-1.56	-20.03	0.0357
Std. Error	0.19	2.49	0.0070	Std. Error	0.15	1.97	0.0066
Combined	-1.42	-18.16	0.0225	Combined	-1.55	-19.79	0.0267

(c)				(d)			
Run	Mobility	Zeta Potential (mV)	Rel. Residual	Run	Mobility	Zeta Potential (mV)	Rel. Residual
1	2.95	37.81	0.0193	1	2.19	28.06	0.0159
2	3.13	40.09	0.0186	2	2.04	26.16	0.0143
3	2.98	38.11	0.0323	3	2.05	26.23	0.0137
4	3.40	43.50	0.0169	4	2.20	28.12	0.0157
5	3.12	39.92	0.0215	5	2.29	29.25	0.0135
Mean	3.12	39.89	0.0217	Mean	2.15	27.57	0.0146
Std. Error	0.08	1.01	0.0027	Std. Error	0.05	0.60	0.0005
Combined	3.11	39.86	0.0118	Combined	2.15	27.48	0.0072

3.2.6 Microscopic Analysis

3.2.6.1 Scanning Electron Microscopy (SEM)

SPION was in the range of 10 to 15 nm (Figure 3.27 a). Functionalization of SPIONs had enlarged the dimensions to 20 nm (Figure 3.27 b), as the drug loaded, it too increased the size to 35 nm (Figure 3.27 d). At last the core-shell was made by coating with chitosan and the size appears between 40 and 45 nm (Figure 3.27 d). EDX analysis is clearly stating the involvement of the chemicals in every step (Figure 3.27 a,b,c,d EDX spectra). As the size increased the shape too modified. The shape of the particles appears to be spherical. After curcumin loading (Figure 3.27 c) the image appears by some means agglomerated. But after encapsulation with chitosan the image appears free of agglomeration (Figure 3.27 d) telling the previous agglomeration insignificant. Moreover, in the final image a considerable amount of chitosan polymer also found which did not involve in encapsulation.

Proper washing of core-shell would dissuade such residual polymer molecules.

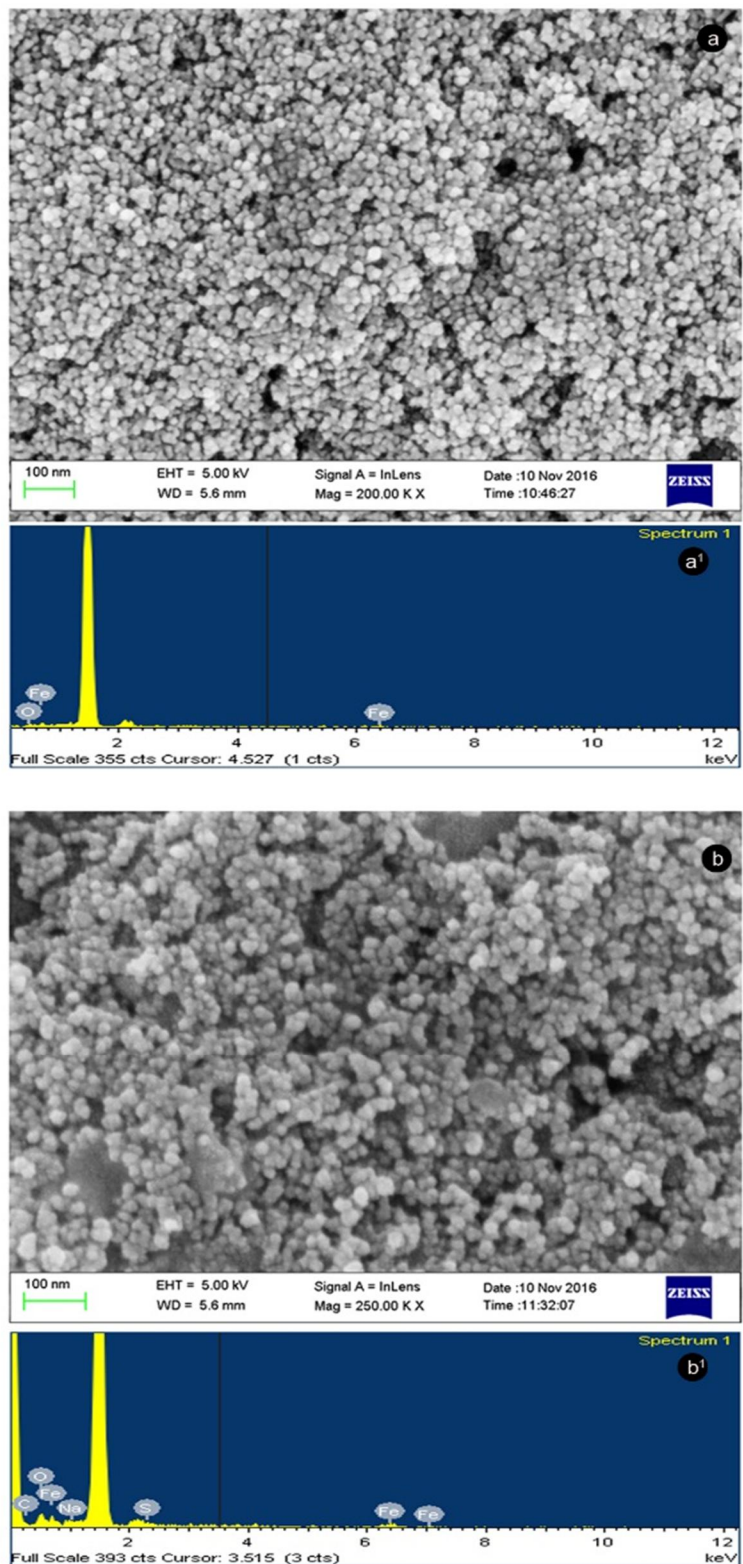


Figure 3.27 (Continued)

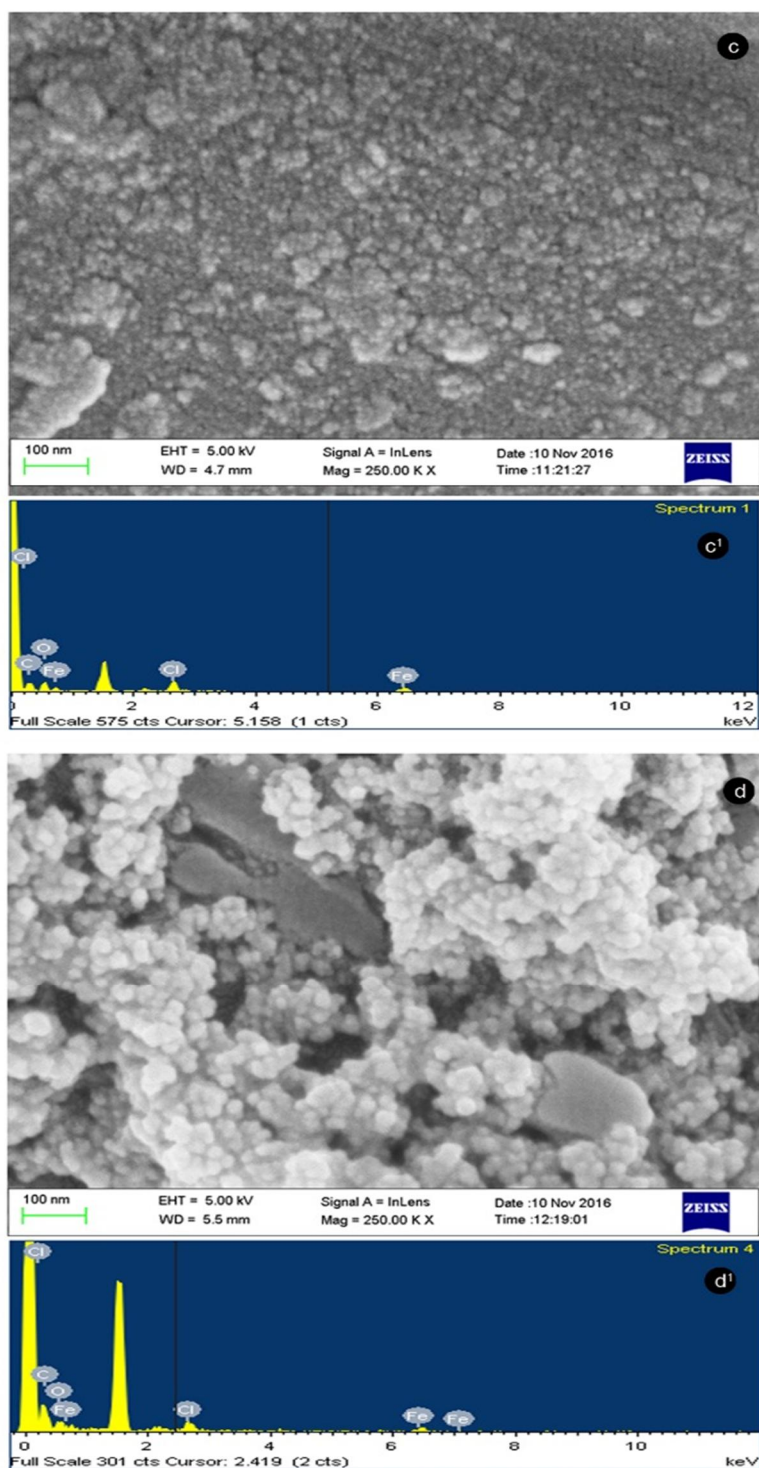


Figure 3.27 SEM – EDX analysis of the four phases of producing Coreshell-SPIONs (a) Naked SPIONs, (b) functionalized with SDS, (c) tagged with curcumin, (d) encapsulated with chitosan

3.2.6.2 Atomic Force Microscopy (AFM))

AFM result was on par with the SEM results (Figure 3.28 a - d). there was agglomeration of particles seen as the level of coating was increased. Agglomeration in the image would be the physical process while drying the sample on the glass slide.

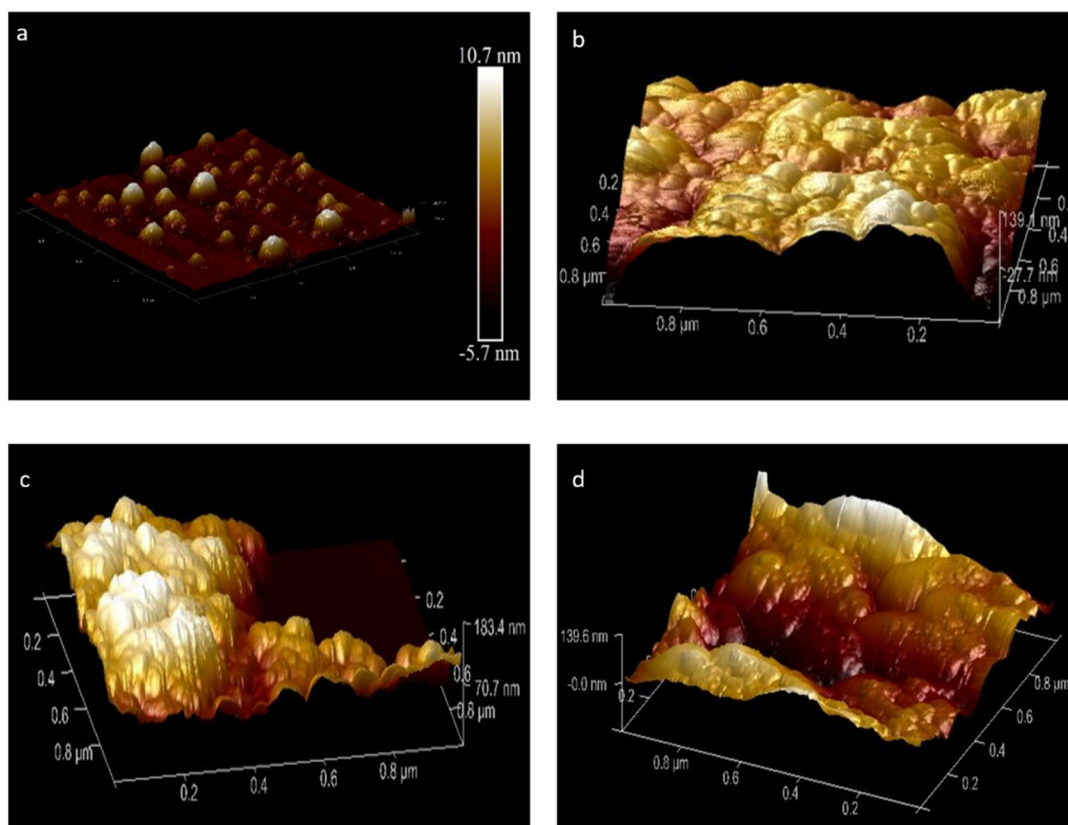


Figure 3.28 AFM analysis of the four phases of producing Coreshell-SPIONs (a) Naked SPIONs (b) functionalized with SDS (c) tagged with curcumin (d) encapsulated with chitosan

3.2.7 X-Ray Photoelectron Spectroscopy (XPES)

The chemical states of Fe, over the phases of core-shell preparation is presented in Figure 3.29 a – d and Table 3.10. Peaks at

706.7, 709.6, 710.8, and 710.4 eV are representing the binding energy for Fe, FeO, Fe₂O₃, and FeCl₂ respectively. Involvement of oxygen in all the phases is demonstrated in Figure 3.30 a – d and Table 3.11. Spectral ranges 529 to ~535 eV broad spectrum in SPIONs says the involvement of oxygen in metal oxide and its energy level. Similarly, energy levels of carbon is found as C-O, C=O and O-C=O at 284.8, ~ 286, ~ 288.5 respectively (Figure 3.31 a – d and Table 3.12) The three major elements Fe, Oxygen and Carbon played a vital role in the formation of SPIONs and their energy states also determined the type of SPIONs. Elemental invariance in energy levels all through the phases of core-shell preparation substantiates the unaltered integrity of SPIONs and the substances involved in the experiment. Other than the four major elements the energy spectrum for Mg and (Figure 3.32 a – c; Table 3.13 a – c) and Cl (Figure 3.33 a, b; Table 3.14 a, b) and Na (Figure 3.33 c; Table 3.14 c). The presence of such elements in the core-shell preparation were essential as they involved in stabilization, curcumin tagging and polymer coating. Preserving the integrity of chemical substances involved in the reaction processes is one of the major prerequisite for a better formation of drug carrying core-shell. For biological application this is an essential aspect. The complete XPES energy spectra of the four phases of core-shell preparation is given in Figure 3.34. The changes are clearly observable in the complete spectra where Fe spectral range is moderated from a – d. The compositional state of Oxygen, Carbon are augmented. Other minor elements begin to appear at 'c' and well preserved at 'd'. The complete energy levels of elements present in the four phases of core-shell preparation is given in Table 3.15.

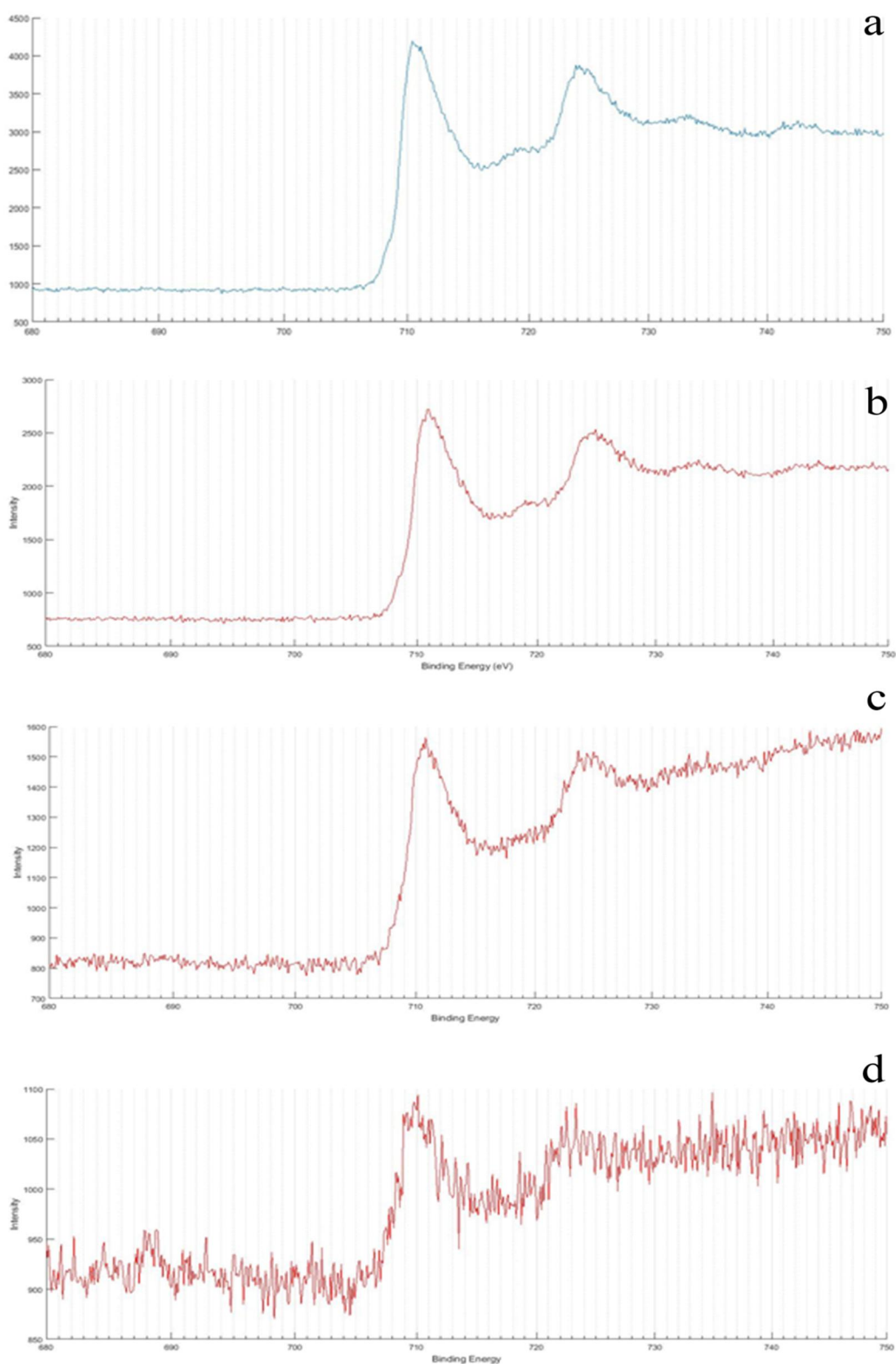


Figure 3.29 XPS spectra for the energy state of Fe over the four phases of producing Coreshell-SPIONs: (a) Naked SPIONs, (b) functionalized with SDS, (c) loaded with curcumin, (d) encapsulated with biopolymer coating

Table 3.10 Energy Levels of Fe (a) Naked SPIONs, (b) functionalized with SDS, (c) tagged with curcumin, (d) encapsulated with biopolymer coating

Chemical state	Binding energy Fe2p _{3/2} / eV	
Fe metal	706.7	a
FeO	709.6	
Fe ₂ O ₃	710.8	
FeCl ₂	710.4	

Chemical state	Binding energy Fe2p _{3/2} / eV	
Fe metal	706.7	b
FeO	709.6	
Fe ₂ O ₃	710.8	
FeCl ₂	710.4	

Chemical state	Binding energy Fe2p _{3/2} / eV	
Fe metal	706.7	c
FeO	709.6	
Fe ₂ O ₃	710.8	
FeCl ₂	710.4	

Chemical state	Binding energy Fe2p _{3/2} / eV	
Fe metal	706.7	d
FeO	709.6	
Fe ₂ O ₃	710.8	
FeCl ₂	710.4	

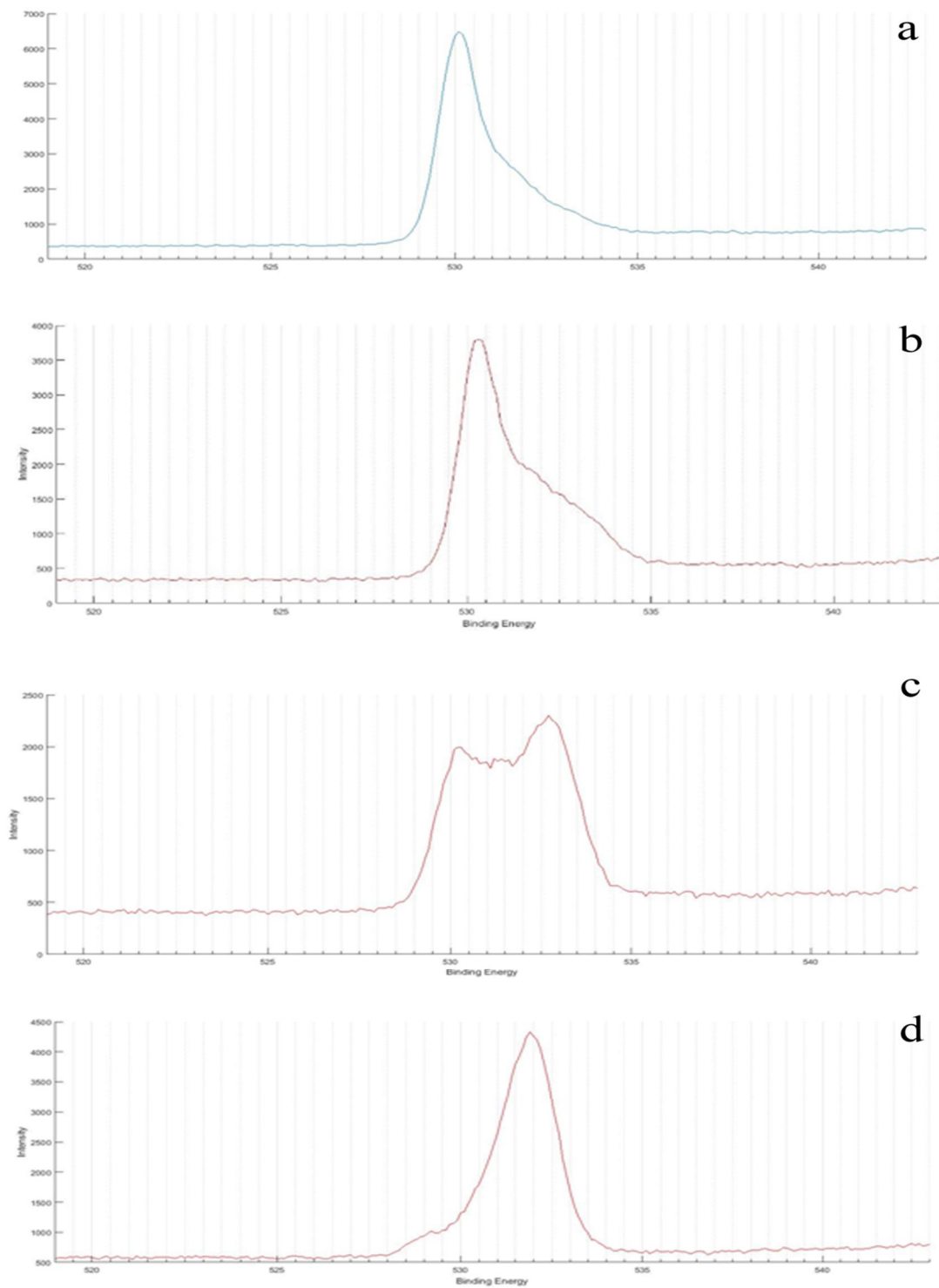


Figure 3.30 XPS spectra for the chemical states of oxygen over the four phases of producing Coreshell-SPIONs: (a) Naked SPIONs, (b) functionalized with SDS, (c) loaded curcumin, (d) encapsulated with biopolymer coating

Table 3.11 Energy Levels of Oxygen (a) SPIONs, (b) functionalized with SDS, (c) loaded with curcumin, (d) encapsulated with biopolymer coating

Chemical state	Binding energy O1s / eV	
Metal oxides	529–530	a
Organic C-O	531.5–532	
Organic C=O	~533	
O-F _x	~535	

Chemical state	Binding energy O1s / eV	
Metal oxides	529–530	b
Organic C-O	531.5–532	
Organic C=O	~533	
O-F _x	~535	

Chemical state	Binding energy O1s / eV	
Metal oxides	529–530	c
Organic C-O	531.5–532	
Organic C=O	~533	
O-F _x	~535	

Chemical state	Binding energy O1s / eV	
Metal oxides	529–530	d
Organic C-O	531.5–532	
Organic C=O	~533	
O-F _x	~535	

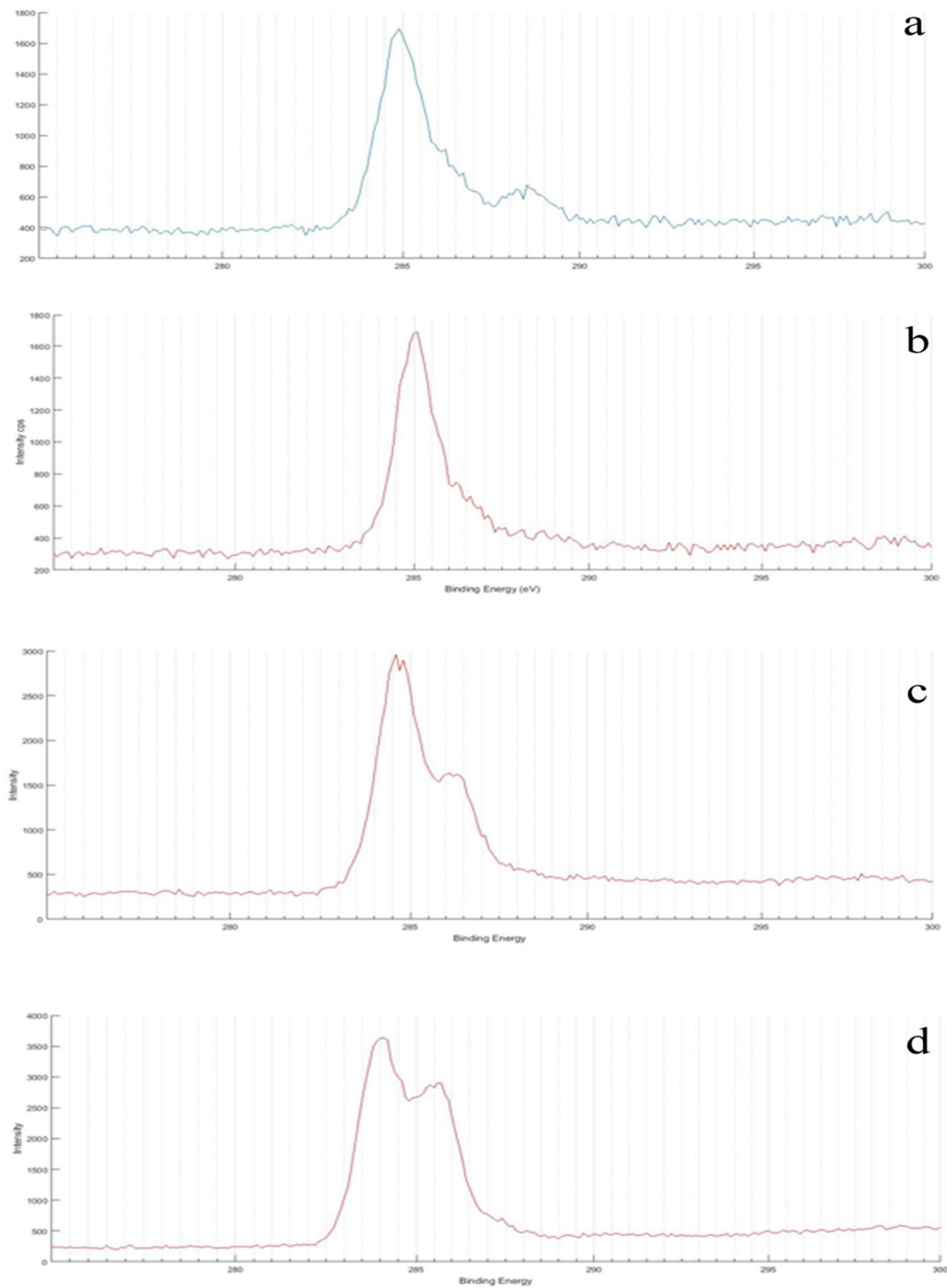


Figure 3.31 XPS spectra for the chemical states of carbon over the four phases of Coreshell-SPIONs: (a) naked SPIONs, (b) functionalized with SDS, (c) loaded with curcumin, (d) encapsulated with biopolymer coating

Table 3.12 Energy Levels of Carbon (a) naked SPIONs, (b) functionalized with SDS, (c) loaded with curcumin, (d) encapsulated with biopolymer coating

Chemical state	Binding energy C1s / eV	
C-C	284.8	a
C-O-C	~286	
O-C=O	~288.5	

Chemical state	Binding energy C1s / eV	
C-C	284.8	b
C-O-C	~286	
O-C=O	~288.5	

Chemical state	Binding energy C1s / eV	
C-C	284.8	c
C-O-C	~286	
O-C=O	~288.5	

Chemical state	Binding energy C1s / eV	
C-C	284.8	d
C-O-C	~286	
O-C=O	~288.5	

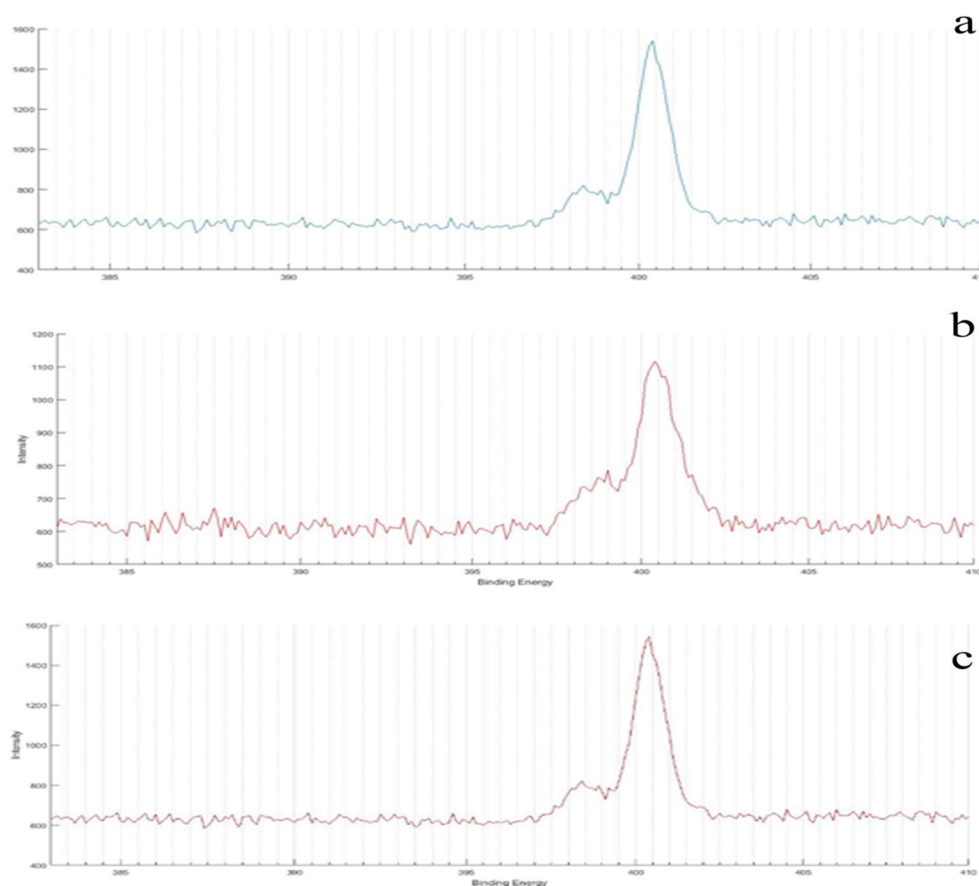


Figure 3.32 Energy spectra of Mg present after (a) synthesis of SPIONs, (b) after curcumin loading, and (c) after biopolymer coating (Coreshell-SPIONs)

Table 3.13 Tabulation of the energy level of Mg present in different phases of Coreshell-SPIONs production

Chemical state	Binding energy Mg1s / eV	
Metal nitrides	~397	a
C-NH ₂	~400	
Nitrate	>405	
Chemical state	Binding energy Mg1s / eV	
Metal nitrides	~397	b
C-NH ₂	~400	
Nitrate	>405	
Chemical state	Binding energy Mg1s / eV	
Metal nitrides	~397	c
C-NH ₂	~400	
Nitrate	>405	

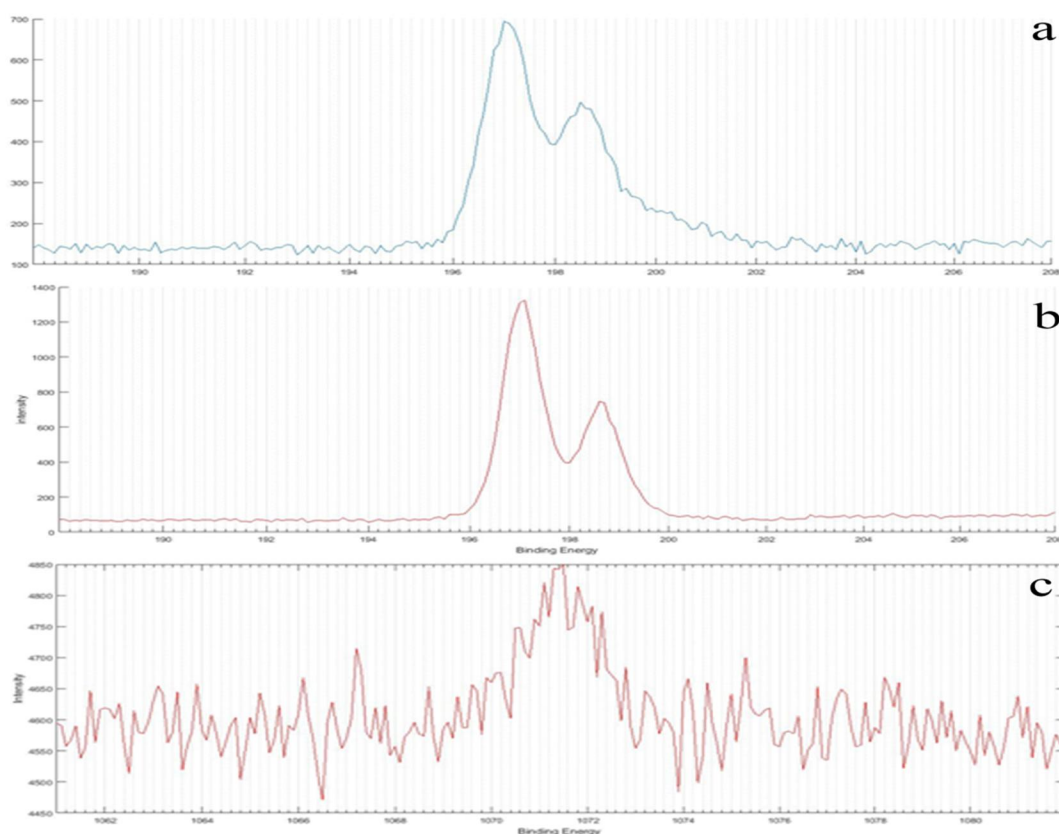


Figure 3.33 Energy spectra of Cl analyzed (a) after Synthesis of SPIONs and (b) after coreshell-SPIONs preparation. (c) Spectrum for Na

Table 3.14 Tabulation of the energy levels of Cl, and Na present in different phases of core-shell preparation

Chemical state	Binding energy Cl _p _{3/2} / eV	
Organic CL	200	a
Metal chloride	~198.5–199	
Chemical state	Binding energy Cl _p _{3/2} / eV	
Organic CL	200	b
Metal chloride	~198.5–199	
Chemical state	Binding energy Na1s / eV	
Sodium compounds	1071–1071.5	c

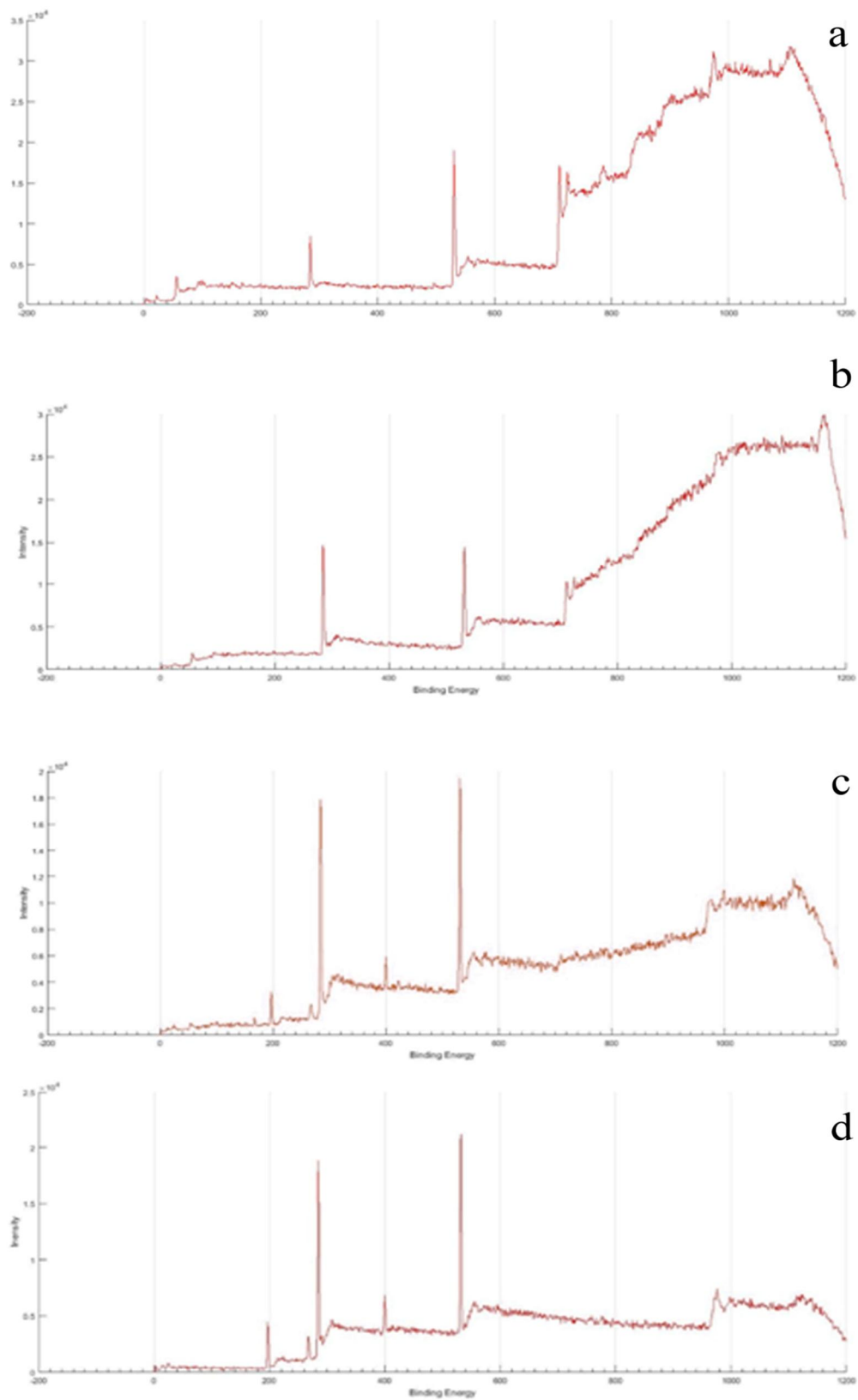


Figure 3.34 Complete XPS energy spectrum of the four phases of producing Coreshell-SPIONs

Table 3.15 Energy states of elements summarized from the complete spectra of core-shell preparation

Elements	(a)	(b)	(c)	(d)
Fe ₂ O ₃	710.8	710.8	710.8	710.8
Metal Oxide	529-530	529-530	529-530	529-530
Organic C-O C=O	531.5 --533	531.5 --533	531.5 --533	531.5 --533
Carbon C-C C-O- C O- C	284.8 --288.5	284.8 --288.5	284.8 -- 288.5	284.8 -- 288.5
Mg	-	~400	~400	~400
Cl	~198.5-199	~198.5-199	-	-
Na	-	1071-1071.5	-	-

3.2.8 Superconducting Quantum Interference Device (SQUID) Analysis

Superparamagnetic state was found to be preserved all over the stages (Figure 3.35 a – d). In ZFC magnetization (Figure 3.36 a – d) there observed saturation magnetization till 350 K and in FC mode (Figures 3.37 a - d), the saturation magnetization is observed up to 250 K - 260 K except for naked SPIONs. In case of naked SPIONs a slight fluctuation is observed which then is rectified after stabilization with SDS. Therefore, the SPIONs can be used for various medical purposes like drug delivery, imaging and hyperthermia and thus these can be used for hyperthermia. SQUID results are supported by VSM results (Figures 3.38 a – d; 3.39 a – d; 3.40 a – d).

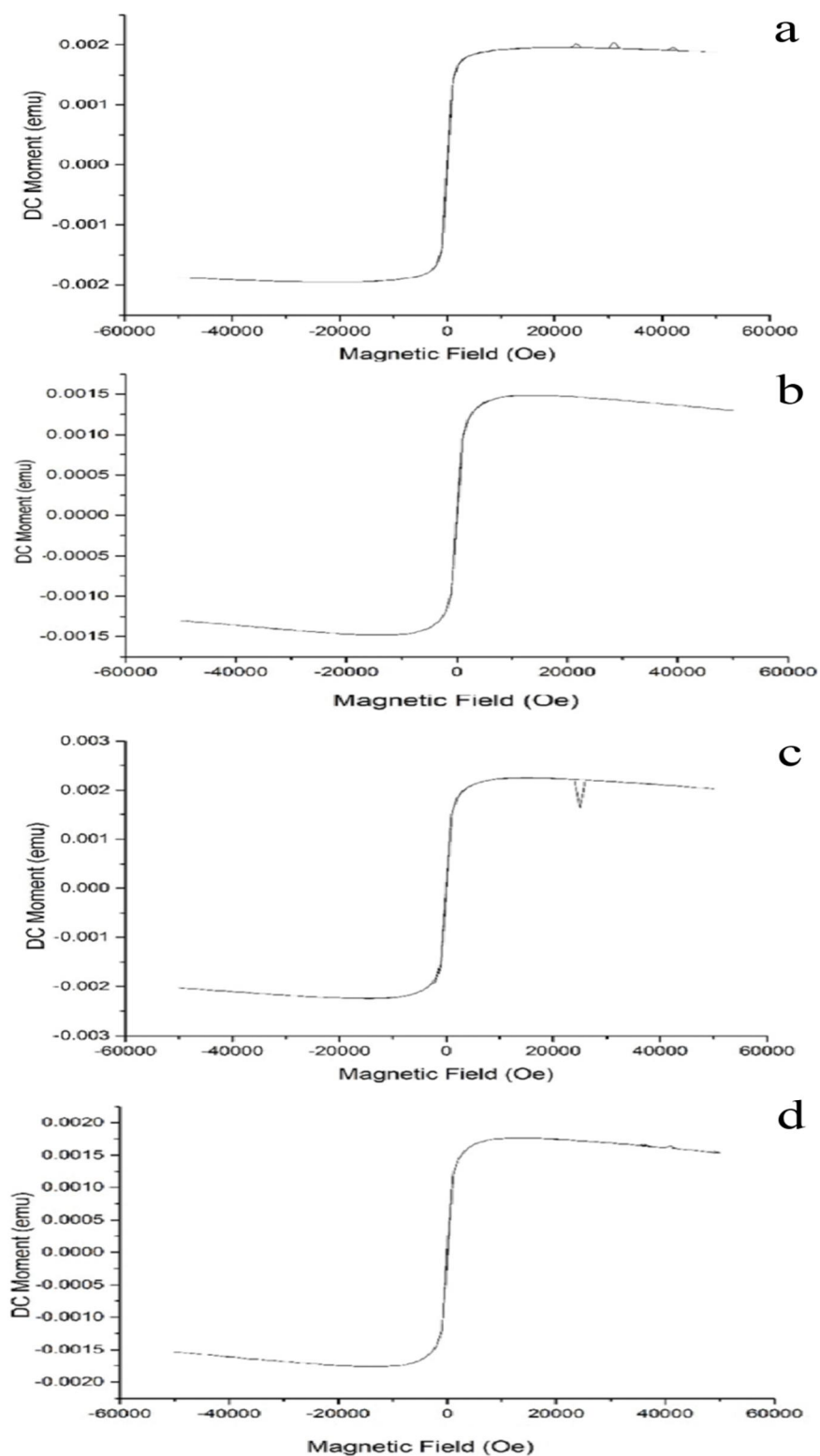


Figure 3.35 Magnetic hysteresis obtained from SQUID: (a) naked SPIONs, (b) after functionalizing with SDS, (c) after curcumin loading, (d) after encapsulating with biopolymer coating.

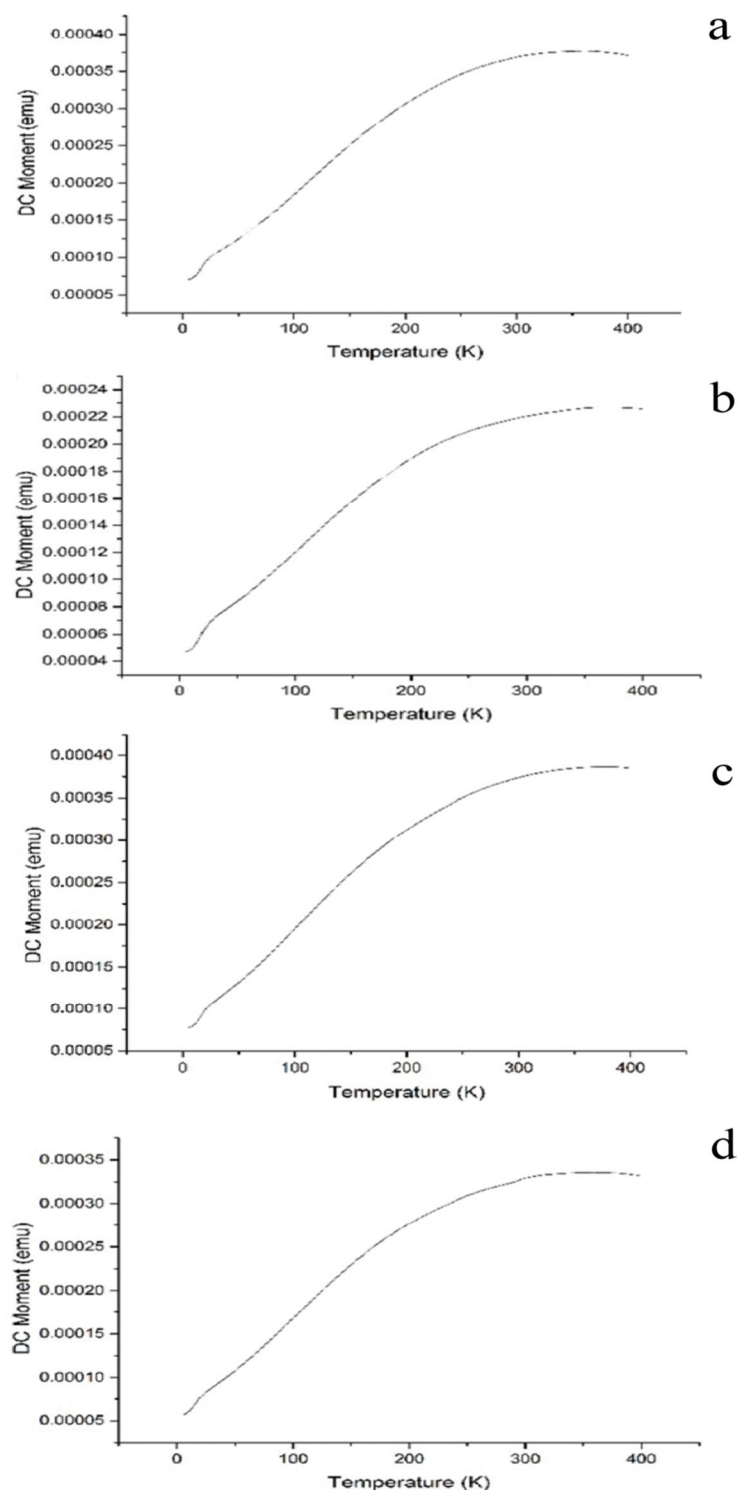


Figure 3.36 SQUID Magnetization measurement (ZFC mode) all through the four phases of Core-shell-SPIONs: (a) naked SPIONs, (b) after functionalizing with SDS, (c) after curcumin loading, (d) after encapsulating with biopolymer coating.

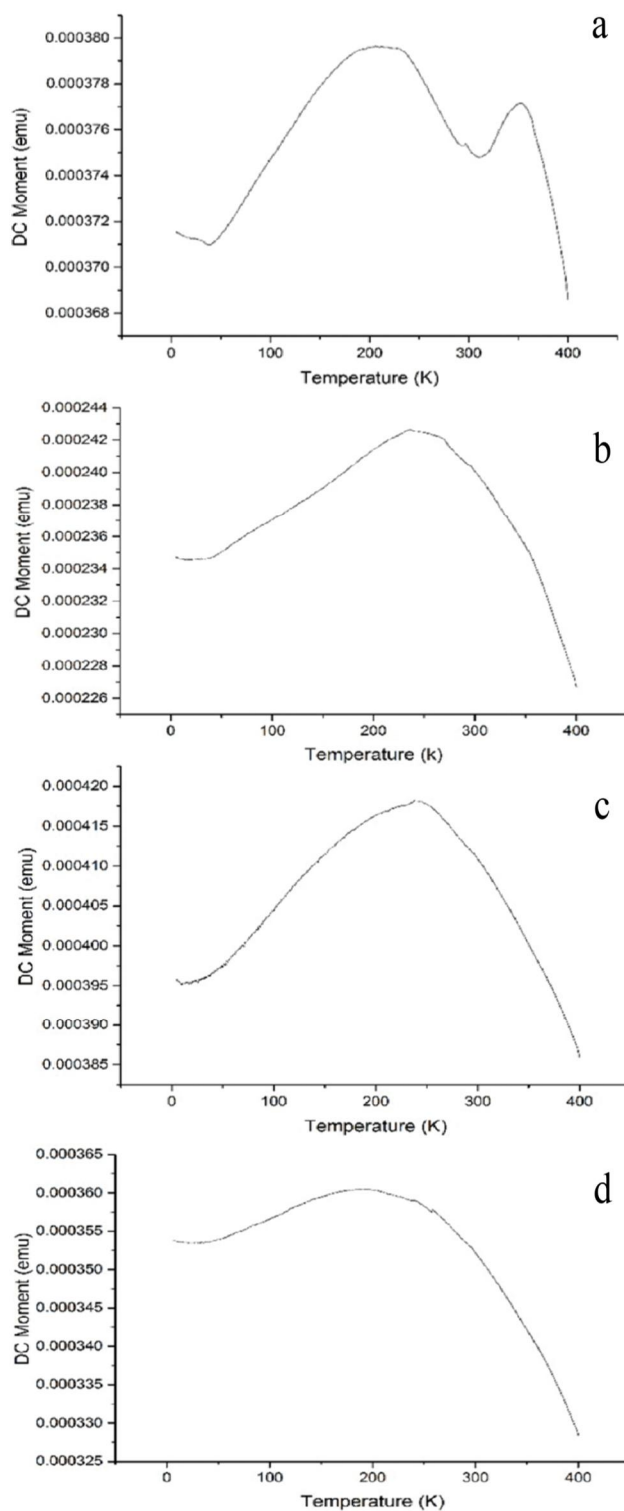


Figure 3.37 SQUID Magnetization measurement (FC mode) all through the Coreshell-SPIONs production: (a) naked SPIONs, (b) after functionalizing with SDS, (c) after curcumin loading, (d) after encapsulating with biopolymer coating

3.2.9 Vibration Sample Magnetometer (VSM) Analysis

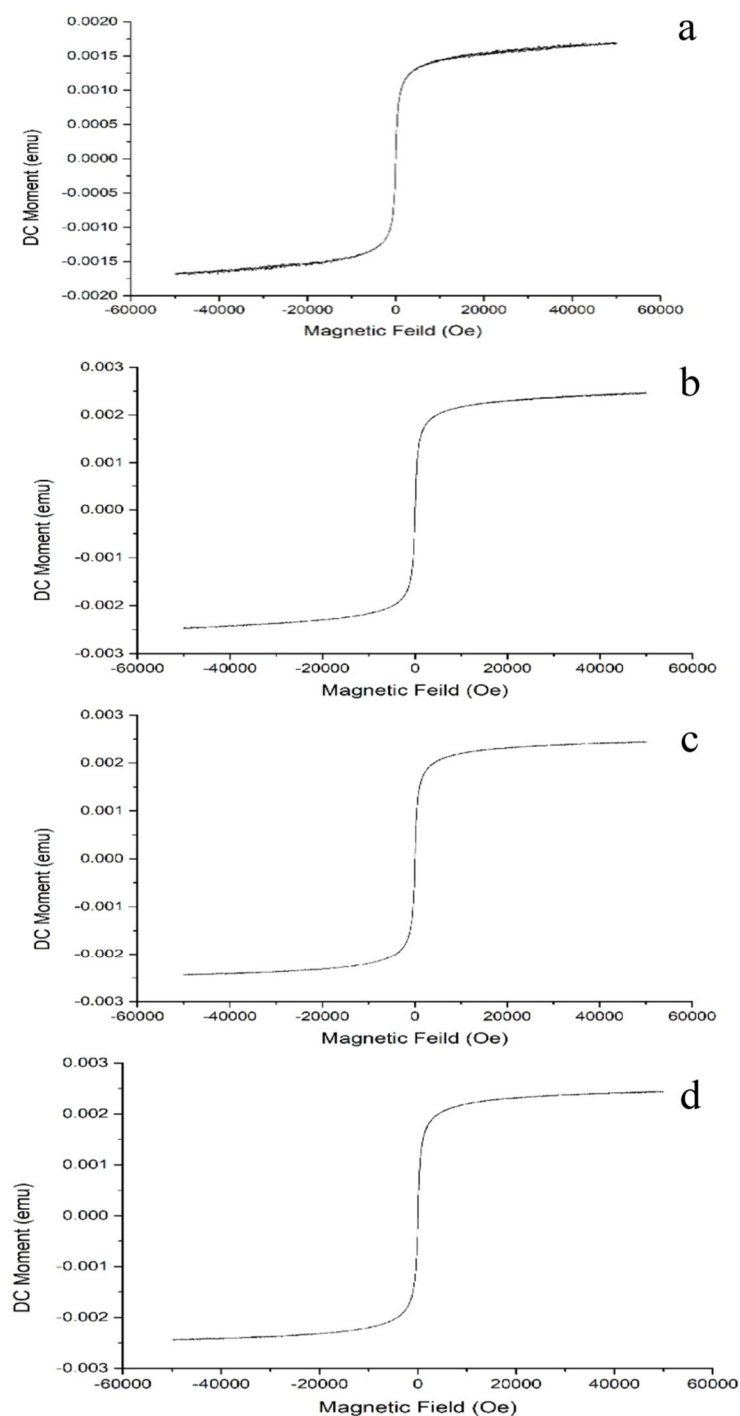


Figure 3.38 Magnetic hysteresis obtained from VSM: (a) naked SPIONs, (b) after functionalizing with SDS, (c) after curcumin loading, (d) after encapsulating with biopolymer coating

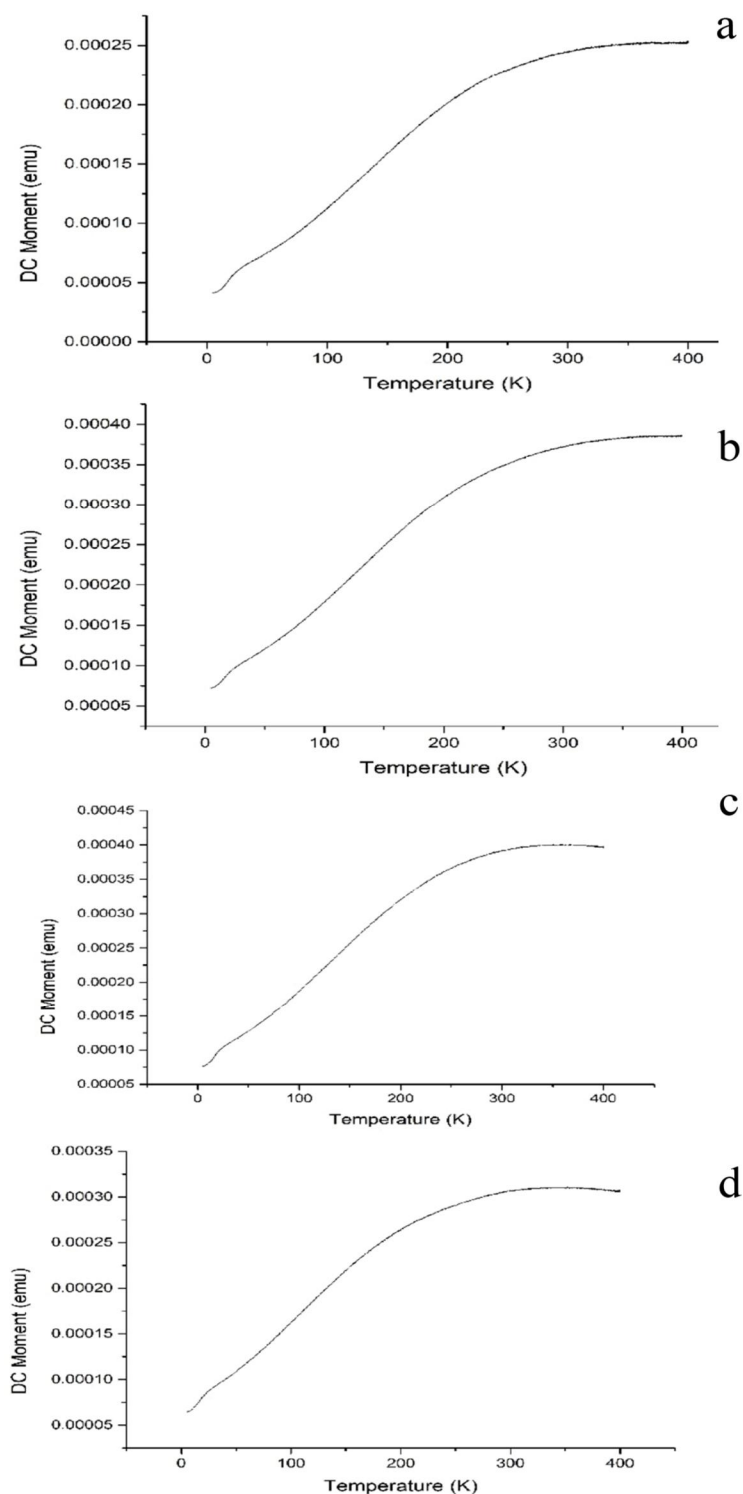


Figure 3.39 Magnetization measurement obtained from VSM (ZFC mode) all through the Coreshell-SPIONs production: (a) naked SPIONs, (b) after functionalizing with SDS, (c) after curcumin loading, (d) after encapsulating with biopolymer coating

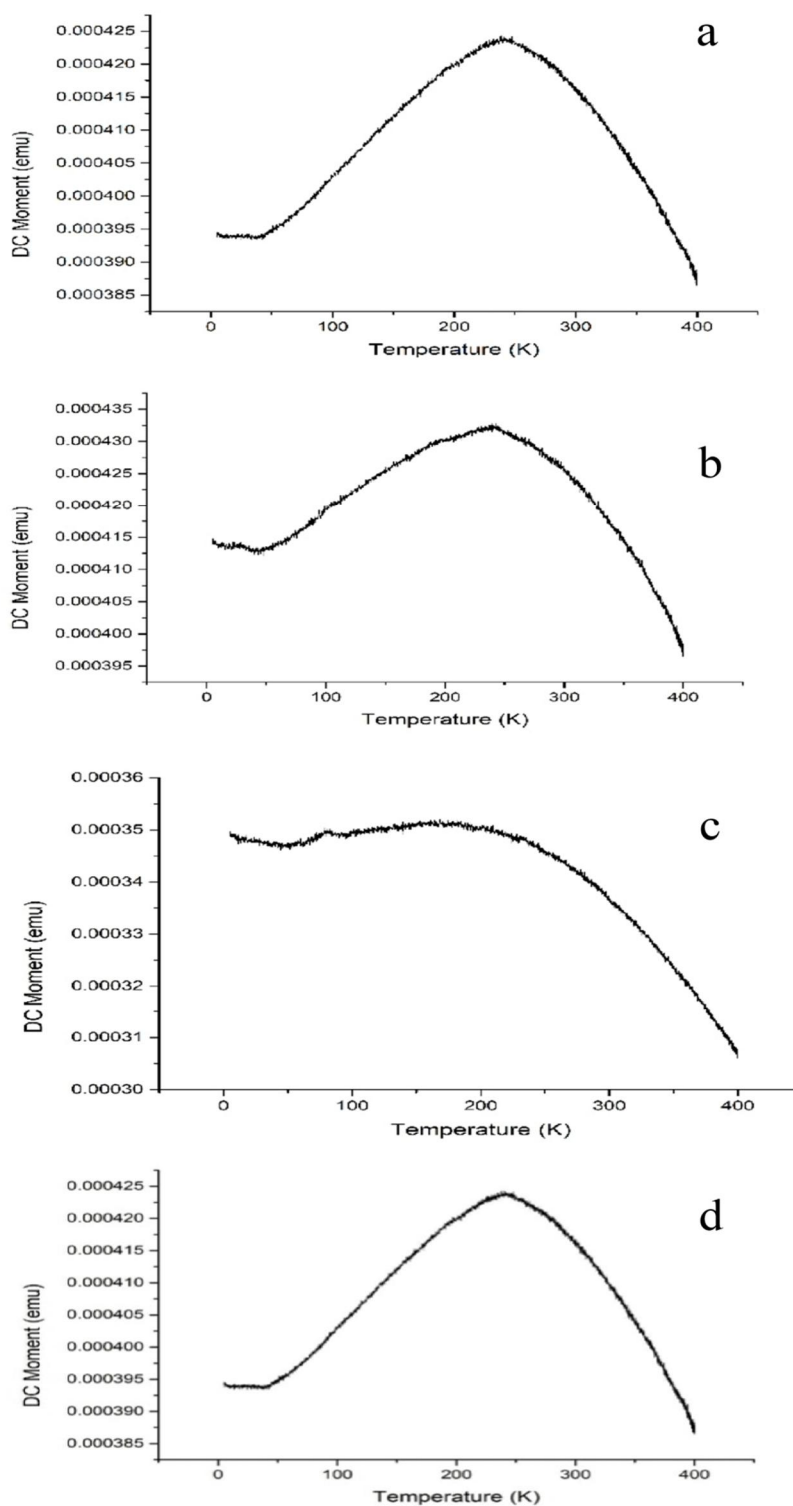


Figure 3.40 VSM magnetization measurement (FC mode) through the Coreshell-SPIONs production: (a) naked SPIONs, (b) after functionalizing with SDS, (c) after curcumin loading, (d) after encapsulating with biopolymer coating

3.3 IN VITRO DRUG DELIVERY ASSAYS

3.3.1 MTT Assay

Cell cytotoxicity was directly proportional to the concentration of core-shell (Figure 3.41). Curcumin is known to have anticancer activity against several cell lines. IC₅₀ (inhibitory concentration) was found at 30 μg for HeLa cells and 80 μg for HCT116 cells.

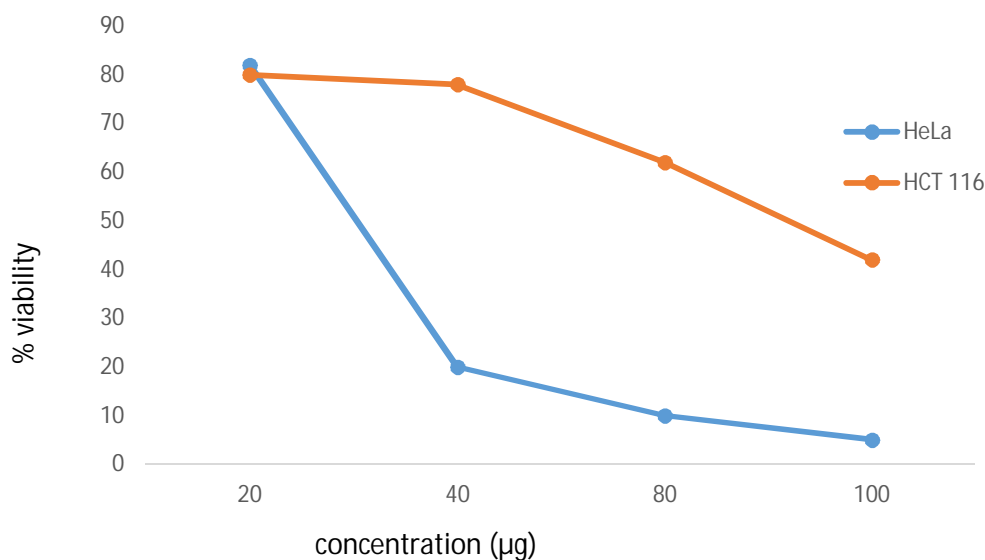


Figure 3.41 MTT assay of Coreshell-SPIONs

3.3.2 Nuclear Staining

Core-shell was found to induce apoptosis in the HeLa and the HCT 116 Cells, which was evidenced Pre-apoptotic cells observed through Hoechst staining (Figure 3.42 and 3.43).

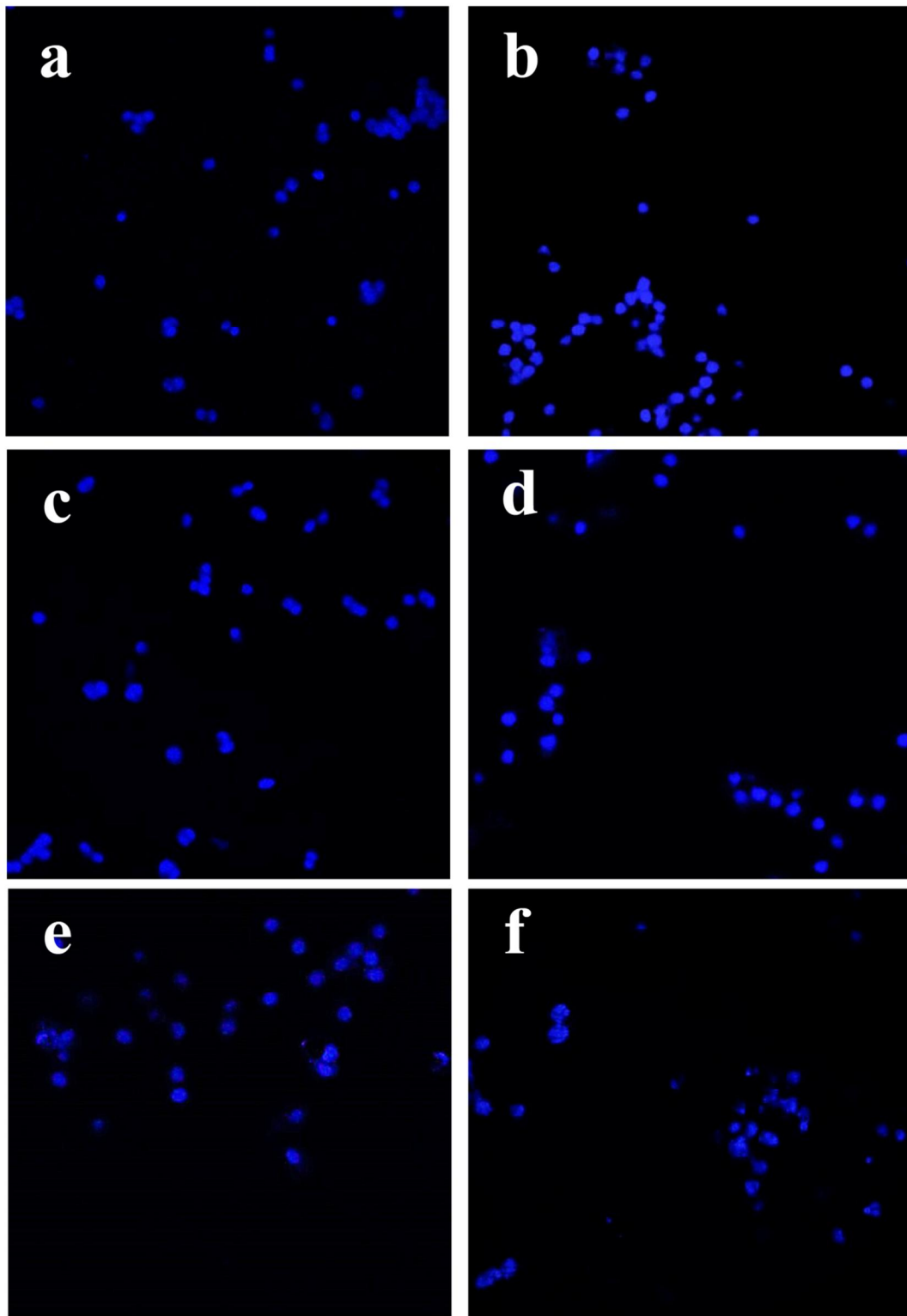


Figure 3.42 Nuclear staining of HeLa cells treated with Coreshell - SPIONs (a) CPT, (b) Untreated, (c) 2 hours treated (d) 6 hours treated, (e) 12 hours treated, (f) 24 hours treated

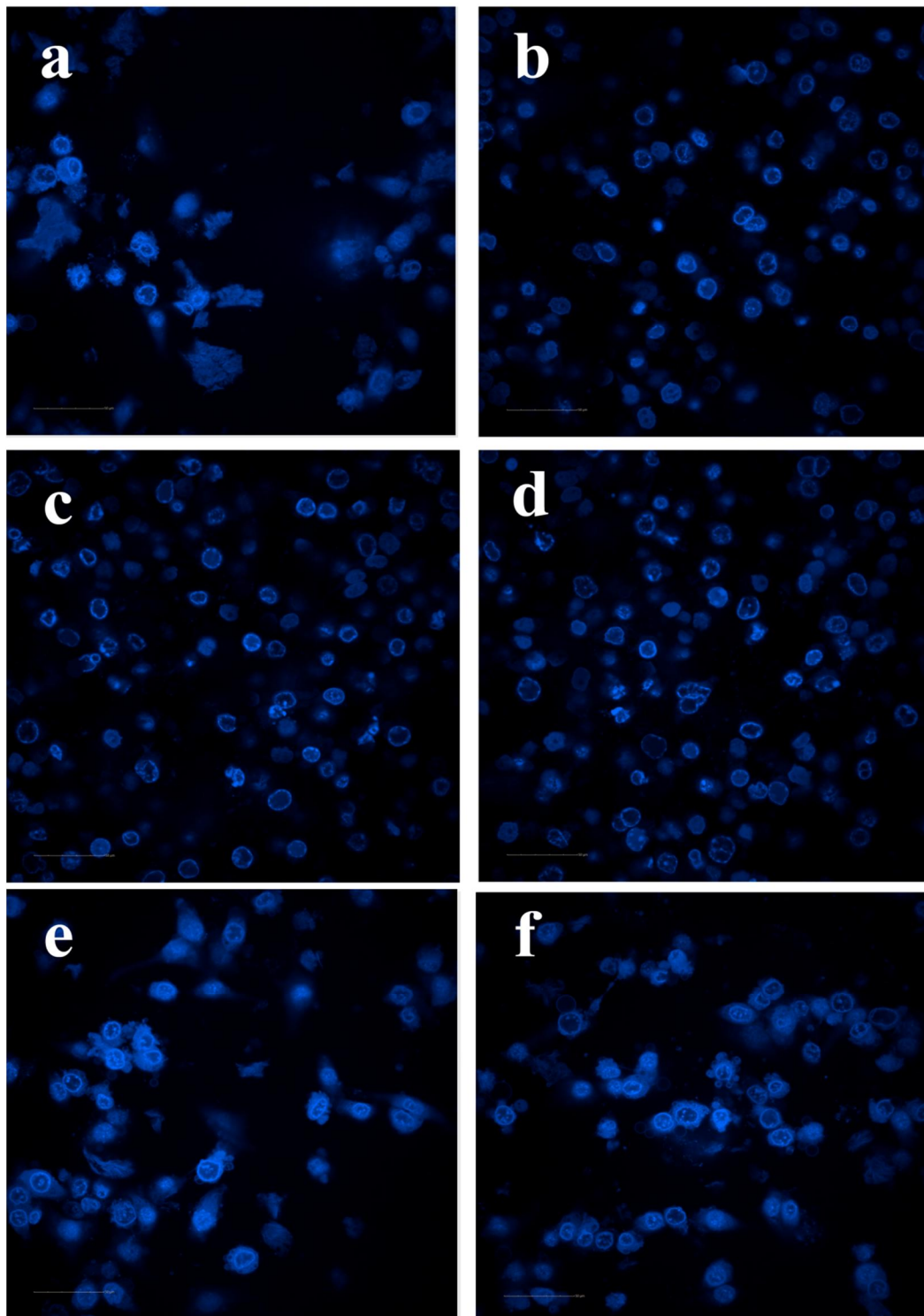


Figure 3.43 Nuclear staining of HCT 116 cells treated with Coreshell-SPIONs, (a) CPT, (b) Untreated, (c) 2 hours treated, (d) 6 hours treated, (e) 12 hours treated, (f) 24 hours treated

3.3.3 Apoptotic Assay

Apoptosis is a usual physiologic progression which befalls through embryonic growth as well as in upkeep of tissue homeostasis. The apoptotic program is characterized by certain morphologic features, including loss of plasma membrane, asymmetry and attachment, condensation of the cytoplasm and nucleus, and internucleosomal cleavage of DNA. Loss of plasma membrane is one of the earliest features. In apoptotic cells, the membrane phospholipid phosphatidylserine (PS) is translocated from the inner to the outer leaflet of the plasma membrane, thereby exposing PS to the external cellular environment. Annexin V is a 35-36 kDa Ca^{2+} dependent phospholipid-binding protein that has a high affinity for PS, and binds to cells with exposed PS. Annexin V may be conjugated to fluorochromes including FITC. Since externalization of PS occurs in the earlier stages of apoptosis, FITC Annexin V staining can identify apoptosis at an earlier stage than assays based on nuclear changes such as DNA fragmentation. FITC Annexin V staining precedes the loss of membrane integrity which accompanies the latest stages of cell death resulting from either apoptotic or necrotic processes. Therefore, staining with FITC Annexin V is typically used in conjunction with a vital dye such as propidium iodide (PI) or 7-Amino-Actinomycin (7-AAD) to allow the investigator to identify early apoptotic cells (PI negative, FITC Annexin V positive). Viable cells with intact-membranes exclude PI, whereas, the membranes of dead and damaged cells are permeable to PI. For example, cells that are considered viable are FITC Annexin V and PI negative; cells that are

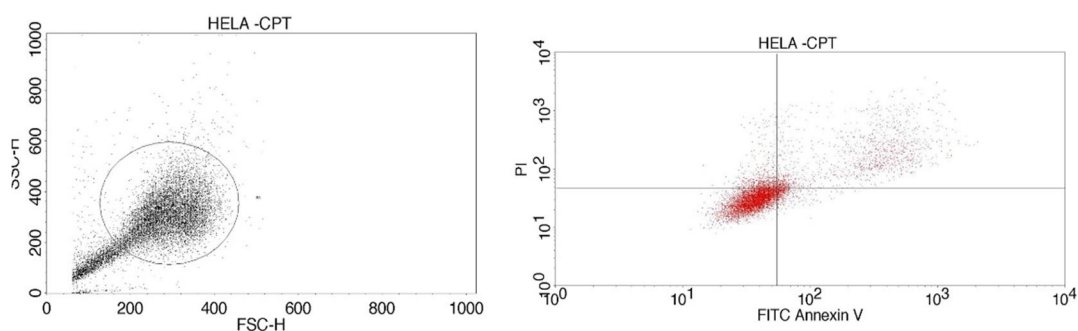
in early apoptosis are FITC Annexin V positive and PI negative; and cells that are in late apoptosis or already dead are both FITC Annexin V and PI positive. This assay does not distinguish between cells that have undergone apoptotic death versus those that have died as a result of a necrotic pathway because in either case, the dead cells will stain with both FITC Annexin V and PI. However, when apoptosis is measured over time, cells can be often tracked from FITC Annexin V and PI negative (viable, or no measurable apoptosis), to FITC Annexin V positive and PI negative (early apoptosis, membrane integrity is present) and finally to FITC Annexin V and PI positive (end stage apoptosis and death). The movement of cells through these three stages suggests apoptosis. In contrast, a single observation indicating that cells are both FITC Annexin V and PI positive, in itself, reveals less information about the process by which the cells underwent their demise.

Apoptotic assay was performed at IC₅₀ concentration against both the cell lines, 30 μ g and 80 μ g respectively, which are illustrated in Figure 3.41. Two to six hours of treatment of HeLa cells showed a minor difference where 12th hour of incubation increases apoptotic cells (15%) and it reached 57.75% (UR-29.94 + LR-00.18 + UL-27.63 = 57.75%) in 24th hour including early/late apoptosis. Time to time apoptotic variations occurred are given in the figures 3.44 – 3.49 and the comparison is given in Figure 3.50 with quadrant statistics and described in nutshell in Table 3.16. Similarly, in HCT 116 cells also apoptosis is induced time to time proving the slow and steady drug delivery. At 24th hour of incubation of HCT 116 cells with core-shell

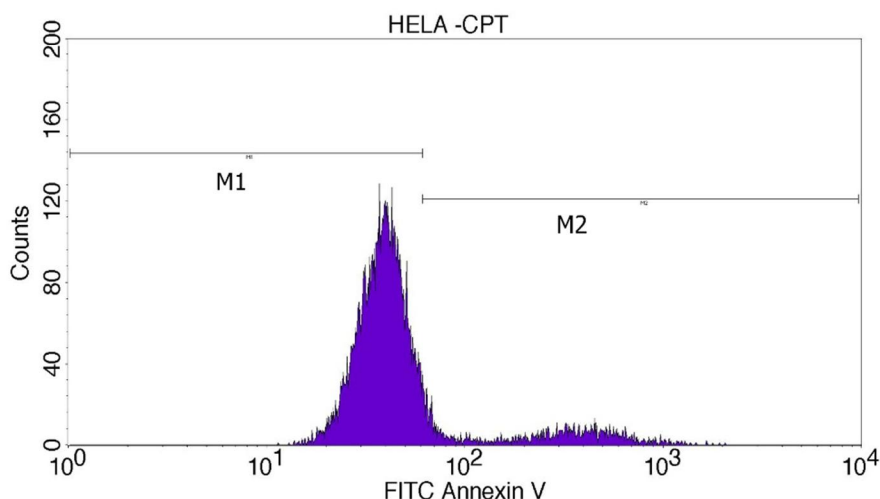
SPIONs induced apoptosis (UR-12.49 + LR-20.63 + UL-00.83 = 33.95%) considerably lesser than that worked in HeLa cells. Time to time apoptotic variations occurred are given in figures 3.52 – 3.57 and the comparison is given in Figure 3.58, quadrant statistics and in Figure 3.59 histogram statistics. Similar results were recorded by Rajan *et al.*, (2017) against HeLa cells while using camptothecin loaded magnetite nanoparticle.

3.3.3.1 Flow Cytometry Analysis HeLa Cells

The figures from 3.44 to 3.59 represent flow cytometry analysis data in quadrant and histogram statistics from Annexin V-FITC staining for HeLa and HCT 116 cells. In the quadrants there are four cases: Upper Right (UR), Upper Left (UL), Lower Right (LR) and Lower Left. The data found in UR represents apoptotic cells and necrotic cells (late apoptosis). The data found in UL represents necrotic cells / cell debris. The data found in LR represents early apoptotic cells and the data found in LL represents viable cells / live cells. The histogram data show the comparison of the distribution of Annexin V negative cells (M1) and Annexin V positive cells (M2).



Quad	Events	% Gated	% Total	X Mean	X Geo Mean	Y Mean	Y Geo Mean
UL	853	8.94	6.94	42.79	42.07	99.11	71.48
UR	1478	15.49	12.03	321.05	220.56	266.91	164.57
LL	6698	70.20	54.52	36.45	35.43	29.86	28.62
LR	512	5.37	4.17	65.53	63.67	38.79	38.11



Marker	Left, Right	Events	% Gated	% Total	Mean	Geo Mean	CV	Median	Peak Ch
All	1, 9910	9541	100.00	77.66	82.66	49.28	178.54	40.32	36
M1	1, 60	8032	84.18	65.38	38.38	37.14	24.88	38.20	36
M2	60, 9560	1546	16.20	12.58	312.23	215.46	85.41	259.46	60

Figure 3.44 Apoptosis assay in HeLa is found positive to Camptothecin when it is used as the positive control. According to quadrant statistics the cells are positive leading to apoptosis in 24 hours' treatment. The same phenomenon is confirmed with histogram statistics (M2 12.58%) positive and (M1 65.38%) negative. The statistics evidentially vindicate the cells are prone to CPT positive.

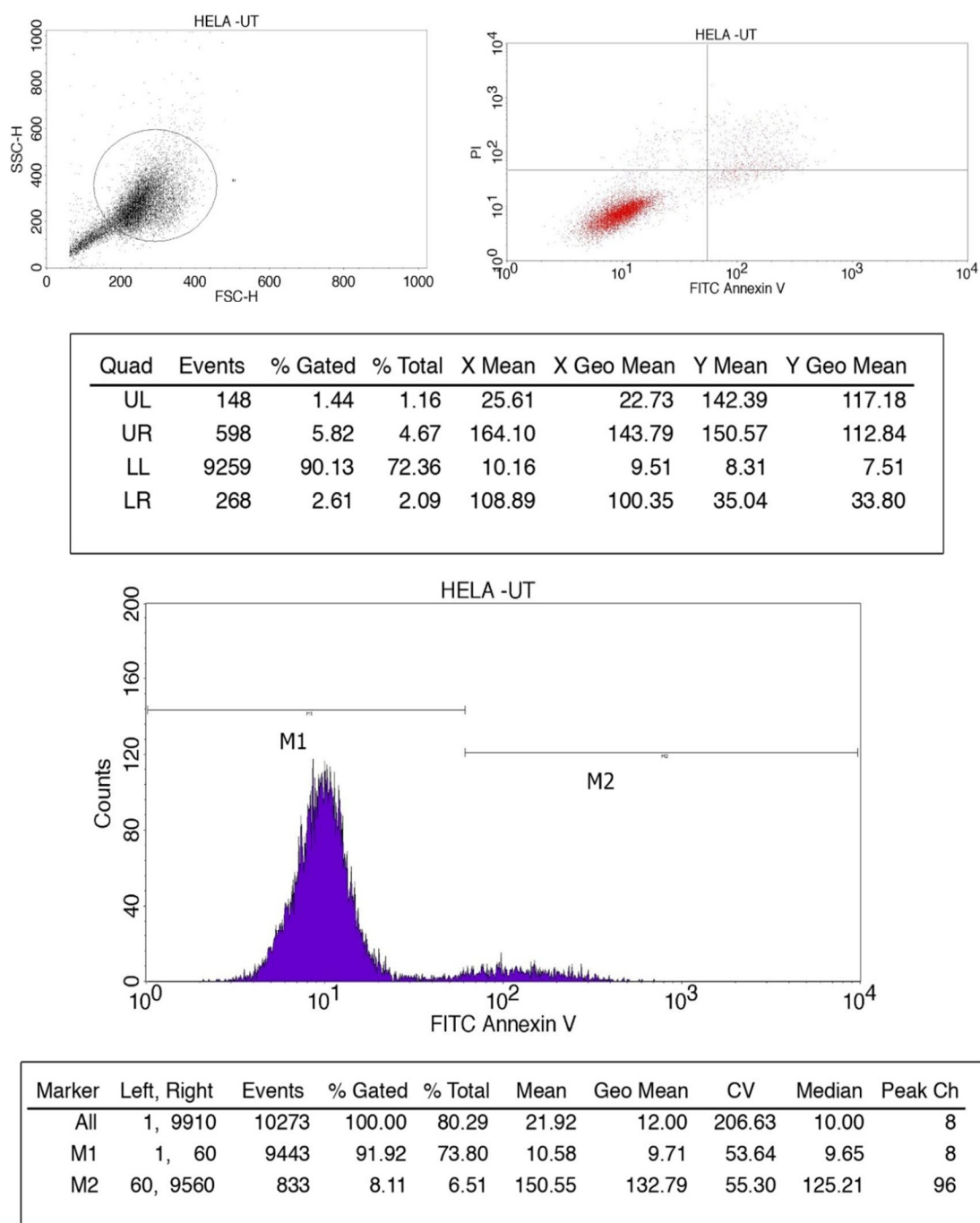


Figure 3.45 HeLa - Untreated: In quadrant the cells in LL (72.36%) are viable; UL (1.16%) necrotic/cell debris; UR (4.67%) necrotic; LR (2.09%) early apoptotic cells. In histogram M1 (73.80%) are Annexin V negative and M2 (6.51%) are Annexin V positive. In untreated more viability is found even after 24 hours of culture.

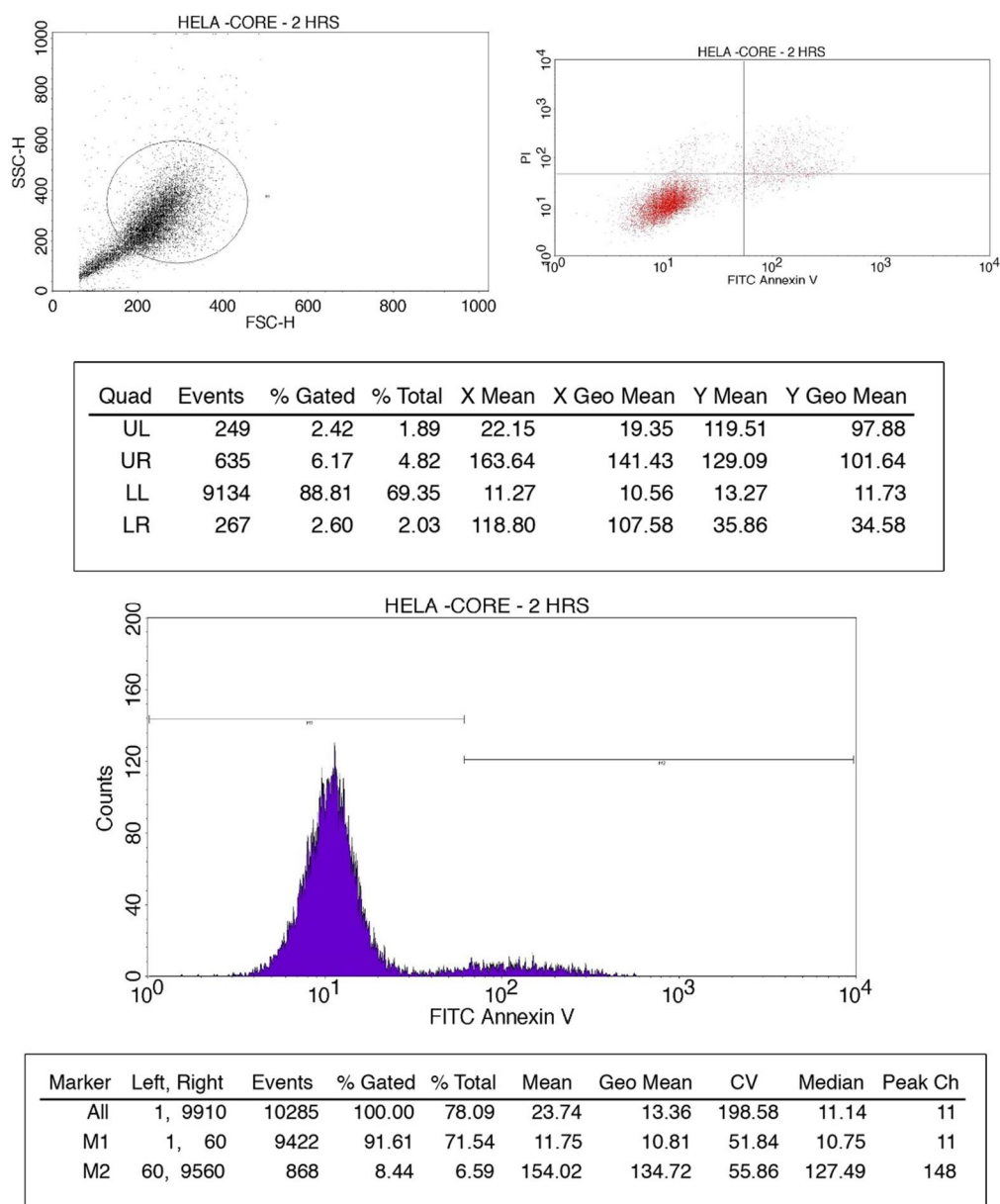


Figure 3.46 HeLa - Core-shell treated for 2 hours: In quadrant the cells in LL (69.35%) are viable; UL (1.89%) necrotic/cell debris; UR (4.82%) necrotic; LR (2.03%) early apoptotic cells. In histogram M1 (71.54%) are Annexin V negative and M2 (6.59%) are Annexin V positive. Initiation of apoptosis is found after 2 hours of culture with core-shell. Curcumin begins to get released from the core-shell.

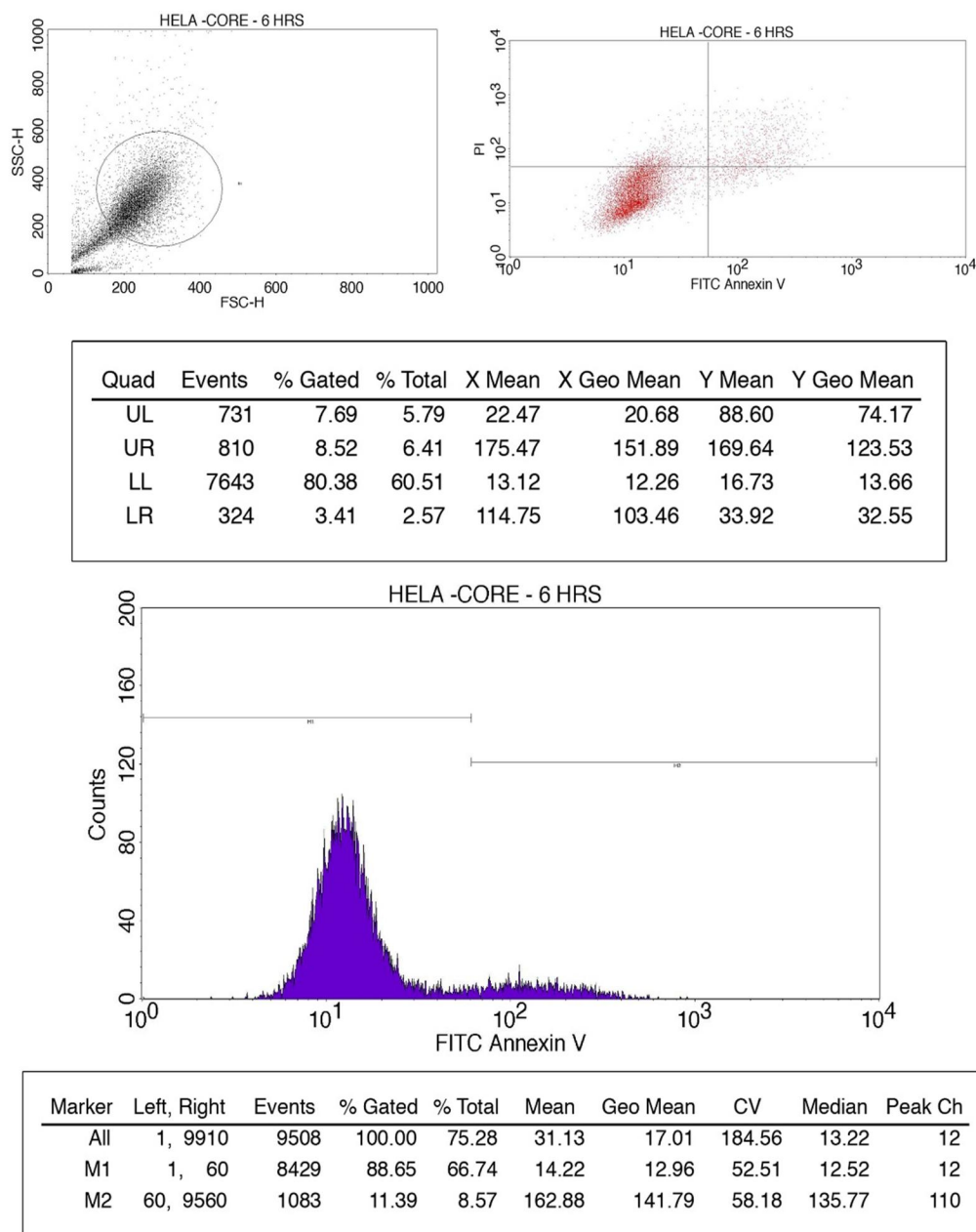


Figure 3.47 HeLa - Core-shell treated for 6 hours: In quadrant the cells in LL (60.51%) are viable; UL (5.79%) necrotic/cell debris; UR (6.41%) apoptotic/necrotic; LR (2.57%) early apoptotic cells. In histogram M1 (66.74%) are Annexin V negative and M2 (8.57%) are Annexin V positive. Initiation further moves at 6 hours of culture with core-shell. Curcumin begins to get released from the core-shell but still slower.

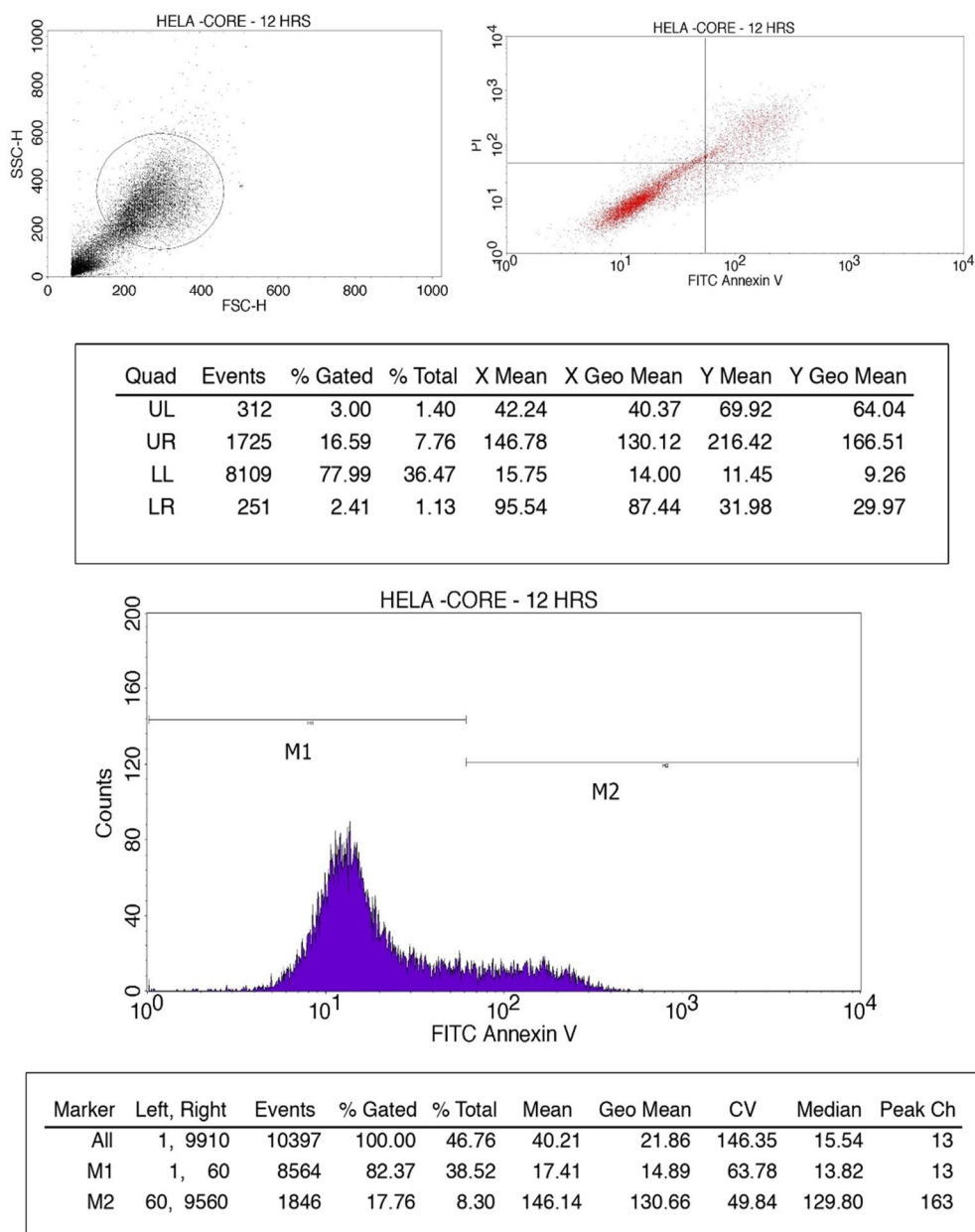


Figure 3.48 HeLa - Core-shell treated for 12 hours: In quadrant the cells in LL (36.47%) are viable; UL (1.40%) necrotic/cell debris; UR (7.76%) apoptotic/necrotic; LR (1.3%) early apoptotic cells. In histogram M1 (38.52%) are Annexin V negative and M2 (17.76%) are Annexin V positive. Initiation is further intensified at 12 hours of culture with core-shell. Curcumin begins to get released from the core-shell leading towards a considerable effect in the cell line.

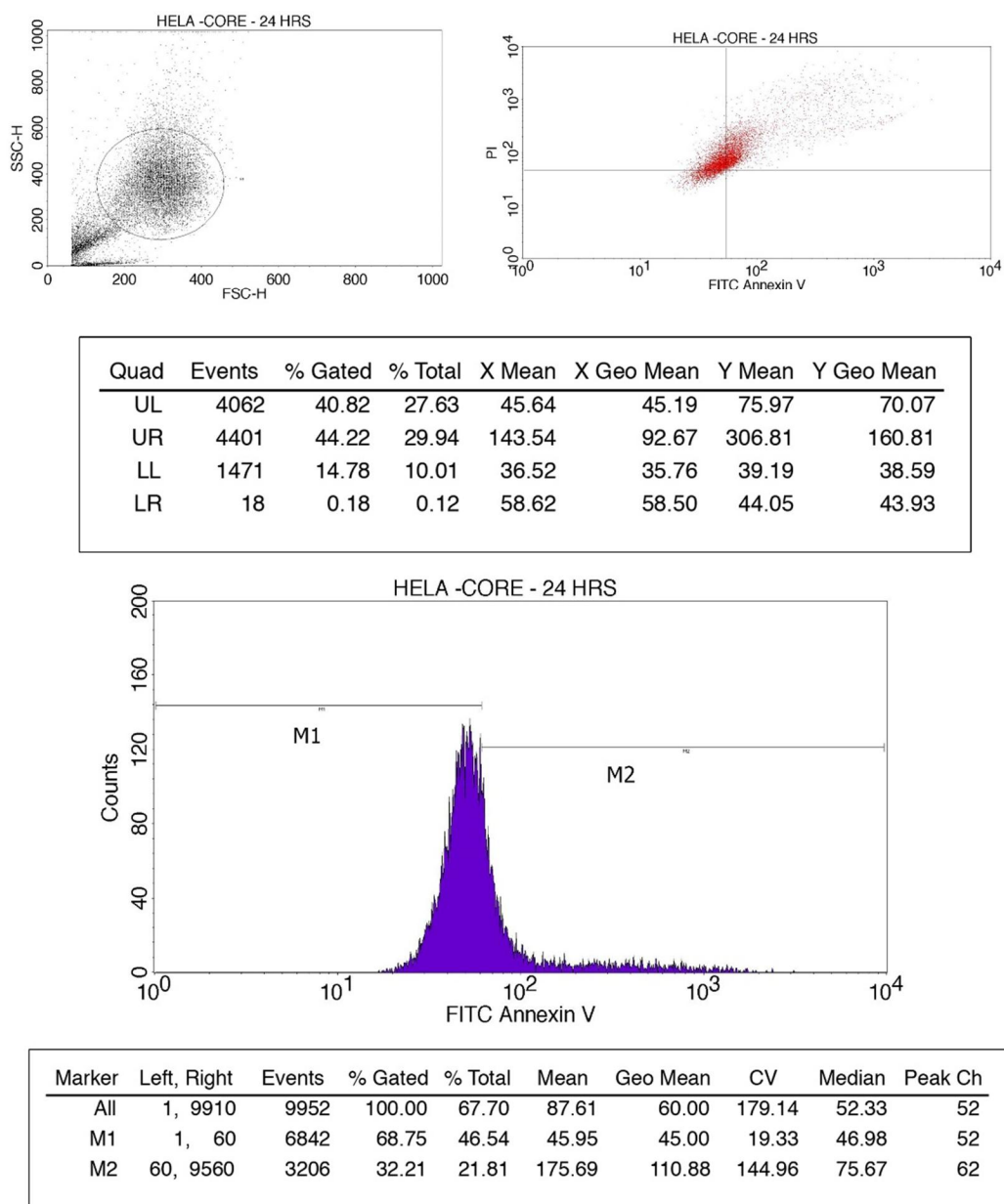


Figure 3.49 HeLa - Core-shell treated for 24 hours: In quadrant the cells in LL (10.01%) are viable; UL (27.63%) necrotic/cell debris; UR (29.94%) apoptotic/necrotic; LR (0.12%) early apoptotic cells. In histogram M1 (46.54%) are Annexin V negative and M2 (21.81%) are Annexin V positive. The drug release is further intensified at 24 hours of culture with core-shell. Curcumin begins to get released from the core-shell leading towards a greater effect in the cell line.

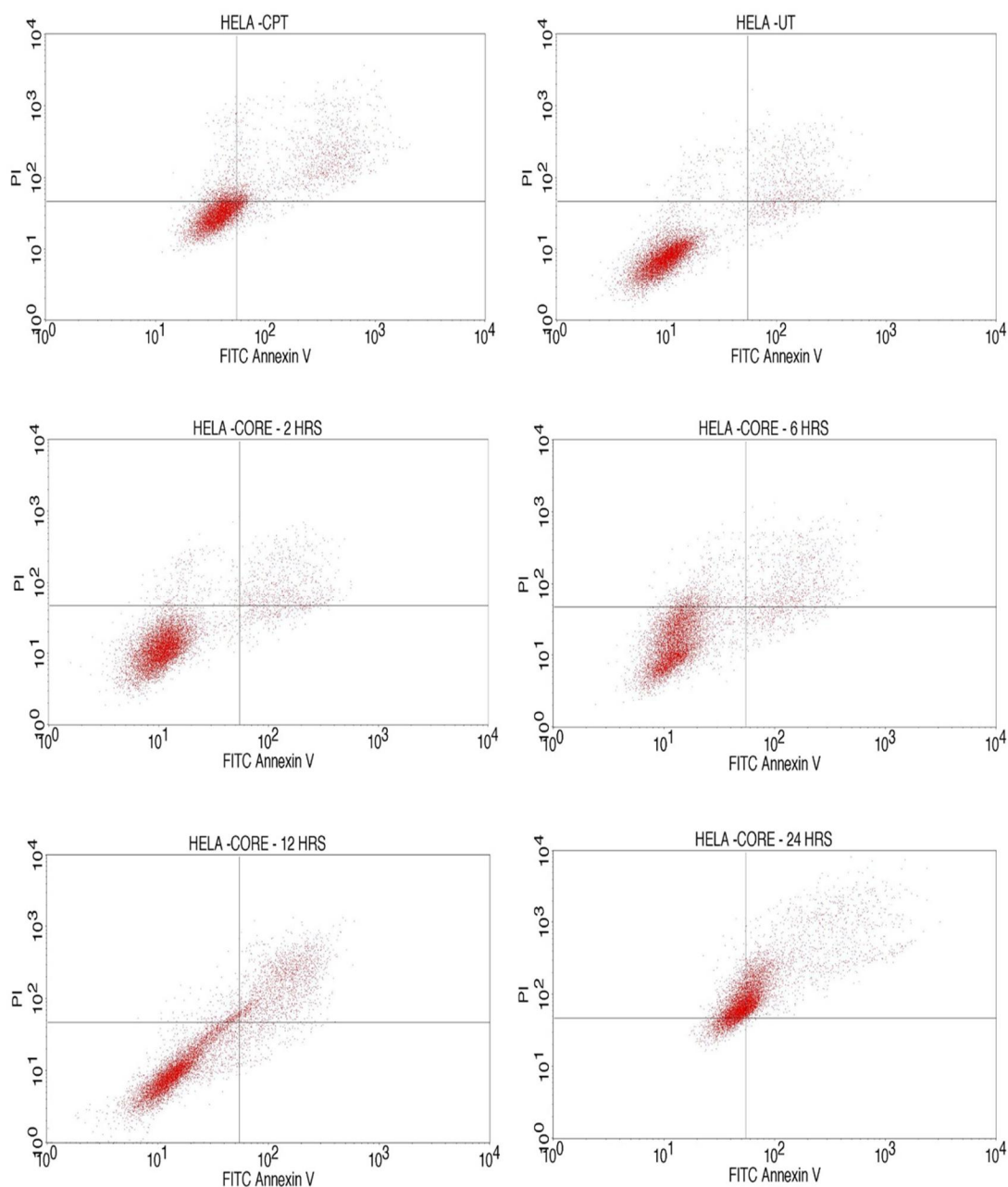


Figure 3.50 Comparing the effect of curcumin delivery in HeLa all through the four time durations in quadrant statistics (a) CPT, (b) Untreated, (c) 2 hours, (d) 6 hours, (e) 12 hours, (f) 24 hours. From the above quadrant statistics, it is understood that HeLa cells are highly prone to curcumin. Cell viability is declined at time to time release of the drug leading to greater effect at 24 hours' treatment.

Table 3.16 Tabulation of HeLa quadrant results

Events	CPT	UT	2 hours	6 hours	12 hours	24 hours
Total events	12285	12795	13170	12630	22235	10700
Gated events	9541	10273	10285	9508	10397	9952
UL %	06.94	01.16	01.89	05.69	01.40	27.63
UR %	12.03	04.67	04.82	06.41	07.76	29.94
LL %	54.52	72.36	69.35	60.51	36.47	10.01
LR %	04.17	02.09	02.03	02.57	01.13	00.18

As per the data UT remains with 72.36% of viable even after 24 hours. In comparison with the UT there is a slow and steady increase in the apoptotic / necrotic cells. It reaches up to 29.94% at 24 hours' time. It proves the slow and steady release of drug during the course of 24 hours. Further, in comparison with LL this phenomenon is more evident. In 24 hours the population in LL decreased to 10.01% i.e., the viability is higher at 2 hours with 69.35%. Moreover, it is observable that all through the drug releasing period of time a small portion of cells found in LR representing early apoptosis. In UL at 24 hours there found 27.63% of cells exhibit necrosis (late apoptosis) or would have reached to the state of cell debris.

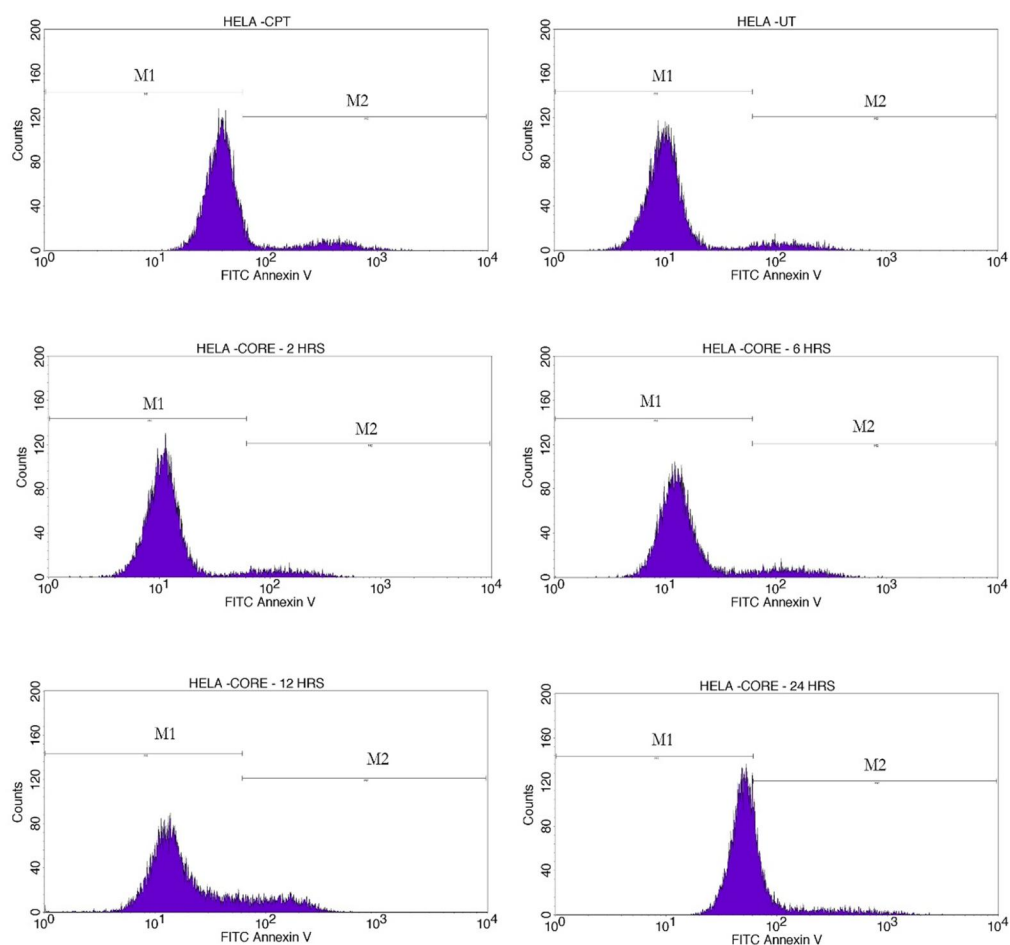


Figure 3.51 Comparing the effect of curcumin delivery in HeLa all through the four time durations in histogram statistics (a) CPT, (b) Untreated, (c) 2 hours, (d) 6 hours, (e) 12 hours, (f) 24 hours

Table 3.17 Comparing HeLa apoptosis obtained in histogram statistics where Annexin V positive (M2) increases while Annexin V negative (M1) decreases as curcumin is released from the core-shell as a proof for sustained curcumin delivery.

	CPT	UT	2 hours	6 hours	12 hours	24 hours
Events	9545	10273	10285	9508	10397	9952
M1 %	65.38	73.80	71.54	66.74	38.52	46.54
M2 %	18.52	6.51	6.59	8.57	8.30	21.81

3.3.3.2 Flow Cytometry Analysis of HCT116 Cells

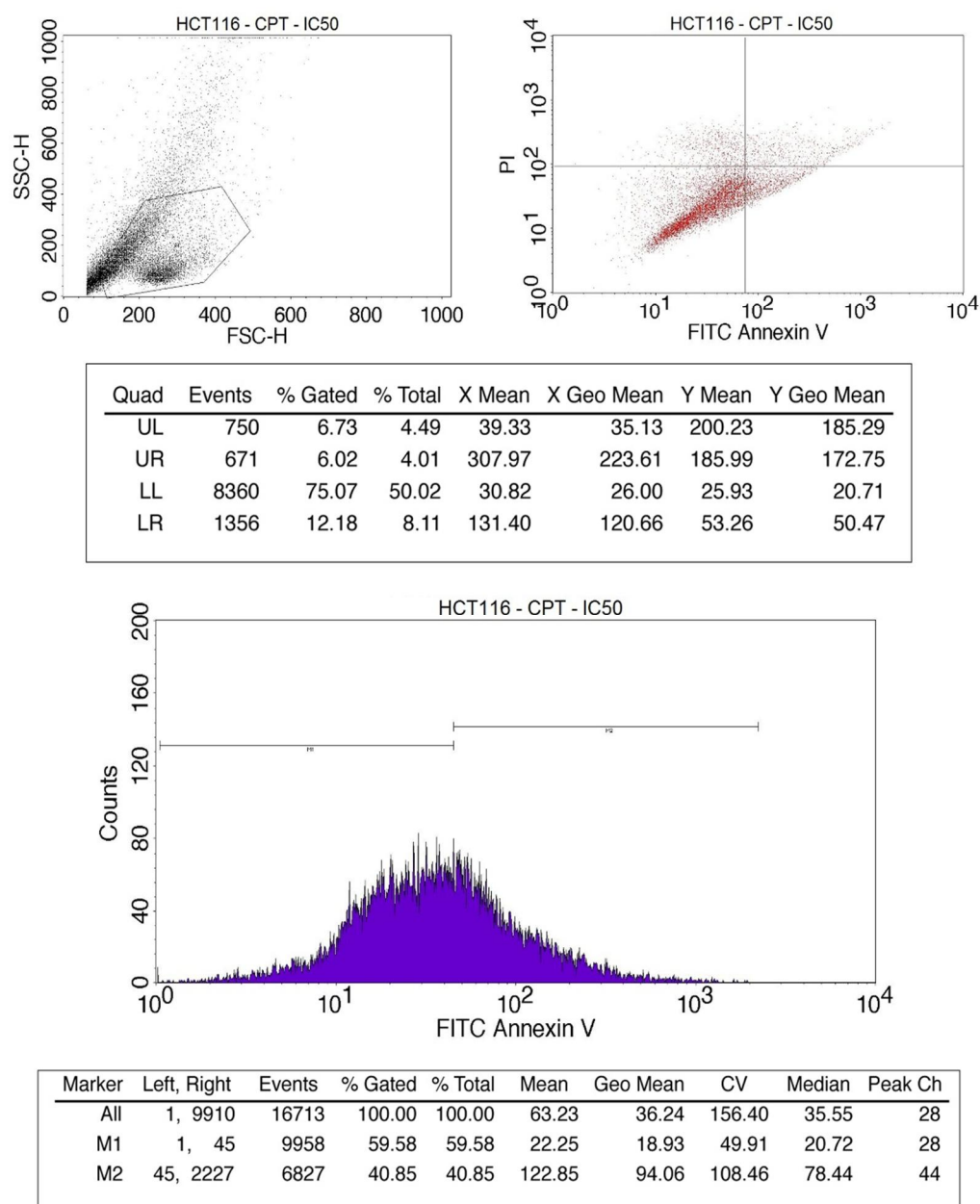


Figure 3.52 Apoptosis assay in HCT 116 is found positive to Camptothecin when it is used as the positive control. According to quadrant statistics the cells are positive leading to apoptosis in 24 hours' treatment. The same phenomenon is confirmed with histogram statistics (M2 40.85%) positive and (M1 59.58%) negative. The statistics evidentially vindicate the cells are prone to CPT positive.

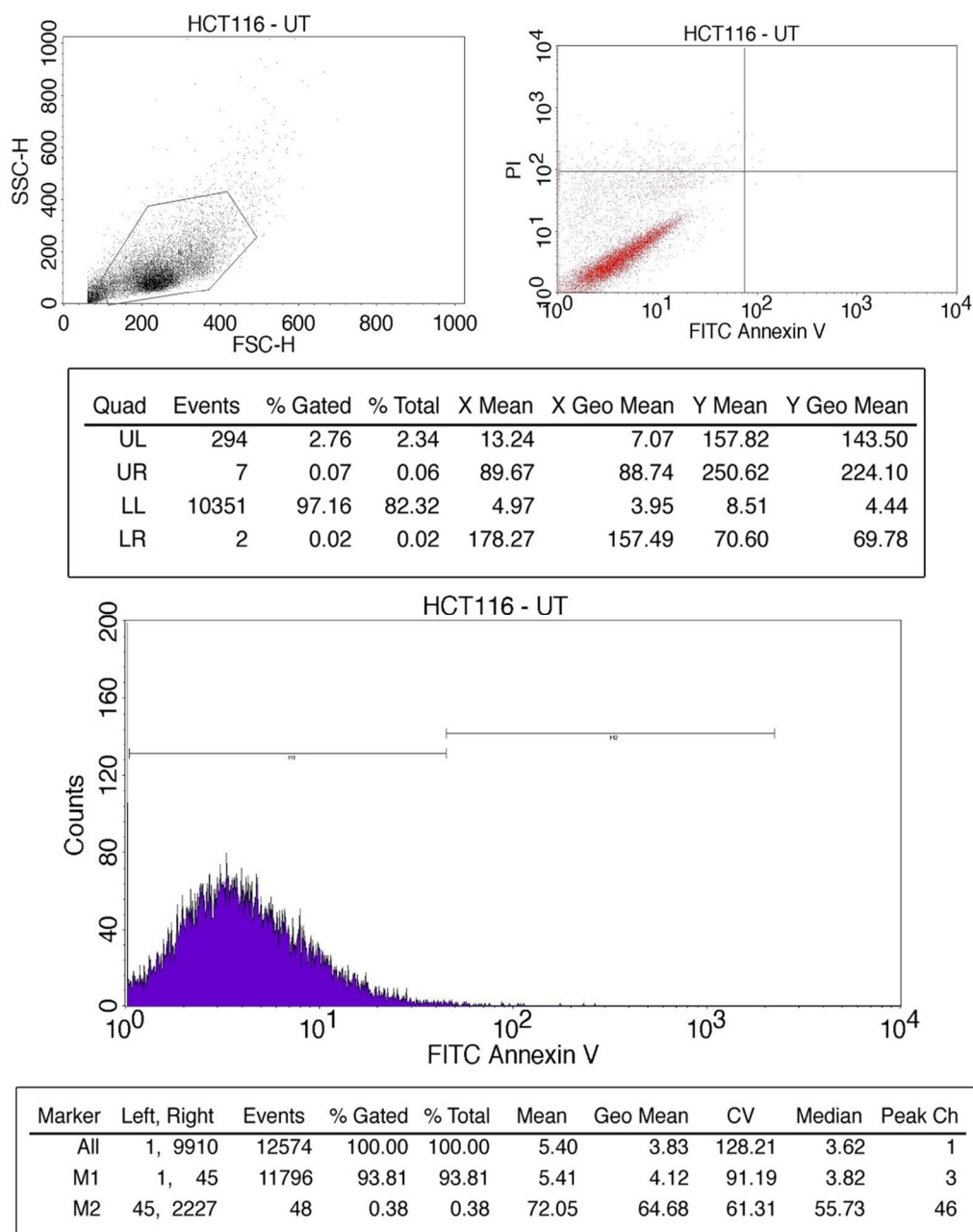


Figure 3.53 HCT 116 - Untreated: In quadrant the cells in LL (82.32%) are viable; UL (2.34%) necrotic/cell debris; UR (0.06%) necrotic; LR (0.02%) early apoptotic cells. In histogram M1 (93.81%) are Annexin V negative and M2 (0.38%) are Annexin V positive. More viability is found in untreated even after 24 hours of culture.

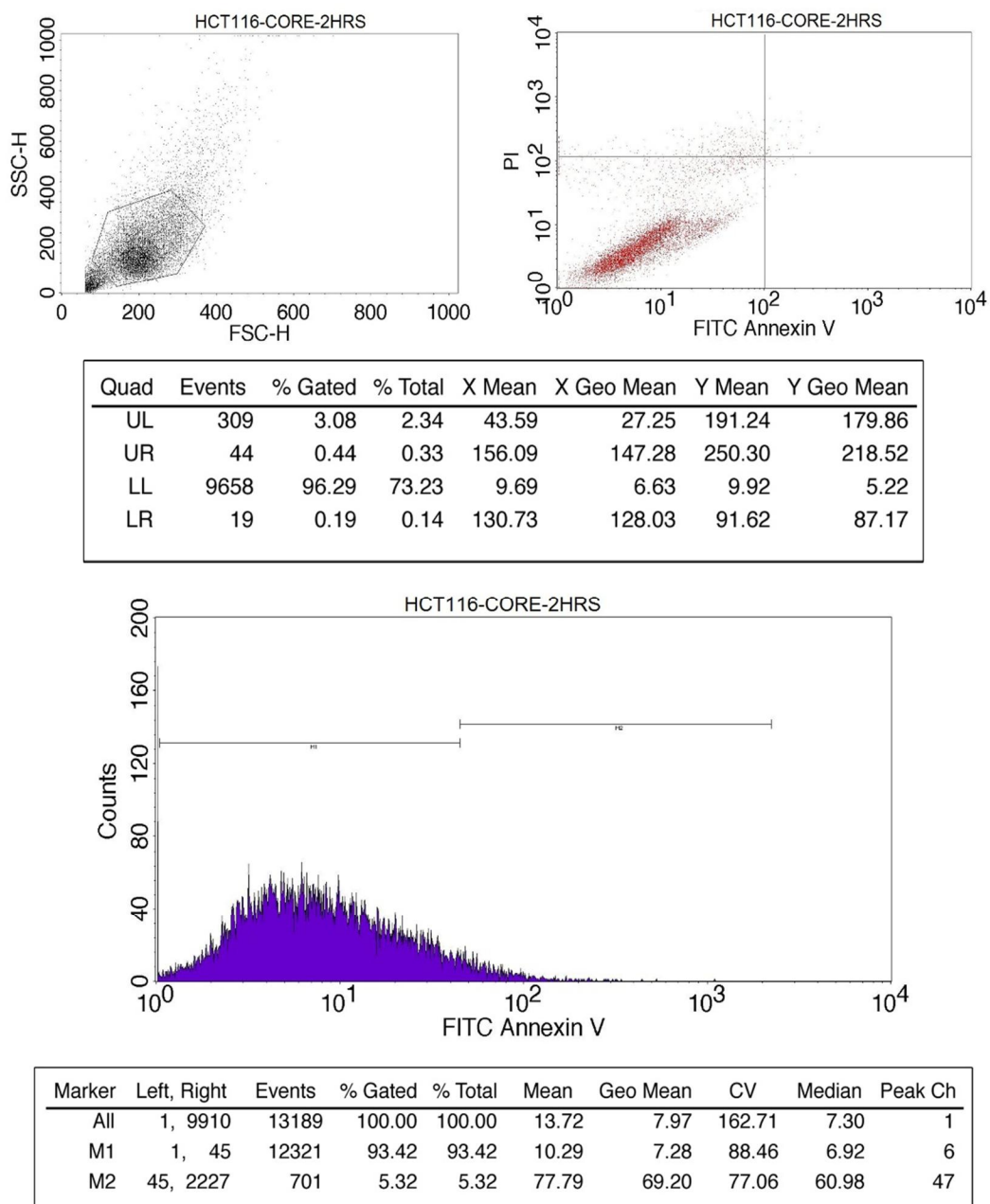


Figure 3.54 HCT 116 - Core-shell treated for 2 hours: In quadrant the cells in LL (73.23%) are viable; UL (2.34%) necrotic/cell debris; UR (0.33%) necrotic; LR (0.14%) early apoptotic cells. In histogram M1 (93.42%) are Annexin V negative and M2 (5.32%) are Annexin V positive. Initiation of apoptosis is found after 2 hours of culture treated with core-shell. Curcumin begins to get released from the core-shell.

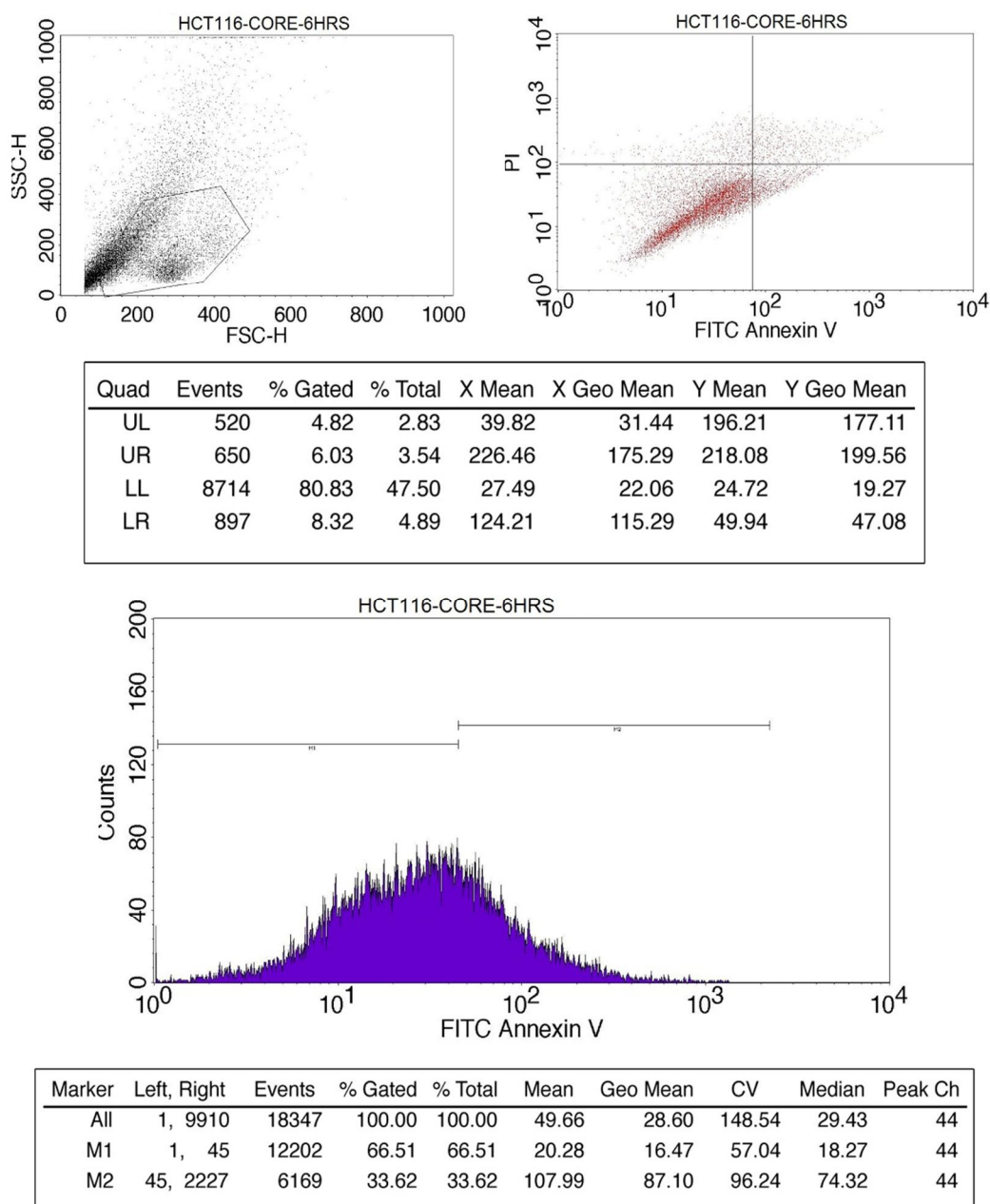


Figure 3.55 HCT 116 - Core-shell treated for 6 hours: In quadrant the cells in LL (47.50%) are viable; UL (2.83%) necrotic/cell debris; UR (3.54%) apoptotic/necrotic; LR (4.89%) early apoptotic cells. In histogram M1 (66.51%) are Annexin V negative and M2 (33.62%) are Annexin V positive. Initiation of curcumin release further moves at 6 hours. Unlike HeLa cells HCT 116 are found to be more uniform in responding to the drug.

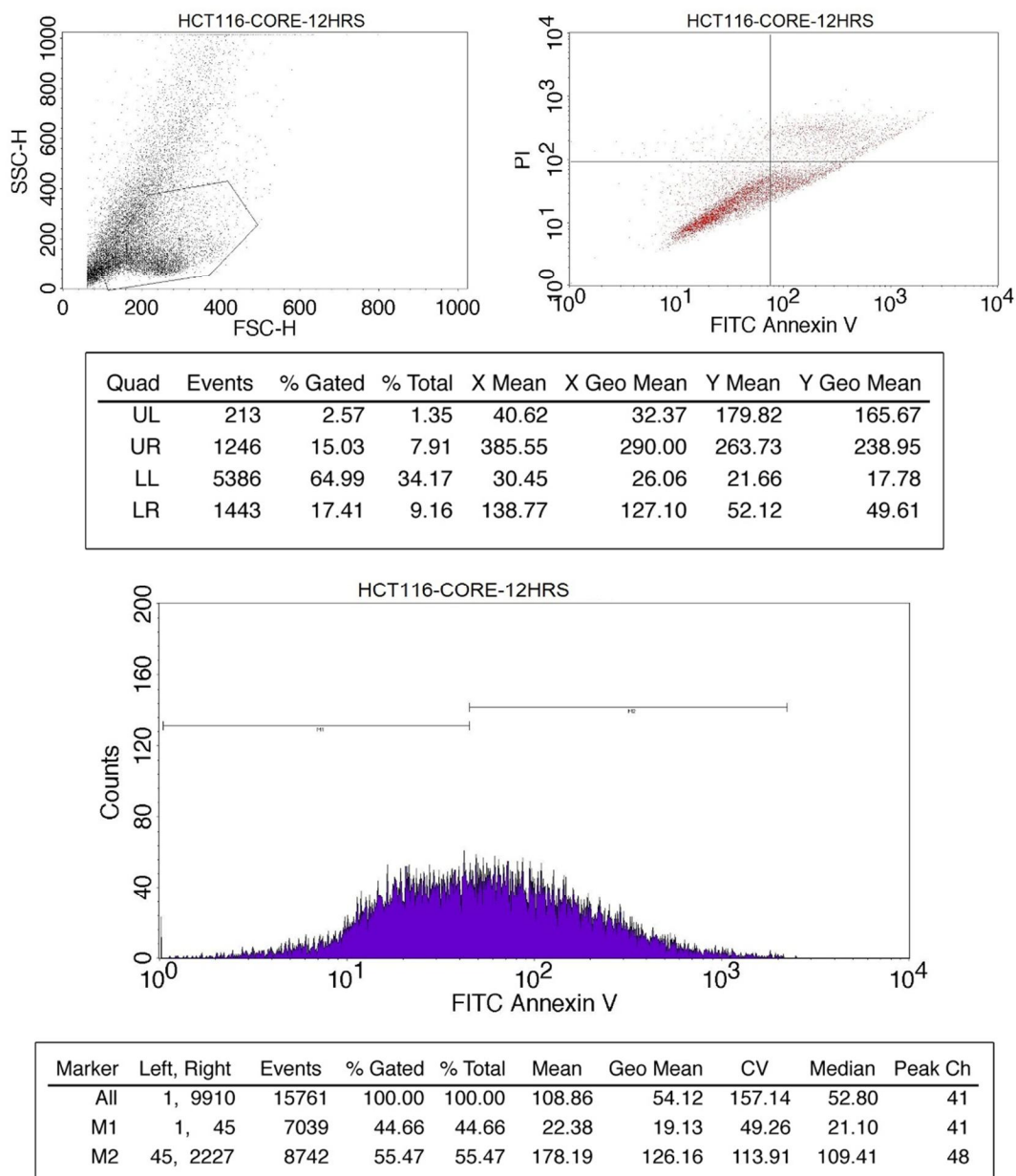


Figure 3.56 HCT 116 Cells - Core-shell treated for 12 hours: In quadrant the cells in LL (34.17%) are viable; UL (1.35%) necrotic/cell debris; UR (7.91%) apoptotic/necrotic; LR (9.16%) early apoptotic cells. In histogram M1 (44.66%) are Annexin V negative and M2 (55.47%) are Annexin V positive. Initiation is further intensified at 12 hours of culture treated with core-shell. Curcumin released from the core-shell leading to a considerable effect in the cell line.

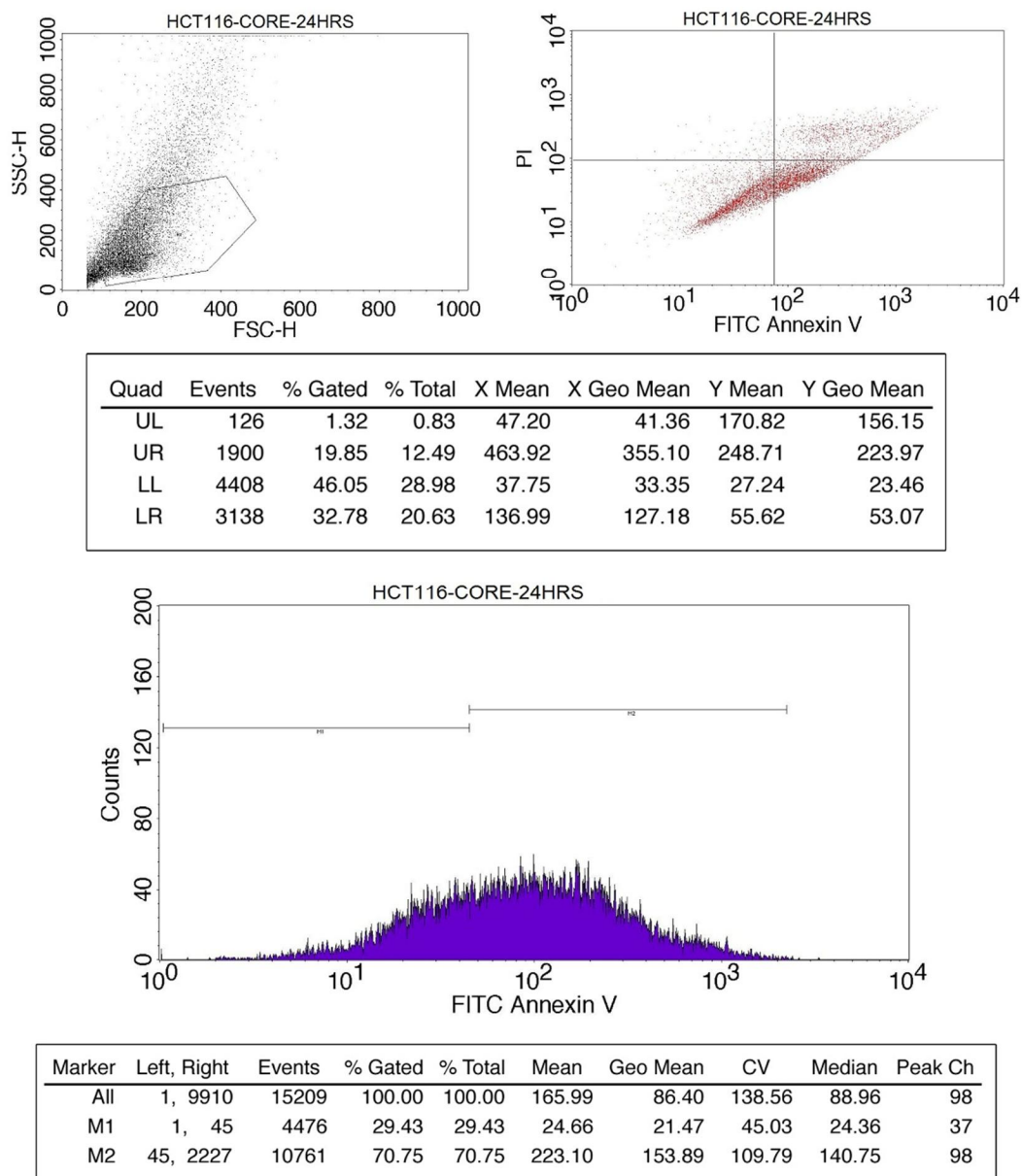


Figure 3.57 HCT 116 - Core-shell treated for 24 hours: In quadrant the cells in LL (28.96%) are viable; UL (0.83%) necrotic/cell debris; UR (12.49%) apoptotic/necrotic; LR (20.63%) early apoptotic cells. In histogram M1 (29.43%) are Annexin V negative and M2 (70.75%) are Annexin V positive. The drug release is further intensified at 24 hours of culture. Curcumin begins to get released from the core-shell leading towards a greater effect in the cell line which is evidenced by Annexin V positive cells.

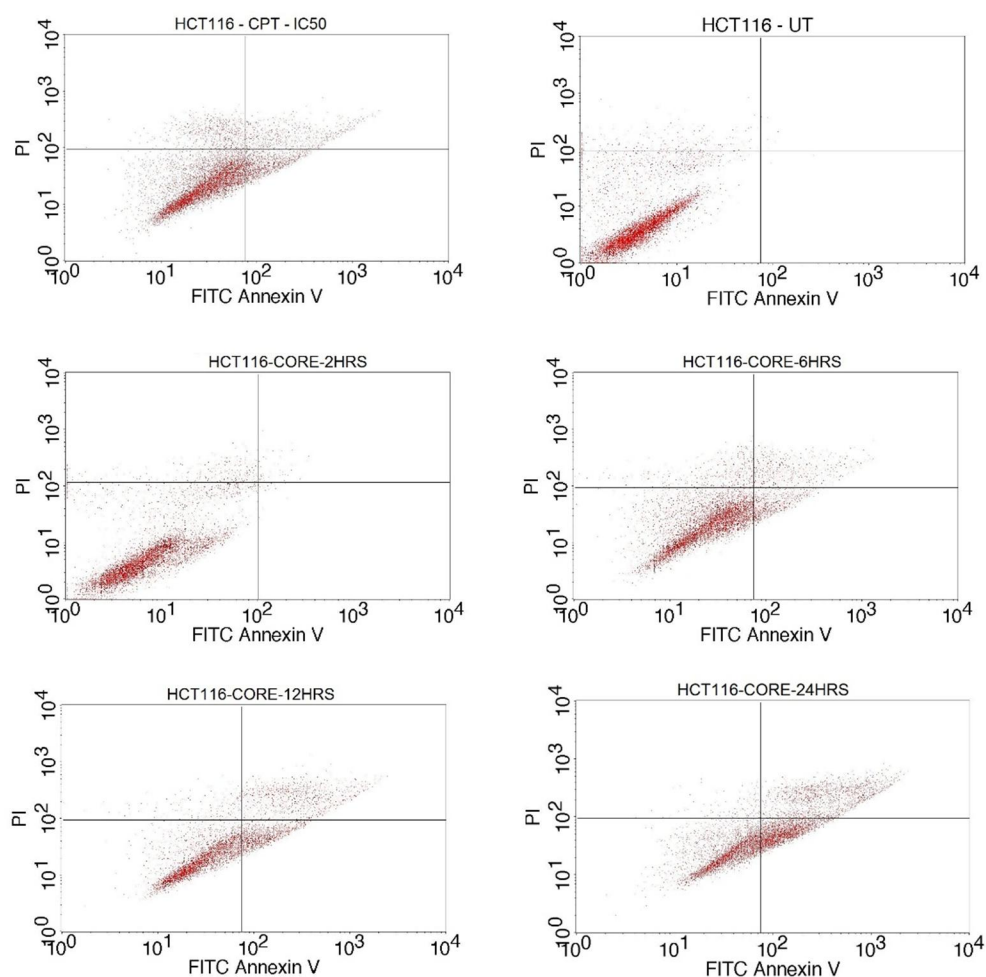


Figure 3. 58 Comparing the effect of curcumin delivery in HCT 116 cells all through the four time durations in quadrant statistics (a) CPT, (b) Untreated, (c) 2 hours, (d) 6 hours, (e) 12 hours, (f) 24 hours

Table 3.18 Tabulation of HCT 116 quadrant results

Events	CPT	UT	2 hours	6 hours	12 hours	24 hours
Total events	16713	12574	13189	18347	15761	15209
Gated events	11137	10654	10030	10781	8288	9572
UL %	00.49	02.34	02.34	02.83	01.35	00.83
UR %	04.01	00.06	00.33	03.54	07.91	12.49
LL %	50.02	82.36	73.23	47.50	34.17	28.98
LR %	08.11	00.02	00.14	04.89	09.16	20.63

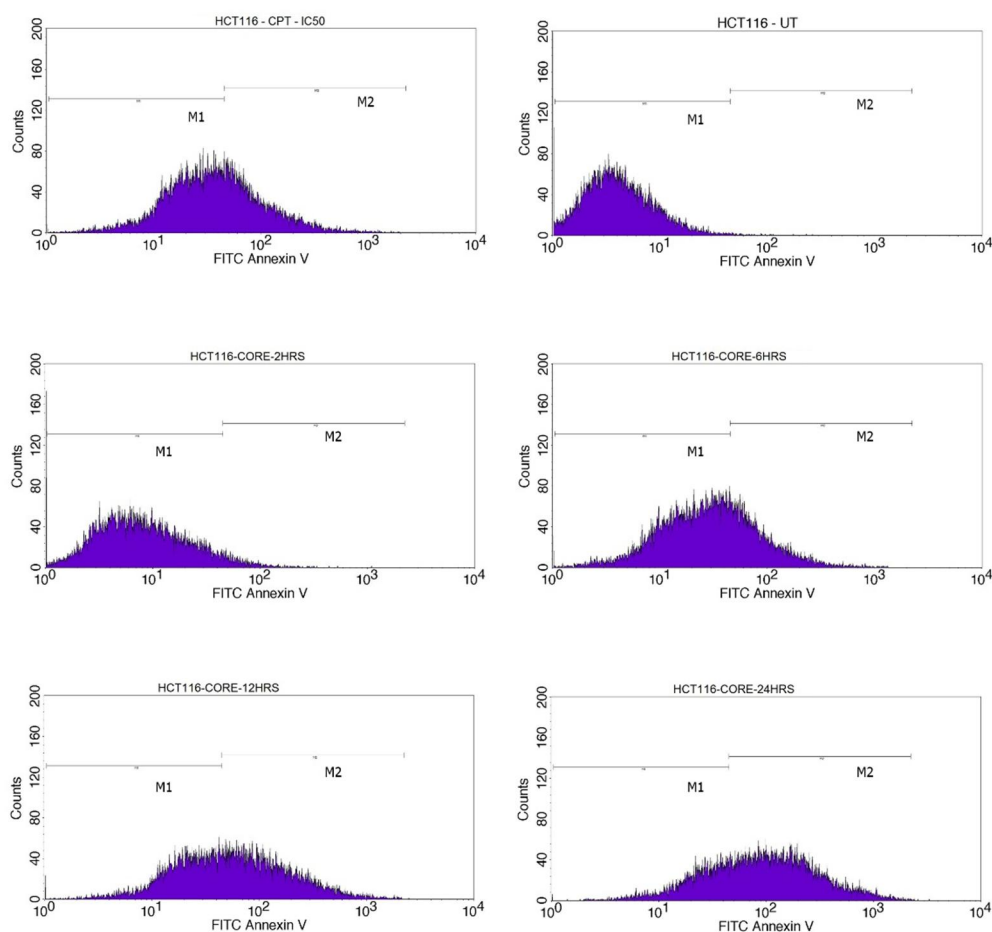


Figure 3.59 Comparing the effect of curcumin delivery in HCT 116 cells all through the four time durations in histogram statistics (a) CPT, (b) Untreated, (c) 2 hours, (d) 6 hours, (e) 12 hours, (f) 24 hours

Table 3.18 Comparing HCT 116 apoptosis obtained in histogram statistics where Annexin V positive (M2) increases while Annexin V negative (M1) decreases supporting the response of cells to the slow and steady release of curcumin

	CPT	UT	2 hours	6 hours	12 hours	24 hours
Events	16713	12514	13189	18347	15761	15209
M1	59.58	93.81	93.42	66.51	44.66	29.43
M2	40.85	0.38	5.32	33.62	55.47	70.75

3.3.4 Caspase 3 Expression Assay

Steady increase in caspase 3 expression was observed in both the cell lines.

3.3.4.1 HeLa cells

Magnetite nanoparticle loaded with camptothecin was also reported to enhance caspase 3 in HeLa cells.

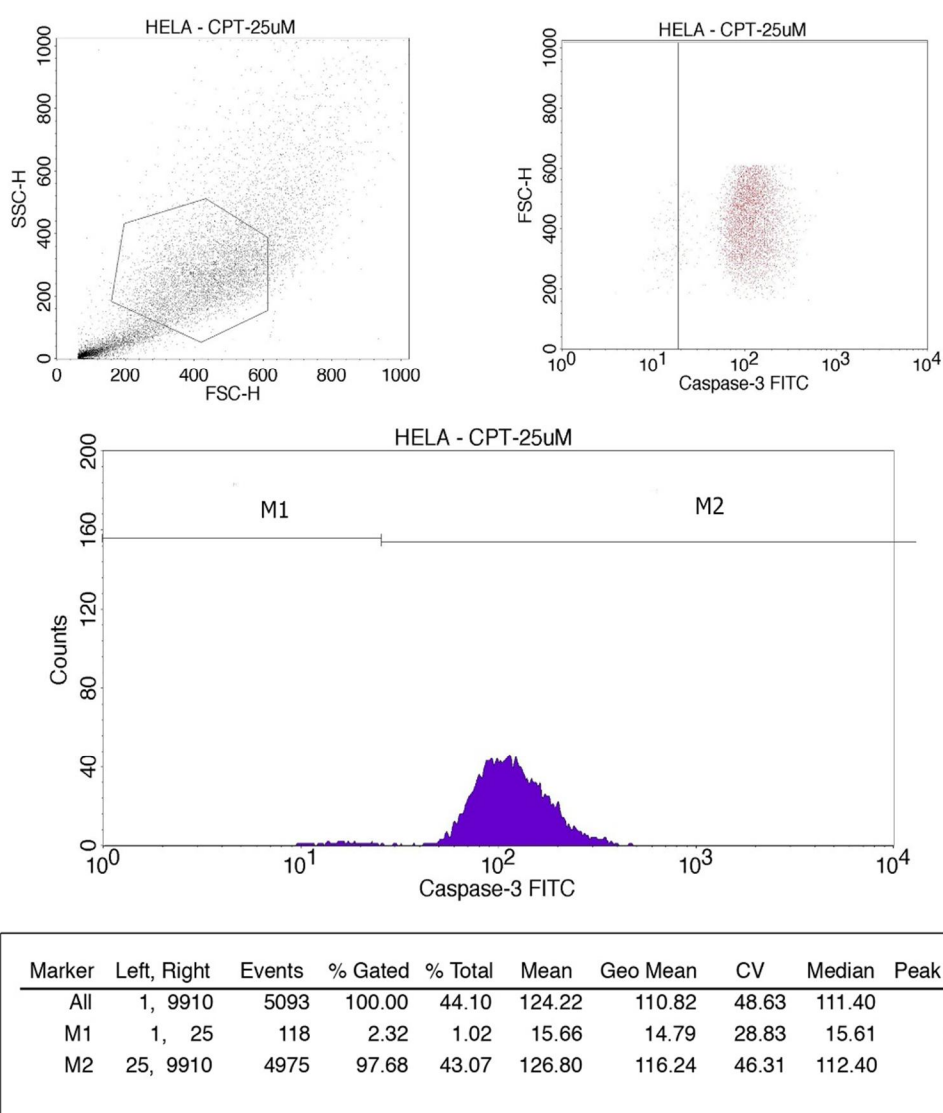
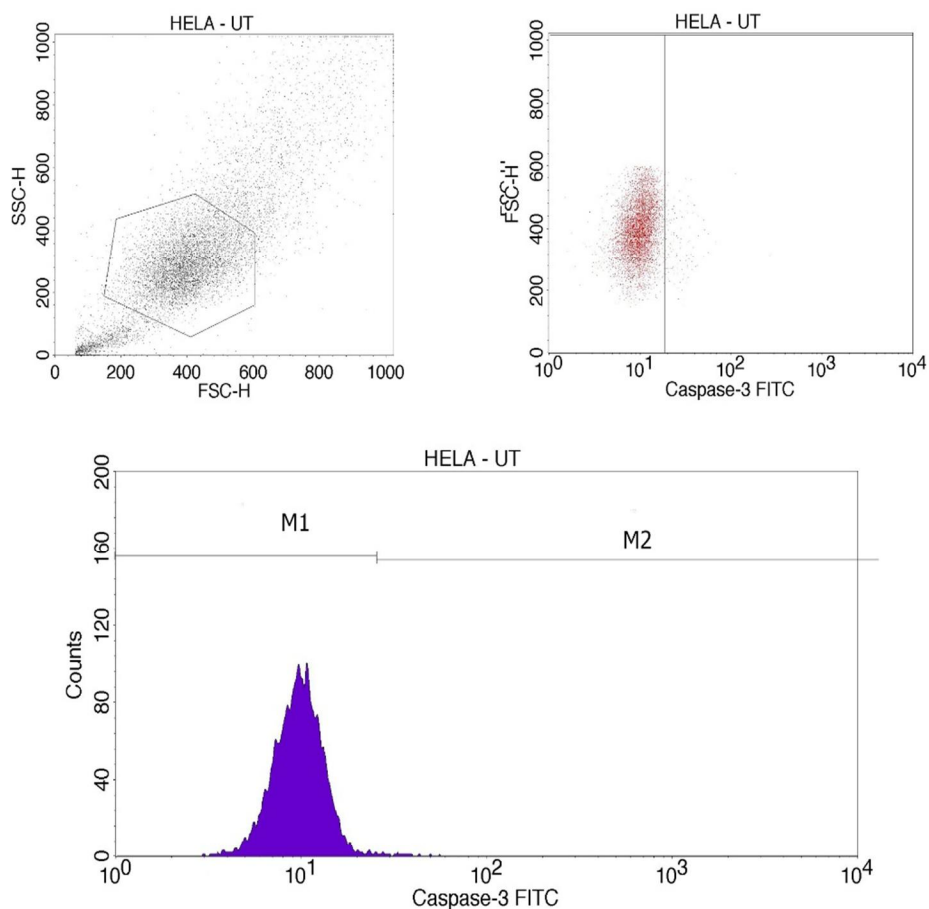
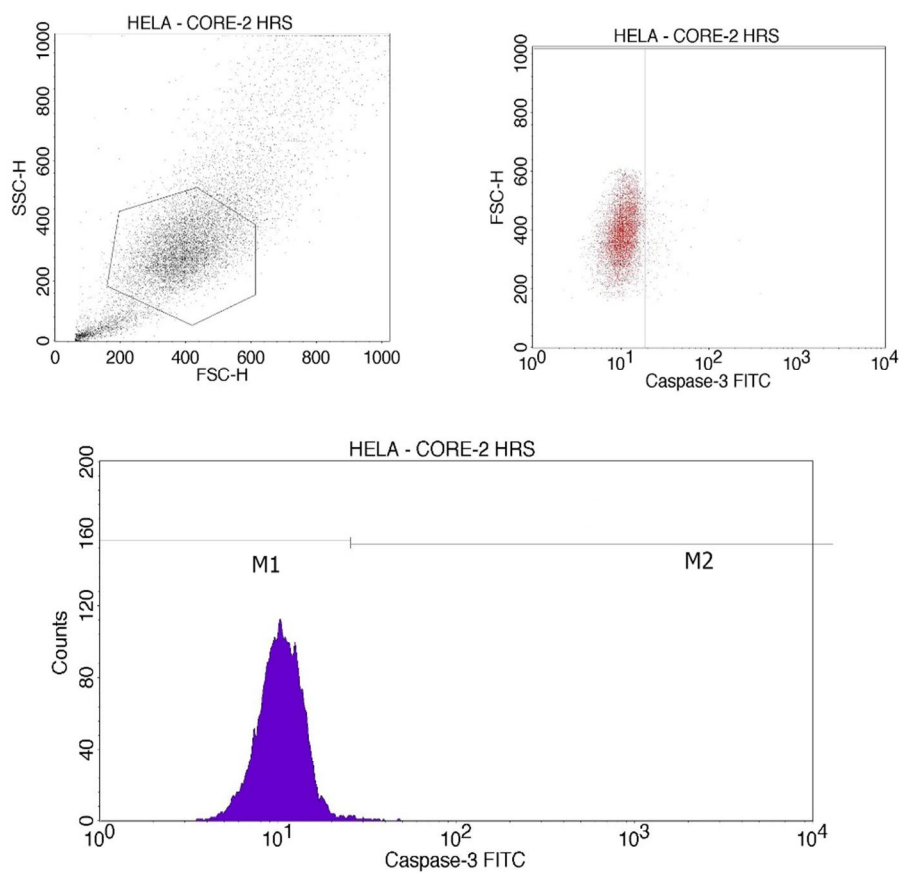


Figure 3.60 Caspase 3 expression in HeLa is found positive to Camptothecin when it is used as the positive control (M2 43.07%) and negative (M1 1.02%).



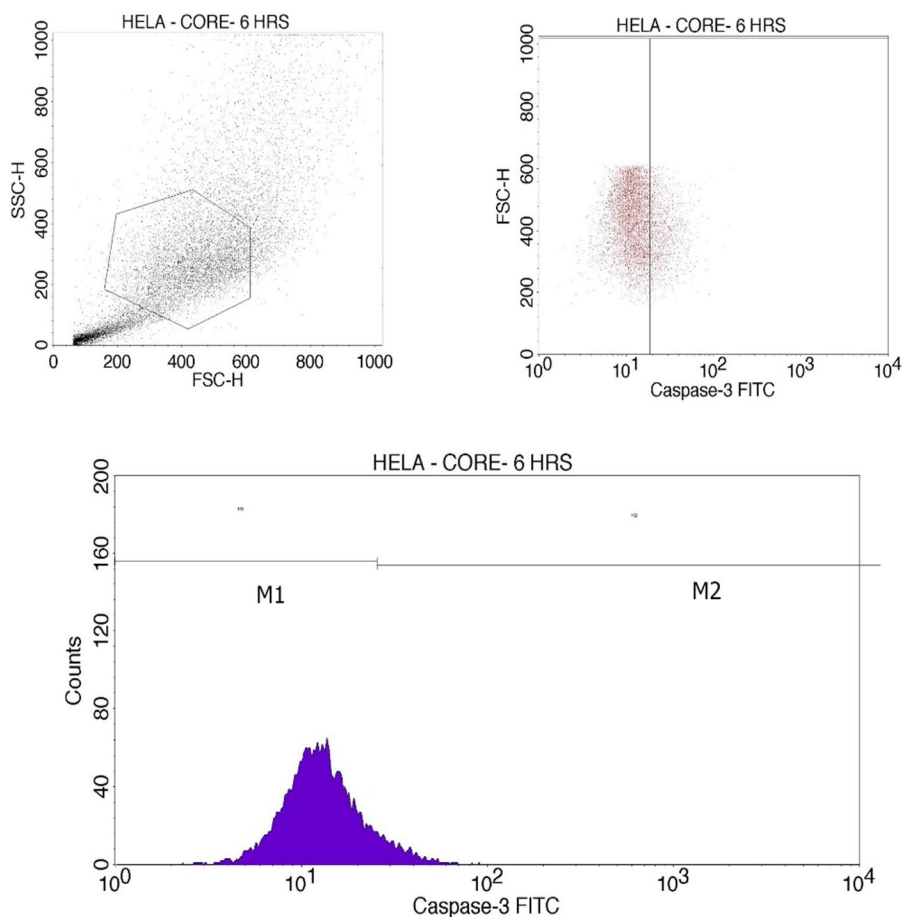
Marker	Left, Right	Events	% Gated	% Total	Mean	Geo Mean	CV	Median	Peak Ch
All	1, 9910	7533	100.00	65.31	10.16	9.59	47.75	9.65	10
M1	1, 25	7473	99.20	64.79	9.92	9.49	29.71	9.65	10
M2	25, 9910	63	0.84	0.55	38.90	34.98	80.26	32.49	27

Figure 3.61 Caspase 3 expression in HeLa for untreated remains negative at the highest percentage (M1 64.79%) and positive to caspase-3 FITC in a very minor percentage (M2 0.55%).



Marker	Left, Right	Events	% Gated	% Total	Mean	Geo Mean	CV	Median	Peak Ch
All	1, 9910	8348	100.00	65.24	10.87	10.30	55.60	10.27	10
M1	1, 25	8278	99.16	64.70	10.60	10.19	28.14	10.27	10
M2	25, 9910	74	0.89	0.58	41.99	35.22	111.37	30.78	26

Figure 3.62 Caspase 3 expression in HeLa for 2 hours' core-shell treated remains negative at the highest percentage (M1 64.70%) and positive to caspase-3 FITC in a very minor percentage (M2 0.58%).



Marker	Left, Right	Events	% Gated	% Total	Mean	Geo Mean	CV	Median	Peak Ch
All	1, 9910	7086	100.00	44.19	14.78	13.00	60.34	12.52	13
M1	1, 25	6416	90.54	40.01	12.61	11.75	36.90	11.97	13
M2	25, 9910	686	9.68	4.28	35.33	33.95	35.32	31.91	27

Figure 3.63 Caspase 3 expression in HeLa for 6 hours' cores-shell treatment remains considerably negative (M1 40.01%) and positive to caspase-3 FITC at an enhanced percentage (M2 4.26%). At 6 hours the drug begins to get released and the cells positively respond to it.

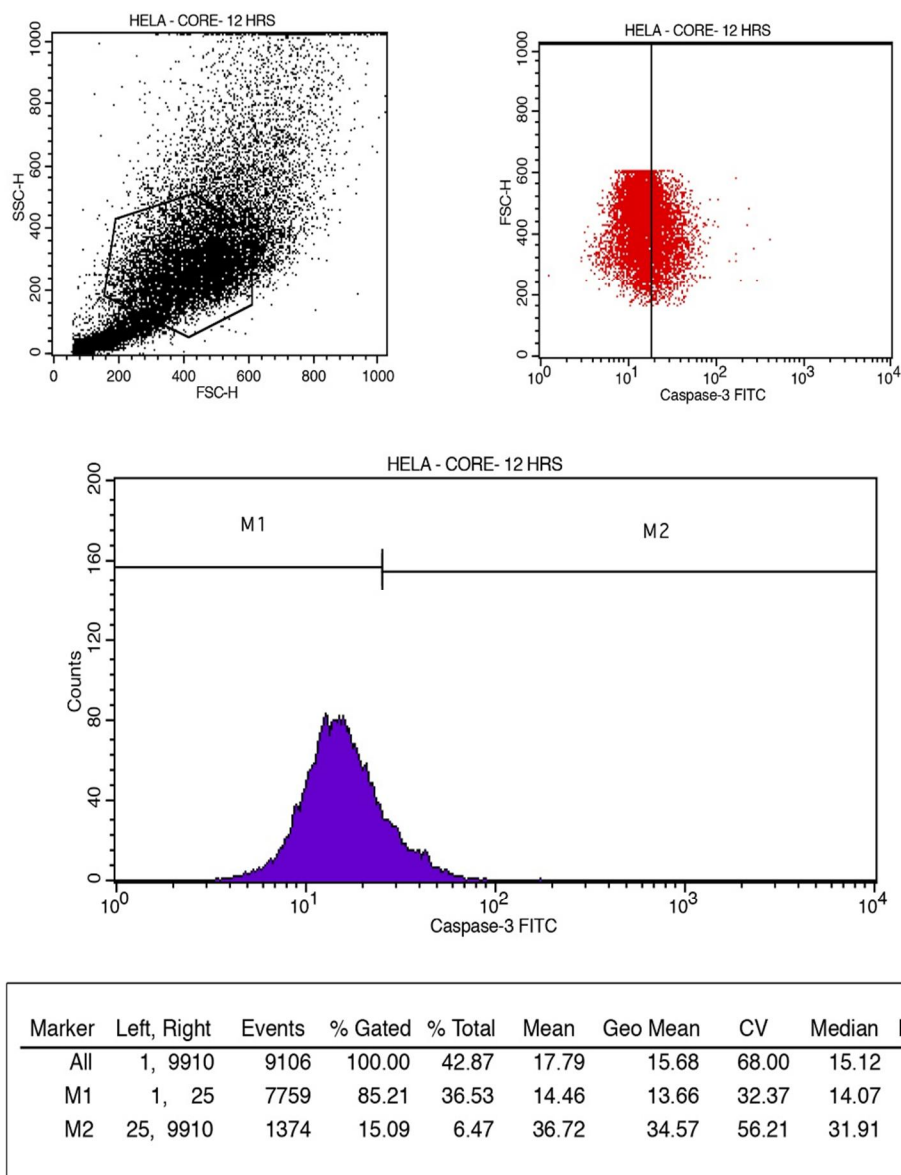


Figure 3.64 Caspase 3 expression in HeLa for 12 hours' cores-shell treatment remains considerably negative (M1 35.53%) and positive to caspase-3 FITC further at an enhanced percentage (M2 6.47%). At 12 hours the drug remains get released and the cells positively respond to it at an elevated level.

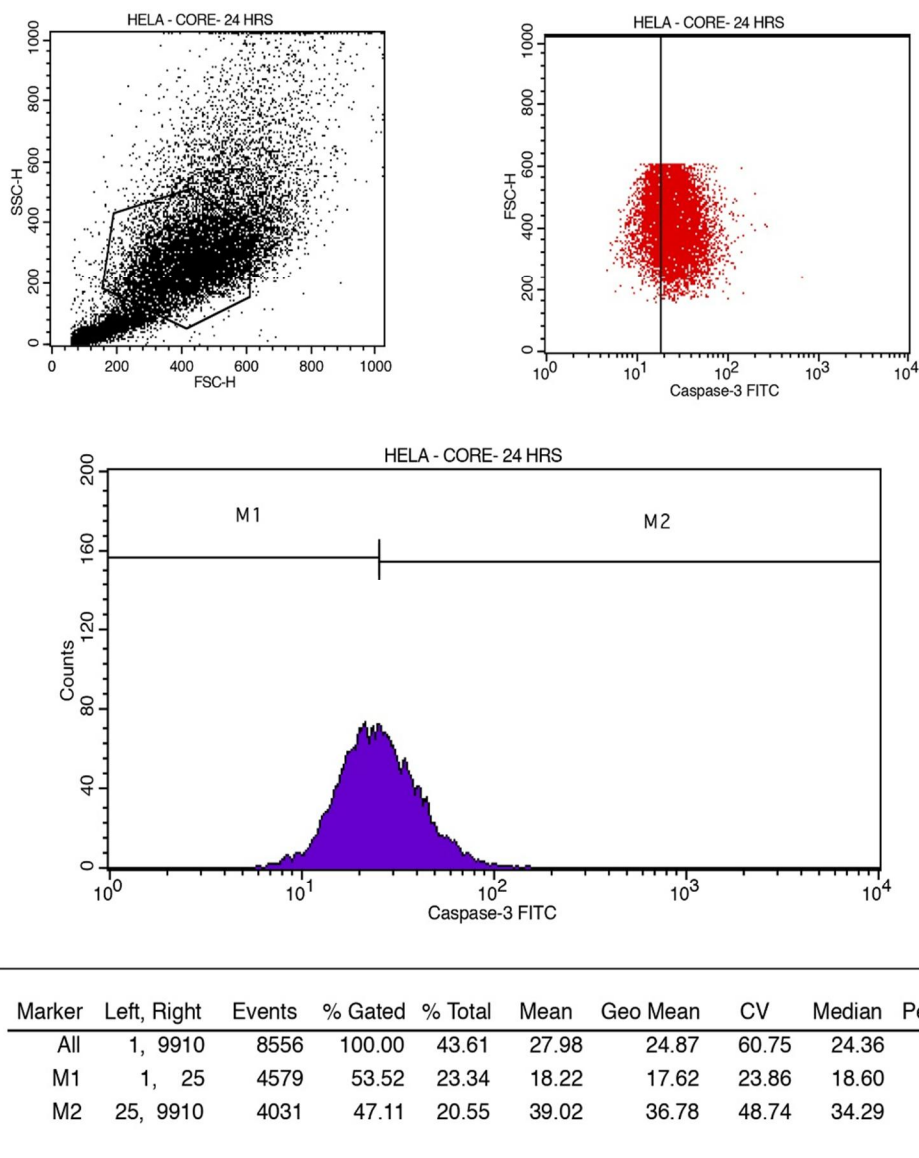


Figure 3.65 Caspase 3 expression in HeLa for 24 hours' cores-shell treatment moves to an equatorial level (M1 23.34%) negative and positive to caspase-3 FITC (M2 20.55%). At 24 hours the drug still remains get released and the cells positively respond to it at an elevated level.

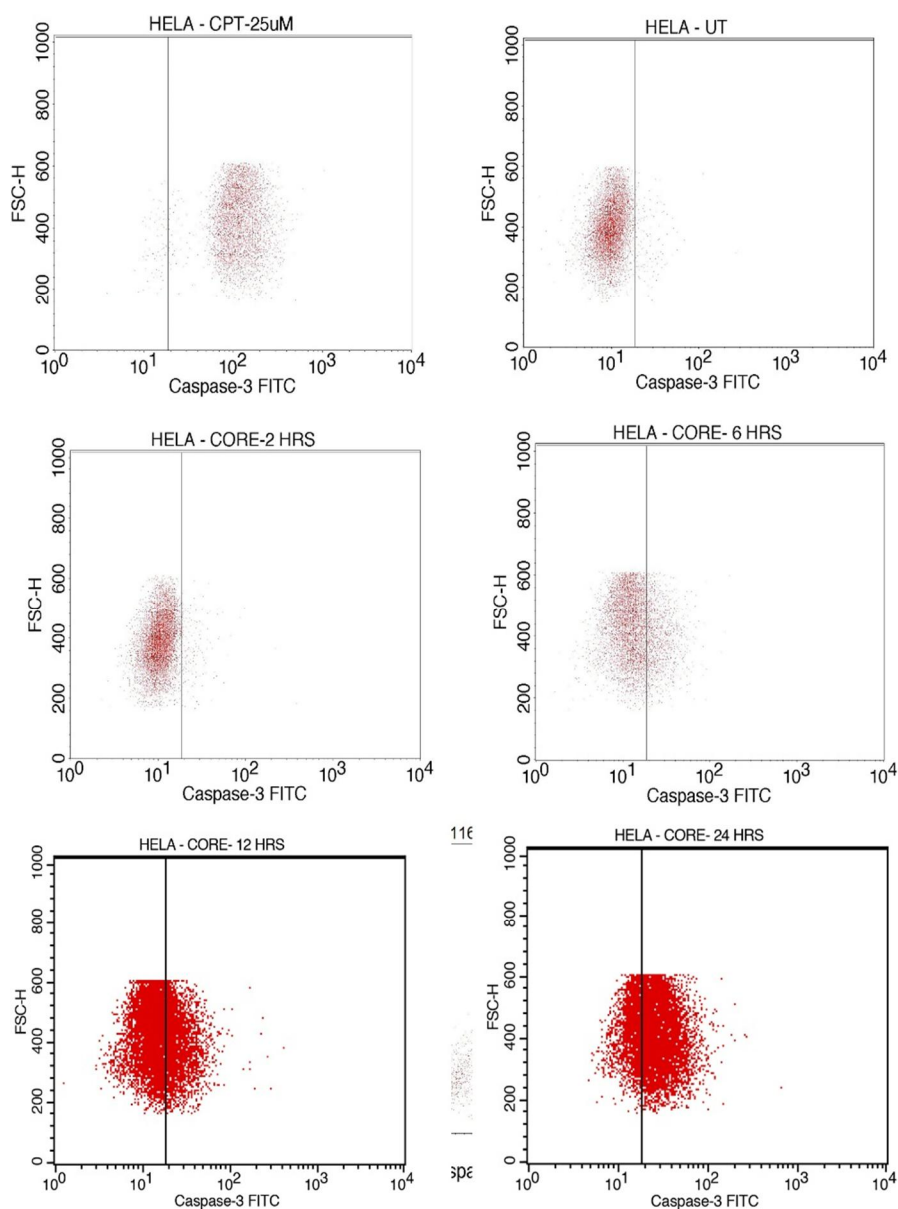


Figure 3.66 Comparison of Caspase-3 Expression in HeLa all through the four time durations. Though 24 hours' core-shell treatment is not as that of the positive control camptothecine the highest percentage of caspase-3 expression provides the perpetual response of the cells further.

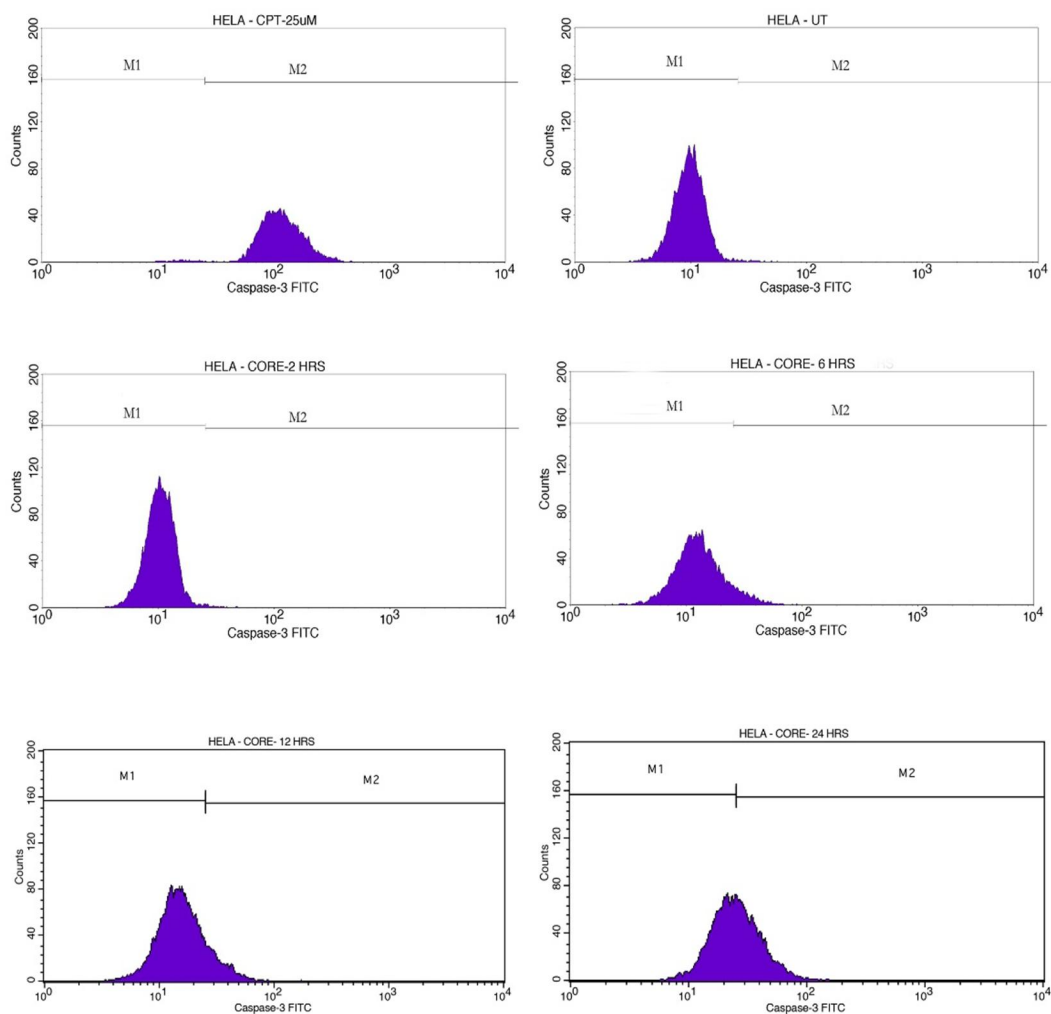


Figure 3.67 Caspase-3 Expression in HeLa Cells depicted in histogram statistics and the values given in Table 3.19

Table 3.19 Tabulation of histogram statistics of caspase-3 expression in HeLa cells. As the caspase-3 negative cells (M1) decrease caspase-3 positive cells increase (M2). At 24 hours the positive cells begin to out high in caspase-3 expression proving sustained delivery of curcumin.

	CPT	UT	2 hours	6 hours	12 hours	24 hours
Events	5093	7533	8348	7086	9106	8556
M1	1.02	64.79	64.70	40.01	36.53	23.34
M2	43.07	0.55	0.58	4.28	6.47	20.55

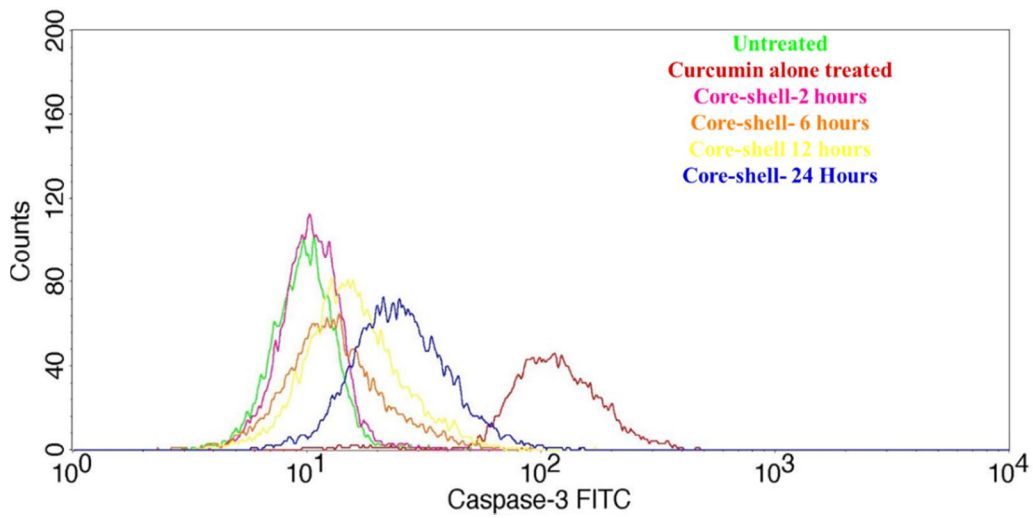
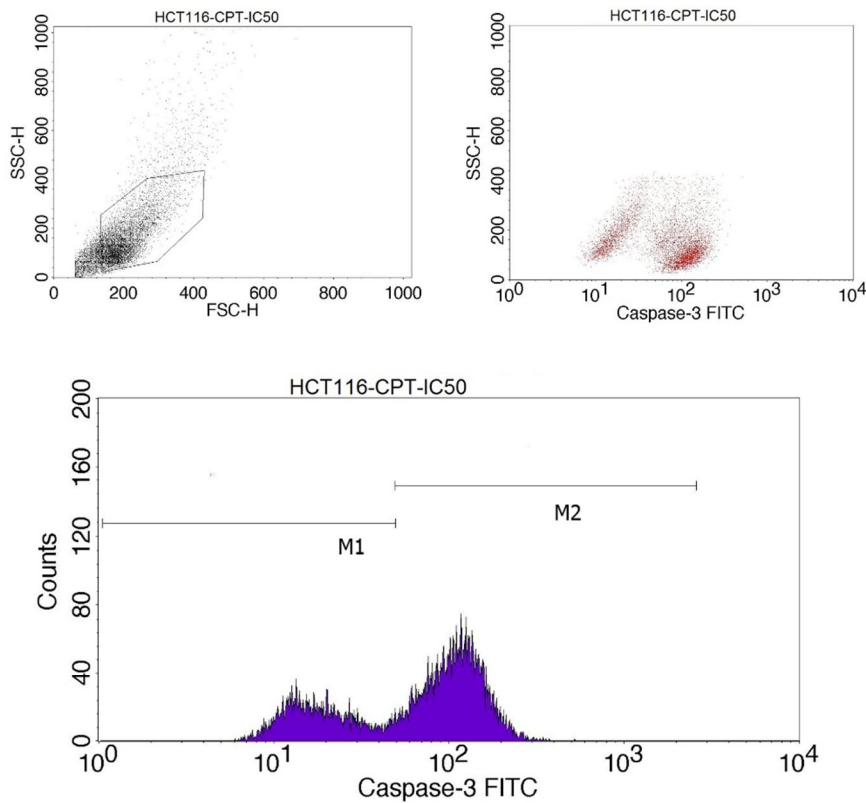


Figure 3.68 Overlay of Caspase-3 Expression by core-shell treated HeLa cells all through the four hours

3.3.4.2 Caspase-3 expression assay in HCT 116 cells



Marker	Left, Right	Events	% Gated	% Total	Mean	Geo Mean	CV	Median	Peak Ch
All	1, 9910	8745	100.00	72.81	83.02	59.17	68.22	82.79	115
M1	1, 49	2945	33.68	24.52	20.44	18.21	50.66	17.31	13
M2	48, 2548	5839	66.77	48.61	114.36	107.09	37.10	109.41	115

Figure 3.69 Caspase 3 expression in HCT 116 is found positive to Camptothecin when it is used as the positive control (M2 48.61%) and negative (M1 24.52%).

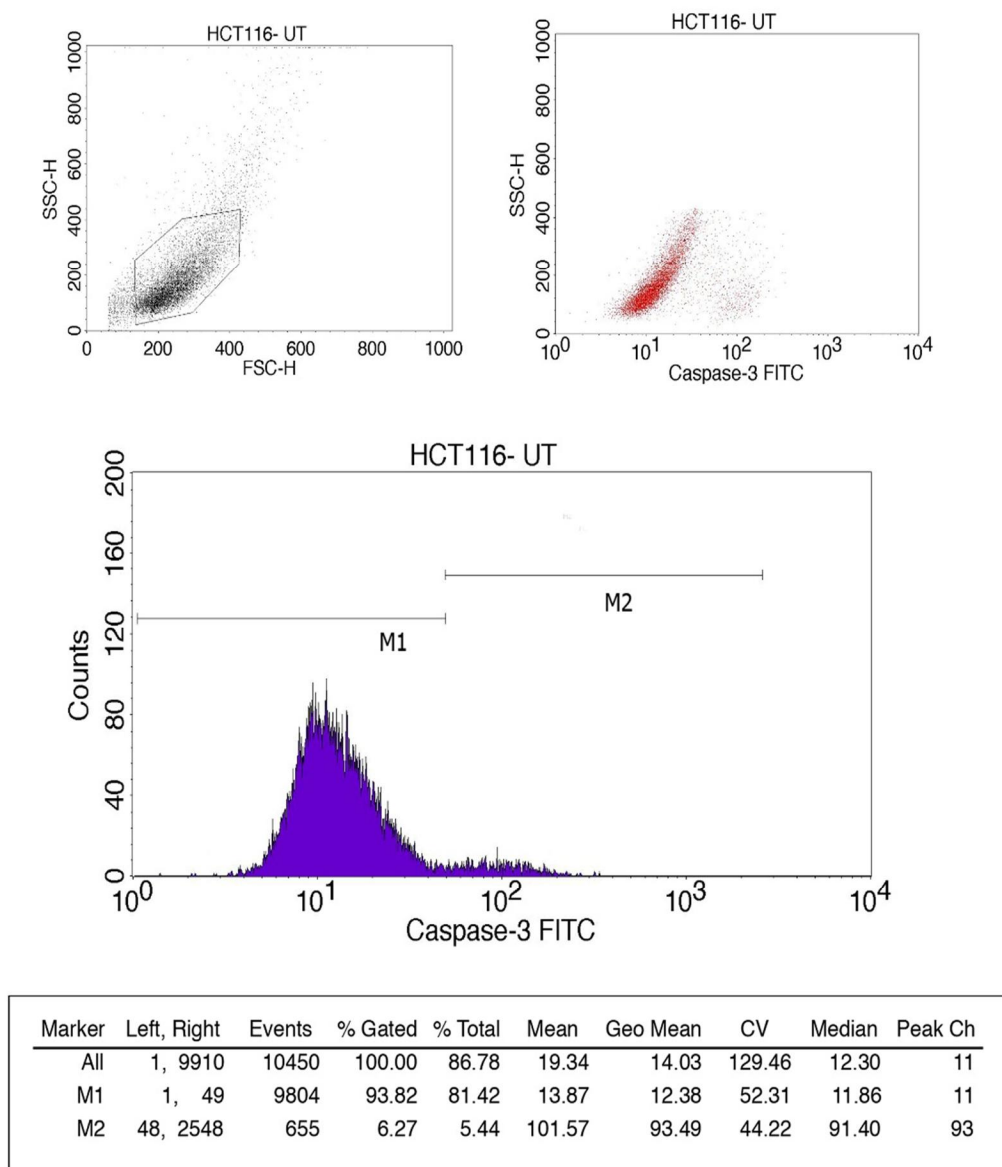


Figure 3.70 Caspase 3 expression in HCT 116 untreated remains negative at the highest percentage (M1 81.42%) and positive to caspase-3 FITC in a very minor percentage (M2 5.44%).

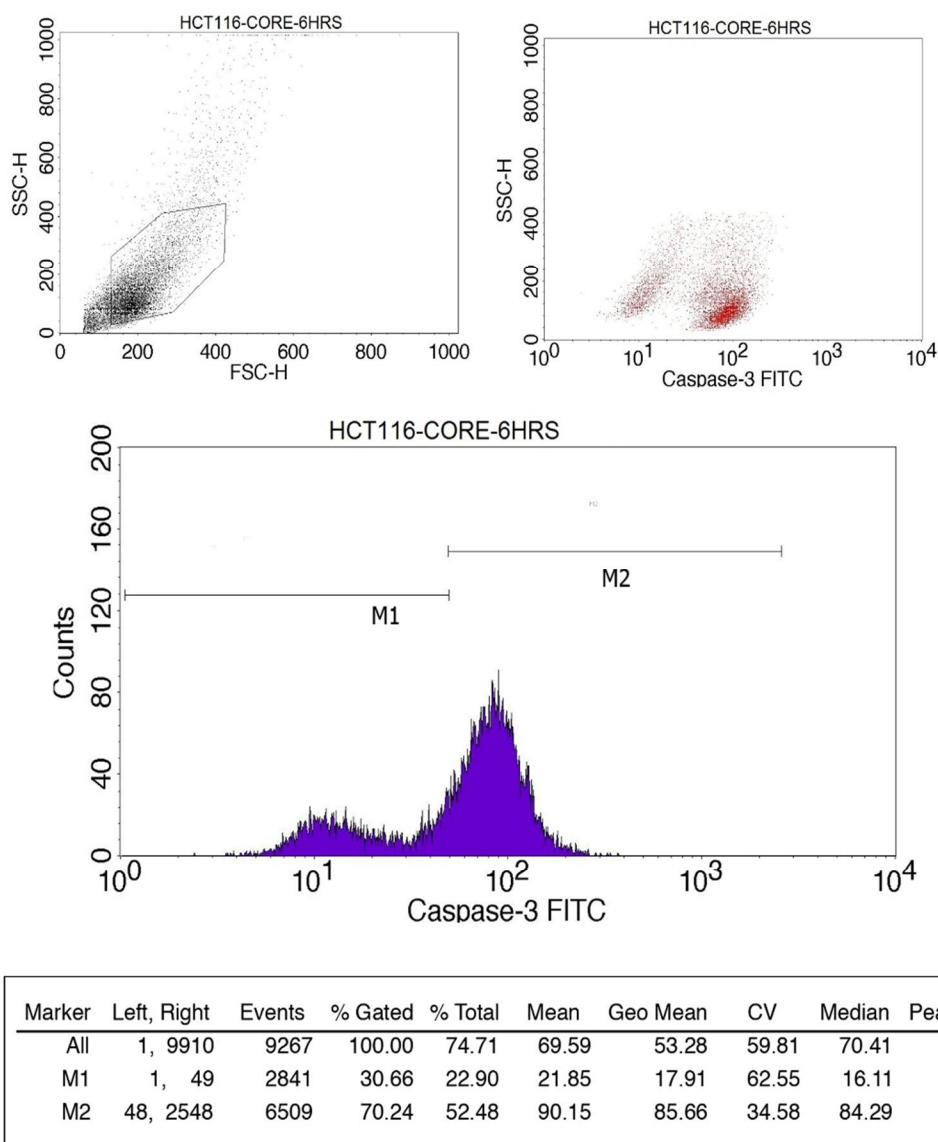


Figure 3.71 Caspase 3 expression in HCT 116 for 6 hours' coreshell treatment remains considerably negative (M1 22.90%) and positive to caspase-3 FITC at an enhanced percentage (M2 52.48%). At 6 hours the drug furthermore gets released and the cells positively respond to it.

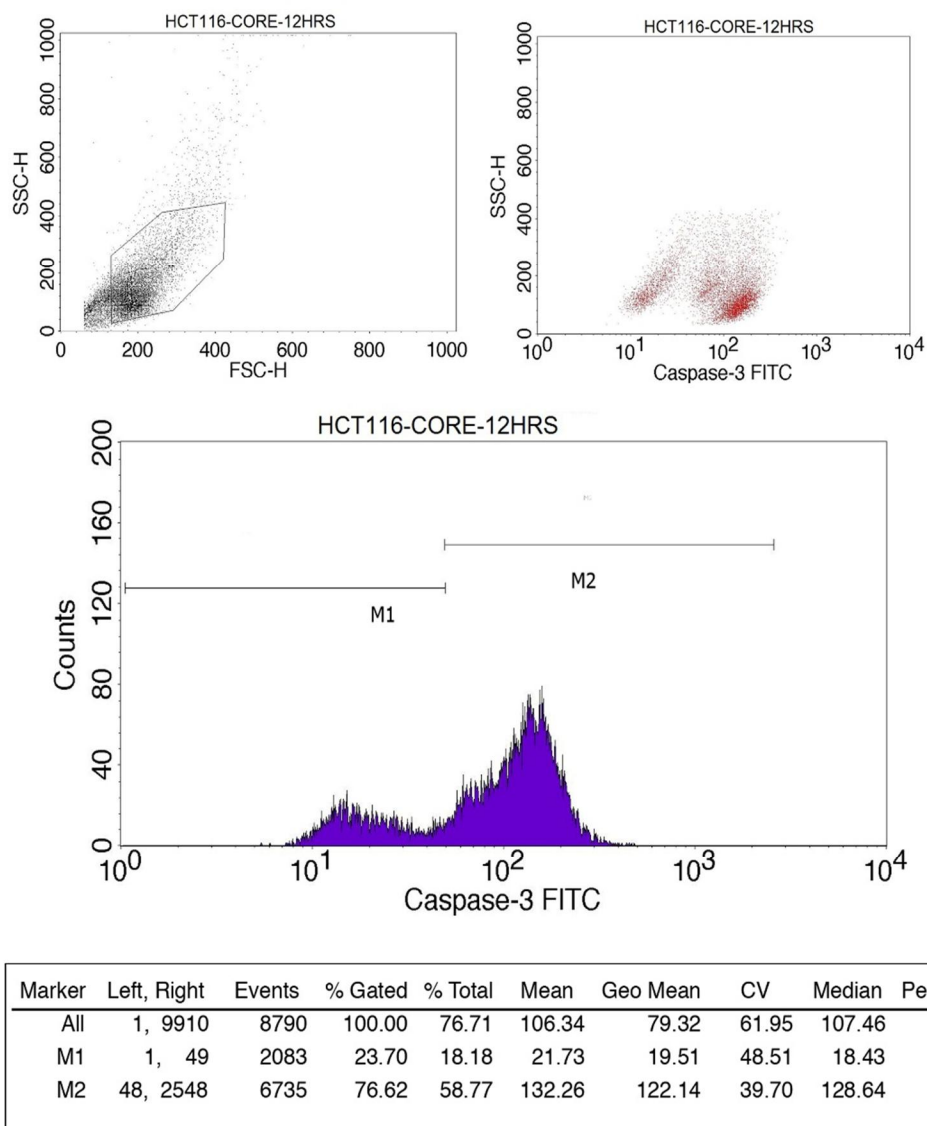


Figure 3.72 Caspase 3 expression in HCT 116 for 12 hours' core-shell treatment found a drop in negative (M1 18.18%) and up-rise in positive to caspase-3 FITC further at an enhanced percentage (M2 58.77%). At 12 hours the drug remains get released and the cells positively respond to it at an elevated level. It is leading to further sustained delivery of curcumin.

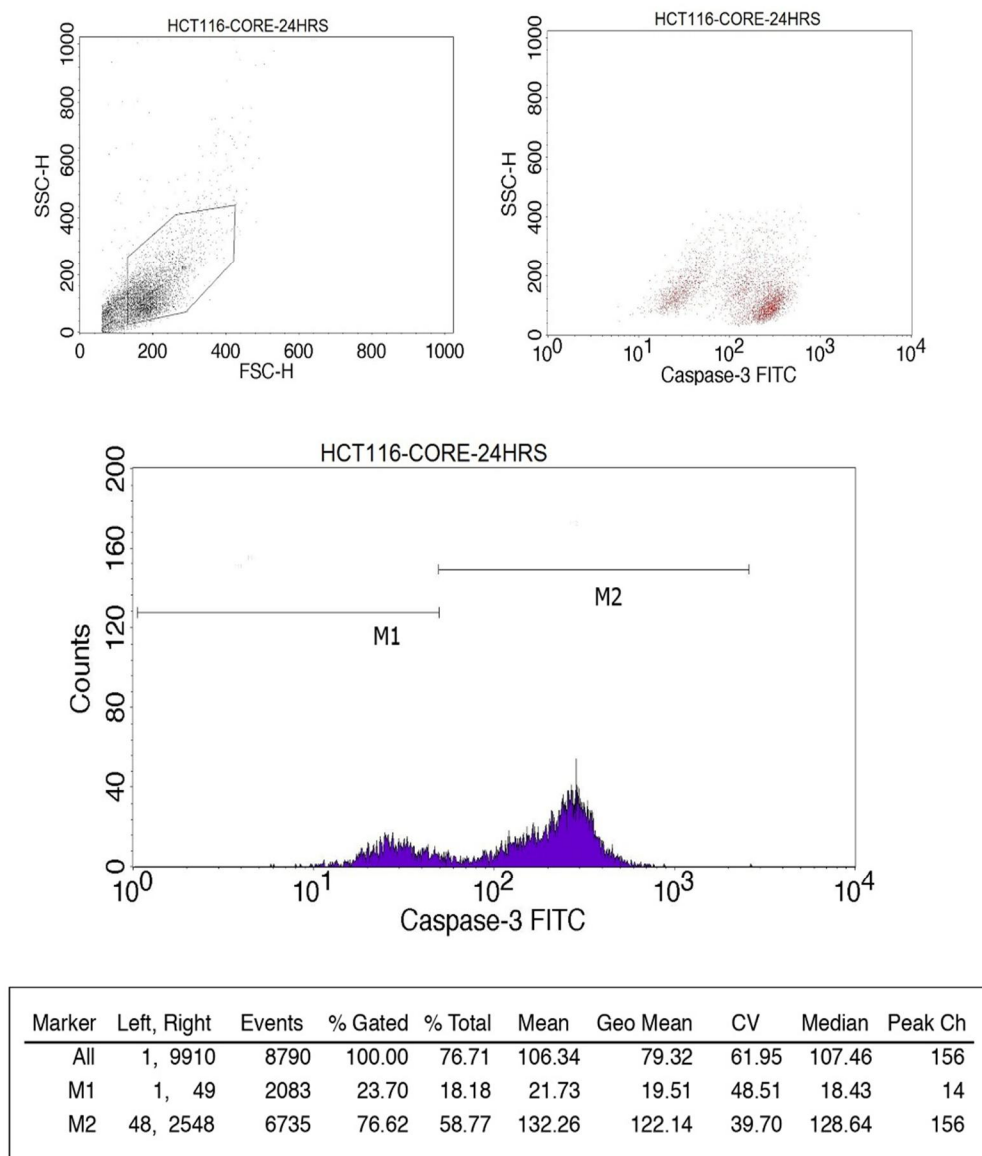


Figure 3.73 Caspase 3 expression in HCT 116 for 24 hours' coreshell treatment moves highly positive (M2 58.77%) negative to caspase-3 FITC (M1 18.18%). At 24 hours the drug still remains get released and the cells positively respond to it at an elevated level. It justifies the slow and steady release of curcumin from Coreshell-SPIONs. Delivery of the loaded drug still continues to get released at sustained level.

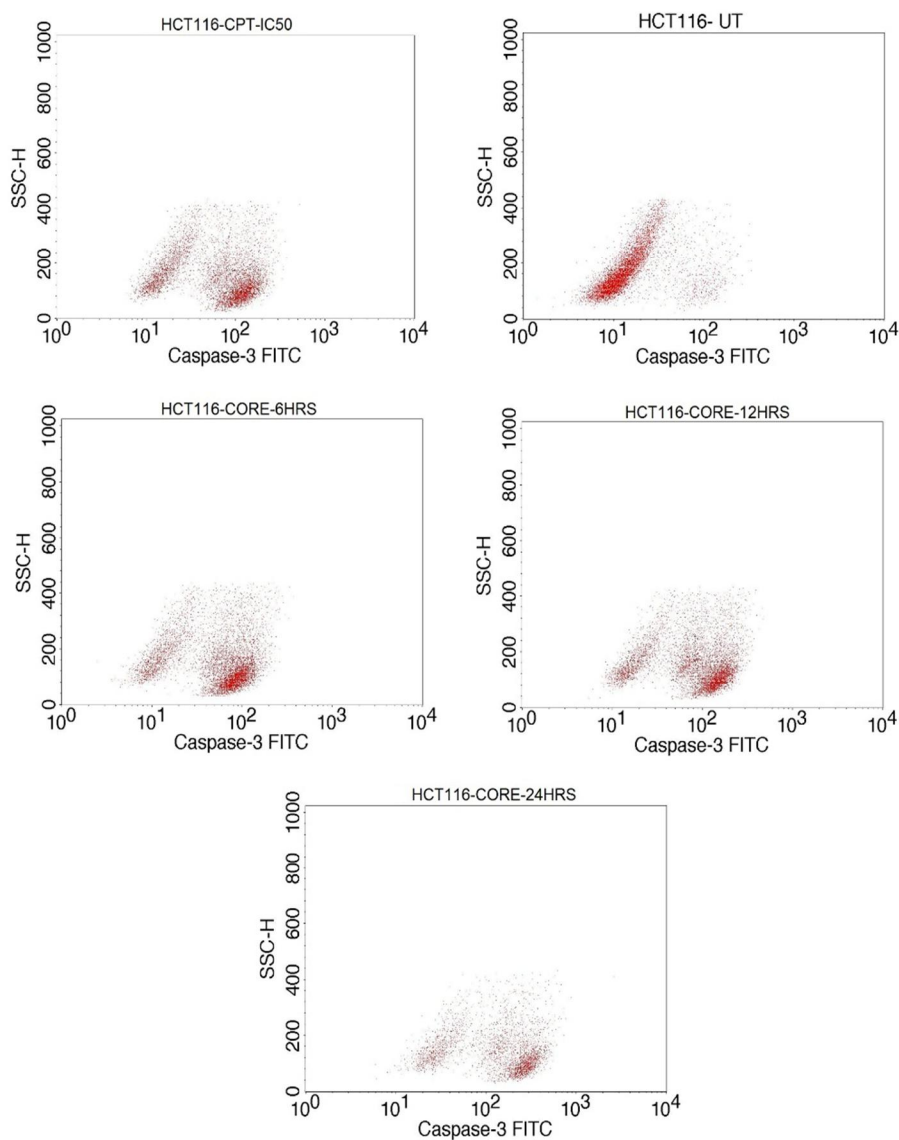


Figure 3.74 Comparison of Caspase-3 Expression in HCT 116 all through the three time durations. The response of cells to caspase-3 FITC at 24 hours' core-shell treatment went beyond to the level of the positive control camptothecine. There is a considerable variance found in between 12 hours and 24 hours, validating the expression of caspase-3 and proving sustained delivery of curcumin from the Coreshell-SPIONs.

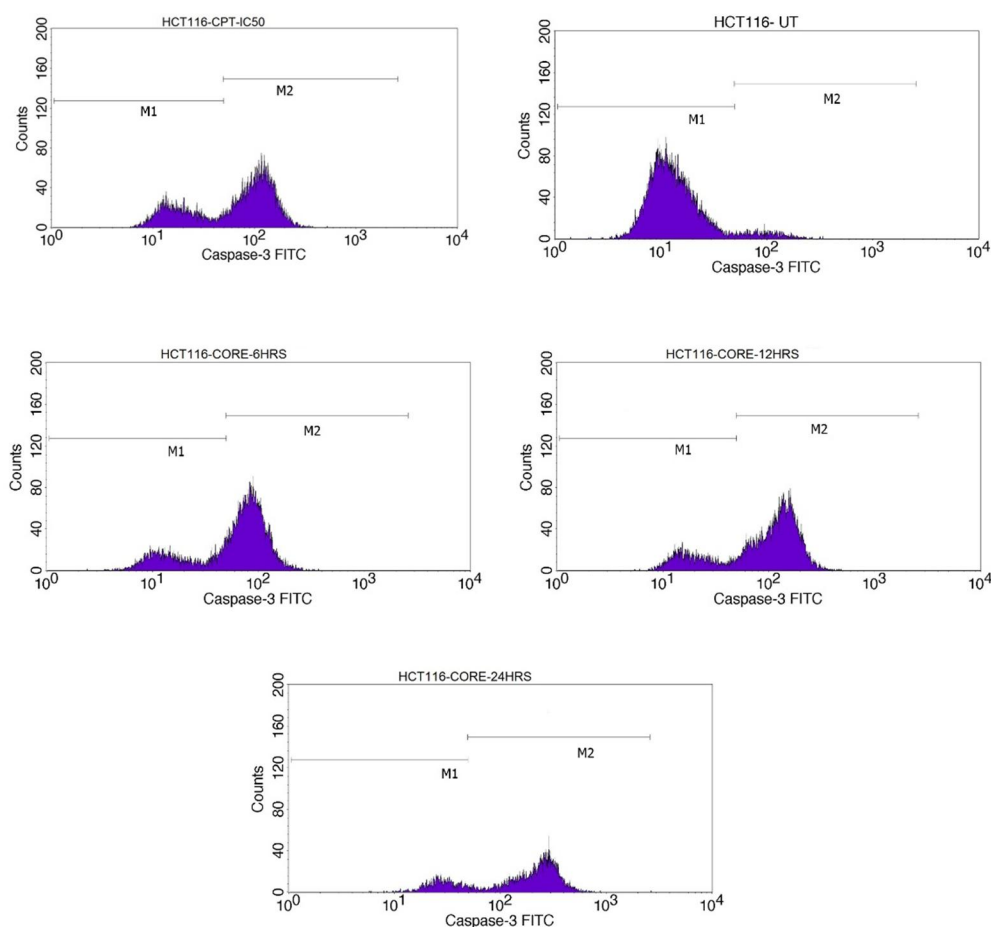


Figure 3.75 Tabulation of histogram statistics of caspase-3 expression in HCT 116 cells. As the caspase-3 negative cells (M1) decreases in number caspase-3 positive (M2) cells increase. At 24 hours caspase-3 expression appears highly raised up in comparison with that of the total events taken into consideration.

Table 3.20 Tabulation of histogram statistics of caspase-3 expression in HCT 116 cells. As the caspase-3 negative (M1) cells decreases caspase-3 positive (M2) cells increase. At 24 hours, positive appears out-high in caspase expression

	CPT	UT	2 hours	6 hours	12 hours	24 hours
Events	8745	10450	-	9267	8790	4426
M1	24.52	81.42	-	22.90	18.18	16.40
M2	48.61	5.44	-	52.48	58.77	51.73

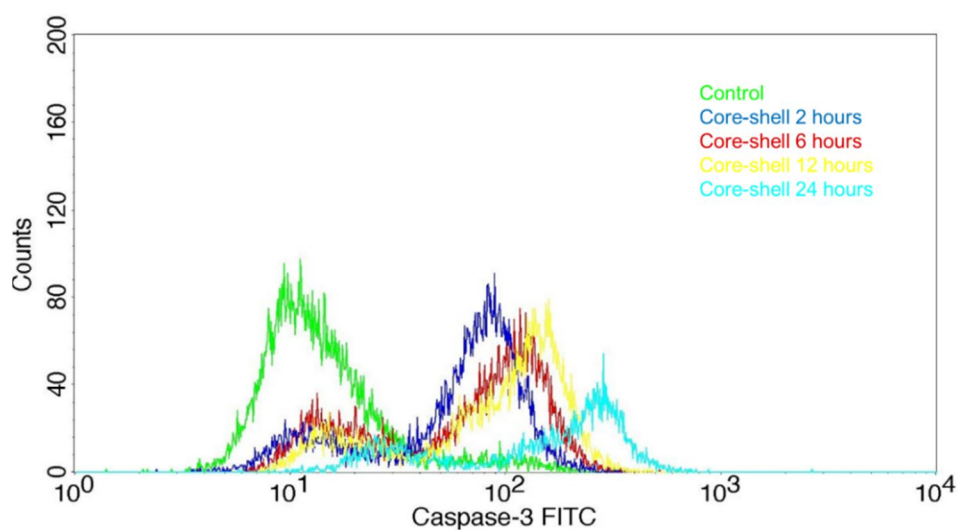


Figure 3.76 Overlay of caspase 3 Expression by core-shell treated HCT116 cells

3.4 X-RAY IMAGING

SPIONs were helping in visualizing the quail's egg clearly and they were enhancing the effect of X-ray and it could be used as contrasting agent in X-ray imaging. Even the SPIONs were obeying to magnetic field (Figure 3.77 d).

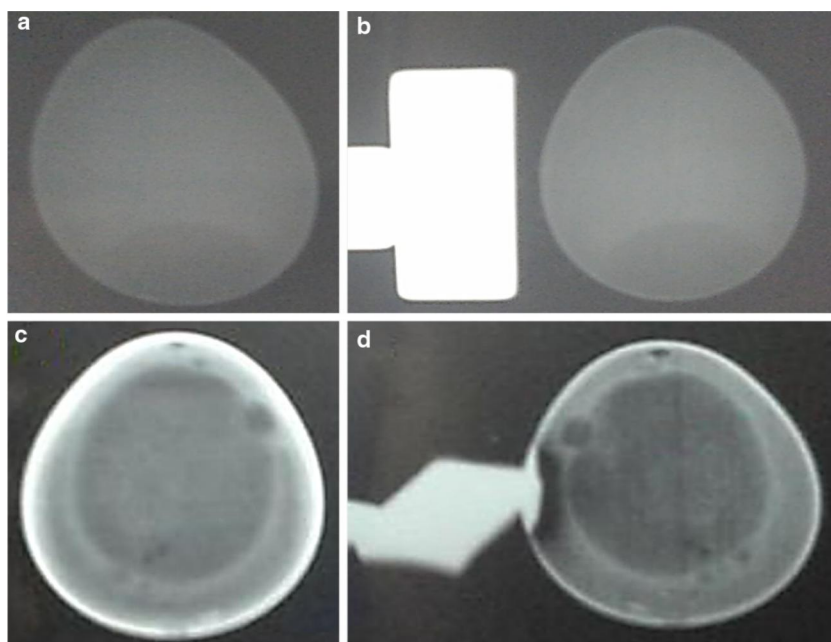


Figure 3.77 X-ray imaging of quail's egg. a) Control egg; b) Applied magnetic field; c) SPIONs introduced, d) SPIONs dispersed with applied magnetic field

3.5 TOXICITY STUDIES

Gut was found to be disintegrated was seen in earthworms exposed to higher concentrations, i.e. 200 and 400 ng (Figure 3.78 b-d). Silver and gold nanoparticles were found to cause cytotoxic effects (Samrot et al., 2018a; Samrot et al., 2018b). Earthworms were tending to accumulate iron oxide into the system, which was evidenced by prussian blue staining (Figure 3.79 b-d).

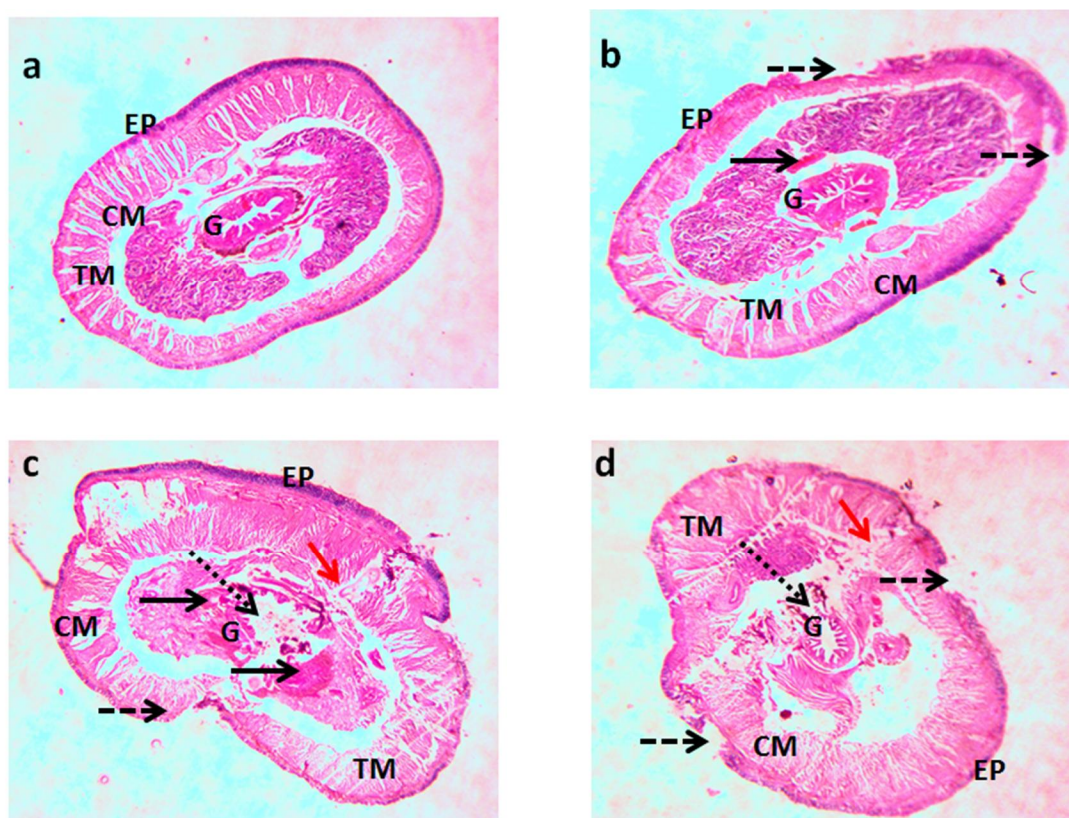


Figure 3.78 H&E staining of earthworm exposed to SPIONs (a) Control, (b) 100 ng/10 ml exposed, (c) 200 ng/10 ml, (d) 400 ng/10 ml exposed. EP epidermis, CM circular muscle, TM transverse muscle, and G gut region. b–d Solid arrows show the impact with some granular lipofuscin-like deposits, b–d erosion of the epidermis (dashed arrow), c, d with fibrosis of the circular muscle (purple arrow) and with gut disintegration (dotted arrow)

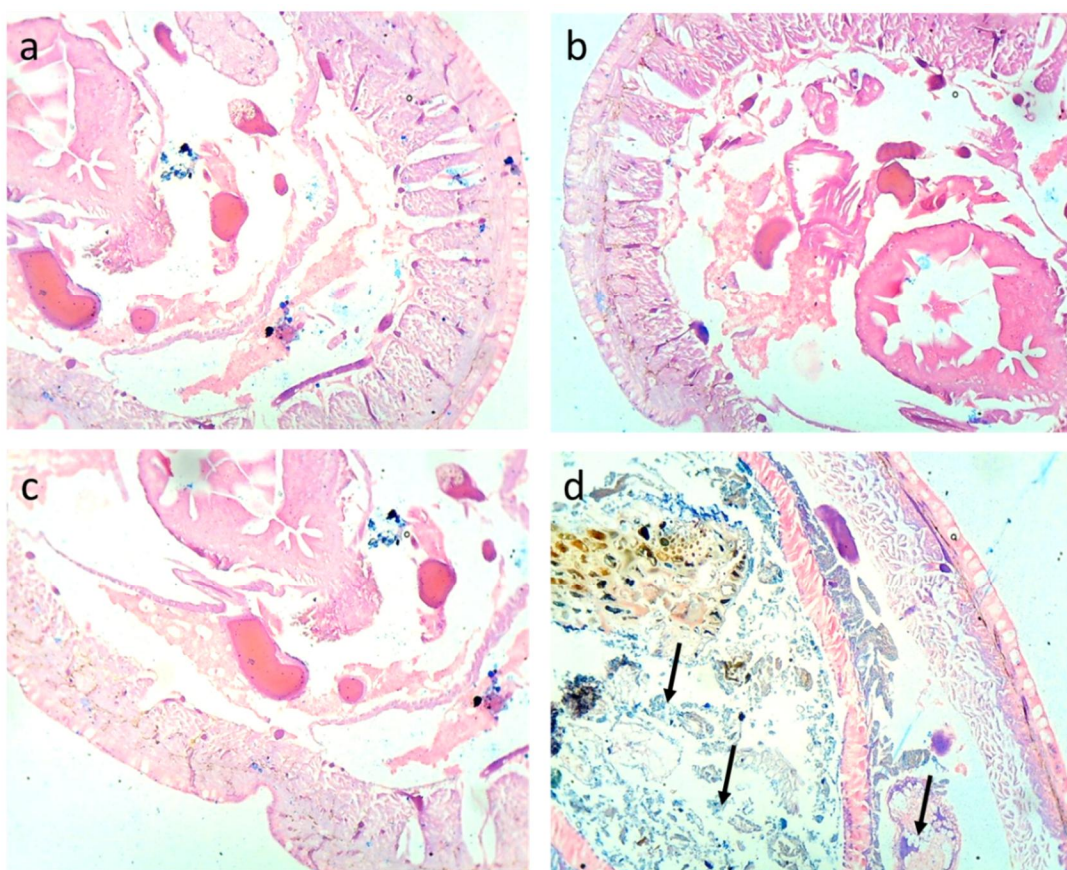


Figure 3.79 Prussian blue staining of earthworm exposed to SPIONs a) Control, b) 100 ng/10 ml exposed, c) 200 ng/10 ml, d) 400 ng/10 ml exposed. Solid arrows show the stained region of iron accumulation.

Table 3.21 Phenotypic changes observed in earthworm

S.No	Parameter analyzed	Control	100ng exposed	200ng exposed	400ng exposed
1.	Color change	Nil	Brown	Brown	Brown to black
2.	Behavioral change	Nil	Nil	Nil	Nil
3.	Death	Nil	Nil	Nil	Nil

CHAPTER 4

SUMMARY

- Targeted drug delivery is possible when the drug is tagged with a proper carrier. The carrier can be moved to the target site and the drug be delivered to interact at the required site.
- SPIONs are better nano-carriers which can be moved to any site. SPIONs could be moved by applied magnetic field to the target site.
- In this study, SPIONS production was standardized and it was found to be produced with 0.133% of precursor iron molecular solution and under external applied magnetic field, where the other concentrations showed aggregation and bigger in size.
- Once the SPIONs production was optimized, it was used for tagging curcumin, which was not much easier until it was functionalized with SDS.
- When the SPIONs were functionalized with SDS, it increased the stability of SPIONs, which was identified and analyzed by zetapotential analysis.
- Functionalized SPIONs were tagged with curcumin and encapsulated with a biopolymer – chitosan.
- The obtained Coreshell-SPIONs were found to be below 35 nm, stable and also crystalline.

- The chemical structure, morphology etc. of naked SPIONs and Coreshell-SPIONs were analyzed microscopically and spectroscopically.
- The Coreshell-SPIONs were checked for their anticancer activity against two cancer cell lines: HeLa cells and HCT 116 cells.
- IC50 was determined by MTT assay as 30 μg and 80 μg against HeLa and HCT116 cell lines respectively.
- This concentration was further used for other anticancer activity studies like nuclear staining, flow-cytometry and caspase-3 expression assay.
- Coreshell-SPIONs were found to cause apoptosis in both the cell lines as the drug released in sustained manner.
- After evaluating its potency as nano-drug-carrier, it was used as contrasting agent for X-Ray imaging of Quail's egg. It was acting as a good contrasting agent and enhanced the inner content of egg clearly. Moreover, the SPIONs were obeying applied magnetic field inside the egg and opening a way for enhanced X-ray imaging technique.
- SPIONs were also evaluated for their toxicity against earthworms, where it was not causing any evident activity on morphology but it was causing lipofuscin like accumulation and erosion on epithelium.
- SPIONs were found getting accumulated inside the experimental earthworm tissue, which was evidenced by prussian blue staining.

CHAPTER 5

CONCLUSION

In this research work, super paramagnetic iron oxide nanoparticles (SPIONs) production was optimized and 0.133% precursor solution was found to be producing mono dispersed SPIONs of size between 15 and 20 nm. SPIONs were functionalized with an anionic detergent. Functionalization was found aiding the tagging of a hydrophobic drug curcumin, following this, it was encapsulated with chitosan biopolymer. Every stage was characterized by SEM, TEM, AFM, FTIR, UV-Vis, XRD, XPES, Raman Spectroscopy, SQUID, VSM. Thus made Coreshell-SPIONs were subjected for drug delivery against two cancer cell lines (1) HCT 116 and (2) HeLa cells and were showing IC₅₀ at 30 µg and 800µg concentration against HeLa and HCT 116 cell lines respectively. Anticancer studies were taken forward with IC₅₀ concentration by nuclear staining (Hoechst staining), flow cytometry (to detect the stage of cells) and expression of caspase 3 (apoptosis inducing enzyme). The Coreshell-SPIONs were reported to be effective and found inducing apoptosis by caspase 3 expression. The sustained delivery of curcumin was well analyzed according to four time durations: 2 hours, 6 hours, 12 hours and 24 hours. Viability of both HeLa and HCT 116 cells were found declining as the drug continued to get released from the Coreshell-SPIONs. As part of the imaging technique SPIONs were researched for their efficiency as contrasting agent in X – ray imaging. It was found enhancing the imaging of inner

matter of quails' egg where egg yolk was clearly visualized. SPIONs were also found responding well to the simultaneous application of X-ray in the presence of applied magnetic field. As part of the toxicity studies SPIONs were analyzed by administering them against earthworm, where it caused some impacts like erosion of epithelium, lipofuscin deposition etc. Through this study, SPIONs were found to be highly useful for carrying the desired drug (curcumin). It was found that SPIONs could be used as drug delivery vehicle in a sustained manner. SPIONs could be used as contrasting agent in X-ray imaging technique. In case of the disposal of SPIONs care must be taken.

REFERENCES

- [1] Alwi R, Telenkov S, Mandelis, Leshuk T, Gu F, Oladepo S, Michaelian K (2012), Silica-coated super paramagnetic iron oxide nanoparticles (SPION) as biocompatible contrast agent in biomedical photoacoustics, *Biomed Opt Express*, Vol. 3 (10), pp. 2500 – 2509.
- [2] Anamaria Durdureanu-Angheluta, Mariana Pinteala and Bogdan C. Simionescu (2012), Tailored and functionalized magnetite particles for biomedical and industrial applications. Centre of advanced research in bionanoconjugates and biopolymers, “PetruPoni” Institute of macromolecular chemistry of Romanian academy, Iasi, Department of natural and synthetic polymers, “Gh.Asachi” Technical university of Iasi, Iasi, Romania, DOI: 10.772/30217.
- [3] Anand Sadanandan Remya, Mathan Ramesh, Manoharan Saravanan, Rama Krishnan Poopal, Subramanian Bharathi, Devaraj Nataraj (2015), Iron oxide nanoparticles to an Indian major carp, *Labeorohita*: Impacts on hematology, ion regulation and gill Na^+ / K^+ ATPase activity, *Journal of King Saud University – Science*, Vol. 27, pp.151 -160.
- [4] Andreas Fieldler, detlef Schroder, Helmut Schwarz, Brenda L.Tjelta, and P.B. Armentrout. (1996) “Bare” Iron Methoxide Cation: A Simple Model T Probe the Mechanism of β -Hydrogen Transfer in Organometallic Compounds, TechnischeUniversitat Berlin, and University of Utah, *Journal of the American Chemical Society*, Research Gate, Vol. 118, 21, pp.5047-5055.
- [5] Apreotesei G, Badescu R, Udrea LE, Rotariu O (2007), The Study of the Magneto-Birefringence Relaxation for an Aqueous Ferrofluid on the Polyvinyl Alcohol Base, *Research and Development for Technical Physics*, Romania *Journal of Physics*, Vol. 53 (3 – 4), pp. 535 – 544.

- [6] Ashraf Shah Mohammad, Mansoor, Farooq Ahmad Dar (2017), Influence of precursor on structural, morphological and optical properties of hematite (α -Fe₂O₃) nanoparticles, Current Nanomaterials, Vol.2, pp. 1 – 6.
- [7] Asraf Shah Mohammad, Mansoor.A, Farooq Ahmad Dar (2017), Influence of Precursor on Structural, Morphological and Optical Properties of Hematite (α -Fe₂O₃) Nanoparticles, DOI: 10.2174/2405461502666170405169916
- [8] Backett. A.H (2003), A Dictionary of Chemistry, CBS Publishers & Distributers, New Delhi, India, p.150, 170.
- [9] Bersani, D.; Lottici, P. P.; Montenero, A. J. (1999), Raman Spectroscopy, Vol.30, pp.355.
- [10] Bogren Sara, Andrea Fornara, Frank Ludwig and Maria Del Puerto Morales (2015), Classification of Magnetic Nanoparticle Systems – Synthesis, Standardization and Analysis Methods, International Journal of Molecular Sciences, Vol. 16, pp. 20308 – 20325.
- [11] Bolden Nydeia Wright, Vijaya K.Rangari, and Shaik Jeelani (2008), Synthesis of Magnetic Nanoparticles and its application in Drug delivery systems, NSTI-Nanotech, vol. 2, 978-1-4200-8504-4.
- [12] BorhanMansouri, AfshinMaleki, Seyed A. Johari, NaserReshmanish (2015), Effects of cobalt oxide nanoparticles and cobalt ions on gill histopathology of zebrafish (*Danio rerio*), AACL, Bioflux, Vol. 8, issue 3.
- [13] Brime B, Moreno MA, Frutos G, Ballesteros MP, Frutos P. Amphotericin B in oil-water lecithin-based microemulsions: formulation and toxicity evaluation (2007), Journal of Pharmaceutical sciences, Vol.83, pp.1178 – 1185.
- [14] Carla I. Nieto, Pilar Cabildo, Rosa M. Claramunt, PilarCornago, DionisiaSanz, M.CarmenTorralba, M.Rosario Torres, Marta B.Ferraro, IbonAlkorta, Marta Marin-Luna, Jose Elguero (2015), The structure of β -diketones related to curcumin determined by X-ray crystallography, NMR (solution and solid state) and theoretical calculations, Springer. Struct Chem. DOI 10.1007/s11224-015-0704-7.

- [15] Cengelli F, Maysinger D, Tschudi-Monnet F, Montet X, Corot C, Petri-Fink A, Hofmann H, Juillerat-Jeanneret L, (2006), Interaction of functionalized superparamagnetic iron oxide nanoparticles with brain structures. *J. Pharmacol. Exp.* Vol. 318, pp. 108–116.
- [16] Chime S.A, and C.V.Adibe (2013), Formulation of pyridoxine hydrochloride sustained release capsules: Effect of propylene glycol co-solvent on the in vitro release, *African Journal of Pharmacy and Pharmacology*; Vol.7 (15). pp.809-815.
- [17] Choi Yongo, Terry Yi, Joo Seik Park, and Do Kyung Kim (2011), Electron spin resonance (ESR) and Microwave absorption studies of superparamagnetic iron oxide nanoparticles (SPIONs) for hyperthermia applications, *Journal of the Korean Ceramic Society*, Vol. 48, No.6, pp. 577 – 583.
- [18] Cortajarena L Aitziber, Daniel Ortega, Sandra M.Ocampo, Alberto Gonzalez-Garcia, Pierre Couleaud, Rodolfo Miranda, Cristobal Belda-Iniesta, and Angel Ayuuso-Sacido (2014), Engineering Iron oxide nanoparticles for clinical settings, *Nanobiomedicine*.
- [19] Cristina Iuga, Rodolfo Esquivel Olea, AnnikViver-Bunge (2008), Mechanism and Kinetics of the OH Radical Reaction with Formaldehyde Bound to an (SiOH)₄ Monomer, Department of de Quimica Universidad Autonoma Metropolitana, Iztapalapa, J. Mex. Chem. Soc., p.39.
- [20] Crowley LC, Brooke J. Marfell, and Nigel J (2016), Analyzing Cell Death by Nuclear Staining with Hoechst 33342. *Waterhouse Cold Spring HarbProtoc*; doi:10.1101/pdb.prot087205
- [21] Dan Mo, David B Cochran, Robert A Yokel, Thomas D Dziubla (2013), Binding, Transcytosis and Bio distribution of Anti-PECAM-1 iron oxide nanoparticles for brain-targeted delivery, *PLoS One*, Vol. 8 (11), e81051.

- [22] Delly Gustav John (2008), *Essentials of Polarized Microscopy*, College of Microscopy, Westmont, Illinois, 600559 – 5539.
- [23] Dolgovskiya V, Lebedev V, Colombo S, Weis A, Michen B, Ackermann-Hirschi, Petri-Fink (2015), A Quantitative Study of particle Size Effects in Magnetorelaxometry of Magnetic Nanoparticles Using Atomic Magnetometry, *Journal of Magnetism and Magnetic Materials*, Vol. 379, pp. 13 – 150.
- [24] Edge Deirdre, Christine M Shortt, Oliviero L Gobbo, Stephanie Teughels (2016), Pharmacokinetics and bio-distribution of novel superparamagnetic iron oxide nanoparticles (SPIONs) in the anaesthetized pig, *Clinical and Experimental Pharmacology*, Vol. 43 (3), 1440 -1681.
- [25] Fleischer C Candace and Christine K Payne (2014), Nanoparticle-Cell Interactions: Molecular structure of the protein corona and cellular outcomes, *Accounts of Chemical Research*, Vol. 47(8), pp. 2651 – 2659.
- [26] Gash E Alexander, Thomas M Tillotson, Joe H Satcher, John F Poco, Lawrence W Hrubesh, Randall L Simpson (2001), Use of Epoxides in the Sol-Gel synthesis of porous iron (III) oxide monoliths from Fe(III) salts, *Chem. Mater*, Vol.10, pp.1021.
- [27] GobaDhar, DevlinaChakravarty, JoyitaHazra, JesmitaDhar, AsimPoddar, Mahadeb Pal, PinakChakrabarti, AvadhshaSurolia, and Bhabatarak Bhattacharya (2015), Actin-curcumin interaction: Insights into the mechanism of actin polymerization inhibition. *Pubmed. Biochemistry*, Vol.54,4, pp.1132-1143.
- [28] Gupta Ajay Kumar, Rohan R Naregalkar, Vikas Deep Vaidya, and Mona Gupta (2007), Recent advances on surface engineering of magnetic iron oxide nanoparticles and their biomedical applications, *Nano medicine*, Vol. 2 (1), pp.23-39.
- [29] Hasany SF, Ahmed I, Rajan J, Rehman A (2012), Systematic review of the preparation techniques of iron oxide magnetic nanoparticles, *Nanoscience and Technology*, Vol. 2 (6), pp. 148 – 158.

- [30] Hauff Klaus, Frank Ulrich, Dirk Nestler, Hendrik Niehoff, Peter Wust, Burghard Thiesen, Helmut Orawa, Volker Budach (2011), Efficacy and safety of intratumoral thermotherapy using magnetic iron-oxide nanoparticles combined with external beam radiotherapy on patients with recurrent glioblastoma multiforme, *Journal of Neurooncology*, Vol. 103 (2), pp. 317 – 324.
- [31] Heiman Don (2009), *Nanomagnetism*, Physics U600 – Advanced Physics Lab, Northeastern University, 6/3/09.
- [32] Hong Cheol Seong, Jong Ho Lee, Jaewook Lee, Hyeon Young Kim, Jung Youn Park, Johann Cho (2011), Subtle cytotoxicity and genotoxicity differences in superparamagnetic iron oxide nanoparticles coated with various functional groups, *Int J Nanomedicine*, Vol. 6, pp. 3219 – 3231.
- [33] Huang Gang, Huabing Chen, Ying Dong, Xiuquan Luo, Haijun Yu, Zachary Moore, Erik A. Bey, David A. Boothman, Jinming Gao (2013), Superparamagnetic iron oxide nanoparticles: Amplifying ROS stress to improve anticancer drug efficacy. *Ivyspring, Theranostics*, Vol. 3(2), pp.116 – 126.
- [34] Illes E, Szekeres M, Toth IY, Farkas K, Foldesi I, Szabo A, Ivan B, Tombacz E (2018), PEGylation of superparamagnetic iron oxide nanoparticles with self-organizing polyacrylate-PEG brushes for contrast enhancement in MRI diagnosis, *Nanomaterials*, Vol. 8 (10).
- [35] James S. Wright (2002), Predicting the antioxidant activity of curcumin and crucuminoids. Elsevier, *Journal of molecular structure (Theochem)*, Vol. 591, pp.207-217.
- [36] Jendalova Pavla, Hervnek Vit, Lucia Machova, Katerina Glogarova (2004), Magnetic resonance tracking of transplanted bone marrow and embryonic stem cells labelled by iron oxide nanoparticles in rat brain and spinal cord, *Journal of Neuro Science Research*, Vol. 76(2), pp 232 – 243.

- [37] Jian Li, Xiaodong Liu, Yueniang Lin, Xiaoyan Oiu (2004), Field Induced Transmission of Light in Ionic Ferro-fluids of Tunable Viscosity, *Journal Physics and Applied Physics*, Vol. 37 (24): 3357.
- [38] Jitianu Andrei, Crisan M, Aurelia Meghea, Ileana Rau (2002), Influence of the silica based matrix on the formation of iron oxide nanoparticles in Fe₂O₃ – SiO₂ system, obtained by sol-gel method, *Journal of Material Chemistry*, Vol.12, pp.1401 – 1407.
- [39] Jonathan Roger Woodward (2016), *Radical Pairs in Solution*, Research gate, p.168.
- [40] Jun Young-Wook, Huh Yong-Min, Ji-Sil Choi, Jae-Hyun Lee, Ho-Taek (2005) Nanoscale Size Effect of Magnetic Nanocrystals and Their Utilization for Cancer Diagnosis via Magnetic Resonance Imaging, *J. Am. Chem. Soc.* 2005127165732.
- [41] Kandasamy Ganeshlenin and DipakMaity (2015): Recent advances in superparamagnetic iron oxide nanoparticles (SPIONs) for *in vitro* and *in vivo* cancer nanotheranostics, *International Journal of Pharmaceutics*, Elsevier, Vol. No. 496, pp.191-218.
- [42] Kavirayani Indira and Priyadarsini (2014), The chemistry of curcumin: From extraction to therapeutic agent, *Molecules*, Vol.19 (12), pp.20091-20112.
- [43] Khan Ibrahim, Khalid Saeed, Idreeskhan (2017), Nanoparticles: Properties, applications and toxicities, *Arabian Journal of Chemistry*, pp. 1-24
- [44] Khoshnevisan.K and Barkhi. M (2015), Information about Zeta Potential, Institute of Agricultural Biotechnology, Nano Department, Iran. ResearchGate, DOI: 10.13140/RG.2.1.4554.3844.
- [45] Kievit M Forrest and Miqin Zhang (2011), Surface engineering of Iron oxide nanoparticles for targeted cancer therapy, *Accounts of chemical research*, 10.1021/ar2000277.

- [46] Klaus Schulten and Albert Weller Exploring Fast Electron Transfer Process by Magnetic Fields, Max Plank Institute for Biophysikalische Chemie, Abteilung Spektroskopie, D 3400 Gottingen, Germany, pp.295-303.
- [47] Klein S, Sommer A, Distel LV, Hazemann JL, Kroner W, Neuber W, Muller P, Proux O, Kryschi C (2014), Superparamagnetic iron oxide Nanoparticles as X-ray enhancer for low-dose radiation therapy, PubMed, J Phys Chem B.
- [48] Kolev M Tsonko, Evelina A, Velcheva, Bistra A. Stamboliyska, Michael Spiteller (2005), DFT and experimental studies of the structure and vibrational spectra of curcumin, International Journal of Quantum chemistry, Vol. 102/6, pp.1069-1079.
- [49] Konczol M, Ebeling S, Goldenberg E, Treude F, Gminski R, Giere R, Grobety B (2011), Cytotoxicity and genotoxicity of sie-fractionated iron oxide (magnetite) in A549 human lung epithelial cells: role of ROS, JNK, and NF-kB, Chem Res Toxicol, Vol. 24(9), pp. 1460 – 1475.
- [50] Krishnan P, Rajan M, Kumari S, Sakinah S, Priya SP, Amira F, Danjuma L, Pooi Ling M, Fakurazi S, Arulselvan P, Higuchi A, Arumugam R, Alarfaj AA, Munusamy MA, Hamat RA, Benelli G, Murugan K, Kumar SS (2017), Efficiency of newly formulated camptothecin with β -cyclodextrin-EDTA-Fe₃O₄ nanoparticle-conjugated nanocarriers as an anti-colon cancer (HT29) drug. Vol. 7(1):10962. doi: 1038/s41598-017-09140-1.
- [51] Kwatra Deep, Anand Venugobal, Shrikant Anant (2013), Nanoparticles in radiation therapy: a summary of various approaches to enhance radiosensitization in cancer, Translational Cancer Research, Vol. 2, No. 4, pp. 330 – 342.
- [52] Lam Tina, Pramod K. Avti, Philippe Pouliot, Fued Maafi, Jean-Claude Tardif, Eric Rheume, Frederic Lesage, and Ashok Kakkar (2016), Fabricating water dispersible superparamagnetic iron oxide nanoparticles for biomedical applications through ligand exchange and direct conjugation, MDPI, Nanomaterials, Vol. 6, pp.100

- [53] Laurent Sophie, Delphine Forge, Marc Port (2008), Magnetic iron oxide nanoparticles: Synthesis, stabilization, vectorization, physiochemical characterizations and biological applications; Department of general organic, and biomedical chemistry, NMR and molecular imaging laboratory, University of Mons-Hainaut, Belgium and Guerbet de Recherche, Chem.Rev, pp. 2064.
- [54] Layek Samar, Anjana Pandey, Ashutosh Pandey, and H.C.Verma (2010), Synthesis of γ -Fe₂O₃ nanoparticles with crystallographic and magnetic texture MultiCarft, International Journal of Engineering, Science and Technology, Vol.2, No. 8, pp.33-39.
- [55] Lei Li, Jiang Ling-Ling, Zeng Yun, Liu Gang (2013), Magnetism, magnetic materials and interdisciplinary research Toxicity of superparamagnetic iron oxide nanoparticles: research, strategies and implications for nanomedicine, Chin. Phys., Vol. 22, No. 12, pp. 127503.1 – 10.
- [56] Linderoth S, Peter Vang Hendriksen, Fran Bodker, Stephan Wells (1994), On Spin-canting in Maghemite Particles, Journal of Applied Science, Vol. 75 (10), pp. 6583 – 6585.
- [57] Lodhia J, Giovanni Mandarano, Nicholas J Ferris and Peter Eu (2010), Development and Use of Iron Oxide Nanoparticles (Part 1): Synthesis of Iron Oxide Nanoparticles for MRI, Biomedical Imaging and Intervention Journal, Vol 6 (2): e12.
- [58] Madan R.L. (2015), Chemistry for Degree Students, SW.Chand& Company Pvt.Ltd, Ram Nagar, New Delhi, p.12, 18.
- [59] Magro Massimiliano, Rene Campos, DavideBaratella, Giuseppian Lima, Katerina Hola, Clemens Divoky, Rudolf Stollberger, OndrejMalina, Claudia Aparicio, Giorgio Zappellaro, RadekZboril, and Fabio Vianello (2014), A magnetically drivable nanovehicle for curcumin with antioxidant capacity and MRI relaxation properties. Chem.Eur.J, Vol.20,pp-1-9.

- [60] Mahdavi Mahnaz, Mansor Bin Ahmad, MdJelasHaron, FaridehNamvar, BehzadNadi, Mohamad Zaki Ab Rahman and Jamileh Amin (2011), Synthesis, surface Modification and characterization of biocompatible magnetic iron oxide nanoparticles for biomedical applications, *Molecules* Vol.18, pp.7533-7548.
- [61] Mahmoudi Morteza, Shilpa Sant, Ben Wang, Sophi Laurent, Tapas Sen (2011), Superparamagnetic iron oxide nanoparticles (SPIONs): Development, surface modifications and applications in chemotherapy. *Advanced Drug Delivery. Reviews, Elsevier, Vol. 63, pp.24-46*
- [62] Mandy H.M.Leung, Takaaki Harada and Tak W. Kee (2013), Delivery of curcumin and Medicinal effects of the Copper (II)-curcumin complexes. *Current pharmaceutical design, Vol.19, pp.2070-2083*
- [63] Martindale (2012), *The complete drug reference, (36thEdn). London Pharmaceutical Press, Vol. 100(1), pp.75-76*
- [64] Martinez-Boubeth C, Simeonidis K, Makridis A, Angelakeris M, Iglesias O, Guardia P, Cabot A, Yedra L, Estrade S, Peiro F, Saghi Z, Midgley PA, Conde-Leboran I, Serantes D, Baldomir D (2013), Learning from nature to improve the heat generation of iron oxide nanoparticles for magnetic hyperthermia applications. *Sci Rep* 3:162.
- [65] Maurizi Lionel, Alexis Claveau, Heinrich Hofmann (2015), Polymer adsorption on iron oxide nanoparticles for one-step amino-functionalized silica encapsulation, *Journal of Nanomaterials, Vol. 2015, ID 732719, pp.1 – 6.*
- [66] McCarthy Jason R and Ralph Weissleder (2008), Multifunctional magnetic nanoparticles for targeted imaging and therapy, *National Institutes of Health, Adv Drug Deliv Rev, Vol. 17, 60(11), pp. 1241 – 1251.*
- [67] Melessa Salem, SohrabRohani, and Elizabeth R. Gillies (2014), Curcumin, a promising anti-cancer therapeutic: a review of its chemical properties, bioactivity and approaches to cancer cell delivery, *Royal Society of Chemistry, RSC Adv.,4,10815*

- [68] Michel Picquart (1986), Vibrational mode behavior of SDS aqueous solutions studied by Raman scattering, Laboratoire de physique moleculaire et biologique, Universite Rene Descartes, Vol.45, p.75270
- [69] Mitchell E, De Souza and Gupta R.K (2014), Probing on the hydrothermally synthesized iron oxide nanoparticles for ultra-capactor applications, Department of Chemistry, Pittsburg State University, Pittsburg, Powder technology, Vol.272, pp.295-299
- [70] Mohan Krishna P.R, Sreelakshmi G, Muraleedharanc.V, Roy Joseph (2012), Water soluble complexes of curcumin with cyclodextrins: Chrectrization by FT-Raman spectroscopy. Elsevier, Vibrational spectroscopy Vol. 62, pp.77-84.
- [71] Morrish A, Haneda K, Schurer, P (1976), Surface Magnetic Structure of Small γ -Fe₂O₃ Particles, Journal of de Physique Colloques, Vol. 37 (C6), pp.C6-301-C6305.
- [72] Morsy M.I. Salwa (2014), Role of surfactants in nanotechnology and their applications, International journal of current microbiology and applied sciences, Vol. 5, pp.237-260).
- [73] Nandwana Vikas, Mrinmoy De, Shihao Chu, Manish Jaiswal, Matt Rotz, Thomas J Meade (2015), Theranostic Magnetic Nanostructures (MNS) for cancer, US National Library of medicine, Cancer Treat Res Vol. 166, pp. 51 – 83.
- [74] Nano Composix.com (2012), Zetapotential analysis of nanoparticles, Nano Composix, 4878 Ronson CT STEK V.11, pp. 1 – 6.
- [75] Nanocomposix (2012), Zeta potential analysis of nanoparticles, Nano Composix. San Diego, Vol. 1.1
- [76] Narang S. Ajith, David Delmarre, Danchen Gao (2007), Stable drug encapsulation in micelles and microemulsions. International journal of Pharmaceuticals, Elsevier, Vol. 345, pp.9 – 25.

- [77] Nedkov Ivan, Robert E Vandenberghe, Marinova, Thailhades (2006), Magnetic structure and collective Jahn-Teller distortions in nanostructured particles of CuFe₂O₄, Applied Nano Science, Vol. 253 (5), pp. 2589 – 2596.
- [78] Neenu Sing, Gareth JS, Jenkins, Romisa Asadi, Shareen (2010), Potential toxicity of superparamagnetic iron oxide nanoparticles (SPION), Nano Reviews, Vol.1:10, 3402.
- [79] Onyishi, S.A.Chime, and C.V.Adibe (2013), Formulation of pyridoxine hydrochloride sustained release capsules: Effect of propylene glycol co-solvent on the in vitro release. African Journal of Pharmacy and Pharmacology; Vol.7 (15). pp.809-815
- [80] Panta and Bergmann (2015), Raman spectroscopy of iron oxide nanoparticles (Fe₃O₄). Journal of Material Sciences and Engineering, Vol. 5 (1), 10.4172.
- [81] Quanguo He, Changzhong (2008), Magnetic iron oxide nanoparticles: synthesis and surface functionalization strategies, Nanoscale Res Lett. Vol. 3 (11), pp. 397 – 415.
- [82] Rachmawati Heni, Citra Ariani Edityaningrum and Rachmat Mauludin (2013), Molecular inclusion complex of curcumin- β -cyclodextrin nanoparticles to enhance curcumin skin permeability from hydrophilic matrix gel. Springer, AAPS Pharm Sci. Tech, Vol. 14 (4), pp. 1303 – 1312.
- [83] Radjaram Achmad, AchmadFuadHafid, DwiSetyawan (2013), Dissolution enhancement of curcumin by hydroxypropyl- β -cyclodextrin, 5 (suppl 3), pp.401-405. Sasha Vega-Alvarez, Adrina Herrera, Carlos Rinadi, Franklin A Carrero-Martine (2014), Tissue-specific direct microtransfer of nanomaterials into *Drosophila* embryos as a versatile *in vivo* test bed for nanomaterial toxicity assessment, International journal of nanomedicine, Vol.9, pp. 2031-2061.
- [84] Retif Paul, Sophie Pinel, Magali Toussaint, Celine Frochot, Rima Chouikrat, Thierry, Bastogne, Muriel Barberi-Heyob (2015), Nanoparticles for radiation therapy enhancement: the Key parameters. Ivyspring, Theranostics vol.5/9, pp. 1030-1044.

- [85] Sakai S, Yamada Y, Zenke T, Kawakami K (2009), Novel chitosan derivative soluble at neutral pH and in-situ gellable via peroxidase-catalyzed enzymatic reaction. *Journal of Materials Chemistry.*, Vol. 19(2), pp. 230-235.
- [86] Saravanan. M, Suganya.R, Ramesh.M, PoopalR.K, Gobalan.N, Ponpandian.N. (2015), Iron oxide nanoparticles induced alterations in haematological, biochemical and ionoregulatory responses of an Indian major carp *Labeorohita*, *J nanopart Res*, Vol.17, p.274.
- [87] Schleich N, P. Sibret, P. Danhier, B. Ucakar, S. Laurent, R.N. Muller, C. Jerome, B. Gallez, V. Preat, F. Danhier (2013), Dual anticancer drug/superparamagnetic iron oxide-loaded PLGA-based nanoparticles for cancer therapy and magnetic resonance imaging, Elsevier, *International Journal of Pharmaceutics*, Vol. 447, pp. 94 – 101.
- [88] Seong Cheol Hong, Jong Ho Lee, Jaewook Lee, Hyeon Yong Kim, Jung Youn Park, Johann Cho, Jaebeom Lee, Dong-Wook Han (2011), Subtle cytotoxicity and genotoxicity differences in superparamagnetic iron oxide nanoparticles coated with various functional groups, *International Journal of Nanomedicine*, Vol. 6, pp. 3219 – 3231.
- [89] Sharma Gaurav, Amitkumar, Shweta Sharma, Mu Naushad, Ram Prahash (2019), Novel development of nanoparticles to bimetallic nanoparticles and their composites: A review, *Journal of King Saud University – Science*, Vol.31, Issue 2, pp.257- 269
- [90] Sherman R (2003) Raising earthworms successfully. North Carolina Cooperative Extension Service, EBAE. 103-83
- [91] Shinji Sakai, Yusuke Yamada, Takashi Zenke and Koei Kawakami (2008), Novel chitosan soluble at neutral P^H an in-situ gellable via peroxidase-catalyzed enzymatic reaction; *Journal of Material Chemistry*, Vol.19, pp.230-235.
- [92] Shubayev Veronica, Thomas R Pisanic, Sungho Jin (2009), Magnetic Nanoparticles for Theranostics, *Advanced Drug Delivery Reviews*, Vo. 61 (6), pp. 467 – 477.

- [93] Soenen SJ, Nuytten N, De Meyer SF, De Smedt Sc, De Cuyper M (2010), High intracellular iron oxide nanoparticles concentration affect cellular cytoskeleton and focal adhesion kinase mediated signaling, Vol.6, pp.832 – 842.
- [94] Sophie Laurent, Delphine Forge, Marc Port et al (2008), Magnetic iron oxide nanoparticles: Synthesis, stabilization, vectorization, physicochemical characterizations and biological applications; Department of general organic, and biomedical chemistry, NMR and molecular imaging laboratory, University of Mons-Hainaut, Belgium and Guerbet de Recherche, France, Chem.Rev, p2064
- [95] Sruthi PD, Sahithya CS, Justin C, SaiPriya C, Bhavya KS, Senthilkumar P, Samrot AV (2018), Utilization of Chemically Synthesized Super Paramagnetic Iron Oxide Nanoparticles in Drug Delivery, Imaging and Heavy Metal Removal, Journal of Cluster Science DOI: 10.1007/s10876-018-1454-7
- [96] Steiner E Ulrich and Thomas Ulrich (1989), Magnetic field effects in chemical kinetics and related phenomena. Revised Manuscript – 1968, Chem. Rev. Vol. 89, pp. 51-147
- [97] Sushilkumar A. Jahav and Roberta Boniovanni (2012), Synthesis and organic functionalization approaches for magnetite (Fe_3O_4) nanoparticles. Adv.Mat.Lett., Vol. 3(5), pp.356-3361.
- [98] Tartaj P. Morales MP, Veintemillas S, Gonzalez Carreno T Serna CJ (2013), The preparation of magnetitic nanoparticles for applications in biomedicine, Journal of Physics and Applied Physics, cross reference, V. 36 R 182.
- [99] Teran Francisco Jose, Casado C, Nikolai Mikuszeit, Salas G (2012), Accurate determination of the specific absorption rate in superparamagnetic nanoparticles under non-adiabatic conditions, Applied Physics Letters, Vol. 101(6), pp.062413.
- [100] Tharani K and Nehru LC (2015), Synthesis and Characterization of Iron Oxide Nanoparticle by Precipitation Method, International Journal of Advanced Research in Physical Sciences (IJARPS), Vol. 2, pp. 47 – 50.

- [101] Thorek J Daniel, Antony K Chen, Julie Czupryna, and Andrew Tsourkas (2006), Superparamagnetic iron oxide nanoparticle probes for molecular imaging, *Annal of Biomedical Engineering*, Vol. 34, No.1, pp. 23 – 38.
- [102] Tombacz, Toth. I.Y, Neszztor, E.Illes, Hajdu.A, Szekeres.M, Vekas.L (2013), Absorption of organic acids on magnetite nanoparticles, pH-dependent colloidal stability and salt tolerance, *Colloids and Surfaces*, Vol.435 pp.91 –96
- [103] Totsuka Yukhan, Kousuke Ishino, Tatsuya Kato, Sumio Goto, Yukie Tada, Dai Nakae et al (2014), Magnetite nanoparticles induce genotoxicity in the lungs of mice via inflammatory response, *Nanomaterials*, Vol. 4(1), pp. 175 – 188.
- [104] Vikram. S, M.Dhaksnamoorthy, R.Vasanthakumari, A.R.Rajamani, Murali Rangarajan, and Takuya Tsuzuki (2015), Tuning the Magnetic properties of iron oxide nanoparticles by room-temperature air-atmosphere (RTAA) co-precipitation method, *Journal of Nanoscience and Nanotechnology* ,American scientific publishers, Vol.15, pp.3870-3878.
- [105] Wahajuddin, Sumit Arora (2012), Superparamagnetic iron oxide nanoparticles: magnetic nanoplatforms as drug carriers, *International Journal of Medicine*, Vol.7, pp. 3445 – 3471.
- [106] Wang Jun, Baoan Chen, Nan Jin, Guohua Xia, Yue Chen, Ying Zhou, Xiaohui Cai, (2011), The changes of T lymphocytes and cytokines in ICR mice fed with Fe₃O₄ magnetic nanoparticles, *International Journal of Nanomedicine*, Vol.6, pp. 605 – 610.
- [107] Wang X, Niessner R and Knopp D. Magnetic Bead-Based Colorimetric Immunoassay for Aflatoxin B1 Using Gold Nanoparticles Sensors (2014), Vol. 14(11), pp. 21535-21548.
- [108] Whitmore.G. (2009), *Chemical Crystallography and Liquid Crystals*, Sarup Book Publishers Pvt.Ltd, New Delhi, p.72.

- [109] Williams Marc, Enrique Sánchez, Esther Rani Aluri, Fraser J. Douglas, Donald A. MacLaren, Oonagh M. Collins Edmund J et al (2016), Microwave-assisted synthesis of highly crystalline, multifunctional iron oxide nanocomposites for imaging applications, RSV Adv, Vol. 6, pp. 83520 – 83528.
- [110] Won Jun Yang, Jong Ho Lee, Seong Cheol Hong, Jaewook Lee, Jaebeom Lee (2013), Difference between toxicities of iron oxide magnetic nanoparticles with various surface-functional groups against human normal fibroblasts and fibrosarcoma cells. Materials, Vol.6, pp. 489 – 4706.
- [111] Xiaoming Li, Lu Wang, Yubo, Quingling Fen, Fu-zhai Cui (2012), Biocompatibility and toxicity of Nanoparticles and nanotubes, Vol.2012, Article ID 548389, pp.19.
- [112] Xiaoshan Zhu, shengyan Tian, ZhonghuaCai (2012), Toxicity assessment of iron oxide nanoparticles in zebrafish (*Danio rerio*) early life stages, PLOS ONE, Vol. 7, issue 9, e46286
- [113] Xie Jin and Sangyong Jon (2012), Magnetic Nanoparticles-Based Theranostics, Theranostics , Vol. 2 (1), pp 122 – 124
- [114] Xu Piao, Guang Ming Zeng, Dan Lian Huang, Chong Ling Feng, Shuang Hu, Mei Hua Zhao, Cui Lai, Zhen Wei, Chao Huang, Geng Xin Xie, Zhi Feng Liu (2012), Use of iron oxide anomaterials in aste water treatment, Elsevier, Science of the Total Environment, Vol. 424, pp.1 – 10.
- [115] Yadav M S (2001), Chemistry of Transition Metals, Dominant Publishers and Distributors, New Delhi, p 45.
- [116] Yadollahpour Ali (2015), Magentic nanoparticles in medicine: A review of synthesis methods and important characteristics, Orient J Chem, ISSN: 0970 – 020X, online ISSN: 2231 – 5039.
- [117] Yang Won Jun, Jong Ho Lee, Seong Cheol, Hong, Jaewook Lee, Dong Wook Han (2013), Difference between toxicities of iron oxide magnetic nanoparticles with various surface functional groups against human normal fibroblasts and fibrosarcoma cells, Materials, Vol. 6 (10), pp. 4689 – 406.

- [118] Yi Zhang, Zhuyao Wang, Xiaojiao Li, Lu Wang, Min Yin, Lihua Wang, Nan Chen, Chunhai Fan, and Haiyun (2015), Dietary iron oxide nanoparticles delay aging and ameliorate neurodegeneration in *Drosophila*, *Advanced Materials*, Vol. 28, pp.1387-1393
- [119] Yiteng Zhang, Gennady P.Berman, Sabre Kais (2015), Radical Pair Mechanism and Avian Chemical Compass: Quantum Coherence and Entanglement, Department of physics and Astronomy, Purdue University, West Lafayette, IN, 47907, p.3.
- [120] Zhang Jin, Christopher Q.Lan, Michael Post, Benoit Simard, Yves Deslandes, and Tsung Han Hsieh (2006), Design of nanoparticles as drug carriers for cancer therapy, *Cancer genomics and proteomics*, Vol.3, pp.147-158
- [121] Zhang, Z.; Wei, B. Q.; Ajayan, P. M. *Appl. Phys. Lett.* (2001), 79, 4207. (b) Hu, X.; Yu, J. C.; Gong, J. J. *Phys. Chem. C* (2007), 111, 11180
- [122] Ziyun Di, Xianfeng Chen, Shengli Pu, Xio Hu, and Yuxing Xia (2006), Magnetic Field-Induced Birefringence and Particle Agglomeration in Magnetic Fluids, *Applied Physics. Lett.* 89, 211106.

LIST OF PUBLICATIONS

1. **C. Justin**, Sheryl Ann Philip, Antony V. Samrot (2017), Synthesis and Characterization of Superparamagnetic Iron Oxide Nanoparticles (SPIONs) and Utilization of SPIONs in X-ray Imaging. *Published online: 20th August 2017*. Appl Nanoscience, Vol. 7, pp. 463 – 475 DOI 10.1007/s 13204-017-0583. (Impact Factor 2.951).
2. **C. Justin**, Antony V Samrot, Durga Sruthi P., Chamarthi Sai Sahithya, Karanam Sai Bhavya, C.Saipriya (2018), Preparation, Characterization and Utilization of Coreshell Superparamagnetic Iron Oxide Nanoparticles for Curcumin Delivery. *Published July 18, 2018*. PLoS ONE, Vol. 13 (7), pp. 1 – 18 e0200440. (Impact Factor 2.77).
3. Antony V. Samrot, **C. Justin**, S. Padmanaban, Ujjala Burman (2017), A Study on the Effect of Chemically Synthesized Magnetite Nanoparticles on Earthworm: *Eudrilus eugeniae*. *Published online: 1 December 2016*. Appl Nanosci, Vol. 7, pp. 17 – 23 DOI 10.1007/s13204-016-0542. (Impact Factor – 2.951).
4. **Justin Chellapan**, Antony Vincent Samrot, An Arun Annamalai, Raikamal Bhattacharya, Padmanaban Sathyamoorthy, and Chamarthi Sai Sahithya (2018), Biopolymer Coated Coreshell Magnetite Nanoparticles for Rifampicin Delivery, Oriental Journal of Chemistry, Vol. 34, No. 5, pp.2389 – 2396. (Impact Factor 0.17).
5. Durga Sruthi P, Chamarthi Sai Sahithya, **Justin C**, Saipriya C, Karanam Sai Bhavya, Senthil Kumar P, Antony V Samrot (2018), Utilization of Chemically Synthesized Super Paramagnetic Iron Oxide Nanoparticles in Drug Delivery, Imaging and Heavy Metal Removal, Journal of Cluster of Science, Vol. 10. 1007/s10876-018-1454-7. (Impact Factor 1.74).

International conference

1. **Justin C**, Durga Sruthi P, C Sai Sahithya, Saipriya et all. Chemically Synthesized SPIONs/metal Coupled SPIONs and its Application as Theranostic Agent. Sathyabama Institute of Science and Technology. ICBHE-2018. OP – 14a. 08th – 10th Jan 2018. ISBN: 978-93-83490-40-2.

CURRICULUM VITAE

I, Fr. Justin C, was born on 18th December, 1974 at Nadaikkavu, Kanyakumari (District) – 629153, Tamilnadu, India. I did primary education in St. Antony's MSC School, Methukummal and high school education in Mar Gregorios MSC school, Kirathoor. After the school education I joined in St. Aloysius Minor Seminary for the formation of Priesthood and secured Pre-degree from Kerala University. As part of the next level of Priestly Formation, I was send to Malankara Major Seminary, Thiruvananthapuram, Kerala, where I studied philosophy and simultaneously secured Bachelor's Degree in Philosophy from the University of Kerala. I studied Theology in St Mary's Malankara Seminary for four years and became an Ordained Catholic Priest in 2001, December, at Kristu Raja Church, Nadaikkavu, for the Diocese of Marthandom. Out of my curiosity in Science and having felt the need of a Priest who knows the trends of science, the then Bishop of Marthandom, Yoohanon Mar Chrysostom allowed me to take up Biotechnology as my career. Accordingly, I completed BSc in Biotechnology in Thanthai Hans Rover College, Perambalore, and secured the Degree of Bachelor of Science, in 2008, from Bharathidasan University, Trichy. I did Master's Degree in Loyola College, Chennai and obtained Degree of Master of Science in Biotechnology from the University of Madras, in 2010. I started the Ph.D. Research program in the field of Drug Delivery in 2013 in Sathyabama University. Currently I am doing the ministry of education in St. Joseph's Public School (CBSE), Chemboor, and rendering the Pastor's Service in the Diocese of Parasala, Thiruvanthapuram, Kerala. I have published five scientific papers in well reputed journals with good impact factor. I have presented the research work in national and international seminars.